

Sung In Jeong

# Comparative Study of Linear Oscillating Generators



Cuvillier Verlag Göttingen  
Internationaler wissenschaftlicher Fachverlag



## Comparative Study of Linear Oscillating Generators





# Comparative Study of Linear Oscillating Generators

Von der Fakultät für Elektrotechnik, Informationstechnik, Physik  
der Technischen Universität Carolo-Wilhelmina zu Braunschweig

zur Erlangung des Grades eines Doktors  
der Ingenieurwissenschaften (Dr.- Ing.)

genehmigte Dissertation

von : Sung In Jeong  
aus : Seoul, Süd Korea

eingereicht am : 08. 07. 2015  
mündliche Prüfung am : 18. 08. 2015

1. Referent : Prof. Dr. -Ing. Wolf-Rüdiger Canders  
2. Referent : Prof. Dr. -Ing. Michael Kurrat  
Prof. Dr. -Ing. Jürgen Meins

2015



Dissertation an der Technischen Universität Braunschweig,  
Fakultät für Elektrotechnik, Informationstechnik, Physik





## **Bibliografische Information der Deutschen Nationalbibliothek**

Die Deutsche Nationalbibliothek verzeichnet diese Publikation in der Deutschen Nationalbibliografie; detaillierte bibliografische Daten sind im Internet über <http://dnb.d-nb.de> abrufbar.

1. Aufl. - Göttingen: Cuvillier, 2015

Zugl.: (TU) Braunschweig, Univ., Diss., 2015

© CUVILLIER VERLAG, Göttingen 2015

Nonnenstieg 8, 37075 Göttingen

Telefon: 0551-54724-0

Telefax: 0551-54724-21

[www.cuvillier.de](http://www.cuvillier.de)

Alle Rechte vorbehalten. Ohne ausdrückliche Genehmigung des Verlages ist es nicht gestattet, das Buch oder Teile daraus auf fotomechanischem Weg (Fotokopie, Mikrokopie) zu vervielfältigen.

1. Auflage, 2015

Gedruckt auf umweltfreundlichem, säurefreiem Papier aus nachhaltiger Forstwirtschaft.

ISBN 978-3-7369-9117-0

eISBN 978-3-7369-8117-1



## Acknowledgements

The dissertation work was done during my career as scientific research assistant at Institute for Electrical Machines, Traction and Drives, IMAB, in Technical University Braunschweig.

First, I would like to express my sincere gratitude to Prof. Dr.-Ing. Wolf-Rüdiger Canders for provided me very good topic for my dissertation. His valuable guidance on my work contributed greatly to the dissertation work. My special thanks go to Prof. Dr.-Ing. Jürgen Meins for accepting the role as head of the examination committee. My foremost thanks also go to Prof. Dr.-Ing. Michael Kurrat who shows interest in my work as well as for being my co-examiner.

I thank Prof. Dr.-Ing. Markus Henke, Director of IMAB for his interest and concern. My special thanks go to Dipl.-Ing. Jan Hoffmann from IMAB who took responsibility for the manufacture and experiment of the test bench. I would like to acknowledge all the colleagues at IMAB who accompanied me by making the work very enjoyable and memorable. I thank Dipl.-Ing. Quirin Maurus and Frau Barbara Tiedge for all their support.

I would like to express deep gratitude to Dr.-Ing. Dohyun Kang of Korea Electrotechnology Research Institute, KERI, in South Korea, for his encouragement and advices that helped to shape my research skills. I thank Ph. D. Yondo Chun of KERI for his friendly solicitude. I also thank all seniors and juniors including of Energy Conversion Laboratory, ECL, at Hanyang University in South Korea, for their motivation and support.

I would like to express my heartfelt gratitude to Prof. Ph. D. Ju Lee, Director of ECL for the financial support and for the unbounded interest and solicitude. His unspoken encouragement provided me with another teaching.

I am really grateful to all my family members and especially my mother Jeongsoon An for giving me moral support. I am also grateful to my wife Jonghee Ha, my daughter Jiwon and my son Jiwoo for their patience and who made me happy.

Finally, I devote this dissertation in front of portrait of the deceased of my father, Jinmoon Jeong who passed away during these times.

Braunschweig, September 2015





## Abstract

This thesis presents the comparative study of linear oscillating generators for hybrid electric vehicle application. The focus of the work is the suggestion of the optimal model through the comparison of each topology. First of all, there are five topologies of the proposed to this study on the basis of the existing literatures ; Cartesian topology, cylindrical topology, hybrid stepping generator, cylindrical reluctance machine, and transverse flux machine. All topology is achieved using equivalent magnetic circuit considering leakage elements as initial modeling.

First, the proposed topology is Cartesian topology with ironless translator. It is investigated by number of phases and number of pole pairs. In addition, the optimal process is performed by parameter studies of the design variables under the constraints. Second, cylindrical topology with back-iron translator is described by number of phases and displacement of stroke. Thirdly, new flux concentrating PMs mover of the hybrid stepping generator is proposed based on the symmetrical and non symmetrical stator cores of the surface mounted PMs mover, and non slanted PMs and slanted PMs of the flux concentrating PMs mover. The next thing, reluctance machine with cylindrical topology is studied. The shape of mover teeth in geometric aspect is used as the method for the force ripple minimization and increasing magnetic flux. Finally, transverse flux machine is considered by dividing the transverse flux electric excited type and the transverse flux permanent magnet excited type. Additionally, three-dimensional analysis in this machine is accomplished due to asymmetric structure with another three axes.

Among the five proposed topologies, the optimal topology is selected as cylindrical topology with back-iron translator of single-phase system by advantages / disadvantages of each topology, academic difference of single- and three-phase, and comparative evaluation by weight factors. The detailed design of the optimal model takes the magnetic saturation effects into account. Besides, the losses will be examined not only iron loss such as hysteresis and eddy-current by various materials but also copper loss and eddy-current loss of PM.

Of importance is also thermal and mechanical robustness, because the generator is usually operating in close vicinity to the combustion chamber and has to withstand high accelerations resulting from the oscillating masses. Therefore, the design of shaft and bolt is achieved by fatigue analysis based on the kinetic equation considering mechanical load. Also, the thermal characteristic is analyzed by the operating frequency.

The results of this study will give elaborate information about the design rules and the performance data of linear oscillating gensets and in parallel tools for the calculation, simulation and the design of linear oscillating machines will be available.





## Kurzfassung

Die vorliegende Arbeit beschäftigt sich mit der vergleichenden Untersuchung Linear schwingender Generatoren im Anwendungsgebiet der Applikation von Hybridfahrzeugen. Der Schwerpunkt liegt dabei in der Suche nach dem optimalen Modell durch den Vergleich unterschiedlicher Topologien. Es gibt fünf Topologien, die in dieser Untersuchung nach der einschlägigen Literatur zugrunde liegen ; kartesischer- und zylindrischer (topologischer) Ansatz, Hybrid-Schrittmaschine, zylindrische Reluktanzmaschine und Transversalflussmaschine. Allen Topologien ein magnetisches Ersatzschaltbild unter Berücksichtigung der magnetischen Verluste als Modell zugrunde.

Der als erstes betrachtete kartesische Ansatz beinhaltet einen eisenlosen Läufer. Das Modell beinhaltet die Anzahl der Phasen und Pohlpaare. Zusätzlich wird der Prozess optimiert durch Parametervariation unter den Voraussetzung im zugrundeliegenden Modell. Zweitens die zylindrische Topologie mit einem Eisenrückschluss Läufer ist besonders geprägt durch die Anzahl der Phasen und die Verschiebung des Hub. Drittens, neue Flusskonzentration PMs Läufer eines Hybridschrittgenerator basierend auf einem symmetrischen und nicht symmetrischen Stator kern auf dem oberflächen befestigten PMs Läufer, und schräger und gerade genuteter PMs des flusskonzentrierenden PMs Läufer. Als Nächstes wird die Reluktanzmaschine in zylindrischer Topologie untersucht. Die Variation der geometrische Form der Läuferzähne wird benutzt um die Kraftverlauf zu glätten und den magnetischen Fluss zu vergrößern. Am Schluss werden beide Typen der Transversalflussmaschine betrachtet ; die fremd- und Permanentmagnet-erregte. Zusätzlich wird eine drei dimensionale Analyse dieser Maschine durchgeführt wegen der asymmetrischen Struktur auch in drei anderen Achsen.

Zwischen diesen fünf vorgestellten Topologien wurde der zylindrische Ansatz unter Abwägung der Vor- und Nachteile jeder Topologie, den Unterschieden ein- und drei Phasen, der Berücksichtigung von Gewichtsaspekten ausgewählt.

Das Design im Detail des optimalen Modells berücksichtigt magnetische sättigungs Effekte. Es werden nicht nur die Eisenverluste sondern auch Hysterese- und Wirbelstrom Veruste unterschiedlicher Materialien und Kupferverluste sowie Wirbelstromverluste durch den Permanentmagnet betrachtet.

Die Bedeutung der thermischen- und mechanischen Robustheit ist wichtig, weil der Generator normalerweise in einer direkter Nähe zum Verbrennungsmotor betrieben wird. Er ist so, grossen Beschleunigungen und schwingenden Massen stark ausgesetzt. Deswegen wird das optimale Design von Welle und Bolzen erreicht durch eine Alterungsanalyse basierend auf dem kinetischen Vergleich unter mechanischer Belastung. Ebenso werden die thermischen Eigenschaften unter Nennfrequenz betrachtet.



Das Ergebnis der Studie erarbeitet die Regeln zur Auslegung und die Performancedaten von linear schwingenden Maschinen gensets und parallel dazu Werkzeuge zur Berechnung und Simulation von neuen Maschinen.



---

# Table of Contents

<b>1</b>	<b>Introduction</b>	<b>1</b>
<b>2</b>	<b>Linear Oscillating Machines</b>	<b>5</b>
2.1	Linear Machine .....	5
2.2	Linear Oscillating Machine .....	6
2.2.1	Introduction .....	6
2.2.2	Period Studies and Application .....	7
2.3	Application Fields .....	8
2.3.1	Hybrid Vehicles .....	8
2.3.2	Free Piston Generator .....	9
<b>3</b>	<b>Analysis Procedure</b>	<b>11</b>
3.1	Proposed Topologies .....	12
3.1.1	Cartesian .....	12
3.1.2	Cylindrical .....	13
3.1.3	Hybrid Stepping .....	14
3.1.4	Tubular Reluctance .....	14
3.1.5	Transverse Flux .....	15
3.2	Equivalent Magnetic Circuit .....	16
3.2.1	Leakage Fluxes .....	17
3.2.2	Effects by EMC Analysis .....	17
3.3	Finite Element Analysis .....	17
3.4	Calculation for Magnetic Energy .....	18
3.4.1	Method I .....	19
3.4.2	Method II .....	20
<b>4</b>	<b>Cartesian Topology</b>	<b>21</b>
4.1	Introduction .....	21
4.2	Principle of Force Generation .....	22
4.3	Comparison of Type I, II and III .....	23
4.4	Analytical Calculation .....	25
4.4.1	One-Phase System with Two Magnets and Two Pole-Pairs .....	26
4.4.2	Two-Phase System with One Magnet and One Pole-Pair (Half-Side) .....	28
4.4.3	Two-Phase System with One Magnet and One Pole-Pair (Double-Side) .....	30



4.5	Optimal Design .....	31
4.5.1	Height of Magnet .....	33
4.5.2	Width of Magnet .....	33
4.5.3	Width of Yoke .....	34
4.5.4	Length of Yoke .....	35
4.5.5	Width of Teeth .....	35
4.5.6	Length of Slot-Opening .....	36
4.5.7	Summary .....	37
4.6	Discussion .....	39
<b>5</b>	<b>Cylindrical Topology</b> .....	<b>41</b>
5.1	Introduction .....	41
5.2	Configuration .....	42
5.3	Principle of Force Generation .....	43
5.4	Numerical Calculation .....	44
5.5	Analytical Calculation .....	44
5.5.1	One-Phase System .....	45
5.5.2	Two-Phase System .....	49
5.5.3	One-Phase System with 3 Coils and Long Stroke .....	49
5.6	Discussion .....	52
<b>6</b>	<b>Hybrid Stepping Generator</b> .....	<b>53</b>
6.1	Introduction .....	53
6.2	Proposed Topologies .....	54
6.2.1	Surface Mounted PMs Mover .....	55
6.2.2	Flux Concentrating PMs Mover .....	55
6.3	Analytical Calculation .....	56
6.4	Comparison Results .....	57
6.4.1	Surface Mounted PMs Mover .....	57
6.4.2	Flux Concentrating PMs Mover .....	58
6.5	Selection of Surface Mounted and Flux Concentrating PMs Mover Types .....	59
6.6	Proposal Model .....	60
6.6.1	Analytical Calculation of Proposed Model .....	61
6.6.2	Comparison of Flux Concentrating Slanted PMs and Proposed Model .....	63
6.7	Discussion .....	65
<b>7</b>	<b>Cylindrical Reluctance Machine</b> .....	<b>67</b>
7.1	Introduction .....	67
7.2	Configuration .....	68



7.3	Cylindrical Linear Switched Reluctance Machine .....	69
7.4	Proposal of Study Models .....	70
7.4.1	Case I .....	71
7.4.2	Case II (Rectangle Shape) .....	71
7.4.3	Case III (Trapezoid Shape) .....	72
7.5	Analytical Calculation .....	74
7.5.1	Rectangular Shape .....	75
7.5.2	Trapezoidal Shape .....	77
7.6	Comparison Results .....	79
7.7	Discussion .....	81
<b>8</b>	<b>Transverse Flux Machine</b> .....	<b>83</b>
8.1	Introduction .....	83
8.2	Subjects of Investigation .....	84
8.2.1	Single-sided TFE .....	85
8.2.2	Double-sided TFPM .....	86
8.3	Analytical Calculation of TFE .....	87
8.3.1	Fundamental Operation Principle .....	87
8.3.2	Analytical Calculation of MMF .....	88
8.3.3	Thrust Force in the Direction of X-axis .....	90
8.3.4	Lateral Force in the Direction of Y-axis .....	91
8.3.5	Attractive / Normal Force in the Direction of Z-axis .....	92
8.4	Analytical Calculation by 2-D EMC .....	93
8.5	Analytical Calculation of TFPM .....	95
8.5.1	Two-Dimension EMC .....	95
8.5.2	Three-Dimension EMCN .....	97
8.6	Comparison Results .....	104
8.6.1	Limitations of 2-D Analysis .....	105
8.6.2	FE Simulation by 3-D Analysis .....	105
8.6.3	Verification by 3-D FEM .....	106
8.7	Discussion .....	106
<b>9</b>	<b>Selection of Optimal Topology</b> .....	<b>107</b>
9.1	Introduction .....	107
9.2	Operating Characteristic .....	107
9.2.1	Voltage Equations .....	108
9.2.2	Generator in Stand-alone Operation .....	109
9.3	Evaluation Standard .....	111
9.3.1	Characteristics Evaluation of Each Topology .....	112



9.3.2	Academic Difference of Single-Phase and Three-Phase .....	113
9.3.3	Comparative Evaluation by Factor Variations .....	116
9.4	Discussion .....	119
<b>10</b>	<b>Detailed Design of Optimal Model</b> .....	<b>121</b>
10.1	Introduction .....	121
10.2	Magnetic Saturation Effects .....	122
10.3	Design considering Nonlinearity of Core .....	124
10.3.1	Calculation of Magnetic Field Distribution .....	124
10.3.2	Flux Calculation .....	127
10.3.3	Resistance Calculation .....	129
10.3.4	Flux Linkage and Force Calculation .....	129
10.3.5	Comparison of Force Characteristics between Analytical and Numerical Calculation .....	129
10.4	Calculation of Machine Weight .....	131
10.4.1	Stator Region .....	131
10.4.2	Mover Region .....	132
10.4.3	Coil Region .....	132
10.4.4	PM Region .....	132
10.4.5	Summary .....	133
10.5	Calculation of Losses .....	133
10.5.1	Hysteresis Loss .....	134
10.5.2	Eddy Current Loss .....	135
10.5.3	Excess Loss .....	136
10.5.4	Total Losses .....	137
10.5.5	Comparison of the Loss Calculation using Example M250-35 .....	137
10.5.6	Loss Analysis for using Example M400-50 .....	139
10.5.7	Calculation of Iron Loss Improvement of the Approach for Eddy Current Loss .....	140
10.5.8	Comparison of the Iron Loss using Example Soft Magnetic Composites .....	143
10.5.9	Copper Loss .....	144
10.5.10	Eddy Current Loss in Permanent Magnets .....	145
10.5.11	Comparison Results .....	149
10.6	Concrete Dimension of Single-Phase Cylindrical Linear Generator .....	150
10.7	Discussion .....	151
<b>11</b>	<b>Shaft Design through Kinetic Characteristic</b> .....	<b>153</b>
11.1	Introduction .....	153
11.2	Kinetic Equation considering Mechanical Load .....	154



11.2.1	Numerical Calculation .....	154
11.2.2	Analytical Calculation .....	155
11.3	Determination of Shaft Diameter .....	156
11.3.1	Design Procedure .....	157
11.3.2	Fatigue Failure .....	157
11.3.3	Determination of Shaft Diameter .....	160
11.4	Machine Elements Assemblies with Shaft .....	160
11.4.1	Bolt of Uniform Strength .....	160
11.4.2	Tensile and Compressive Strength in Forms of Normal Stress .....	162
11.4.3	Choice of Bolt .....	163
11.5	Concrete Dimension of Machine Elements and Shaft .....	165
11.6	Discussion .....	165
<b>12</b>	<b>Thermal Analysis</b> .....	<b>167</b>
12.1	Introduction .....	167
12.2	Determination of Heat Transfer Coefficients .....	167
12.2.1	Nusselt Number using Dittus-Boelter equation .....	168
12.2.2	Prandtl Number .....	168
12.2.3	Reynolds Number .....	169
12.2.4	Convection Heat Transfer by Water .....	170
12.3	Assignment of Heat Transfer Coefficients .....	171
12.4	Simulation Results .....	172
12.4.1	Comparison by Each Region .....	172
12.4.2	Comparison by Frequency .....	174
12.4.3	Summary .....	176
12.5	Discussion .....	177
<b>13</b>	<b>Assessment</b> .....	<b>179</b>
13.1	Introduction .....	179
13.2	Determination of the Parameters of the Equivalent Circuit from Test Data .....	180
13.2.1	Open Circuit Test .....	181
13.2.2	Short Circuit Test .....	181
13.3	Measurements .....	182
13.3.1	Open Circuit Test .....	182
13.3.2	Short Circuit Test .....	183
13.3.3	On Load Test .....	185
13.4	Discussion .....	187



<b>14 Conclusion &amp; Outlook</b>	<b>189</b>
14.1 Conclusion .....	189
14.2 Outlook .....	190
<b>Symbols and Acronyms</b>	<b>191</b>
<b>List of Figures</b>	<b>197</b>
<b>List of Tables</b>	<b>201</b>
<b>Bibliography</b>	<b>203</b>



---

# 1. Introduction

A broad variety of energy converters for primary energy (e.g. *Internal Combustion* machines, *IC* machines) are using oscillating principles. In general, these oscillating motions are converted to a continuous rotary motion by means of drive rod and crank shaft. The further energy conversion into electrical energy is achieved by a conventional rotating generator. This crank gear reduces the efficiency by introducing additional friction, requires additional weight and volume and causes wear. By using an oscillating linear generator these disadvantages can be avoided and very efficient, nearly wear free, small sized and lightweight electrical gensets can be constructed.

*Hybrid electric vehicle (HEV)* taking advantages of a lightweight linear oscillating generator may be a good solution to the problems of energy crisis and environmental pollution today. Also using these gensets as an *Auxiliary Power Unit (APU)* was often considered. The hybridization of automotive power-trains is a key step towards reducing emissions and improving fuel economy [1]. Of the various hybrid vehicle formats, series hybrids arguably offer the greatest modularity and potential for low cost, optimal energy utilization and emissions reduction being achieved by controlling the apportionment of energy between the energy storage devices, the IC engine / electrical generator and the electrical traction drive [2]. A linear oscillating generator converts the translator's kinetic energy directly to electrical energy, and is a potential energy efficient power source for use in a series hybrid vehicle power train. These features make it very suitable as a power unit in a series hybrid vehicle.

Furthermore, the free piston principle can be used by using linear oscillating motion. A free piston energy converter is a combination of a linear combustion engine and a linear electrical machine converting chemical into electrical energy.

The free piston energy converter has features as follows :

- The electrical machine can be used as a motor to start and stop the translator, as a generator for energy conversion and as an actuator to control the combustion.
- There is no crankshaft constraining the translator motion, which enables variable compression.

Meanwhile, test results of some prototype equipment with linear IC engines have been published. But a comprehensive study of linear oscillating generators is still missing. Especially questions concerning the generator topology, number of phases, excitation method, bearing construction, voltage stability under load, sensor and inverter equipment are not satisfying answered.

As task for this study, it has been the investigation and assessment of different generator topologies



in terms of

- Power to weight and volume ratio,
- Efficiency,
- Reactive power consumption,
- Size of the additional oscillating mass and
- Shaft design taking acceleration force into account

Generally, several methods have been presented to evaluate characteristic of linear oscillating motion. Among these, the equivalent magnetic circuit network method calculates the characteristics after dividing magnetic field into small regions and constructing magnetic network like electric circuit. This method is comparatively flexible and allows for fast determination of the properties of different machine topologies. At the end of the design process, the chosen topology is modelled by Finite Element Method (FEM) which takes nonlinear materials properties into account and accurate results close to the experimental ones can be expected. FEM has a solution that is close to experimental results and can model complicate magnetic field including nonlinear material properties.

All proposed topologies will be analyzed for the average force and force density using magnetic energy by 2-D equivalent magnetic circuit network method. The analysis of each topology considering leakage reactance is compared to the result of FEM by static magnetic field, and then the optimal model will be selected by characteristics and results of all topologies. Finally, the optimal topology will be approached through detailed design taking nonlinear properties of iron-core into account. Especially, it is absolutely essential to analyze by 3-D Finite Element Analysis (FEA) in case of transverse flux machine that is not symmetrical in anything axis. Accordingly, the result of transverse flux machine through 3-D equivalent magnetic circuit will be also compared with that of the 2-D equivalent magnetic circuit. In addition, comparison results between this analytical calculations and 3-D of simulation will be evaluated.

Of importance is also thermal and mechanical robustness, because the generator is usually operating in close vicinity to the combustion chamber and has to withstand high accelerations resulting from the oscillating masses.

Concerning the topologies at least the most important types shall be investigated :

### 1 Cartesian Topology

- 1-1 One-phase system with two magnets and two pole-pairs
- 2-1 Two-phase system with one magnet and one pole-pair (Half-side)
- 3-1 Two-phase system with one magnet and one pole-pair (Double-side)

- 2 Cylindrical Topology
  - 2-1 One-phase system
  - 2-2 Two-phase system
  - 2-3 One-phase system with 3 coils and long stroke
- 3 Hybrid Stepping Machine
- 4 Tubular Reluctance Topology
- 5 Transverse Flux Machines
  - 5-1 Single-sided system with reluctance type
  - 5-1 Double-sided system with magnets

To collect data about existing machines a literature study is necessary. The next step will be the development of analytical design data for the different machines and the checking of the design by numerical field calculations and thermal calculations. In addition, shaft design will be performed considering acceleration force by load mass because the shaft is seriously affected by bending and axial loads. A simulation of the generator taking into account also nonlinear effects of the combustion process will complete the knowledge about the operational behaviour of the machine and inverter. At last a scheme for the assessment of the different types of machines has to be elaborated and the assessment process has to be performed.

The results of this project will give elaborate information about the design rules and the performance data of linear oscillating gensets and in parallel tools for the calculation, simulation and the design of linear oscillating machines will be available.



## 2 Linear Oscillating Machines

### 2.1 Linear Machine

The need of electro-mechanical power generation has increased dramatically in industrial field as time goes by. In general, linear motion is mostly produced by devices which transform rotating movement into linear movement in factory and office automatic system. Using rotating devices increases complexity of the system, reduces efficiency by mechanical losses and declines precision by framework limitations and restrictions of driving speed. On the other hand, linear machines have fewer limits than rotating machines in driving speed. Also, linear machines are direct drives which need no gears to generate linear thrust force. In this reason, its application field shows increasing diversification since linear machines have been proposed by Professor *Laithwaite* in the middle of 19<sup>th</sup> century [3].

In most cases the linear machines are treated as cut and unrolled conventional rotating machines, that is, the machines with rather complicated structure. In some case such treatment is good, especially studying linear machines for continuous translation.

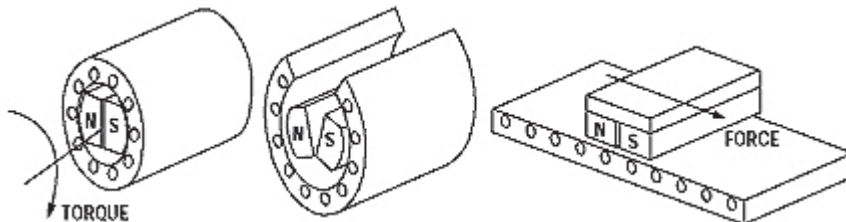


Figure 2.1 : Linear Machine

The majority of electrical machines are designed to produce rotary motion. In behalf of pointing out certain differences between a linear and its rotary counterpart, we consider a polyphase rotary machine. By the imagination, a rotary machine will be transformed into a linear machine if the stator of rotary machine is cut at a radial plane and unrolled and the rotor is replaced by at least two adjacent PM and back iron like in figure 2.1. The stator is named the *primary* and the rotor is the *secondary*. As a result, the primary has a finite length, called the *active length*. Additionally now *End Effects* occur which is unique to linear machines and does not exist in conventional rotating machines [4].

This PM excited linear machine has been considered to be the most suitable electric machine for linear control with high speed and high precision. The thrust of the linear machine is one of the important factors to specify machine performance. Maximum thrust can be obtained by increasing



the magnitude of current in the conductors and is relative to the size of conductor and PM. It can directly perform linear motion without auxiliary machine parts such as gears or cranks. Since it is possible to make smaller machine with high power, it has also been applied to small-sized precision products such as hard disk and CD player [5].

Based on above properties, linear machines exhibit the following advantages in contrast to the conventional rotational machines :

- High Precision
- High Acceleration
- High Stiffness
- High Efficiency
- No Limit of Motion
- Simplicity in Maintenance, Repair, Replacement and in Structure

## 2.2 Linear Oscillating Machine

### 2.2.1 Introduction

An object of this study is one kind of special machines with peculiarities of mechanical movement, that is, with periodical movement (oscillation) of the moving part. These oscillating machines have appeared already at daybreak of electro-mechanics, however nowadays they are nearly imperceptible in the whole of the special electrical machines. Partly, it is the result of imperfection of classification and grouping of electrical machines with specific properties of movement : it is necessary to classify them separately by the temporal and spatial properties of movement. Thus, the oscillating machines are distinguished by their specific temporal property of movement, meanwhile the spatial property (a trajectory) can be various. Also, it is proven that oscillating machines are a specific and independent type of electrical machines. These machines can be analyzed in the unified way, irrespective of the concrete domain of their application [6].

Linear type oscillating machines based on above properties, which are electromagnetic devices which develop directly short travel progressive linear motion, have already found some applications and are fabricated in moderate numbers for machine tool sliding tables, pen recorders, textile sewing machine, free piston pumps and compressors. In addition to high efficiency, the parameters of a linear oscillating machine should be nearly constant regardless of the amount of the current flow and position of the piston in order to control the position of piston without an additional sensor [7]. Several types of the linear oscillating machines are investigated to meet reliable enough and has more efficiency requirements. A structure of moving PM machine with back iron was designed for its high force density and efficiency in electrical features and strong structural advantages. They are built in very large numbers for a wide range of applications from home appliance to industry fields.

Recently they have been proposed for free piston engine in hybrid vehicles. Moreover, extensive use of high energy PMs has brought the thrust densities and energy conversion ratios to market competitive levels. A similar impact has been made by power electronics and digital nonlinear control. Thus, vigorous research and industrial developments in linear oscillating electrical machines are expected in the near future with an ever wider range of applications.

### 2.2.2 Period Studies and Application

More serious studies and application of linear oscillating machines have begun at the turn of 19<sup>th</sup> and 20<sup>th</sup> century. In the beginning of the 20<sup>th</sup> century (in the period from 1900 to 1910) *Paul Boucherot* from France was the first to perform serious theoretical and experimental researches of oscillating synchronous machines [8]. He tried to create a single-phase commanded speed motor of continuous rotation on a base of oscillating motor for traction. The weight of this motor was about 1000 [kg]. The calculated output power was 15 [kW] and speed 60 [rpm], but real one was only 5 [kW] and 40 [rpm] with approximate 50 [%] efficiency because of some mistakes of theoretical study. So, in the 20<sup>th</sup> century we can observe more or less profound studies of different oscillating machines for separated domains of application. These studies were more intensive during different periods and in different countries.

In 1930 ~ 40, in different countries some patents were issued for oscillating motor-compressors, including compressors for refrigerators. It seems that the most active job was done in Germany. For instance, interesting motor-compressor of *W. Koenig* [9] : The oscillating synchronous pulsating current motor with the control by electromagnet valve.

Numerous patents show that those different oscillating motor compressors were being created in the USA for many decades. The *Ray W. Herrick* Laboratories at Purdue University is one of the centers of research and development for oscillating motor compressors. In the period 1967 ~ 80, there were defended three Ph.D. thesis on electrodynamic oscillating compressors [10 ~ 12].

As we see, there was some rise of researches and development of the compressors driven by an oscillating machine of the last century. Maybe some unsolved problems (or solving with difficulty) have decreased researcher's enthusiasm.

However in the last years (or even decades) we can observe certain renaissance of interest for the oscillating motor-compressor. Many facts confirm such situation. The works of *Sunpower Inc.* (USA) could be marked out as studies since 1975 of oscillating motor-compressor, which are continued actually as well. In 2001, Korea firm *LG Electronics* started successfully manufacturing household refrigerators [13], the first compressor variant of which was created by the above mentioned Sunpower Inc.

As it was mentioned above, even in the early period of oscillating electrical machines development, the oscillating generators were proposed. Markedly later, in the period 1955 ~ 65 the brothers *Jean* and *Jaques Jarret* (France) achieved interesting results in creating an alternator with free piston internal combustion engine. [14].

The present-day problems of the protection of environment stimulate to create more effective, more economic and decreasing pollution mobile source of electric energy, which could compete with traditional diesel generator. Many specialists of electricity and mechanics have studied the oscillating machines continuously.

This topic will be designed to characterize the linear oscillating generator for hybrid vehicle vehicles. However, it can be involved for free piston linear generator in parallel. Thus, the tendency of development of linear oscillating generators as specific devices is well-founded and promising.

## 2.3 Application Fields

### 2.3.1 Hybrid Vehicles

The interest in HEV has increased dramatically the last year. The rising oil price has made it more appealing to have a vehicle with a good fuel economy and as hybrid solutions can achieve this without deteriorated performance [15]. So, the HEV is a good solution to the energy crisis and environmental pollution problems, considering the limit of the energy density of batteries today [16]. It integrates the functions of a combustion engine, the crankshaft, the connecting rod, and the rotating electrical generator used in conventional hybrid schemes into a single unit, which may have the advantages of high efficiency, compact structure, and reliable operation [17]. It has promising applications in series hybrid vehicles and in distributed generation units. The series HEV has a powertrain where the primary power unit should generate electrical power. The configuration is illustrated in figure 2.2.

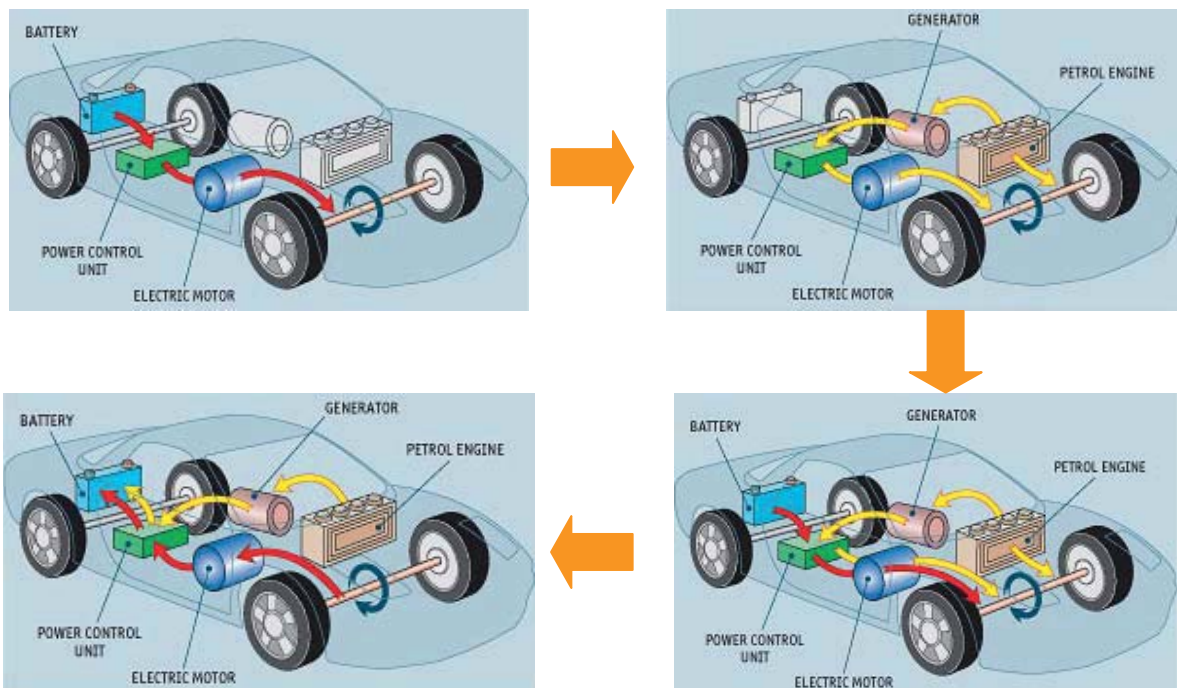


Figure 2.2 : Typical Series Hybrid Electric System

When a starting and running at low speeds, the vehicles runs on battery power alone which drives the electric motor. In normal driving conditions, power from the petrol engine is divided and used both to drive the wheels directly, and to turn the generator, which in turn drives the electric motor. When sudden acceleration is needed, the battery provides extra power to the electric motor, supplementing the power from the petrol engine. The battery is recharged in two ways. When braking, the electric motor acts as a generator, converting the vehicle's kinetic energy into electrical energy and storing it in battery. The engine can also recharge the battery directly when necessary.

### 2.3.2 Free Piston Generator

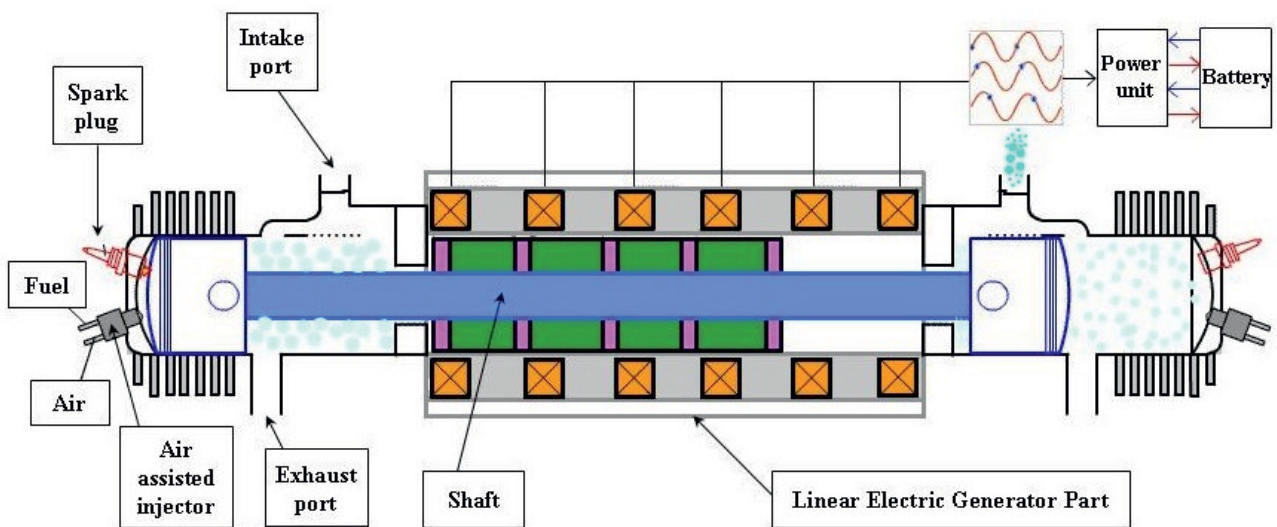


Figure 2.3 : Free Piston Linear Combustion Engine [18]

The hybrid vehicle concept is environmentally friendly, highly efficient, and is gaining popularity by the day. The free piston generator concept is one of the relatively new (and still emerging) hybrid vehicle concepts that could offer good solutions to some of these demands. The free piston generator is an energy conversion device that integrates a combustion engine and an electrical generator into a single unit. Thereby the intermediary crankshaft stage present in conventional hybrid topologies is eliminated. This has benefits in efficiency, weight reduction, robustness, variable compression operation and multi-fuel possibilities. This is shown in figure 2.3. The rod that connects the two oppositely placed combustion chambers also acts as a prime mover for the generator. The reciprocating, ignition and compression processes, in the two chambers cause the connecting rod to have an oscillating motion [19].

Now, if this rod is combined with a linear generator, it can produce electricity directly from the linear motion of the pistons.



### 3 Analysis Procedure

This chapter proposes an analytical approach that is generalized for the design of various types of linear oscillating generator based on a physical magnetic circuit model. Conventional approaches have been used to predict the behavior of electric machines but have limitations in accurate flux saturation analysis and hence machine dimensioning at the initial design stage. In particular, magnetic saturation is generally ignored or compensated by correction factors in simplified models since it is difficult to determine the flux in each stator tooth for machines with any slot-pole combinations. In this first step, the properties of each proposed topology are investigated by machine dimensioning with help of the equivalent circuit method. The optimal model will be selected by comparing each topology from result of electrical analysis by equivalent magnetic circuit and structural aspect. In the next step, the model will be designed in detail taking saturation into account. Furthermore it needs thermal analysis because the linear oscillating generator is usually operating in close vicinity to the combustion chamber. To have mechanical robustness, it will be also calculated by shaft fatigue analysis.

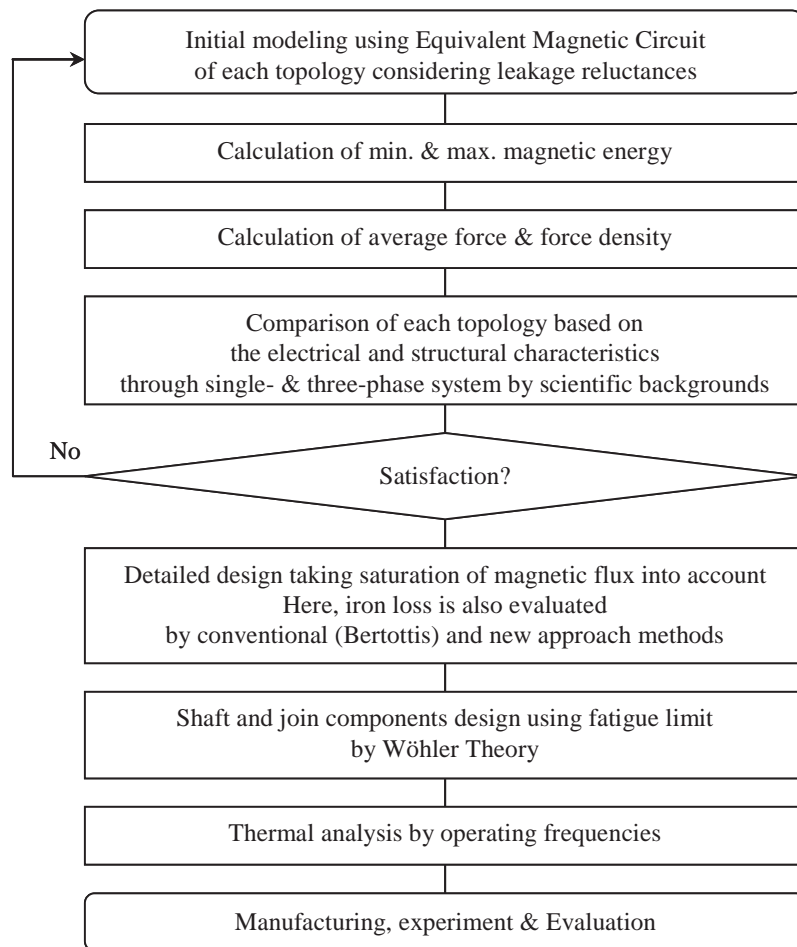


Figure 3.1 : Analysis Flow

When designing an electrical machine, it is important to consider magnetic saturation as it will increase losses and limit machine performance. The equivalent magnetic circuit analysis has been widely applied to analysis and design of electrical machines [20]. Most of the studies are based on the same concept mimicking the electrical circuit behavior. Due to excessive simplification, conventional equivalent magnetic circuit analysis often suffers from the problem of considerably low accuracy, and correction factors based on experiences are often employed for compensation. Therefore, it is commonly used for preliminary design, and confirmation or modification using other approaches (e.g., FEA) is required. The FEM dominating nowadays in the design procedures of electrical machines is applied [21].

### 3.1 Proposed Topologies

This chapter summarizes the results of the design calculations. The different types of linear oscillating generators implemented are overviewed and their main characteristics are discussed. Each topology will be explained concretely with configuration and information in each paragraph.

#### 3.1.1 Cartesian

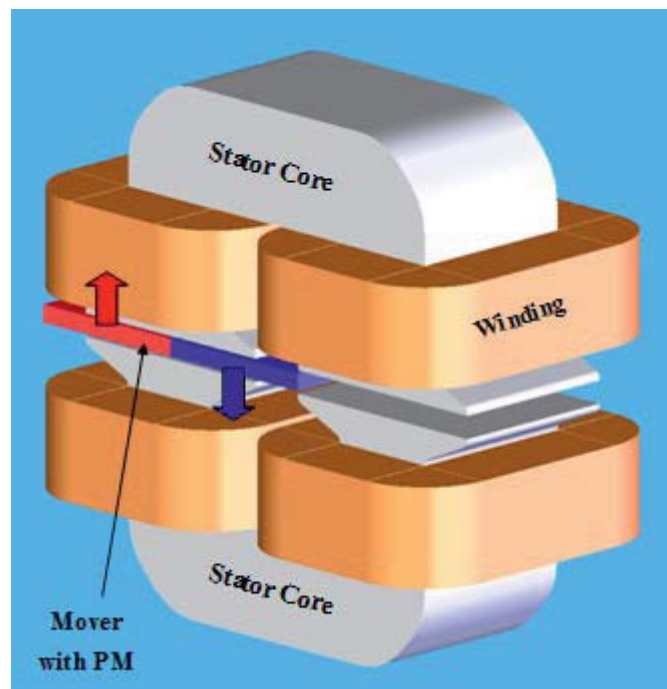


Figure 3.2 : Cartesian Topology

The Cartesian type of linear generator increases the force output of the machine due to generation of the magnetic field created by the armature winding. There is a strong attractive force between the iron-core armature and the permanent magnet. As shown figure 3.2, the upper and lower U-shaped part is the stator core with a winding of coils, meanwhile the center part is the translator composed

of only permanent magnet. By this structure, one of the weaknesses of linear machine has big leakage flux in both end parts of machine as a PM translator moves. Another shortcoming of this topology is that its volume is too large compared to the force.

### 3.1.2 Cylindrical

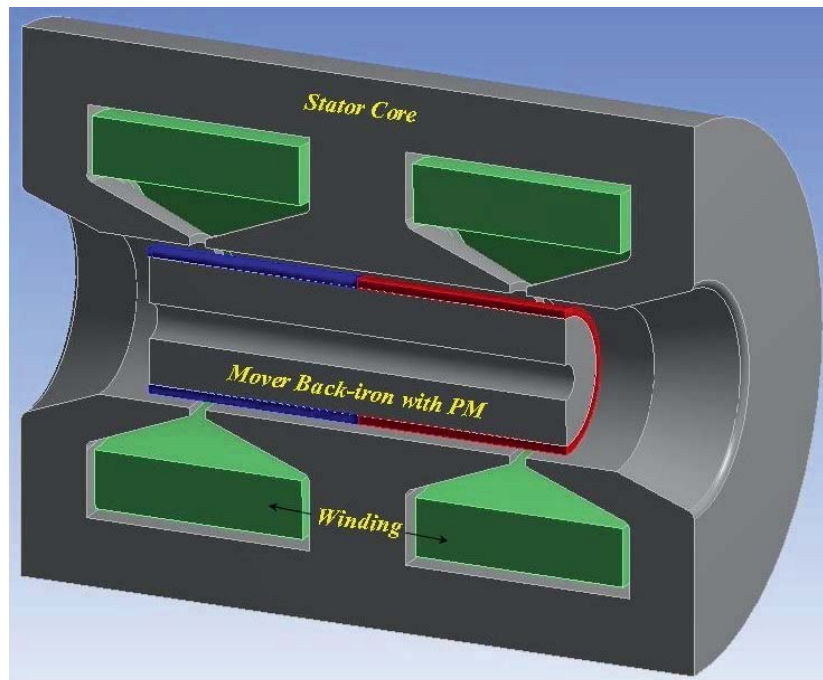


Figure 3.3 : Cylindrical Topology

The previous studies show that flat-type linear oscillating generator is rarely used in free piston gensets and indeed inferior to the tubular-type one in terms of structural merits. The piston has the degree of freedom to rotate without affecting the electrical properties of the generator. The amount of leakage flux is small. Despite these advantages, magnetic ring, laminations stacked stator and the winding in tubular stator are hard to manufacture and to assemble. However, the problems of 3-D flux path can be overcome by *Soft Magnetic Composite (SMC)*. The tubular-type linear generator has higher efficiency and reliability than the flat-type one because of its structural merits. The tubular-type linear generator has some better qualities than the flat-type one. Also the amount of coil is smaller and the benefit of the cylindrical arrangement is that it has no end-windings, therefore the end effects are better than flat-type and the copper loss becomes less than that of flat-type generator.



### 3.1.3 Hybrid Stepping

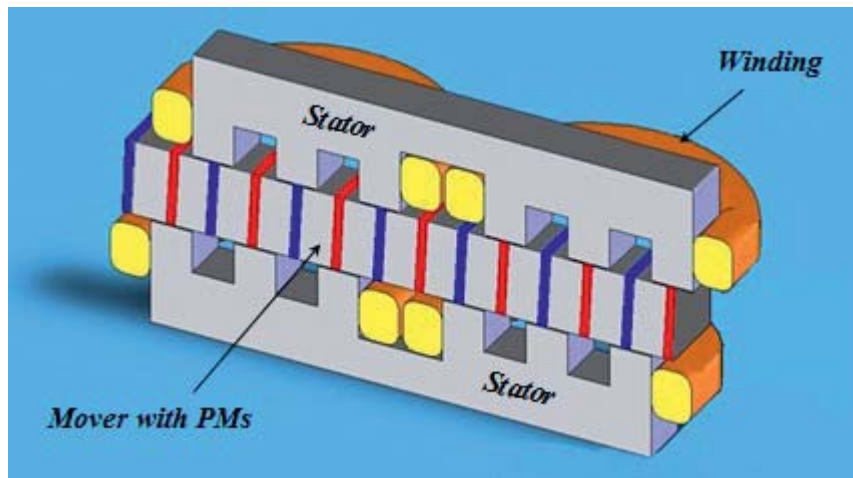


Figure 3.4 : Hybrid Stepping

A hybrid stepping oscillating generator has a simple and robust stator construction with inherently high synchronous reactance. The translator is sandwiched between two stators that carry flux in the longitudinal direction, while the translator carries flux in the transverse direction. Similarly, the flux path of a hybrid stepping machine is longitudinal, or parallel to the direction of movement ; it is distinguished from transverse flux that flux lines go perpendicular to the moving of translator.

This hybrid stepping topology is inevitable to reduce the ripple in the electromagnetic forces due to the attractive force between stator teeth and translator with permanent magnets. It needs in-depth investigation to minimize ripple by buried type of permanent magnet thorough analysis of the magnetic circuit.

### 3.1.4 Tubular Reluctance

The motion is caused by the tangential force which tends to align poles of the moving part with the excited poles of the static part. The linear generators using tubular reluctance configurations have significant advantages in comparison with their counterparts based on reluctance Cartesian configurations. Theoretically enables it neutralization of normal forces, by this allowing a smaller air-gap and better use of active material. Furthermore, this topology has a low reactance and high power factor.

However, since the force for a given excitation current diminishes rapidly as the air-gap length increases, (approximately with the square of air-gap) they are generally only suitable for short stroke applications (typically in the millimeter range).

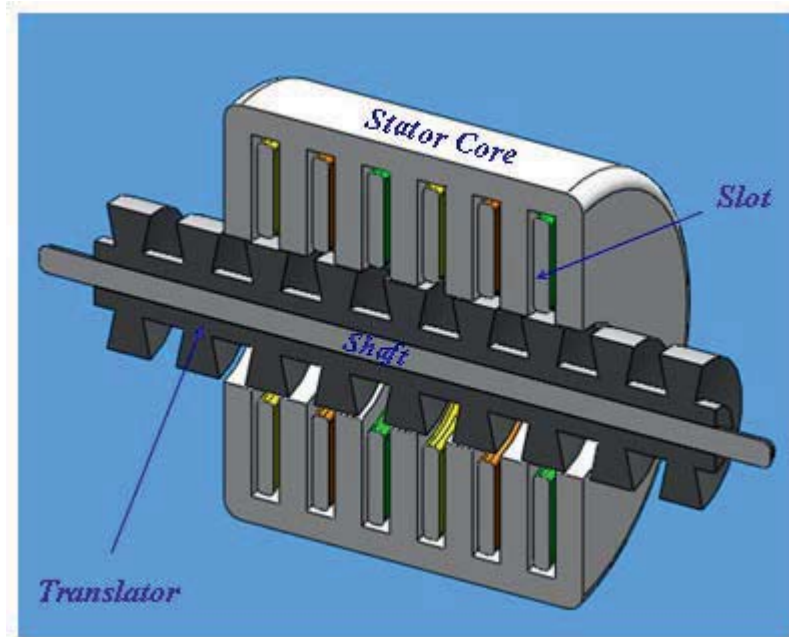
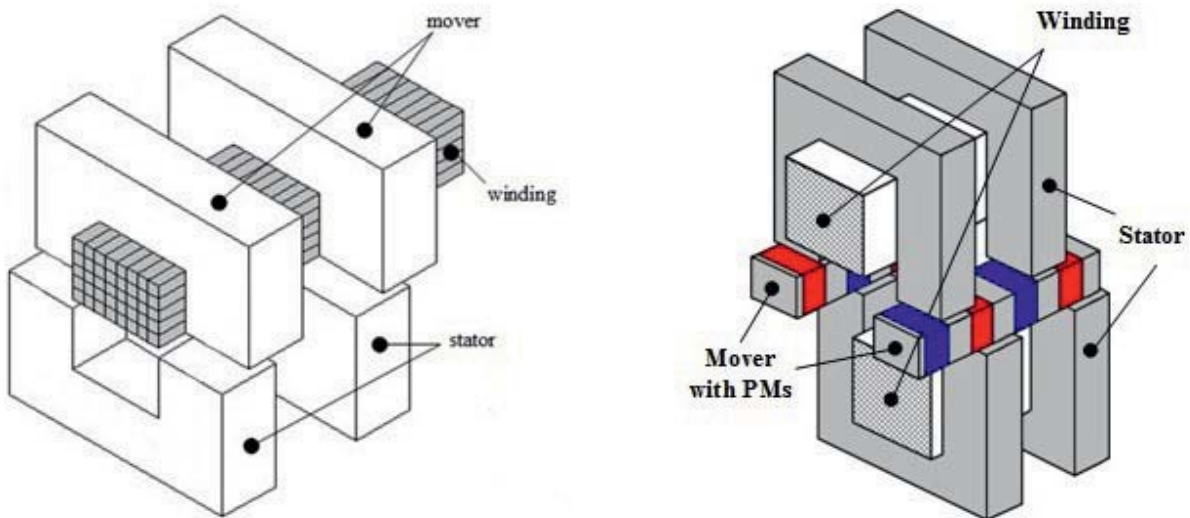


Figure 3.5 : Tubular Reluctance

### 3.1.5 Transverse Flux



Transverse Flux Element excited (TFE)

Transverse Flux Permanent Magnet excited (TFPM)

Figure 3.6 : Transverse Flux Machine (TFM)

Transverse flux machines inherently use unconventional magnetic structures due to their 3-D flux paths. In this machine, the plane on which the flux path lies is transverse, or perpendicular to the direction of movement. There has been discussion favoring the transverse flux because of its capabilities to obtain a high force density. However, there are drawbacks to a transverse flux design in the design and the construction of a transverse flux machine can become difficult due to high leakage reactance resulting in a low power factor as price for a high force density. In addition, this



generates high force ripple by intrinsic magnetic structure. Due to this a transverse flux machine is known to have vibration and force ripple which is greater than with other types of machines, moreover due to the high forces during the combustion process, the stress on the movable part (translator) is high.

#### Longitudinal Flux Machines vs. Transverse Flux Machines

Among many ways to classify types of machines, one way is to categorize according to the direction of magnetic flux : longitudinal flux machines and TFMs. In the longitudinal flux machines, the direction of the magnetic flux is the same as the moving direction of the machines. On the other hand, the direction of the magnetic flux is transverse to the moving direction of the machine in the TFMs. In other words, the direction of an applied current is perpendicular to the moving direction of the machine in case of the longitudinal flux machines, whereas the direction of an applied current is same as the moving direction of the machines in case of the TFMs.

The advantages of TFM topology against the classical longitudinal concept are [22] :

- An increase of pole number does not reduce the magnetomotive force (MMF) per pole.
- The magnetic flux geometry and the coil section can be varied without compromising the dimensions in terms of the design freedom.
- Very simple stator coils are employed and the total conductor length is relatively short.
- The phases in TFMs are magnetically independent and it enables to simplify the control method

### **3.2 Equivalent Magnetic Circuit**

The equivalent magnetic circuit (EMC) has often been introduced as a fast design model for the calculation of the optimal size of the core [23]. This method emerged as a third possibility for electrical machine analysis in the late 1980s and was further developed. It can be considered as a compromise between FEA and analytical models, representing the device as a lumped parameter magnetic circuit (reluctance network).

However, a complete integration of EMC into a commercial analysis or design tool has not been attempted, although preliminary work has been completed in at least one study [24]. Reasons include the limited experience of designers with the method itself, as well as the difficulty of automated reluctance network generation.

Nevertheless EMC is an attractive design tool for the first preliminary design of energy converters. Its advantages are a relatively low computational complexity and respectable accuracy, achieved through a division of the geometry that is coarser than in FEA but finer than in analytical models. As a main advantage, it is easily extended into a 3-D model [25].

EMC networks consist of reluctances, magnetomotive force (MMF) sources, and magnetic flux sources, and are an analogue to resistive electric networks.

### 3.2.1 Leakage Fluxes

The air-gap and leakage fluxes are analytically expressed in terms of the magnetic material properties and the machine dimensions. Both factors are essential quantities for the accurate prediction of the flux distribution within the machine and of the machine force. Therefore, they are desired for the purpose of machine design and optimization.

In constructing leakage flux paths, the flux distribution plot obtained by the FEM can provide considerable assistance. The iron parts are taken to be infinitely permeance and hence flux lines are drawn normal to the iron surface equipotentials. Both the assumed flux paths procedure used and the FE computation assume usually a 2-D field. Additional flux paths can be constructed for 3-D problems as with transverse flux machines. It should be clear that in order to evaluate the exact leakage permeances a 3-D field solution is strictly required, but an approximated method on the basis of the assumed flux paths method can be adopted with considerable time savings.

### 3.2.2 Effects by EMC Analysis

The objectives of this study using EMC are :

- Calculate the leakage reluctances of a simple EMC model in predicting the magnetic loading in a 2-D core (especially, 3-D also in case of transverse flux machine)
- Evaluate the average force and force density by magnetic energy calculation
- Compare the results between EMC and FEA, finally

## 3.3 Finite Element Analysis

A very accurate calculation of leakage flux is only possible by the use of numerical methods. On the other hand, calculation of the magnetic field by the finite element procedure can require both a long computation time and a tedious data preparation stage. Efforts are being made to assist the user with automatic mesh generation using error checking. However, the numerical result obtained from such using procedure does not give an analytical formula which would be very useful for an iterative design process. Even at present it is believed that such detailed numerical computations should be left to the final stages of the machine's design process, or precomputed for a series of nominal configurations to form a data base for reference purposes. Both of these procedures have in fact been applied with success by the present. This is naturally being gradually eroded as time goes on and the cost of computing falls. Rapidly evolving FE technologies particularly with adaptive

meshing are helping with the time consuming data preparation stages. It is consequently still desirable to produce analytical formulae for leakage flux estimation by other methods.

Finally, approximate dimension and force of the machine can be obtained by EMC using leakage reluctances of all topologies. The results are compared and evaluated in accordance with FEA. Additionally, the transverse flux machine will be examined using 3-D EMC network method because it has asymmetric structure  $x$ ,  $y$  and  $z$ -axis one another.

### 3.4 Calculation for Magnetic Energy

Above all, we need to look carefully at that flux behavior in air region is more important reason than that of iron core part. This helps analysis the magnetic energy with two methods : method I and II.

The magnetic field created by an electromagnet is proportional to both the number of turns in the winding,  $N_c$ , and the current in the wire,  $I$ , hence this product,  $N_c I$ , in ampere-turns, is given the name magnetomotive force. For an electromagnet with a single magnetic circuit, of which length  $l_{core}$  is in the core material and length  $l_{air-gap}$  in air-gaps, *Ampere's Law* reduces to :

$$\begin{aligned} N_c \cdot I &= H_{core} \cdot l_{core} + H_{air-gap} \cdot l_{air-gap} \\ &= B \cdot \left( \frac{l_{core}}{\mu} + \frac{l_{air-gap}}{\mu_0} \right) \end{aligned} \quad (3.1)$$

where  $\mu = \frac{B}{H}$

$\mu_0 = 4\pi \times 10^{-7} \frac{H}{m} \left[ \frac{N}{A^2} \right]$  is the permeability of free space (or air) ; note that  $A$  in this definition is amperes. This is a nonlinear equation, because the permeability of the core,  $\mu$ , varies with the magnetic field,  $B$ . For an exact solution, the value of  $\mu$  at the  $B$  values used must be obtained from the core material *hysteresis curve*. If  $B$  is unknown, the equation must be solved by numerical methods. However, if the magnetomotive force is well above saturation, so the core material is in saturation, the magnetic field won't vary much with changes in  $N_c I$  anyway. For most core materials,  $\mu_r = \mu / \mu_0 \approx 1000 \sim 5000$ . So in equation (3.1) above, the second term dominates. Therefore, in magnetic circuits with an air-gap, the behaviour of the magnet depends strongly on the length of the air-gap, and the length of the flux path in the core doesn't matter much. We can consider two methods : using flux density in air-gap and different two materials.

### 3.4.1 Method I

The (3.2) represents the energy per unit volume stored in the magnetic field.

$$\begin{aligned}
 W_m &= \frac{B^2}{2 \cdot \mu_0} \cdot \int dv \\
 &= \frac{B^2}{2 \cdot \mu_0} \cdot \delta \cdot l_E \cdot \tau_p \\
 &= \frac{B}{2 \cdot \mu_0} \cdot \delta \cdot B \cdot l_E \cdot \tau_p \\
 &= B \cdot l_E \cdot \tau_p \cdot \frac{\delta}{2 \cdot \mu_0 \cdot l_E \cdot \tau_p} \cdot \phi \\
 &= \frac{1}{2} \cdot \phi^2 \cdot \frac{\delta}{\mu_0 \cdot l_E \cdot \tau_p} \\
 &= \frac{1}{2} \cdot \phi^2 \cdot R_{m\delta}
 \end{aligned} \tag{3.2}$$

$$\text{where, } \phi^2 = B^2 \cdot l_E^2 \cdot \tau_p^2, \text{ if } \mu_E \rightarrow \infty \tag{3.3}$$

The flux density in air-gap can be summarized as follows, equation (3.4)

$$B = \frac{\mu_0}{2 \cdot \delta} \cdot \Theta \tag{3.4}$$

The square of magnetic flux is expressed as (3.5) substituting for (3.4)

$$\begin{aligned}
 \phi^2 &= \left( \frac{\mu_0}{2 \cdot \delta} \right)^2 \cdot \Theta^2 \cdot l_E^2 \cdot \tau_p^2 \\
 &= \left( \frac{\mu_0 \cdot l_E \cdot \tau_p}{2 \cdot \delta} \right)^2 \cdot \Theta^2 \\
 &= \frac{1}{4} \cdot \left( \frac{\mu_0 \cdot l_E \cdot \tau_p}{\delta} \right)^2 \cdot \Theta^2 \\
 &= \frac{1}{4} \cdot \lambda_\delta^2 \cdot \Theta^2 \\
 &= \frac{1}{4} \cdot \frac{1}{R_{m\delta}^2} \cdot \Theta^2
 \end{aligned} \tag{3.5}$$

Substituting for given (3.2) for (3.5), completed formal for magnetic energy is presented as (3.6).

$$W_m = \frac{1}{8} \cdot \frac{1}{R_{m\delta}} \cdot \Theta^2 \quad (3.6)$$

### 3.4.2 Method II

The magnetic energy  $W_m$  provides another way to calculate the force and the inductance. However, the field energy (field co-energy) is separately determined for a region with a constant permeability and field dependent permeability. While in the area with constant permeability, the energy is directly determined by the product B and H, the energy in the field with field-dependent permeability are integrated [26].

$$\begin{aligned} W_m &= \int_V \frac{1}{2} \cdot B \cdot H \, dV \\ &= \int_{V_1} \frac{1}{2} \cdot \mu \cdot H^2 \, dV + \int_{V_2} \frac{1}{2} \cdot B \cdot H \, dV \\ &= \sum_{i=1}^{n_1} \frac{1}{2} \cdot \mu \cdot H^2 \cdot V_{ie} + \sum_{j=1}^{n_2} \left( \int_0^B \frac{1}{2} \cdot H \, dB \right) \cdot V_{je} \end{aligned} \quad (3.7)$$

$$W_{co} = \sum_{i=1}^{n_1} \frac{1}{2} \cdot \mu \cdot H^2 \cdot V_{ie} + \sum_{j=1}^{n_2} \left( \int_0^H \frac{1}{2} \cdot B \, dH \right) \cdot V_{je} \quad (3.8)$$

$$\begin{aligned} Force &= \left. \frac{\partial W_{co}}{\partial X} \right|_{I=const} \\ &= - \left. \frac{\partial W_m}{\partial X} \right|_{\varphi=const} \end{aligned} \quad (3.9)$$

where,  $V_1$  is a volume of constant permeability and  $V_2$  is a field with field-dependent permeability.

---

## 4 Cartesian Topology

### 4.1 Introduction

This chapter deals not only with one-phase systems by the number of magnet and pole pairs but also two-phase machines in Cartesian coordinate system. All this is carried out for optimum process using geometric parameters based on analytical electromagnetic field research. The best structure for optimum design is selected by a parameter study and it is accomplished with 2-D FEA. The design variables for this parameter study are chosen as follows ; height of magnet, width of magnet, width of yoke, length of yoke, length of slot-opening and width of tooth. Eventually, it suggests new design rules based on optimal design through parameter study.

In a flat type linear generator, the coil windings are inserted into a steel structure to create the coil assembly. There is a strong attractive force between the armature iron-core and the permanent magnet requiring a solid support structure. Achieving linear motion with a generator that needs no gears, couplings or pulleys makes sense for many applications, where unnecessary components that diminish performance and reduce the life of a machine can be removed.

However, there will be end effect related cogging forces due to the finite armature length. In effect, these forces cause noise and vibrations. Consequently, numerous methods can be used to minimize cogging and end effects by utilizing the end effect compensators, semi-closed slots or magnetic slot wedges, varying the length of the air-gap, magnet shape skewing or chamfering magnet length optimization and etc. Therefore, optimizing the magnet or armature iron-core length ensures that the end effect cogging force components can cancel each other. Also, shaping or smoothing the axial end corners also can significantly reduce the cogging force due to the axial end-effects.

We will be able to look into every characteristics following number of phase, magnet and pole pairs as below :

- One-phase system with two magnets and two pole-pairs ; Type I
- Two-phase system with one magnet and one pole-pair (Half-side) ; Type II
- Two-phase system with one magnet and one pole-pair (Double-side) ; Type III

As the configuration example shown in figure 4.1, the Cartesian system with magnet mover consists of three parts ; two stators contain the winding, and the other is the mover with the magnet which is magnetized in y-direction. The flux linked with circular wound coils changes periodically to produce the electromotive force. The upper and lower part that is marked by gray-color is the stator

iron-core. No iron-core required in the mover, so this type has the smallest moving mass allowing high accelerations.

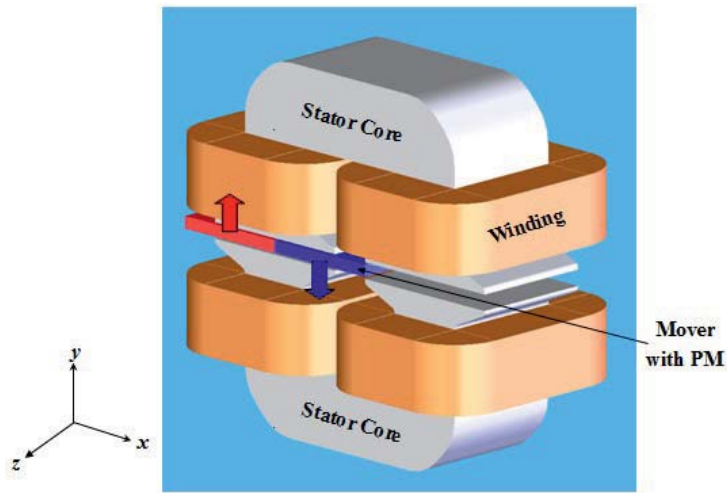
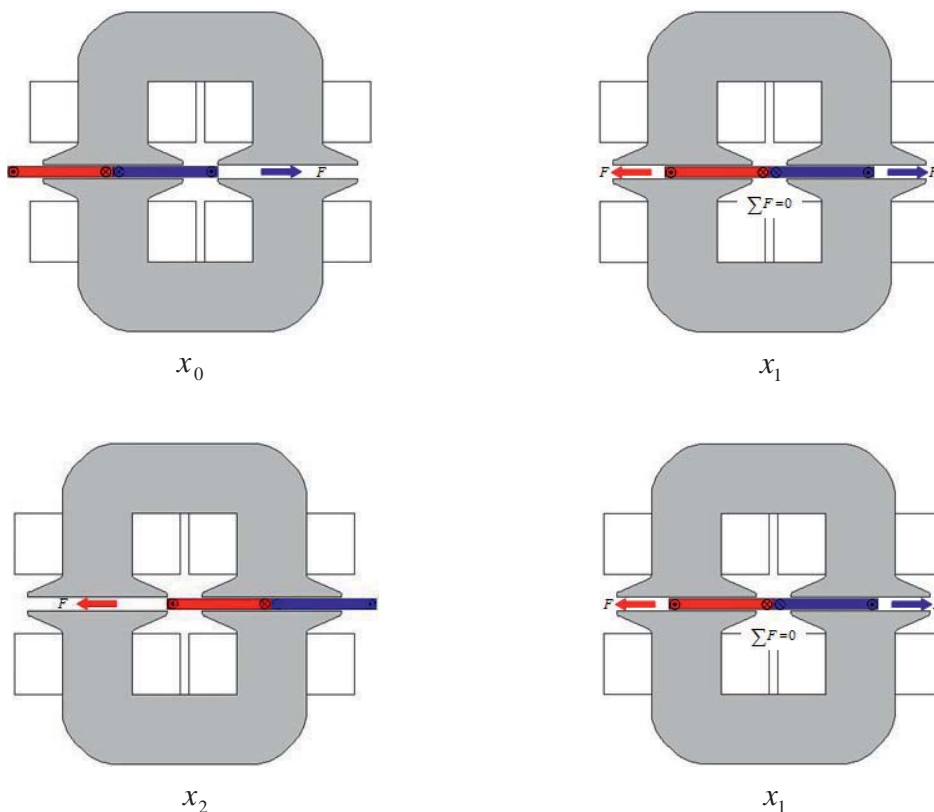


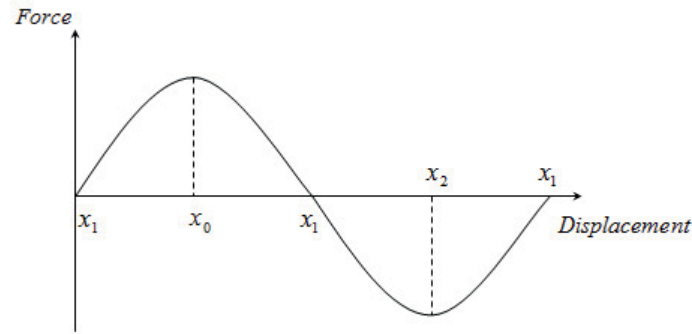
Figure 4.1 : Cartesian Topology

## 4.2. Principle of Force Generation

The Cartesian topology having one pole-pair magnet generates force as it is not aligned with stator teeth. The mover consists of two magnets forming a pole pair.



a. Position of PM mover



b. Force Generation

Figure 4.2 : Force by Interaction of a PM and Stator-Teeth

As shown figure 4.2.a, the force increases with more flux linkage ; flux linkage is the highest when the mover is located in  $x_0$  and  $x_2$ . As the mover goes to the opposite position, the force is reversed into the opposite direction ; accordingly it is required to the switch current regularly to obtain constant force waveform. Figure 4.2.b represents ideal force change trend at the time.

### 4.3 Comparison of Type I, II and III

- Type I : This model has a relatively low leakage flux because there are stator iron cores in upper and lower part guiding the magnetic flux. Besides, it is suitable for short stroke application due to divided two magnets which magnetized perpendicular to the stator winding. Nevertheless, it is inevitable to avoid leakage flux, since the total length of magnet is longer than that of stator teeth.

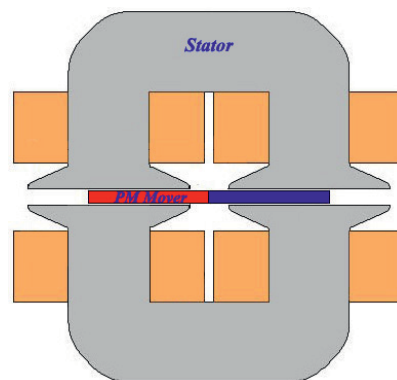


Figure 4.3 : Type I

- Type II : Although this type has an advantage of small volume compared with other Cartesian models, this model is inefficient in terms of structure. The reason is that it is very short or little magnetic flux path which runs through stator iron core and magnet as mover. It has a serious leakage flux structurally because the magnet of mover is only magnetized in one vertical direction. This generates leakage flux at opposite end part even if current is

excited to convert of phase switch in accordance with mover position. As a result, this model should be two-phase system and it has become more complex and increasingly specialized.

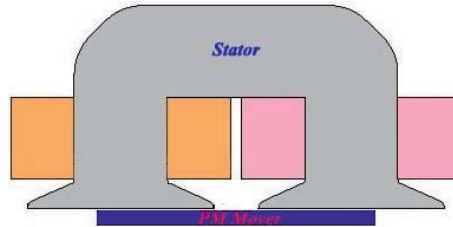


Figure 4.4 : Type II

- Type III : It consists of one longer magnet as mover, in which magnetic flux can be increased effectively. But leakage flux by armature winding is approximately 41.75 [%] bigger in comparison with type I. On the contrary, the effective magnetic flux of opposite end part to interact between magnet and stator teeth is nearly zero when the magnet of mover is aligned.

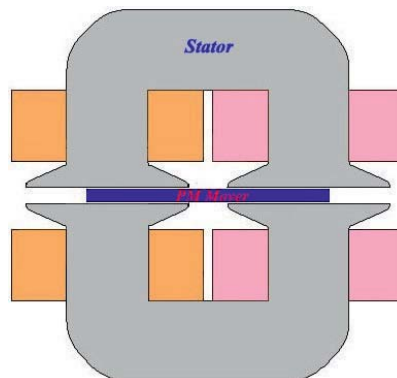


Figure 4.5 : Type III

After considering all the types, we will investigate Cartesian model Type I with respect to force and magnetic energy by equivalent magnetic circuit method. First of all, it should be considered from geometrical structure for low leakage flux and high energy density. Based on their evaluation, it will be accomplished for optimal design by geometrical parameters.

## 4.4 Analytical Calculation

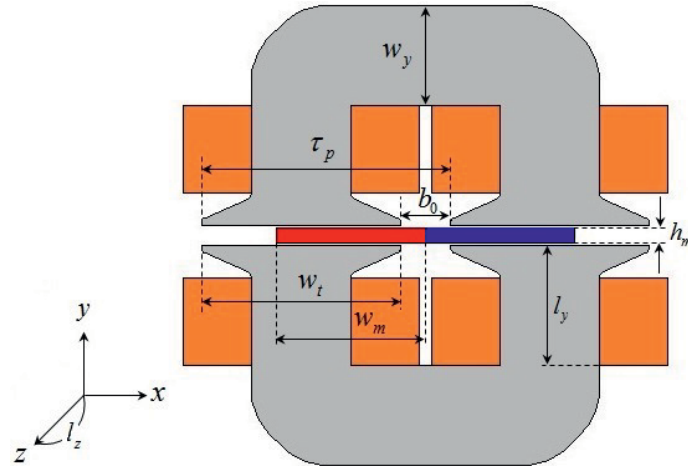


Figure 4.6 : Cross-Section of Cartesian System

The geometric arrangement is important for proper operation of magnet mover and optimization process by parameter study. In figure 4.6,  $\tau_p$  represents the aggregate of width of stator tooth,  $w_t$  and length of slot-opening,  $b_0$ . It requires the calculation of width of magnet which is closely connected with the moving element in this system. The width of the magnet,  $w_m$  should be satisfied that it has to be longer than  $1/2 \cdot \tau_p$ .

It is analyzed in two different methods which are accomplished using equivalent magnetic circuit and optimization by parameter study. The evaluation of electric characteristics by geometric factors such as  $w_t$ ,  $w_m$ ,  $w_y$ ,  $l_y$ ,  $h_m$  and  $b_0$  will be discussed in *Optimal Design*, in paragraph 4.5.

In order to evaluate by an equivalent magnetic circuit, it is necessary to detail the magnetomotive forces of stator and magnet respectively.

$$\Theta_a = N_c \cdot I \quad (4.1)$$

$$\Theta_m = \frac{B_{rem} \cdot h_m}{\mu_0 \cdot \mu_r} \quad (4.2)$$

where,  $N_c$ ,  $I$ , and  $B_{rem}$  indicates a number of coil turns, excited current, and residual magnetic flux density (remanence) of magnet, respectively.

#### 4.4.1 One-Phase System with Two Magnets and Two Pole-Pairs

Figure 4.7 shows a configuration of type I and then equivalent magnetic circuit for magnetic energy calculation. Analytical expression for the force and magnetic energy calculation is as follows.

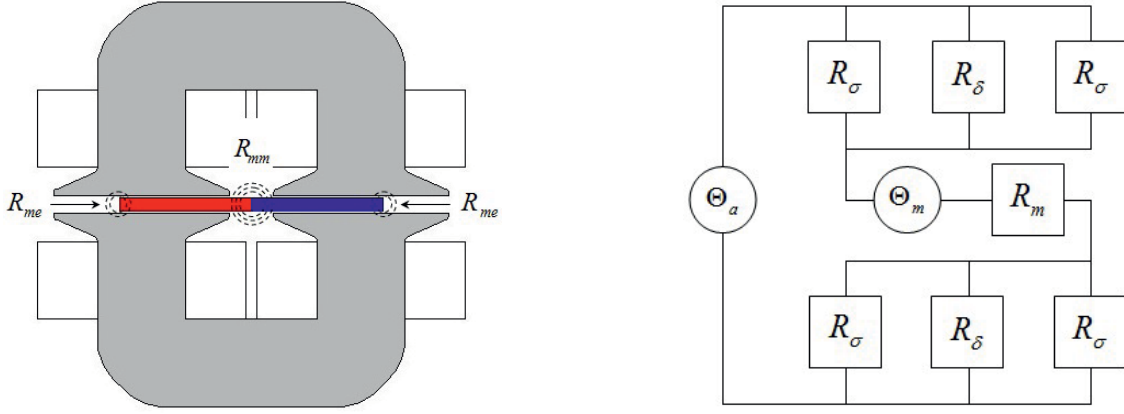


Figure 4.7 : Type I with Assembly

$$R_\delta = \frac{1}{\mu_0} \cdot \frac{2 \cdot \delta}{w_t \cdot l_z} \quad (4.3)$$

$$R_m = \frac{1}{\mu_0} \cdot \frac{h_m}{\mu_r} \cdot \frac{1}{w_m \cdot l_z} \quad (4.4)$$

$$R_\sigma = \frac{1}{\mu_0} \cdot \frac{1}{l_z} \cdot \frac{2 \cdot \delta}{\left(\frac{w_t - w_m}{2}\right)} + \frac{1}{\mu_0} \cdot \frac{\pi}{2} \cdot \frac{1}{l_z} \cdot \frac{1}{\ln\left(\frac{\frac{w_t - w_m}{2}}{2 \cdot \delta + h_m}\right)} + R_{me} + R_{mm} \quad (4.5)$$

where,  $R_\delta$  and  $R_m$  represents a reluctance at air-gap and magnet, respectively. The  $R_\sigma$  means the sum of the leakage reluctances which interacts between armature iron-core and magnet, is generated between the magnets expressed by  $R_{mm}$ , and is caused in magnet edges expressed by  $R_{me}$ . In a magnet pole pair, a leakage flux model for PM machines has been developed. For PM machines, the portion of the magnet to magnet leakage has been well modeled using the circular-arc or straight-arc permeance model [27]. In order to obtain an analytical expression for the leakage flux in terms of the magnetic material properties and the machine dimensions, some assumptions are needed to simplify the problem ; the reluctances associated with iron are negligible. So, it can be expressed by permeance as equation (4.6) through figure 4.8.

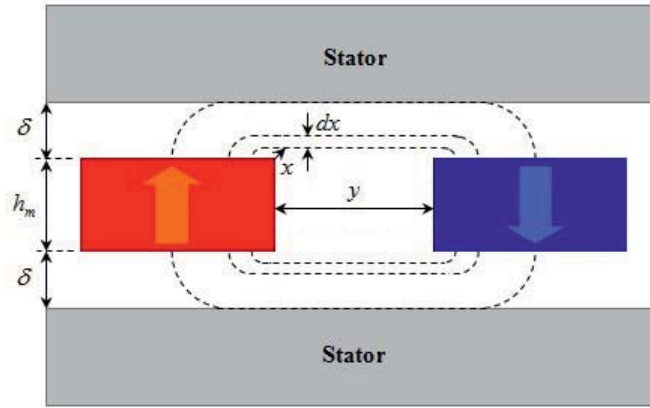


Figure 4.8 : Leakage Flux between Magnets

$$P_{mm} = \frac{1}{R_{mm}} = \sum \frac{\mu_0 \cdot l_z \cdot dx}{\lim_{y=0} \frac{1}{y} + \pi \cdot x} = \int_0^\delta \frac{\mu_0 \cdot l_z}{\lim_{y=0} \frac{1}{y} + \pi \cdot x} dx = \frac{\mu_0 \cdot l_z}{\pi} \cdot \ln \left( 1 + \frac{\pi \cdot \delta}{\lim_{y=0} \frac{1}{y}} \right) \quad (4.6)$$

Meanwhile, the reluctance caused by magnet leakage flux in edge part of mover magnet can be also obtained by calculating its permeance. The circular permeance model is one of the most satisfactory techniques for modeling flux flowing in an air-gap as depicted in figure 4.9. The fringing permeance  $P_{me}$  is an infinite sum of differential width permeance, each of length  $h_m + 2\pi \cdot x$ .

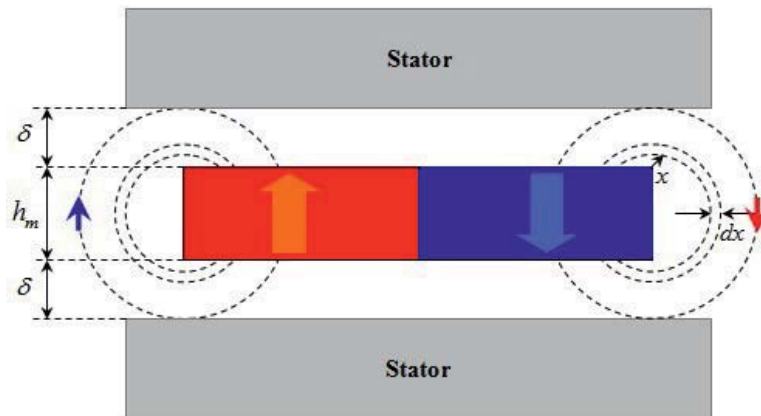


Figure 4.9 : Leakage Flux in Magnet Edge

$$P_{me} = \frac{1}{R_{me}} = \sum \frac{\mu_0 \cdot l_z \cdot dx}{h_m + 2\pi \cdot x} = \int_0^\delta \frac{\mu_0 \cdot l_z}{h_m + 2\pi \cdot x} dx = \frac{\mu_0 \cdot l_z}{2\pi} \cdot \ln \left( 1 + \frac{2\pi \cdot \delta}{h_m} \right) \quad (4.7)$$

Analytical expression for the force and magnetic energy calculation are as follows.

$$\phi_{a\delta} = \frac{\Theta_a \cdot (R_\sigma + R_m)}{(2 \cdot R_\delta + R_\sigma) \cdot R_m + 2 \cdot R_\delta \cdot R_\sigma} \quad (4.8)$$

$$\phi_{a\sigma} = \frac{\Theta_a \cdot (R_\delta + R_m)}{(2 \cdot R_\delta + R_\sigma) \cdot R_m + 2 \cdot R_\delta \cdot R_\sigma} \quad (4.9)$$

$$\phi_{m\delta} = \frac{\Theta_m \cdot R_\sigma}{(2 \cdot R_\delta + R_\sigma) \cdot R_m + 2 \cdot R_\delta \cdot R_\sigma} \quad (4.10)$$

$$\phi_{m\sigma} = \frac{\Theta_m \cdot R_\delta}{(2 \cdot R_\delta + R_\sigma) \cdot R_m + 2 \cdot R_\delta \cdot R_\sigma} \quad (4.11)$$

A magnetic network by *Kirchhoff Law* can be expressed in analogy through electrical circuit theory. By simply equivalence, the average force and force density is derived by using difference of maximum and minimum magnetic energy. The flux equations above are obtained by calculating and the equivalent magnetic circuit in aligned (maximum) and unaligned (minimum) position, respectively.

$$W_{\max} = 2 \cdot (\phi_{a\delta} + \phi_{m\delta})^2 \cdot R_\delta + (\phi_{a\sigma} - \phi_{m\sigma})^2 \cdot R_\sigma + (\phi_{a\delta} - \phi_{a\sigma} + \phi_{m\delta} + \phi_{m\sigma})^2 \cdot R_m \quad (4.12)$$

$$W_{\min} = 2 \cdot (\phi_{a\delta} - \phi_{m\delta})^2 \cdot R_\delta + (\phi_{a\sigma} + \phi_{m\sigma})^2 \cdot R_\sigma + (\phi_{a\delta} - \phi_{a\sigma} - \phi_{m\delta} - \phi_{m\sigma})^2 \cdot R_m \quad (4.13)$$

#### 4.4.2 Two-Phase System with One Magnet and One Pole-Pair (Half-side)

This topology is composed of perpendicular magnetized one-magnet mover and one-side armature iron-core. The organization and its equivalent magnetic circuit are given in figure 4.10.

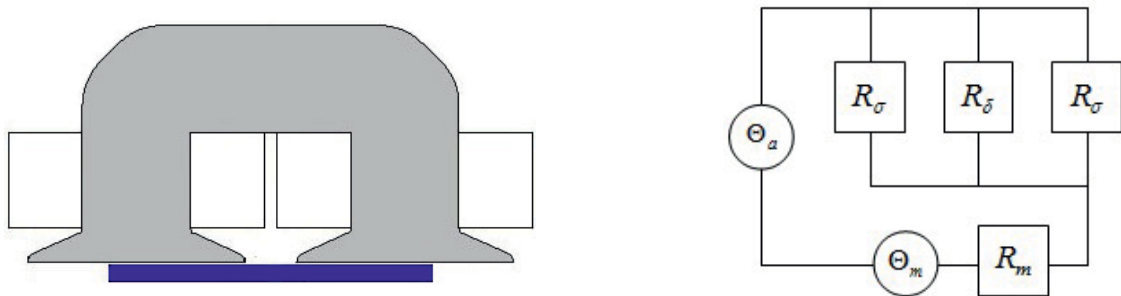


Figure 4.10 : Type II with Assembly

$$R_{\delta} = \frac{1}{\mu_0} \cdot \frac{\delta}{w_t \cdot l_z} \quad (4.14)$$

$$R_m = \frac{1}{\mu_0} \cdot \frac{h_m}{\mu_r} \cdot \frac{1}{w_m \cdot l_z} \quad (4.15)$$

$$R_{\sigma} = \frac{1}{\mu_0} \cdot \frac{1}{l_z} \cdot \frac{\delta}{\left(\tau_p - \frac{w_m}{2}\right)} + \frac{1}{\mu_0} \cdot \frac{\pi}{2} \cdot \frac{1}{l_z} \cdot \frac{1}{\ln\left(\frac{\tau_p - \frac{w_m}{2}}{\delta}\right)} + R_{me} \quad (4.16)$$

$$\phi_{a\delta} = \frac{\Theta_a \cdot \left(\frac{R_{\sigma}}{2} + R_m\right)}{R_{\delta} \cdot \frac{R_{\sigma}}{2} + \left(\frac{R_{\sigma}}{2} + R_{\delta}\right) \cdot R_m} \quad (4.17)$$

$$\phi_{a\sigma} = \frac{\Theta_a \cdot (R_{\delta} + R_m)}{R_{\delta} \cdot \frac{R_{\sigma}}{2} + \left(\frac{R_{\sigma}}{2} + R_{\delta}\right) \cdot R_m} \quad (4.18)$$

$$\phi_{m\delta} = \frac{\Theta_m \cdot \frac{R_{\sigma}}{2}}{R_{\delta} \cdot \frac{R_{\sigma}}{2} + \left(\frac{R_{\sigma}}{2} + R_{\delta}\right) \cdot R_m} \quad (4.19)$$

$$\phi_{m\sigma} = \frac{\Theta_m \cdot R_{\delta}}{R_{\delta} \cdot \frac{R_{\sigma}}{2} + \left(\frac{R_{\sigma}}{2} + R_{\delta}\right) \cdot R_m} \quad (4.20)$$

$$W_{\max} = \frac{1}{2} \cdot (\phi_{a\delta} + \phi_{m\delta})^2 \cdot R_{\delta} + \frac{1}{4} \cdot (\phi_{a\sigma} - \phi_{m\sigma})^2 \cdot R_{\sigma} + \frac{1}{2} \cdot (\phi_{a\delta} + \phi_{a\sigma} + \phi_{m\delta} - \phi_{m\sigma})^2 \cdot R_m \quad (4.21)$$

$$W_{\min} = \frac{1}{2} \cdot (\phi_{a\delta} + \phi_{m\delta})^2 \cdot R_{\delta} + \frac{1}{4} \cdot (\phi_{a\sigma} + \phi_{m\sigma})^2 \cdot R_{\sigma} + \frac{1}{2} \cdot (\phi_{a\delta} - \phi_{a\sigma} + \phi_{m\delta} - \phi_{m\sigma})^2 \cdot R_m \quad (4.22)$$

The structure has inefficient flux paths to pass flux, in other words, the leakage flux is significantly large. Thus it should be supported structurally such at least two magnets for effective operation.

### 4.4.3 Two-Phase System with One Magnet and One Pole-Pair (Double-sided)

This system has a hybrid structure of type I and II as shown in figure 4.11 ; the armature from type I and the magnet mover from type II. Analytical formula for solving equivalent magnetic circuit is as in the following.

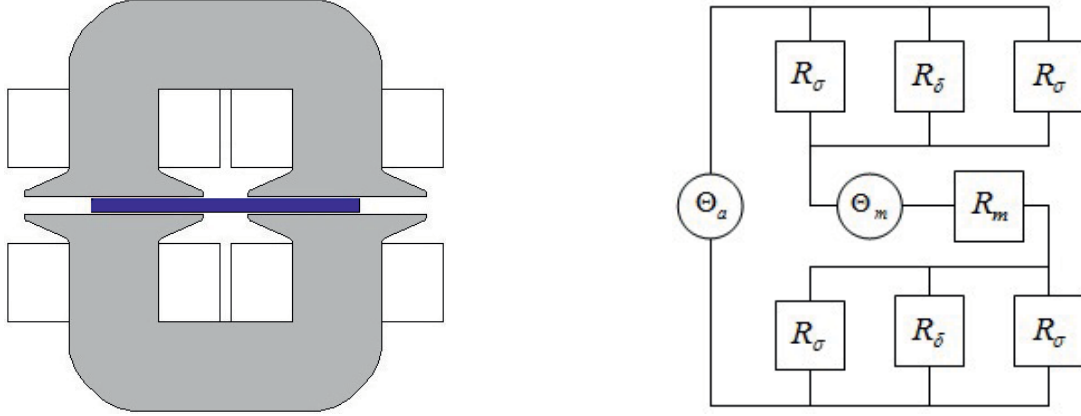


Figure 4.11 : Type III with Assembly

$$R_\delta = \frac{1}{\mu_0} \cdot \frac{2 \cdot \delta}{w_t \cdot l_z} \quad (4.23)$$

$$R_m = \frac{1}{\mu_0} \cdot \frac{h_m}{\mu_r} \cdot \frac{1}{w_m \cdot l_z} \quad (4.24)$$

$$R_\sigma = \frac{1}{\mu_0} \cdot \frac{1}{l_z} \cdot \frac{\delta}{\left(\tau_p - \frac{w_m}{2}\right)} + \frac{1}{\mu_0} \cdot \frac{\pi}{2} \cdot \frac{1}{l_z} \cdot \frac{1}{\ln\left(\frac{\tau_p - \frac{w_m}{2}}{\delta}\right)} + R_{me} \quad (4.25)$$

$$\phi_{a\delta} = \frac{\Theta_a \cdot \left(\frac{R_\sigma}{2} + R_m\right)}{R_\delta \cdot R_\sigma + \left(\frac{R_\sigma}{2} + R_\delta\right) \cdot R_m} \quad (4.26)$$

$$\phi_{a\sigma} = \frac{\Theta_a \cdot (R_\delta + R_m)}{R_\delta \cdot R_\sigma + \left(\frac{R_\sigma}{2} + R_\delta\right) \cdot R_m} \quad (4.27)$$

$$\phi_{m\delta} = \frac{\Theta_m \cdot \frac{R_\sigma}{2}}{R_\delta \cdot R_\sigma + \left(\frac{R_\sigma}{2} + R_\delta\right) \cdot R_m} \quad (4.28)$$

$$\phi_{m\sigma} = \frac{\Theta_m \cdot R_\delta}{R_\delta \cdot R_\sigma + \left(\frac{R_\sigma}{2} + R_\delta\right) \cdot R_m} \quad (4.29)$$

$$W_{\max} = (\phi_{a\delta} + \phi_{m\delta})^2 \cdot R_\delta + \frac{1}{2} \cdot (\phi_{a\sigma} - \phi_{m\sigma})^2 \cdot R_\sigma + \frac{1}{2} \cdot (\phi_{a\delta} + \phi_{a\sigma} + \phi_{m\delta} - \phi_{m\sigma})^2 \cdot R_m \quad (4.30)$$

$$W_{\min} = (\phi_{a\delta} - \phi_{m\delta})^2 \cdot R_\delta + \frac{1}{2} \cdot (\phi_{a\sigma} + \phi_{m\sigma})^2 \cdot R_\sigma + \frac{1}{2} \cdot (\phi_{a\delta} - \phi_{a\sigma} - \phi_{m\delta} - \phi_{m\sigma})^2 \cdot R_m \quad (4.31)$$

The total magnetic energy of all types can be obtained by difference between maximum and minimum magnetic energy. Using the formula, average force ( $F_{ave}$ ) and force density ( $F_{den}$ ) is given as below equations.

$$F_{ave} = \frac{W_{\max} - W_{\min}}{\tau_p} \quad (4.32)$$

$$F_{den} = \frac{F_{ave}}{2 \cdot \tau_p \cdot l_z} \quad (4.33)$$

## 4.5 Optimal Design

In a general concept for the optimum design, it is to minimize of time and cost for design process. The conventional design process can lead to uneconomical designs and can involve a lot of calendar time. In these cases, the designer would find it difficult to decide whether to increase or decrease of the size of a particular structural element to satisfy the constraints. The optimum design process forces the designer to identify explicitly a set of design variables, an objective function to be optimized, and the constraint functions for the system. Thus, the best approach would be an optimum design process that is aided by the parameter study of design variables [28].

Any modeling system has a mechanism that allows you to perform investigation of the model's reaction to its parameters. In simple words, parameters are any numerical quantity that characterizes a given some aspect of the model. In this study, the force maximization is selected as the main aspect under given conditions which are by design variables. Evaluation of electrical characteristics

of Cartesian topology depends essentially on the geometry design parameters. The geometric design parameters are relative to the structural factors, especially height of magnet ( $h_m$ ), width of magnet ( $w_m$ ), width of yoke ( $w_y$ ), length of yoke ( $l_y$ ), length of slot-opening ( $b_0$ ) and width of tooth ( $w_t$ ).

Based on the above mentioned description, the equivalent magnetic circuit considering leakage reluctances is used to calculate the force as object function. The parameter study for optimal process is performed using Type I which has an advantage in the effective magnetic flux.

Table 4.1 : Object Function, Design Variables, and Constraints

-	Symbol	Initial Value	Constraints
Design Variables	$h_m$ [mm]	5	$1 \leq h_m \leq 16$
	$w_m$ [mm]	22	$20 \leq w_m \leq 27$
	$w_y$ [mm]	28	$18 \leq w_y \leq 36$
	$l_y$ [mm]	16	$8 \leq l_y \leq 24$
	$b_0$ [mm]	4	$2 \leq b_0 \leq 10$
	$w_t$ [mm]	25	$24 \leq w_t \leq 33$
Object Function	Force [N]	235	-
Flux Density in Core	B [T]	-	1.6 ~ 1.7

First of all, it is very important to decide an initial value and the constraints of each design variables because an optimal result could be changed by them. The flux density in armature iron-core should be not more than 1.6 ~ 1.7 [T]. The selected design variables have a significant effect on characteristics in Cartesian topology. Moreover, proper choice of initial values makes it more easily and rapidly to access the optimal result. If it is unreliable initial values, it brings about wrong results. An initial value should be selected taking into account electrical and geometrical properties under reasonable constraint condition.

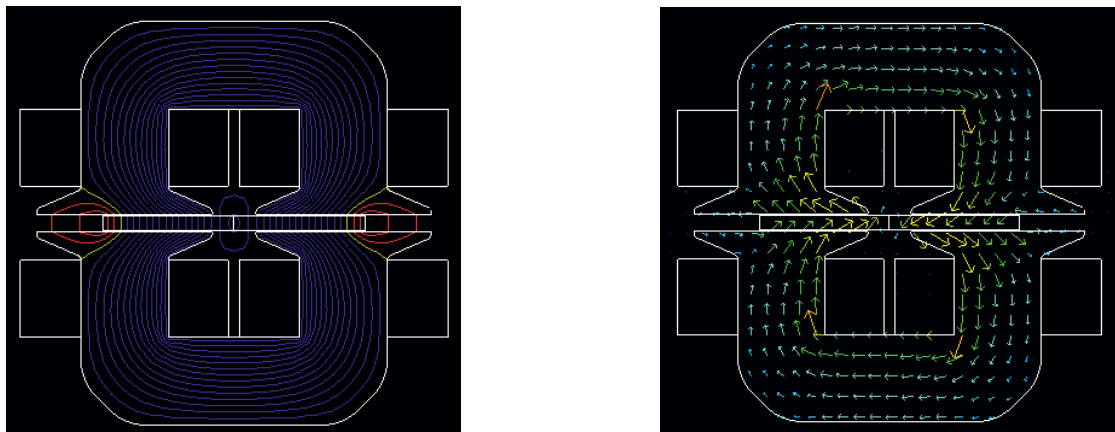


Figure 4.12 : Magnetic Flux Characteristics

Figure 4.12 shows a typical magnetic field line and vector plot in a cross-section view of the overall model.

We discuss optimization process through the parameter study of each design variables. It will be investigated that each design variables affects the object function, and is also affected by the constraint conditions.

### 4.5.1 Height of Magnet

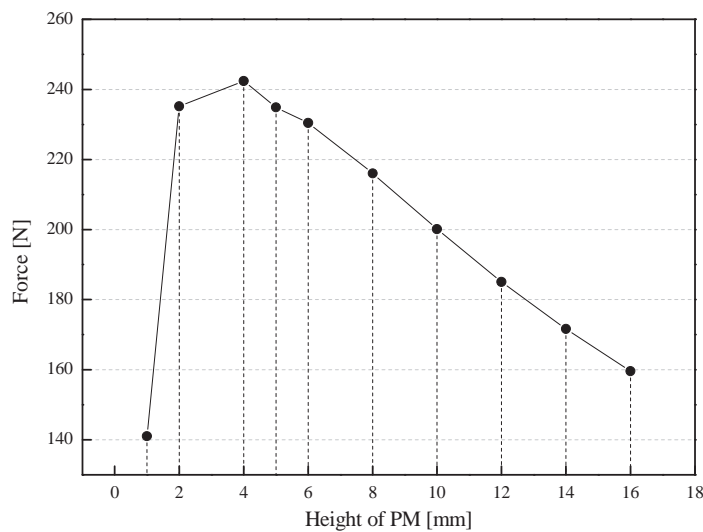


Figure 4.13 : Force by Height of PM

An electromagnet force made from coils is usually called the ‘force constant’ (But, it would be more accurate to refer to it as the force-current relation because it is significantly affected by many factors). Due to interaction such electromagnetic force and force by magnet, it needs optimal selection of magnet height. It can be given by parameter study as figure 4.13 ; we can observe aspect of force profile. Especially, when the height of magnet is 4 [mm], the value of force is approximately 245 [N] and it is the biggest under the given constraint,  $1 \text{ [mm]} \leq h_m \leq 16 \text{ [mm]}$ . If the height is larger than 4 [mm], the force is decreasing slowly. For this effect mainly saturation is responsible.

### 4.5.2 Width of Magnet

The effect of the width of magnet should be viewed in parallel to the height of magnet. The dimension of the magnet affects the flux density in armature iron-core and it also influences on the force. Figure 4.14 shows the force characteristic curve by width of magnet. Its minimum size is not

less than pole pitch,  $\tau_p$ , in that magnet as moving part shall be operated. As a result of the analysis, it brings into a satisfying result when a width of magnet is 25 [mm] and the flux density of armature iron-core has almost 1.6 [T] under given whole constraints.

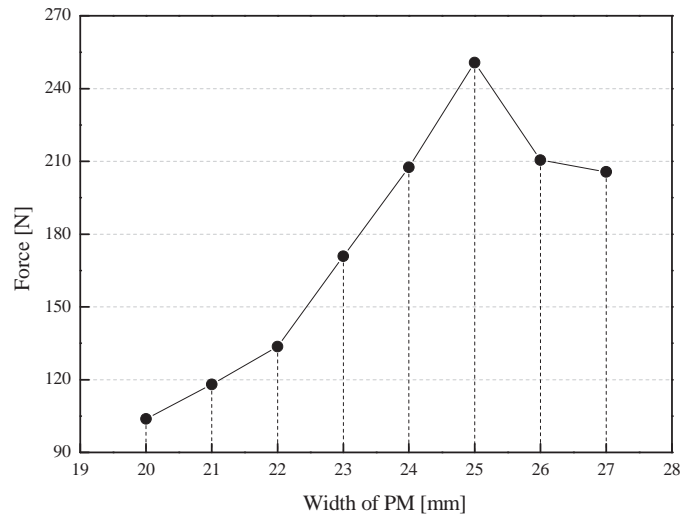


Figure 4.14 : Force by Width of PM

### 4.5.3 Width of Yoke

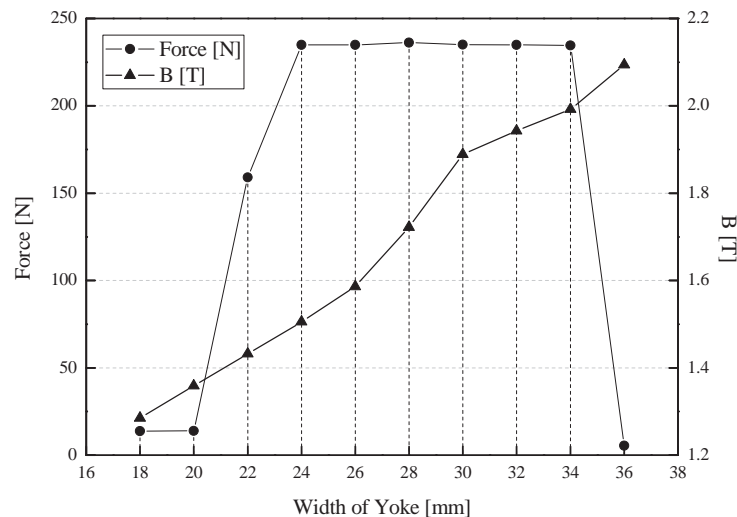


Figure 4.15 : Force and Flux-Density by Width of Yoke

The width of yoke is an essential factor in making decision of geometric size in a 2-D plane. This marked design variable enables magnetic flux to flow the least distance. It will be inefficient due to

the increasing of the force to weight ratio if the width of yoke exceeds 34 [mm]. On the contrary, if the width of yoke is shorter below 24 [mm], it needs higher armature current to keep a maximize force. In this case, the magnetic flux density will saturate the armature iron-core, besides demagnetization phenomenon could occur in the magnet. This is converted to heating and will lead to hysteresis loss. There is nothing to considerable change between 24 [mm] to 34 [mm] as shown figure 4.15. Satisfying flux density as constraint in armature iron-core, it is important to extend the force of object function. As a result, the 28 [mm] is chosen to be optimal value for the width of yoke.

#### 4.5.4 Length of Yoke

Subsequently, a research about length of yoke is performed. There are two curves for the force and the flux density in figure 4.16. The graph of force in length of yoke is almost similar from 10 [mm] to 20 [mm]. Thus, we can not be sure to decide about the length of yoke without constraint. Meanwhile, the curve of flux density shows that there can be wide difference in length of yoke. The focus value of flux density is drawn about 1.6 [T] in armature iron-core. Eventually, optimal point is in the best 16 [mm] of length of yoke corresponding to the force maximization under the given constraint.

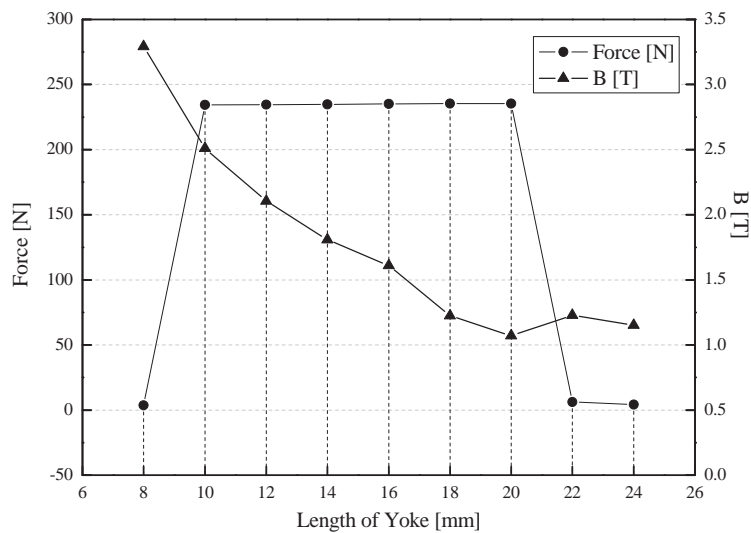


Figure 4.16 : Force and Flux-Density by Length of Yoke

#### 4.5.5 Width of Teeth

The width of teeth ranges from 24 [mm] to 33 [mm]. As shown figure 4.17, force profile shows a symmetrical aspect around the 28 [mm] of width of teeth. The reason that the force value is almost zero at 28 [mm] is the equality of teeth width and width of magnet. In this parameter study, the

width of magnet is used in fixed position of 28 [mm]. It has the maximum value when width of teeth is 25 [mm] and 30 [mm], especially considering in terms of only force values. Although the maximum force value is at the 25 [mm] teeth width under given constraints, the flux density value is much lower than 1.6 ~ 1.7 [T]. This is inefficient on a basic energy conversion principle, therefore we prefer the optimal point at 30 [mm].

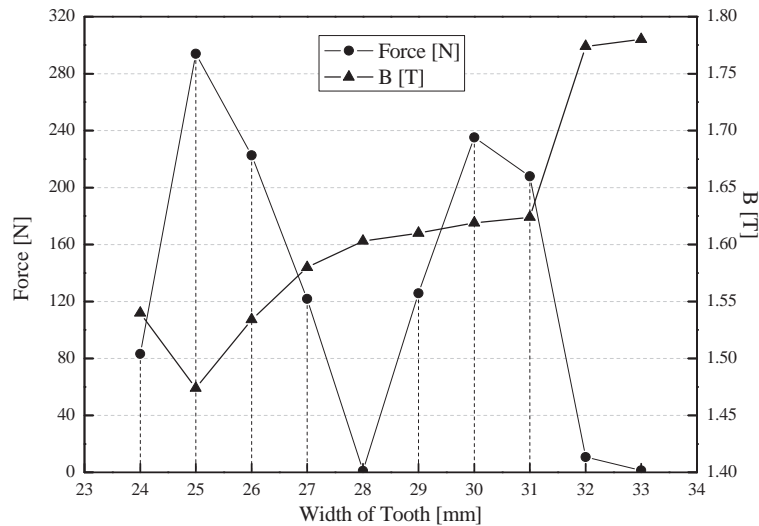


Figure 4.17 : Force and Flux-Density by Width of Teeth

There are some configurations by width of teeth in critical point in figure 4.18.

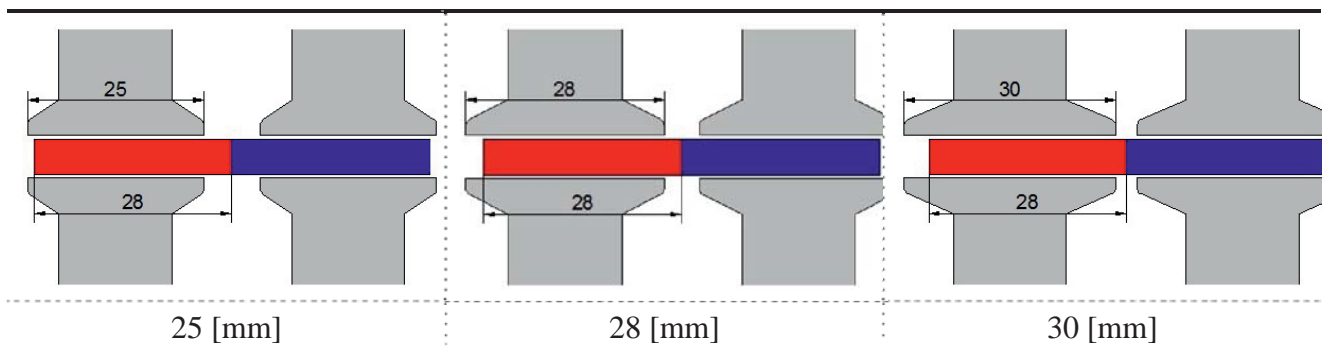


Figure 4.18 : Configurations of Width of Teeth at Constant Width of Magnet

#### 4.5.6 Length of Slot-Opening

With regard to length of slot-opening, the coil winding process should be taken into account and the minimization of detent force. Its initial length is fixed to 2 [mm] at least considering the insertion wound coils. Thus, a geometrical dimension is important to get an optimum result by minimizing

cogging force with proper balance between width of tooth and length of slot-opening. In figure 4.19, we can find optimal point when the length of slot-opening is 8 [mm].

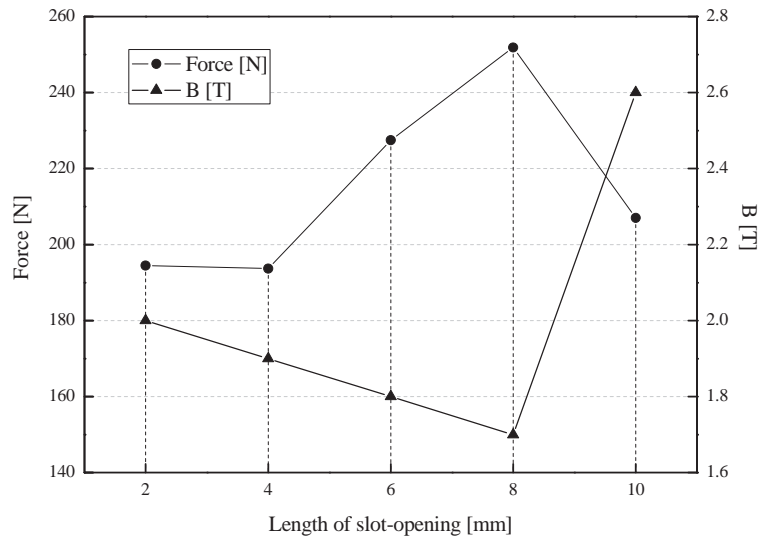


Figure 4.19 : Force and Flux Density by Length of Slot-Opening

#### 4.5.7 Summary

The table 4.2 presents the result of parameter progress about design variables within each constraint. Optimal values of height of magnet, width of magnet, width of yoke, length of yoke and length of slot-opening is almost alike or coincide in initial values.

Table 4.2 : Comparison Result between Initial and Optimal Design

-	Symbol	Initial Value	Optimization
Design Variables	$h_m$ [mm]	5	4
	$w_m$ [mm]	22	25
	$w_y$ [mm]	28	28
	$l_y$ [mm]	16	16
	$b_0$ [mm]	4	8
	$w_t$ [mm]	25	30
Object Function	Force [N]	235	250
Flux Density in Core	B [T]	1.4 ~ 2.0	1.6 ~ 1.7



However, there is a controversial point from results of width of teeth. It is very important to make a decision an initial value of each design variables because an optimal result could be changed by it.

The following question is raised ;

- Why occurs it a big difference between initial and optimal value in width of teeth?

First of all, when the pole pitch is the same as total width of magnet, the flux linkage is relatively low as compared with total width of magnet is longer than pole pitch. The increasing of flux linkage leads to the growth of force because force is proportional to the flux linkage ; this is explained by equation,  $F = J \times B$  if the current is constant. Therefore, it is also essential to achieve an optimal relation between the width of teeth and the width of magnet.

In other view, if the constraint of teeth width is set from 28 [mm] to 33 [mm], the optimal point of tooth teeth will be in 30 [mm]. All of this means that this point exists as *local maximum*<sup>1</sup>. As a part of this case, there is a *global maximum*<sup>2</sup> at 25 [mm] when the range of teeth width is between 24 [mm] and 33 [mm]. Consequently, the choice of initial value and constraints in design variables influences severely the design optimization.

Thus, we can need to consider the selection of the teeth width at 30 [mm] of the second largest force value as shown figure 4.17. Eventually, this parameter has optimum point in 30 [mm] of teeth width which is satisfying maximize force and flux density under given constraints. In conclusion, the desirable choice of local and global maximum in constraints has a major impact on optimum results.

- \* Local maximum<sup>1</sup> : a local maximum also called a relative maximum, is a maximum within some limited neighbourhood. For example, in case of the figure 4.17, if the constraints are set from 24 [mm] to 28 [mm] of design variables, the maximum value (optimal point) exists in 25 [mm]. Then, this value of 25 [mm] is local maximum. However, as mentioned earlier, actual optimal value is 30 [mm] which can be established under the extended boundary condition (constraint). This method has an advantage to find faster an optimal point, whereas it can reach the wrong result if there are two or more maximum values.
- \* Global maximum<sup>2</sup> : the largest value of some function around over entire range. It is impossible to construct an algorithm that will find a global maximum for an arbitrary function. Generally, it is not easy to set the constraint conditions of unknown model. In this case, the optimization is carried out by global maximizing. However, this method has the disadvantage that it takes a lot of time compared with the local maximum.

This study by the optimal process is assumed as the following ;

- Armature reaction and demagnetization of the PM edge is ignored
- Usually, an object function is composed of more than one parameter. However, the optimization study is achieved by 6 proposed variables and their constraints

### 4.6 Discussion

We have investigated the characteristics of three different topologies in Cartesian system. It was analyzed by two methods ; equivalent magnetic circuit and optimization process. A value of force density using magnetic energy calculation is the biggest in type I. The reason is that it allows efficient flow of magnetic flux structurally. In respect to the efficiency, type I is also the highest on account of lower leakage flux compared to another type II and III. Whereas, type II has an inefficient magnetic flux path ; consequently the force density and efficiency is the lowest of among the types. In virtue of effective magnetic flux paths, type I shows better results than type II and III in all of force density and electrical characteristics.

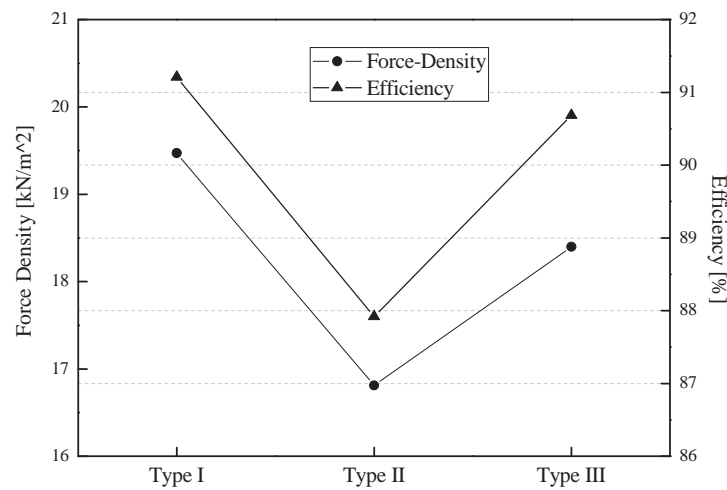


Figure 4.20 : Force Density & Efficiency

The parameters study through design variables is one of the optimal processes, which benefits from good starting guesses. The choice of these parameters should be determined by factors influencing the object function. Also, the constraint such as satisfaction of critical value of flux density can be added for the practical design in the process of optimization. Generally, the optimization problems are best solved rapidly and trustfully when a proper selection of initial values is performed and a number of independent design variables are smaller. It will be helpful to investigate topologies which are not only Cartesian. This will be done in the next chapters using the some optimization method.



---

## 5 Cylindrical Topology

### 5.1 Introduction

Among the various linear generators, cylindrical topologies with magnet excitation are particularly popular, since they hardly experience typical assembly problems of linear machines ; conforming to a compact structure and a low weight compared with the force. The cylindrical type linear generators include an armature and a translator. The former consists of a single conductive wire cylindrically wound and encapsulated, while the latter is a cylindrical assembly of sintered  $NdFeB$  permanent magnets arrayed at an axial *North-South* stack contained in an encasing tube. This topology is brushless, so it needs little maintenance.

Recently, cylindrical linear permanent magnet motor became an attractive candidate for servo systems in need of high precision control, in spite of such disadvantages as difficulty of manufacturing of a magnet mover, maintaining fixed air-gap length and laminating for reduced eddy-current loss. Moreover, linear oscillating generator with tubular configuration has advantages of exhibiting high force to volume ratios and high positioning speed. The amount of the leakage flux is small and the rotation of the piston does not affect the electric characteristics of the linear oscillating generator [29].

Cylindrical type linear generator has some more advantages than flat type one as following aspects ; it has higher efficiency, reliability and leakage is smaller because of its symmetric structural merits. Also the amount of copper is less because no winding overhang is required, therefore the copper loss becomes less than that of flat type linear generator. The shaft is cylindrical and it can be easily connected with the rod of the engine piston without complex mechanical structure. Furthermore, the cylindrical translator can be rotated freely with the piston of the engine and there is no interference to the magnetic characteristics in the linear generator.

Although that the cylindrical type linear generator has numerous advantages, still causing cogging force ripple, the permanent magnets interact with the slotted armature structure and the finite-length stator core. Such a force ripple in linear machines is the sum of two components : the cogging force and *Lorentz Force* due to winding harmonics. The cogging force is minimized by varying the magnetic pole pitch.

From now on, it deals with characteristics and analysis by number of phase and displacement of stroke through the proposed new structure.



## 5.2 Configuration

This chapter focuses on the linear oscillating generator of a cylindrical type. A sketch of this structure is shown in figure 5.1 ; the stationary part consists of the stator iron core and armature winding encapsulated in the stator structure. The moving part is composed of radially magnetized surface mounted permanent magnet on back iron core as translator. A lack of iron in the mover means the forces reduce linearly with current. The axial force is the thrust force, whereas the radial force is perpendicular to the direction of movement and must be resisted by the bearings of the device. For a cylindrical mover the field is in a radial-axial plane ( $r, z$ ) and so the back iron in the mover concentrates the flux ; as a result, it needs the detailed analysis.

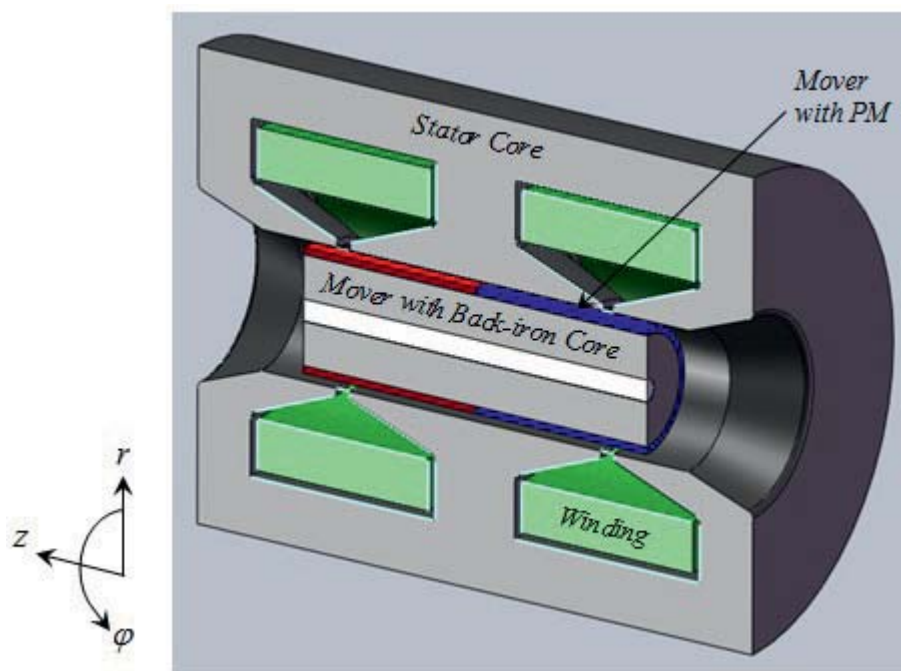


Figure 5.1 : Cylindrical Topology

The proposed model has advantages as follows ;

- Naturalness of Initialization → The mover will be positioned in the center due to the attraction equilibrium between both edges of stator teeth and mover when applying no current.
- Soft movement owing to 3 poles structure → The translator stroke is set to one pole pitch
- Solenoidal coil having cylindrical form → No winding overhang
- Capacity expansion is practicable due to unlimited size of PM  
→ Volume of N-pole and S-pole is same each other
- Low dependence relatively between PM and electromagnet ; naturalness of initialization and soft movement by 3 poles structure using the magnetism

However, this topology has a drawback that the magnetic flux tends to converge in the direction of shaft. Thus, it is very important to avoid saturation of the back iron of the mover.

### 5.3 Principle of Force Generation

The cylindrical topology operates that the translator moves left, center, and right sides sequentially and its stroke is set up to one pole pitch. Figure 5.2.a represents the force curve between electromagnet and permanent magnet following the positions of translator. For such a structure, it enables not only a high capacity but also natural initialization of translator due to same volume of permanent magnet.

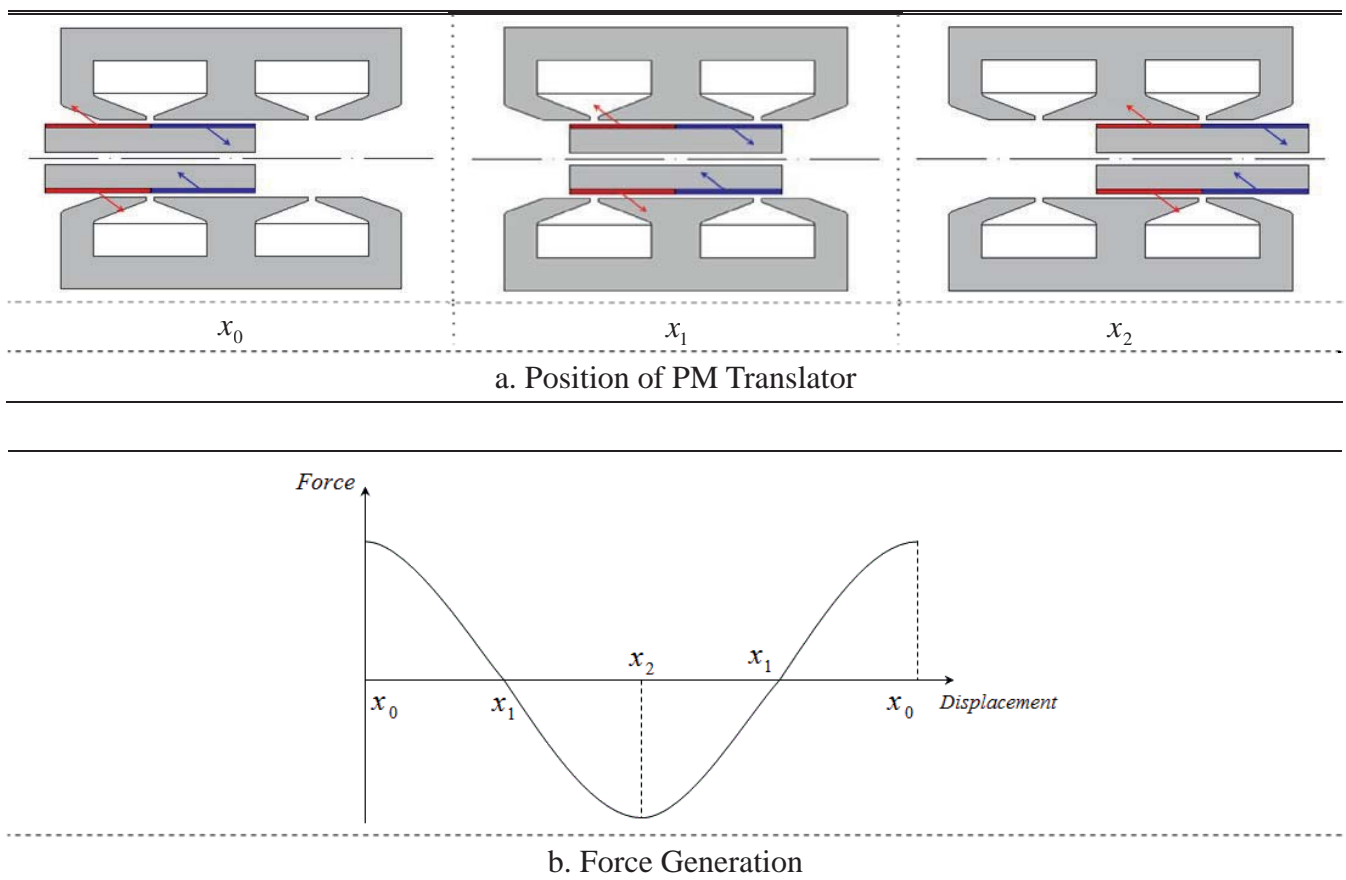


Figure 5.2 : Force by Interaction of a PM and Armature

The translator consists of two poles of permanent magnets magnetized radial. The force increases with linkage flux ; linkage flux is the highest when the translator is located in  $x_0$  and  $x_2$ . As the permanent magnet translator is near by center position of  $x_1$ , force decreases as shown in figure 5.2 ; accordingly, it is required to excite current switching regularly to obtain constant force waveform. Figure 5.2.b represents also the force change trend over the time.



## 5.4 Numerical Calculation

In particular, the flux characteristic under given electrical and geometrical parameters of the armature and field is very important to forecast the characteristic of the machine during design process. Then, the analytical results are compared with those obtained by numerical calculation such as a FEA. A good agreement between the results of the analytical model with those obtained from FEA is recognized by comparing the magnetic quantities and the mechanical forces [30].

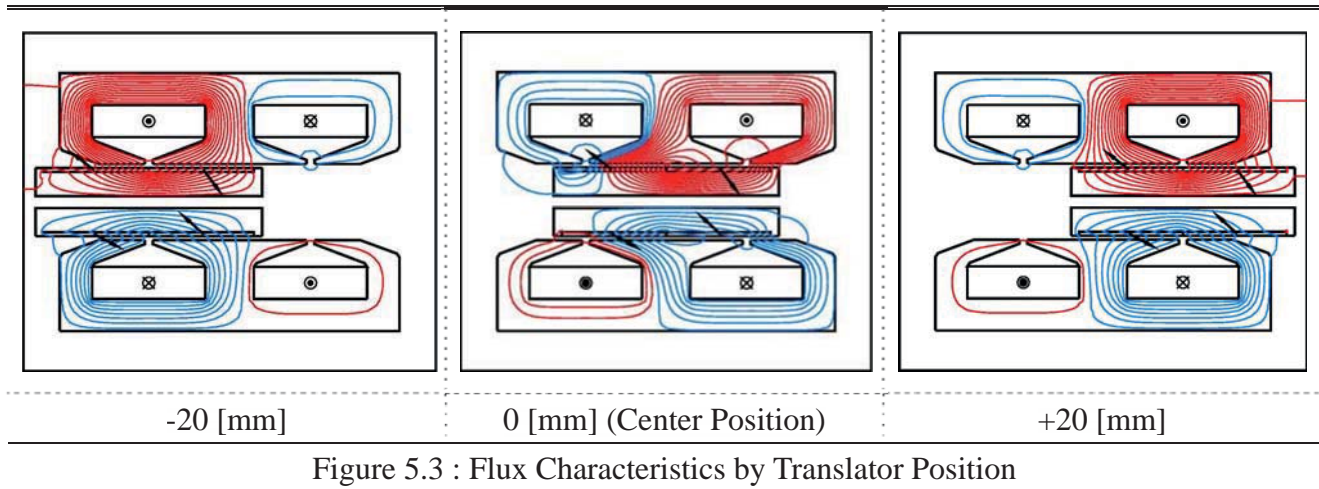


Figure 5.3 represents the flux line at the translator position ; they indicates -20 [mm], 0 [mm], and +20 [mm] of total stroke, respectively. Based on the flux line by FEA, the analytical calculation will be accomplished more accurately.

## 5.5 Analytical Calculation

This research predicts the force characteristics using equivalent magnetic circuit method which provides an accurate means of determining the field distribution. Although equivalent magnetic circuit analysis does not consider a saturation of magnetic flux, it can be a useful tool enough to estimate approximately design parameters on the machine performance. The magnetic energy using the reluctance network of the machine is calculated by dividing aligned and unaligned position which is named by maximum and minimum, respectively.

It is compared with the number of phase by equivalent magnetic circuit network considering leakage reluctance.

- Single-Phase System
- Two-Phase System
- Single-Phase System with 3 Coils and Long Stroke

### 5.5.1 One-Phase System

There is the dimension for the analytical calculation of reluctances and the winding circuit of single-phase system in figure 5.4.

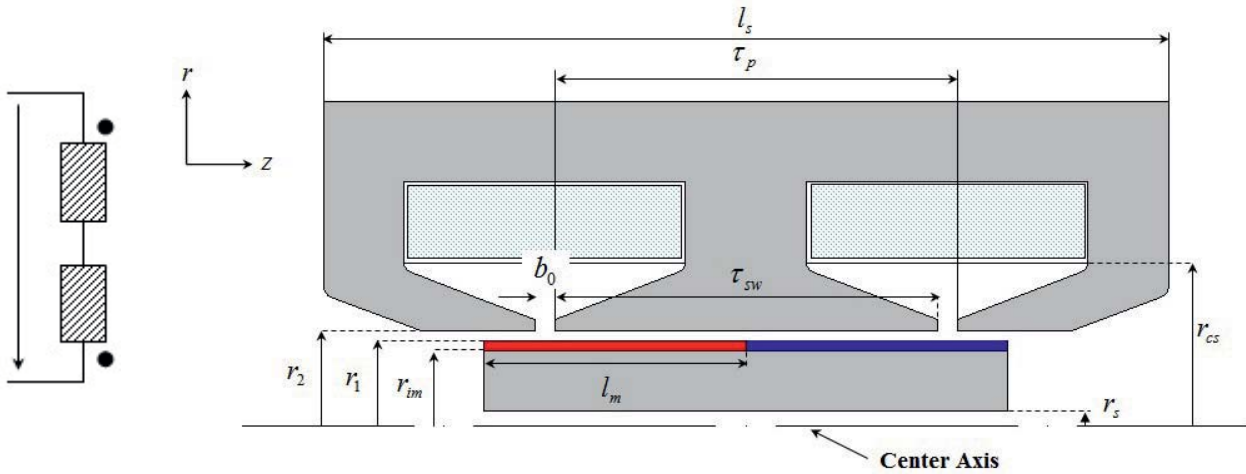


Figure 5.4 : Single-Phase System

Predefined formulation for the reluctance calculation is described by equation (5.1) ~ (5.4).

$$\Theta_a = N_c \cdot I \quad (5.1)$$

$$\Theta_m = \frac{B_{rem} \cdot (r_1 - r_{im})}{\mu_0 \cdot \mu_r} \quad (5.2)$$

$$R_\delta = \frac{1}{\mu_0} \cdot \frac{\delta}{2 \cdot \pi \cdot (r_2 - r_1) \cdot \tau_{sw}} \quad (5.3)$$

$$R_m = \frac{1}{\mu_0 \cdot \mu_r} \cdot \frac{r_1 - r_{im}}{2 \cdot \pi \cdot (r_1 - r_{im}) \cdot l_m} \quad (5.4)$$

The  $R_\delta$  and  $R_m$  indicates the reluctance at air-gap and permanent magnet respectively, where  $\delta$  is length of the air-gap.

#### Maximum Magnetic Energy

To correctly estimate the reluctance variation, it is necessary to model a reasonable formulation of the various reluctances (permeances) of the machines. Now, the characteristic of the maximum magnetic energy can be calculated by equivalent circuit at unaligned position as shown figure 5.5.

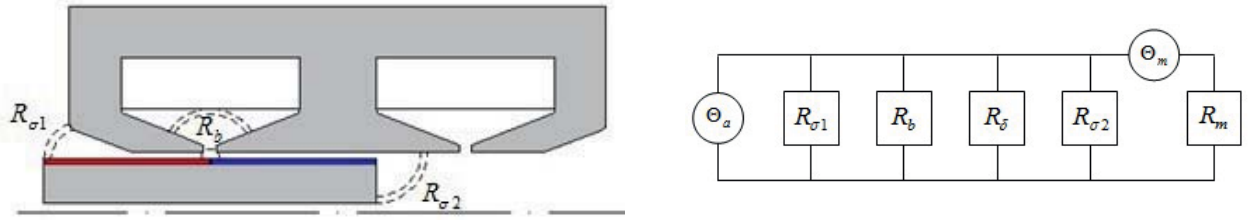


Figure 5.5 : Unaligned Position

In the unaligned position, reluctances are divided into three parts ;  $R_{\sigma 1}$ ,  $R_{\sigma 2}$  and  $R_b$ . They express the leakage reluctance of left-side, right-side and interactive fringing reluctance between permanent magnet poles and end part of the armature tooth in the slot-opening, respectively.

$$R_{\sigma 1} = \frac{1}{\mu_0} \cdot \frac{\delta}{2 \cdot \pi \cdot (r_2 - r_1) \cdot \left( l_m - \frac{\tau_{sw}}{2} \right)} + \frac{1}{\mu_0} \cdot \frac{\pi}{9} \cdot \frac{1}{2 \cdot \pi \cdot (r_2 - r_1)} \cdot \frac{1}{\ln \left( \frac{l_m - \frac{\tau_{sw}}{2}}{\delta} \right)} \quad (5.5)$$

$$R_{\sigma 2} = \frac{1}{\mu_0} \cdot \frac{\delta}{2 \cdot \pi \cdot (r_2 - r_1) \cdot (r_{im} - r_s)} + \frac{1}{\mu_0} \cdot \frac{\pi}{2} \cdot \frac{1}{2 \cdot \pi \cdot (r_2 - r_1)} \cdot \frac{1}{\ln \left( \frac{r_{im} - r_s}{r_1 - r_{im}} \right)} \quad (5.6)$$

Magnifying region  $R_b$  of the figure 5.6, it is as shown in figure 5.5 and represents fringing permeance in equation (5.7).

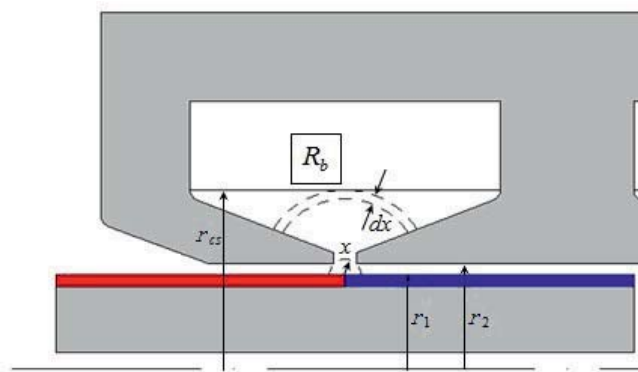


Figure 5.6 : Permeance at Unaligned Position

$$P_b = \sum \frac{\mu_0 \cdot 2 \pi \cdot (r_{cs} - r_2) \cdot dx}{b_0 + \pi \cdot x} = \int_{r_1}^{r_{cs}} \frac{\mu_0 \cdot 2 \pi \cdot (r_{cs} - r_2)}{b_0 + \pi \cdot x} \cdot dx = \frac{\mu_0 \cdot 2 \pi \cdot (r_{cs} - r_2)}{\pi} \cdot \ln \left( 1 + \frac{\pi \cdot (r_{cs} - r_1)}{b_0} \right) \quad (5.7)$$

The reciprocal of permeance is reluctance ; it can be expressed as equation (5.8).

$$R_b = \frac{1}{P_b} \quad (5.8)$$

To obtain the minimum magnetic energy, it should be solved of the reluctance network matrix using the above reluctance formulas.

$$\begin{bmatrix} \phi_1 \\ \phi_2 \\ \phi_3 \\ \phi_4 \\ \phi_5 \end{bmatrix} = \begin{bmatrix} R_{\sigma_1} & -R_{\sigma_1} & 0 & 0 & 0 \\ -R_{\sigma_1} & R_{\sigma_1} + R_b & -R_b & 0 & 0 \\ 0 & -R_b & R_b + R_\delta & -R_\delta & 0 \\ 0 & 0 & -R_\delta & R_\delta + R_{\sigma_2} & -R_{\sigma_2} \\ 0 & 0 & 0 & -R_{\sigma_2} & R_{\sigma_2} + R_m \end{bmatrix}^{-1} \cdot \begin{bmatrix} \Theta_a \\ 0 \\ 0 \\ 0 \\ \Theta_m \end{bmatrix} \quad (5.9)$$

### Minimum Magnetic Energy

An average force can be calculated by gradient between maximum and minimum of magnetic energy. The magnetic energy has a minimum value at the aligned position ; it consists of the  $R_{\sigma_3}$  and  $R_{ns}$  as shown in figure 5.7.

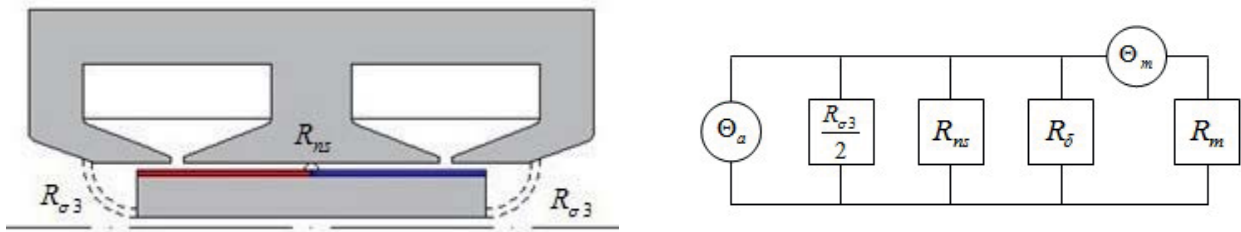


Figure 5.7 : Aligned Position

Under the aligned position, the leakage reluctance at the both ends can be expressed by equation (5.10).

$$R_{\sigma_3} = \frac{1}{\mu_0} \cdot \frac{\delta}{2 \cdot \pi \cdot (r_2 - r_1) \cdot \left(\frac{l_s}{2} - l_m\right)} + \frac{1}{\mu_0} \cdot \left(\frac{\pi}{2} + \frac{\pi}{9}\right) \cdot \frac{1}{2 \cdot \pi \cdot (r_2 - r_1)} \cdot \frac{1}{\ln\left(\frac{r_{im} - r_s}{r_1 - r_{im}}\right)} \quad (5.10)$$

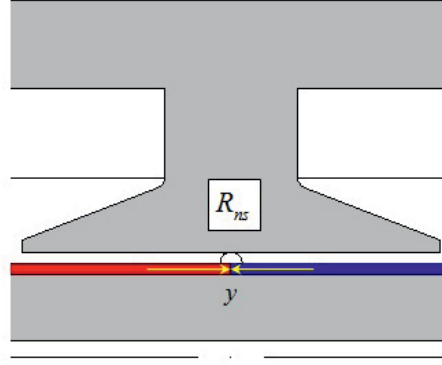


Figure 5.8 : Permeance at Unaligned Position

The  $R_{ns}$  indicates the leakage reluctance between armature teeth and two magnet poles in the air-gap. It can be expressed as equation (5.11) by figure 5.8.

$$P_{ns} = \sum \frac{\mu_0 \cdot 2\pi \cdot (r_2 - r_1) \cdot dx}{\lim_{y \rightarrow \infty} \frac{1}{y} + \pi \cdot x} = \int_0^\delta \frac{\mu_0 \cdot 2\pi \cdot (r_2 - r_1)}{\lim_{y \rightarrow \infty} \frac{1}{y} + \pi \cdot x} \cdot dx = \frac{\mu_0 \cdot 2\pi \cdot (r_2 - r_1)}{\pi} \cdot \ln \left( 1 + \frac{\pi \cdot \delta}{\lim_{y \rightarrow \infty} \frac{1}{y}} \right) \quad (5.11)$$

Just like preceding calculation of maximum magnetic energy, the matrix of reluctance network for minimum magnetic energy by figure 5.7 is as follows.

$$\begin{bmatrix} \phi_6 \\ \phi_7 \\ \phi_8 \\ \phi_9 \end{bmatrix} = \begin{bmatrix} \frac{R_{\sigma 3}}{2} & -\frac{R_{\sigma 3}}{2} & 0 & 0 \\ -\frac{R_{\sigma 3}}{2} & \frac{R_{\sigma 3}}{2} + R_{ns} & -R_{ns} & 0 \\ 0 & -R_{ns} & R_{ns} + R_\delta & -R_\delta \\ 0 & 0 & -R_\delta & R_\delta + R_m \end{bmatrix}^{-1} \cdot \begin{bmatrix} \ominus_a \\ 0 \\ 0 \\ \ominus_m \end{bmatrix} \quad (5.12)$$

### Calculation of Magnetic Energy and Force

As stated in the preceding chapter, 3.4 *Calculation for Magnetic Energy*, the formula for the calculation of the magnetic energy and force is satisfied as below.

$$\Delta W = W_{\max} - W_{\min} = \left( \frac{1}{2} \cdot \phi_{\max}^2 \cdot R_{\max} \right) - \left( \frac{1}{2} \cdot \phi_{\min}^2 \cdot R_{\min} \right) = \frac{1}{2} \cdot [(\phi_{\max}^2 \cdot R_{\max} - \phi_{\min}^2 \cdot R_{\min})] \quad (5.13)$$

where, the suffix of each character such as max and min means the magnetic energy, flux linkage and reluctance at the maximum and minimum position, respectively.

$$F_{ave} = \frac{\Delta W}{\tau_p} \tag{5.14}$$

### 5.5.2 Two-Phase System

In a single-phase linear oscillating generator, the stator has a number of windings connected in series to form a single circuit across which the output voltage is generated. The voltage across all stator windings is equal in phase with each other because the flux linkage is constant. Also, since the stator windings are connected in series, the voltages produced in each winding add up to produce a final generator output voltage that is two times the voltage across each of the individual stator windings.

A two-phase generator is designed to produce two completely separate voltages. Each voltage, by itself, may be considered as a single-phase voltage ; each is generated completely independent of the other. Each winding is made up of two windings that are connected in series so that their voltages add. The translator is identical to that used in the single-phase generator. However, there is the disadvantage of having twice as many stator coils, which require a much more complex control. True two-phase electric machine is essentially obsolete. Special purpose systems may use a two-phase system for control. Today two-phase power is used for stepper motors and a few other specialized applications. This two-phase system was subsequently rendered obsolete, however, by the superior three-phase system that is now universally used throughout the world.

### 5.5.3 One-Phase System with 3 Coils and Long Stroke

Generally, it has a diversity of application fields to choose a displacement of mover by number of phases and coil sides. For instance, figure 5.9 represents a long-stroke system of single-phase with 3 coil-sides.

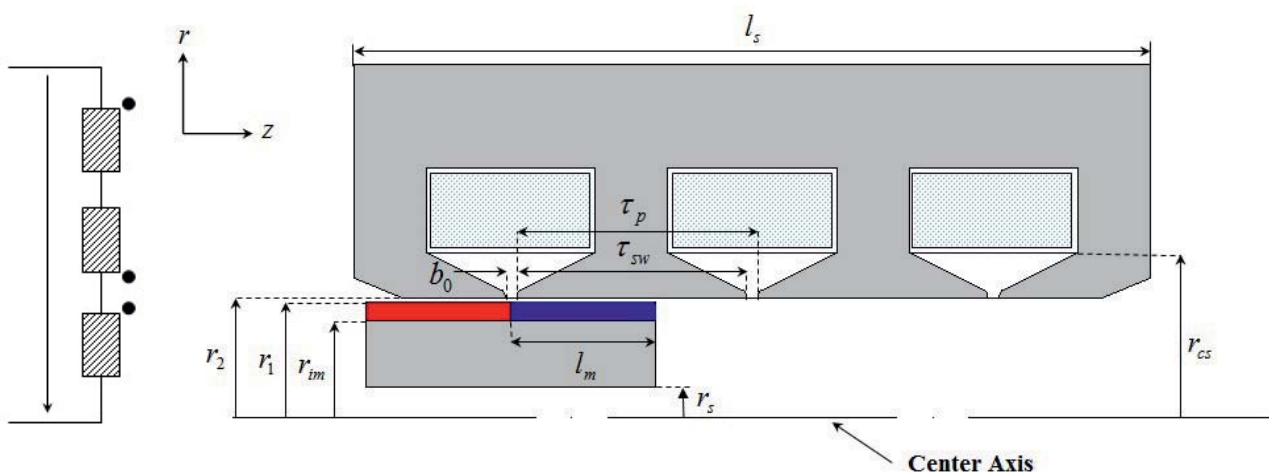


Figure 5.9 : One-Phase System with 3 Coil-Sides

Now make a calculation of the characteristic of the long-stroke system by equivalent magnetic circuit. Above all, the basic equations of long-stroke system for reluctance calculation are identical to that of single-phase system ;  $\Theta_a$ ,  $\Theta_m$ ,  $R_\delta$  and  $R_m$ .

Maximum Magnetic Energy

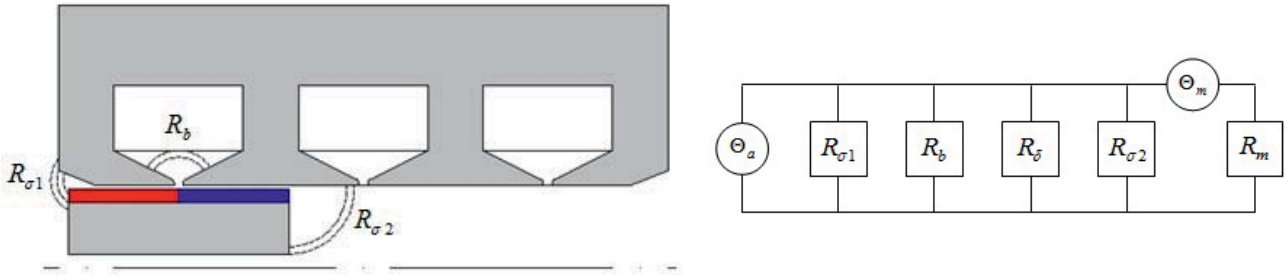


Figure 5.10 : Unaligned Position

$$R_{\sigma 1} = \left[ \frac{1}{\mu_0} \cdot \frac{\delta}{2 \cdot \pi \cdot (r_2 - r_1) \cdot \left( l_m - \frac{\tau_{sw}}{2} \right)} + \frac{1}{\mu_0} \cdot \frac{\pi}{2} \cdot \frac{1}{2 \cdot \pi \cdot (r_2 - r_1)} \cdot \frac{1}{\ln \left( \frac{l_m - \frac{\tau_{sw}}{2}}{\delta} \right)} \right] + \left[ \frac{1}{\mu_0} \cdot \frac{\pi}{1} \cdot \frac{1}{2 \cdot \pi \cdot (r_1 - r_{im})} \cdot \frac{1}{\ln \left( \frac{r_{im} - r_s}{\delta} \right)} \right] \quad (5.15)$$

The leakage reluctance of  $R_b$ , generated mutually by interacting between two teeth inside the slot region, is calculated such as that of single-phase by permeance calculation.

$$R_b = \frac{\pi}{\mu_0 \cdot 2 \pi \cdot (r_{cs} - r_2)} \cdot \frac{1}{\ln \left( 1 + \frac{\pi \cdot (r_{cs} - r_2)}{b_0} \right)} \quad (5.16)$$

$$R_{\sigma 2} = \frac{1}{\mu_0} \cdot \frac{\delta}{2 \cdot \pi \cdot (r_2 - r_1) \cdot \left[ \left( \tau_{sw} + \frac{b_0}{2} \right) - l_m \right]} + \frac{1}{\mu_0} \cdot \frac{\pi}{2} \cdot \frac{1}{2 \cdot \pi \cdot (r_2 - r_s)} \cdot \frac{1}{\ln \left( \frac{r_{im} - r_s}{\delta} \right)} \quad (5.17)$$

The matrix formulation for calculation of maximum magnetic energy is also identical to that of single-phase system.

Minimum Magnetic Energy

The configuration and equivalent magnetic circuit modeling in minimum inductance position is shown figure 5.11. The reluctances interacting with the stator and translator are composed of  $R_{\sigma 3}$  and  $R_{ns}$  from the equation (5.11).

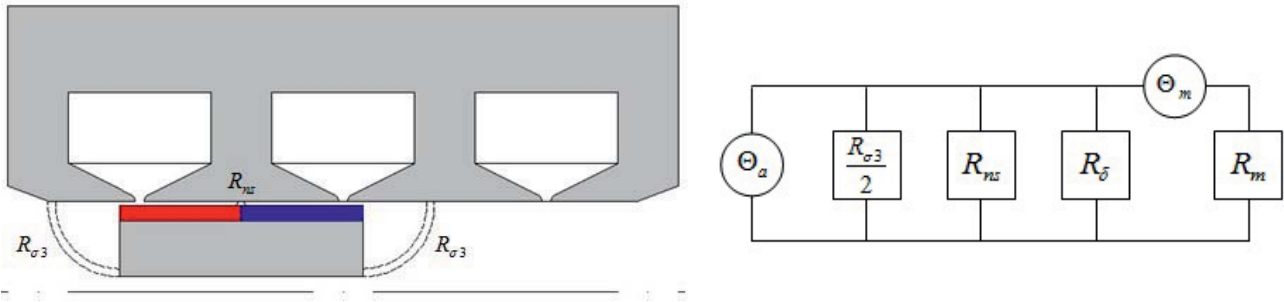


Figure 5.11 : Aligned Position

$$R_{\sigma 3} = \frac{1}{\mu_0} \cdot \frac{\delta}{2 \cdot \pi \cdot (r_2 - r_1) \cdot \left(\frac{l_s}{3} - l_m\right)} + \frac{1}{\mu_0} \cdot \frac{\pi}{2} \cdot \frac{1}{2 \cdot \pi \cdot (r_2 - r_s)} \cdot \frac{1}{\ln\left(\frac{r_2 - r_s}{\delta}\right)} \quad (5.18)$$

In the same way as that of single-phase system, the reluctance of  $R_{ns}$  is calculated inversely by permeance calculation.

$$R_{ns} = \frac{\pi}{\mu_0 \cdot [2 \pi \cdot (r_2 - r_1)]} \cdot \frac{1}{\ln\left(\frac{\pi \cdot \delta}{\lim_{y \rightarrow \infty} \frac{1}{y}}\right)} \quad (5.19)$$

Similarly, the matrix equation in the unaligned position is equal to that of the single-phase system because the equivalent magnetic circuit is same each other in single-phase and long-stroke system. Besides, the analytical expression for magnetic energy and force is also identical to that of single-phase system.



## 5.6 Discussion

This chapter mainly studied about cylindrical type by displacement of stroke in single-phase system. The main advantage of cylindrical linear construction arises from its inherent ability to neutralize normal forces acting between the stator and the translator, which enables accomplishment of the design. In addition, the nonexistence of end-turns brings about not only minimization of power loss but also high force per volume ratio. It conduces to favorable generator characteristics.

This study provides the design process by the characteristic prediction using the numerical and analytical calculation. This helps accomplishment to minimize the leakage and to optimize the back iron in mover. The comparison of results between equivalent magnetic circuit analysis and FEM will be continuously achieved in *chapter 10 Detailed Design*.

---

## 6 Hybrid Stepping Generator

### 6.1 Introduction

The linear PM brushless oscillatory generators have gained momentum recently, HEVs [31]. Most of the research on direct drive application such as HEVs has focused on variable reluctance PM machines, transverse flux PM machines or hybrid stepping machines. Single-phase hybrid stepping machine was first introduced in 1997 by *R. P. Deodhar* [32] for an automobile generator to replace the standard claw pole alternator. This single-phase configuration was fully explored as a generator and not as a motor [33]. The leading feature of these machines is the very high force-to-mass ratio compared with classical machines, which makes them attractive in low speed applications by reason of high pole number [34]. The moving piston of this generator will be directly coupled to rod. Similarly, the flux path of a hybrid stepping machine is longitudinal, or parallel to the direction of movement ; it is distinguished from transverse flux that flux lines go perpendicular to the moving of translator.

The generator will be used for direct-drive power take-off in an IC engine. A combined field and circuit model is used to model and analyze the electromagnetic behavior of the machine. This develops an analytical model for a novel double-sided hybrid stepping linear machine for use in IC engine applications. So, the intent of this study is to introduce a new type of Hybrid Stepping Permanent Magnet (HSPM) linear machine of single-phase for possible use as a direct-drive in future IC engine.

Hybrid stepping machine is a doubly-salient machine with magnets on the mover. The flux linkage by phase concentrated coils in the stator reverses polarity with the traveling of the mover. It has numerous advantages such as simple construction, low inertia and high force density application due to PMs on the mover pole. The stator also offers a large freedom in winding configurations, which is an important tool to reduce cogging forces. The stator winding is made of standard wires with circular cross-section. Furthermore, conductors with circular cross-section made of several strands are very flexible and simplify the winding process of the stator considerably.

This study investigates how different design choices affect the performance of the HSPM generator. As the factors affecting, it is considered by types of magnets. This is an important design variable which determines force performance in given stator tooth. Henceforth, it will be performed in analytical calculation by equivalent magnetic circuit method considering leakage and also characteristics simulated based on finite element formulation.

The schematic diagrams of the hybrid stepping generator are shown figure 6.1.

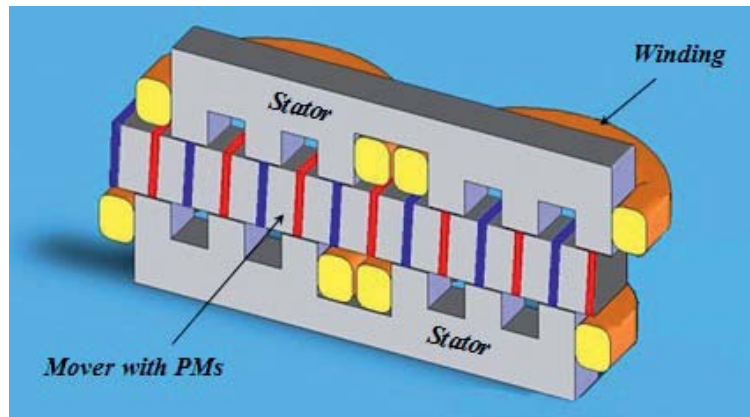


Figure 6.1 : Hybrid Stepping Generator

### 6.2 Proposed Topologies

In this present work two concepts of magnet fixation ; surface mounted magnets and flux concentrating magnets between translator pole shoes have been studied with NdFeB. The topologies are composed of a primary (stator) and a secondary (translator) with surface mounted magnets and flux concentrating magnets. The translator is sandwiched between two stators that carry flux in the longitudinal direction, while the translator carries flux in the transverse direction. Generally, linear oscillating generator refers to that performs a linear motion with a certain stroke at a specific. This proposes a suitable generator for IC engine ; it is hybrid stepping machine which has the advantages of high specific force capability. Therefore, the different configurations are compared with respect to shape of magnets as follows.

- Surface Mounted PMs Mover
  - Symmetrical Stator Cores
  - Non Symmetrical Stator Cores
- Flux Concentrating PMs Mover
  - Non Slanted PMs
  - Slanted PMs
- Novel Flux Concentrating PM Mover

The surface mounted PMs mover model facilitates more mechanically stable drive because iron-core absorbs the shock from the piston, consequently the impulse of magnets shocked directly is small. However, there is a disadvantage in high-speed operation characteristics by increasing of iron-core amount as compared with the flux concentrating PMs mover model. On the other hand, the flux concentrating PMs mover model is suitable for high-speed operation by light weight of iron-core amount, but even it can happen to risk of damage to magnets owing to the shock of piston.

### 6.2.1 Surface Mounted PMs Mover

This topology has two armatures of upper and lower part with surface mounted magnets mover. The mover consists of 14 magnets which magnetized vertical direction in top and bottom of mover iron-core, respectively. However, it has a disadvantage structurally because the mover suffers from a high-speed oscillating motion ; it can be easily separated from the mover iron during the motion or an adhesive part to fix the magnet to mover can be damaged [35]. The stator is made of non-oriented laminated electrical steel with thin insulating coating. Figure 6.2 shows HSPM machine with surface mounted magnets mover which magnetized y-axis ; one is the stator cores consisted of symmetrical structure each other, and the other are misaligned by one pole-pitch of the stator. The mover is made of an iron core with attached NdFeB which is fixed at 10 [mm] of width per one-pole in cross section area.

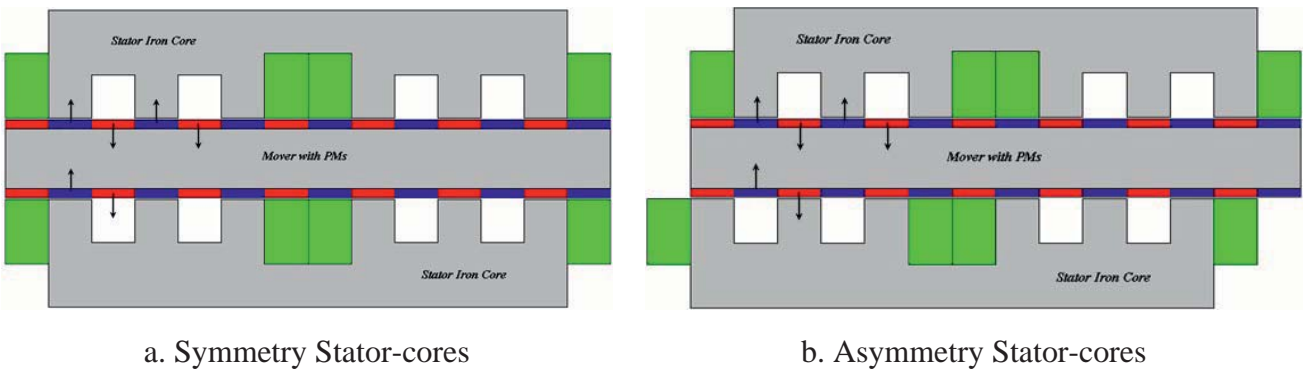


Figure 6.2 : HSPM Machine with Surface Mounted PMs Mover

In the figure 6.2, the flux concentration in the symmetry stator-cores model does not happen in the mover because two armatures of upper and lower part are symmetrical. Meanwhile, the flux in case of the asymmetry stator-cores model is concentrated in the mover because the flux exists in both transverse and longitudinal form simultaneously due to asymmetry of upper and lower stator core. This will be discussed in further in paragraph 6.4 *Comparison Results*.

### 6.2.2 Flux Concentrating PMs Mover

A different longitudinal rectangular shape of the magnets is investigated with respect to the magnetic flux. As seen from the figure 6.3, the magnets should be as long as possible for the chosen volume to maximize the magnetic flux in the circuit. The NdFeB has a relatively high coercivity and the height of magnet can thus be kept small without reducing the magnetic field intensity due to a high demagnetizing field inside the magnets. In this way, increased magnetic flux implies smaller magnet size. The flux concentrating PMs mover model has some good points, such as it can prevent an adhesive part from being removed and damaged.

It also indicates the conceptual design of two models ; non-slanted magnets and slanted magnets in flux concentrating PMs mover model as shown in figure 6.3.

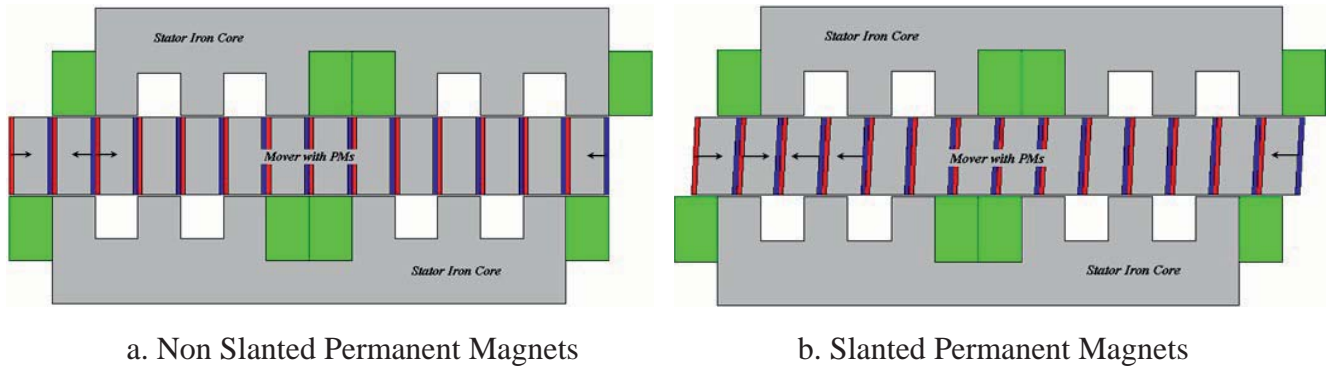


Figure 6.3 : HSPM Machine with Flux Concentrating PMs Mover

The cross-section area of overall mover including magnets in the flux concentrating PMs mover model is equal to that in the surface mounted PMs mover model. It is only different in magnetization direction of the magnets compared to the surface mounted PMs mover model. In addition, the cross-section area of magnet per pole in the flux concentrating PMs mover model is  $18.9 [mm^2]$  ; this is smaller than that of the surface mounted PMs mover model of  $20 [mm^2]$ . Consequently, the flux concentrating PMs mover model has the grab on the weight of mover and material cost aspects.

In order to improve flux linkage, the evaluation in all flux concentrating PMs mover models is considered using the same amount of material such as iron steel, conductor and magnets as well as same input current and remanence. This makes it possible to concentrate a flux ; as a result we can expect the performances that the flux concentrating PMs mover model leads to more improved results than the surface mounted PMs mover model. This scientific background will be presented in next section.

### 6.3 Analytical Calculation

This HSPM topology mentioned at the beginning is inevitable to reduce the force ripple in the electromagnetic force due to the frequent variation of reluctance between stator teeth and translator with magnets. It needs in-depth investigation to optimize the use of expensive magnets and other materials, minimizing force ripple through analyses of the magnetic circuit. Either, HSPM generator is the existence of end of winding, resulting in low power factor. End winding are undesired as they increase the cost of the device and the stator resistance of each phase without proving a useful advantages.

By modeling this generator, the effect of longitudinal leakage flux at the stator ends is neglected.

Since there are so many poles, this effect is minimal [36]. The following numerical process is used in the design of the HSPM generator.

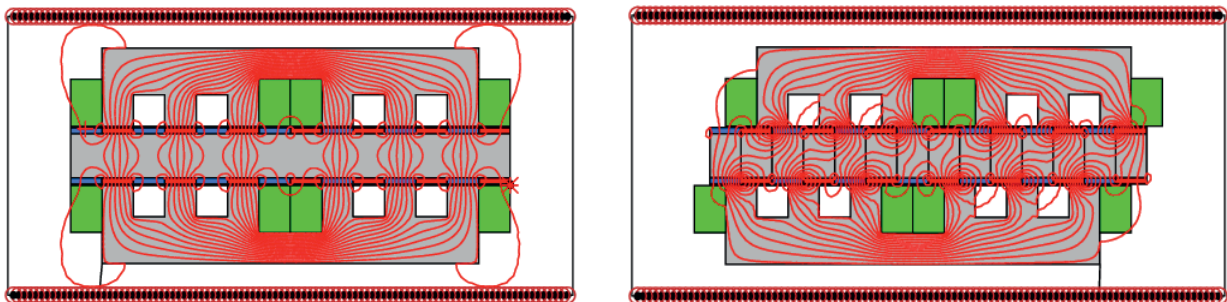
- Use the leakage reluctance in air region and the flux linkage per pole by electromagnetic force
- Now that we have all the machine dimensions, we can find the average force and force density using the stored magnetic energy

FEA is used to evaluate and compare to the analytical results of several types as well as calculate leakage reluctance and flux linkage.

## 6.4 Comparison Results

### 6.4.1 Surface Mounted PMs Mover

A flux characteristic of a surface mounted PMs mover generator is shown in figure 6.4. Aligned stator core type each other lead to increase leakage flux in the end part as called end effect, while the flux feature of misaligned stator core type shows larger leakage flux in air regions of stator relatively. It is an inevitable phenomenon in such a structure since the magnets are magnetized by vertical direction with rectangular shape.

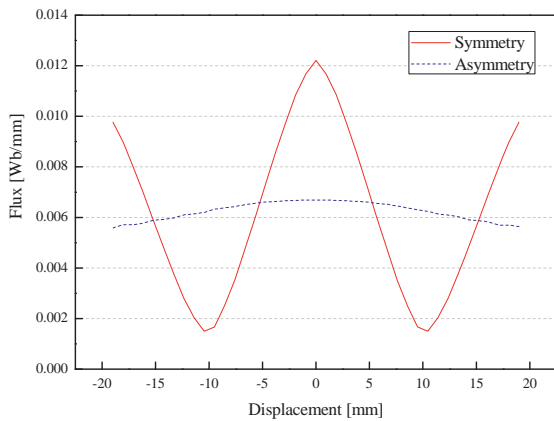


a. Symmetry Stator-cores

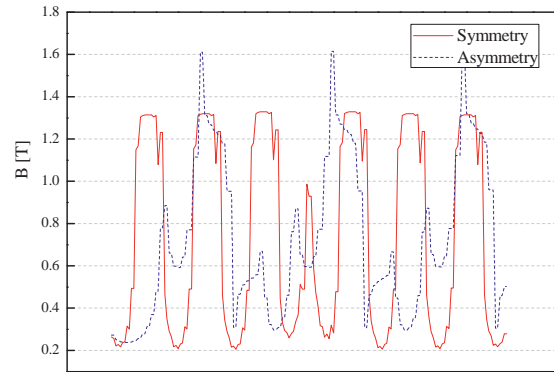
b. Asymmetry Stator-cores

Figure 6.4 : Flux Characteristic of Surface Mounted PMs Mover Machine

By FE analysis of two different types, the flux characteristics are shown in figure 6.5 ; the flux features various from symmetric form of upper and lower stator cores. The solid line represents the flux profile of the symmetrical stator cores model, whereas the dotted line relates to the flux curve of the asymmetrical stator cores model. The flux linkage of the symmetrical stator cores model shows the better result than that of the asymmetrical stator cores model because the symmetrical stator cores model has a steady flux density in the air-gap.



a. Flux Profile

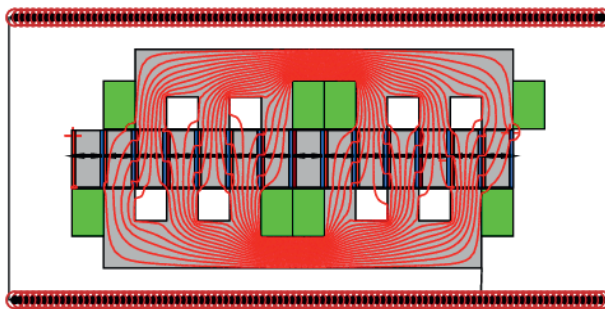


b. Flux Density in Air-gap

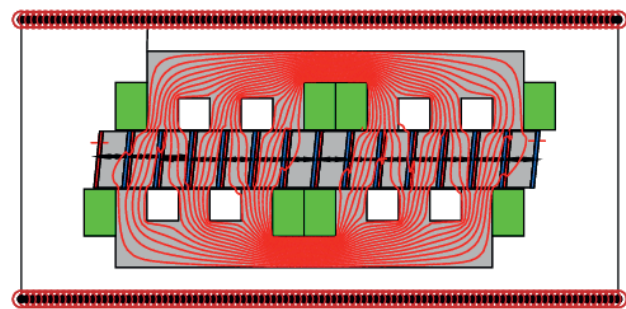
Figure 6.5 : Surface Mounted PMs Mover Machine

### 6.4.2 Flux Concentrating PMs Mover

The flux performances of the flux concentrating PMs mover generator with the non-slanted and slanted magnets are represented in figure 6.6. The slanting angle versus longitude direction of the shaft has a very large effect on the cogging force. By slanting the magnets, it is effective in reducing the cogging force as well as expected to improve force [37]. All of HSPM machines with the flux concentrating PMs mover are shifted as one pole-pitch of the stator.



a. Non Slanted PMs

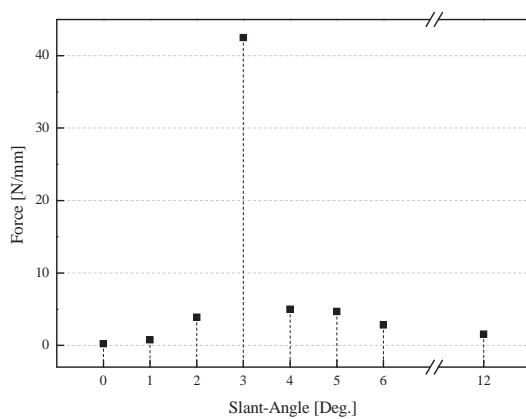


b. Slanted PMs

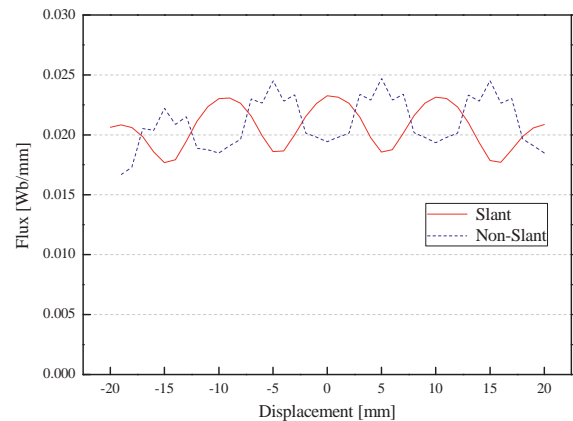
Figure 6.6 : Flux Characteristic of Flux Concentrating PMs Mover Machine

Cogging is not unique to linear generators ; rotary machines have the same problem and there are several methods traditionally used to minimize the effect that can also be employed in linear generators [38]. These include skewing the magnets, shaping of the magnets, and / or skewing the slots in the laminations. All of these reduce cogging by intentionally misaligned the laminations and magnets. This softens the transitions of the laminations teeth from one magnet to the next magnet and reduces cogging. Therefore, the design study will be considered about relationship between force characteristic and slant-angle of magnet to minimize cogging.

Generally, slanting the mover with magnets will also adversely affect the flux linkage. However, there exists an optimum slant-angle that greatly reduces the cogging force but only slightly reduces the flux linkage variation. The force variation by slant-angle of magnets is investigated varying from 1 [Deg.] to 6 [Deg.] at interval 1 [Deg.] and 12 [Deg.] of mechanical degree. This result of the study brings to the important solution to find the optimal slant-angle to minimize cogging force, thereby improving feature of the force. In analysis of slant-angle change from non-slant to 12 [Deg.], the force value is the largest at 3 [Deg.] of slant-angle ; non-slanted magnet means zero [Deg.] in slant-angle.



a. Force by Slant-angle



b. Flux Profile of Slant and Non-slant

Figure 6.7 : Flux Concentrating PMs Mover Machine

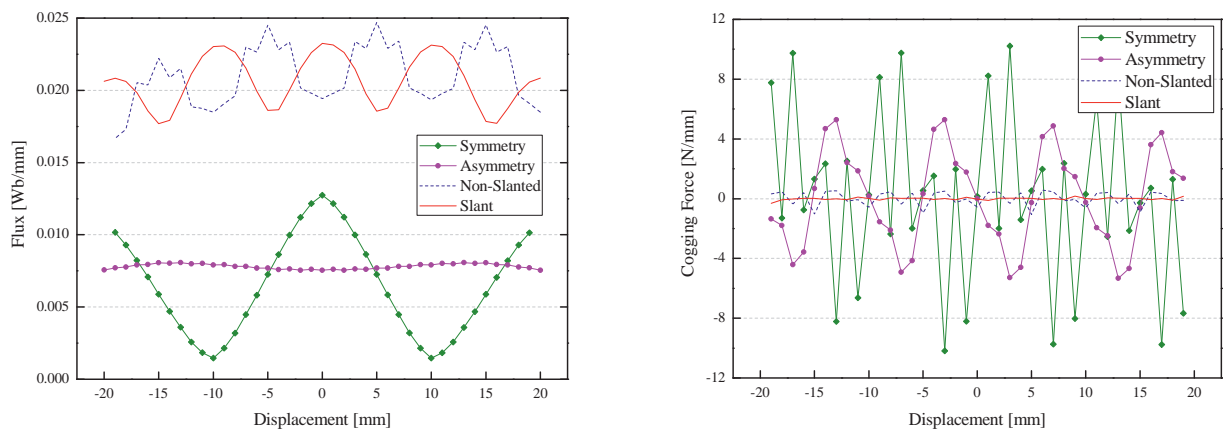
The simulated results show the significant difference in force characteristic for different slant-angle of magnets as shown figure 6.7. The flux performance in slanted magnets model is smoother than non-slanted magnets model. Here, it is clearly illustrated how the shape of the magnets affects the flux path in the magnetic circuit significantly.

## 6.5 Selection of Surface Mounted and Flux Concentrating PMs Mover Types

As mentioned earlier, the sectional area of magnet in the flux concentrating PMs mover type is smaller than that of the surface mounted PMs mover type. All of two types, non-slanted and slanted magnets of flux concentrating PMs mover, the cross-sectional area of magnet per pole is  $10.5 [mm^2]$ . Decreasing the width of magnets causes the reduction of the equivalent current density of the magnets. It has more effects ; one of the most important effects is enhancing the generator output voltage. However, this is not always good, especially when harmonics and peaky components appear in the output voltage. Generally, the flux concentrating PMs mover type shows better characteristics in terms of weight of mover and electrical performances such as the flux linkage and force. The proposed flux concentrating PMs mover type for flux concentration has

some good points, such as the flux linkage is large considerably because the magnetic flux can be concentrated effectively by structure of buried magnet inside mover.

Figure 6.8 indicates the comparison of measured flux performances for the symmetry, asymmetry structures in the surface mounted PMs mover type and non-slanted, slanted in the flux concentrating PMs mover type. It can be observed that the characteristics of the flux concentrating PMs mover types are in good agreement with that of the surface mounted PMs mover types in view of the flux linkage and cogging force. Compared to the symmetry stator cores structure of the surface mounted PMs mover type, magnetic flux value of the slanted magnets type in case of the aligned position is almost twice bigger. Also, the cogging force in the flux concentrating PMs mover types shows positive results than that of the surface mounted PMs mover type. Particularly, it can be seen that the cogging force is reduced considerably in the slanted PMs mover of flux concentrating PMs mover type.



a. Flux Profiles

b. Cogging Force

Figure 6.8 : Comparison of Categories

In conclusion, the flux concentrating PMs mover type can not only concentrates magnetic flux, but also can obtain the soft flux performance and lower cogging force by slanting of magnets. As a result, it gives information that the slanted magnets of 3 [Deg.] in the flux concentrating PMs mover type have the best force performance among different four models.

## 6.6 Proposal Model

As stated above, the flux concentrating PMs mover type is more effective than the surface mounted PMs mover type because it obtains bigger magnetic flux and larger force relatively. Furthermore, the change by slant-angle of magnets seriously affects force performance ; as a result, it could achieve the best result at 3 [Deg.] of slant-angle in force aspects.

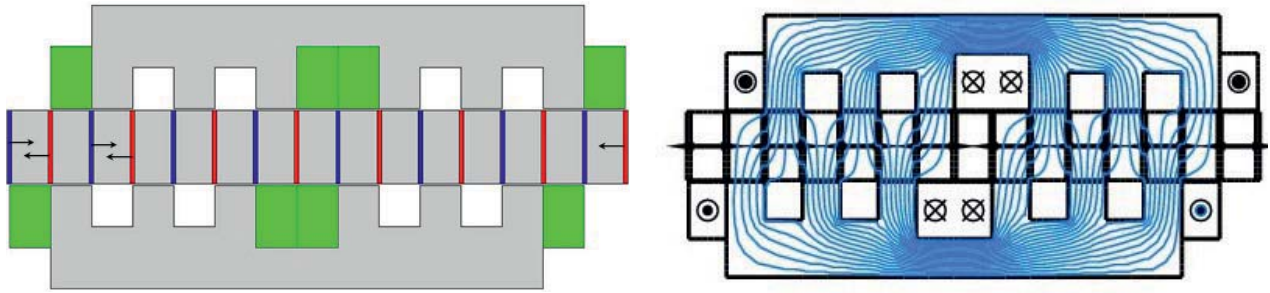
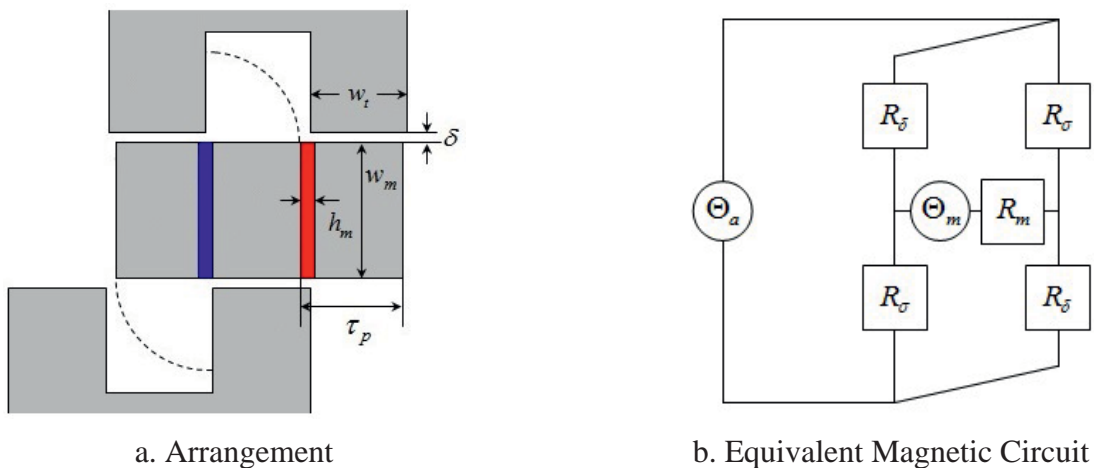


Figure 6.9 : Novel Model

Ultimately, this chapter suggests novel hybrid stepping structure of linear oscillating generator as shown figure 6.9 ; the cross-sectional area of magnet per pole is identical to the flux concentrating PMs mover type, accordingly the whole size of magnets is half of the flux concentrating PMs mover type. Therefore, it can be expected to bring about better results in respect of force performance by high-speed operation one of the advantages of linear machines. In addition, this topology will be analyzed through comparing the flux concentrating slanted PMs mover type by analytical and numerical calculation.

### 6.6.1 Analytical Calculation of Proposed Model

The newly proposed hybrid stepping generator is calculated by dividing maximum and minimum magnetic energy. Figure 6.10 shows the structure and equivalent magnetic circuit of hybrid stepping generator for magnetic energy calculation.



a. Arrangement

b. Equivalent Magnetic Circuit

Figure 6.10 : Configuration of New Hybrid Stepping Generator

Analytical expression for the force and magnetic energy calculation are as follows.

$$\Theta_a = N_c \cdot I \tag{6.1}$$

$$\Theta_m = \frac{B_{rem} \cdot h_m}{\mu_0 \cdot \mu_r} \quad (6.2)$$

The reluctances for magnetic energy calculation are expressed as equation (6.3), (6.4) and (6.5). This indicates the reluctance in air-gap, magnet and leakage, respectively. The  $B_{rem}$  represents residual magnetic flux density (remanence) of magnet.

$$R_\delta = \frac{1}{\mu_0} \cdot \frac{2 \cdot \delta}{l_z \cdot w_t} \quad (6.3)$$

where,  $l_z$  indicates the active length of  $z$ -axis direction.

$$R_m = \frac{1}{\mu_0 \cdot \mu_r} \cdot \frac{h_m}{l_z \cdot w_m} \quad (6.4)$$

$$R_\sigma = \frac{1}{\mu_0} \cdot \frac{h_m}{l_z \cdot (\tau_p - h_m)} + \frac{1}{\mu_0} \cdot \frac{\pi}{2} \cdot \frac{1}{\ln\left(\frac{\tau_p - h_m}{\delta}\right)} \quad (6.5)$$

$$\phi_{a\delta} = \frac{\Theta_a \cdot (2 \cdot R_\sigma + R_m)}{2 \cdot R_\delta \cdot R_\sigma + (R_\sigma + R_\delta) \cdot R_m} \quad (6.6)$$

$$\phi_{a\sigma} = \frac{\Theta_a \cdot (2 \cdot R_\delta + R_m)}{2 \cdot R_\delta \cdot R_\sigma + (R_\sigma + R_\delta) \cdot R_m} \quad (6.7)$$

$$\phi_{m\delta} = \frac{\Theta_m \cdot 2 \cdot R_\sigma}{2 \cdot R_\delta \cdot R_\sigma + (R_\sigma + R_\delta) \cdot R_m} \quad (6.8)$$

$$\phi_{m\sigma} = \frac{\Theta_m \cdot 2 \cdot R_\delta}{2 \cdot R_\delta \cdot R_\sigma + (R_\sigma + R_\delta) \cdot R_m} \quad (6.9)$$

The total magnetic energy can be obtained using the difference between the minimum and maximum magnetic energy as follows.

$$W_{\max} = (\phi_{a\delta} + \phi_{m\delta})^2 \cdot R_\delta + (\phi_{a\sigma} - \phi_{m\sigma})^2 \cdot R_\sigma + \frac{1}{2} \cdot (\phi_{a\delta} - \phi_{a\sigma} + \phi_{m\delta} + \phi_{m\sigma})^2 \cdot R_m \quad (6.10)$$

$$W_{\min} = (\phi_{a\delta} - \phi_{m\delta})^2 \cdot R_{\delta} + (\phi_{a\sigma} + \phi_{m\sigma})^2 \cdot R_{\sigma} + \frac{1}{2} \cdot (\phi_{a\delta} - \phi_{a\sigma} - \phi_{m\delta} - \phi_{m\sigma})^2 \cdot R_m \quad (6.11)$$

The average force and force density can be calculated by difference of maximum and minimum magnetic energy.

$$\Delta W = W_{\max} - W_{\min} \quad (6.12)$$

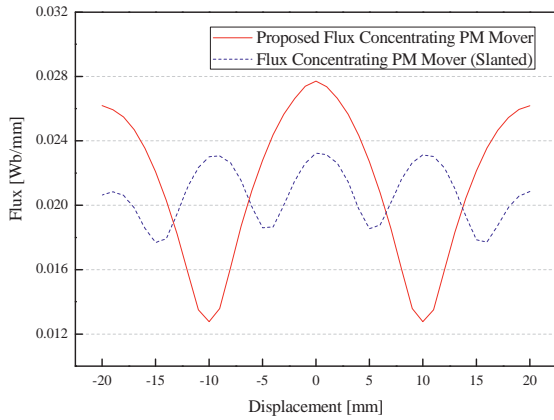
$$F_{ave} = \frac{\Delta W}{\tau_p} \quad (6.13)$$

$$F_{den} = \frac{F_{ave}}{2 \cdot \tau_p \cdot l_z} \quad (6.14)$$

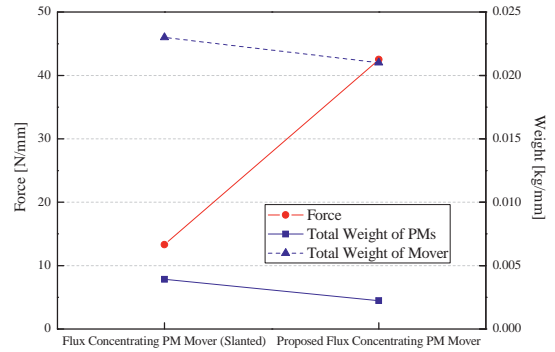
### 6.6.2 Comparison of Flux Concentrating Slanted PMs and Proposed Model

Figure 6.11 presents the comparison of the flux characteristics, the flux density in air-gap under no-load, the cogging force under no-load and the relationship of force and weight of mover with magnets by different two types ; flux concentrating slanted PMs mover and proposed flux concentrating PMs mover type.

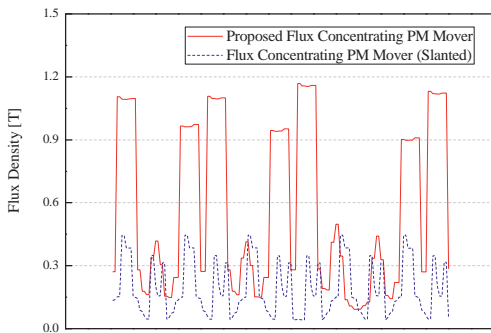
The model of flux concentrating slanted PMs mover shows the best results among the proposed models in the previous paragraph ; 6.5 *Selection of Surface Mounted and Flux Concentrating PMs Mover Types*. Nevertheless, this model has a relatively lower flux performance than proposed flux concentrating PMs mover model by reason that continuity of flux is not satisfied sufficiently ; the flow of the magnetic flux is interfered with a pair of magnets magnetized each other in the opposite direction. For such a reason, the slanted PMs mover can lead to a reduction the generator's force output occasionally because the windings and magnetic fields are no longer optimally aligned. However, the flux concentrating slanted PMs mover model has superiority over the proposed flux concentrating PMs mover model in terms of only the force aspect by increasing the number of the magnets. *Coulomb's Law* supports the result that the force is inversely proportional to the square of the distance between different two poles. As a result, the flux concentrating slanted PMs mover model has a bigger force value due to the structure of two poles attached each other. The cross-section area of the mover with magnets in the compared two models is same completely except for their weight. An increasing in the number of magnet affects the weight of the mover, which in turn is related to the speed reduction of the mover. The ratio of the force to the weight is 3.2 to 1.2.



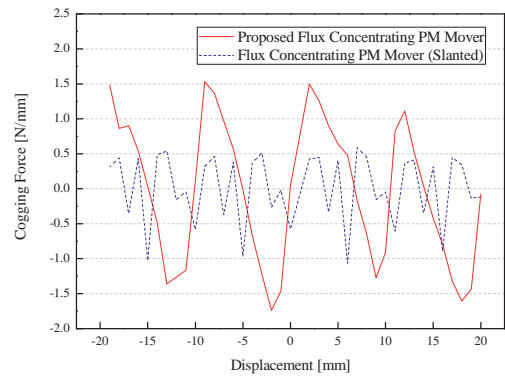
a. Flux Profile



b. Force and Weight



c. Flux Density in Air-gap (No-load)



d. Cogging Force

Figure 6. 11 : Comparison of Flux Concentrating PMs Mover (Slanted) and Proposed Flux Concentrating PMs Mover

The proposed flux concentrating PMs mover model is studied in terms of flux density distribution in air-gap and cogging force under no-load through FE analysis. Compared to the interaction cogging force shown in figure 6.11.d, the cogging force in proposed flux concentrating PMs mover model is quite higher than that of the flux concentrating slanted PMs mover model. If the mover is slanted, the air-gap flux variation will also be reduced correspondingly. Eventually, the slanted mover to reduce the cogging force is successfully. Trade-off may be made between the flux linkage variation and the cogging force. So the slanted PMs mover does not adversely affect the flux variation very much. It is only influence on the cogging force by buried structure of magnets as geometrical variables. This result gives useful information in the design and evaluation of hybrid stepping machine through effective machine structure.

## **6.7 Discussion**

On developing a hybrid stepping linear oscillating generator, the buried forms of magnets are compared ; one is surface mounted PMs mover and the other is flux concentrating PMs mover type. They are analyzed in symmetrical and asymmetrical stator cores in the former case, and in non-slanted and slanted PMs mover in the latter case. Different rectangular shapes of the magnets are investigated with respect to the magnetic flux in the air-gap, flux linkage and force characteristics. Due to concentration of magnetic flux, the flux concentrating PMs mover model shows better results than the surface mounted PMs mover model in terms of the flux linkage and force aspects. However, this model generates cogging force and it has a bad influence on the system. To overcome such difficulty, an improved force characteristic to minimize cogging force by slanting of magnets was found.

This chapter has presented a novel structure reducing the number of magnets to half than the flux concentrating slanted PMs mover structure for hybrid stepping linear oscillating generator. This was investigated by analytical calculation considering leakage reluctances and was compared with FEA. At last, the proposed hybrid stepping generator with the flux concentrating PMs mover has a good performance in flux linkage, flux density in air-gap and weight of mover characteristics than the surface mounted PMs mover and the flux concentrating slanted PMs mover structure. Furthermore, it was necessary to examine how the electrical characteristics in accordance with slant-angle of the mover have an effect in the new flux concentrating PMs mover model.



---

## 7 Cylindrical Reluctance Machine

### 7.1 Introduction

Reluctance generators have a number of advantages over PM generators, in terms of rugged construction and capability to operate in harsh environments and at elevated temperatures. The vast majority of reluctance generators has a variable air-gap and exploits the normal component of force between a stator and the mover. The main feature of their magnetic configuration is each phase winding consists of a single coil which is surrounded by magnetic core.

Cylindrical Linear Reluctance Machine (CLRM) has much simpler bearing construction and self-supporting coils. Furthermore, this machine is easy to assemble and has a better ratio of active to total volume. It can achieve very high speeds because of the lack of conductors or magnets on the mover. However, since the force for a given excitation current diminishes rapidly as the air-gap length increases, it is generally suitable for normal application. Moreover, the rapid increase in force that occurs as the mover approaches the stator means the generator is difficult to control. For applications that require longer strokes and improved controllability, it is necessary to depend on generator topologies that exploit the tangential component of force, despite the fact that they have considerably lower specific force capability [39].

The machine consists of a ferromagnetic mover and stator, which carries the excitation coil. When the coil is excited, the stator and mover teeth will tend to align in order to minimize the magnetic circuit reluctance, thereby producing an axial force. The force is produced on the reluctance principle, i.e. by the tendency of the excited stator poles to align with the mover salience teeth. In other words, when a phase is excited, the force is produced between the stator and the mover at positions in which there is tendency for the phase inductance to change, i.e. where the derivative  $dL/dx$  is not zero. The direction of the force depends on exclusively on the sign of derivative  $dL/dx$ . The fact that the force is independent of the direction of the current flow allows the unidirectional currents to be used for excitation [40]. The motion is caused by the tangential force which tends to align poles of the moving part with the excited poles of the static part. Hence, the machine makes use of the inherent cogging force which contributes to the overall force.

Prediction of performance of reluctance machine requires the knowledge of magnetization data in the form of flux linkage (inductance) / position / current characteristics. These characteristics are nonlinear and for a hypothetical machine defined by geometric parameters, number of turns and  $B$ - $H$  curve can be computed fairly accurately by using numerical field analysis [41]. In preliminary design, there were only reports which referred to performance of the combination of pole arc of

stator or rotor by number of phase in rotating reluctance machine. Meanwhile, the proposed design procedure utilizes the rotating switched reluctance machine design by converting the motion of the linear machine into the equivalent rotary machine.

In this study, the comparison performance of two models with the rectangular and trapezoidal shape of mover teeth is investigated respectively through an attempt at an analytical and verification at a numerical calculation. FEM is used for numerical calculation of the inductance and force characteristic. Using characteristics flux linkage (inductance) versus position at a given current, the force characteristics are computed through the magnetic energies approach by numerical integration and differentiation.

### 7.2 Configuration

The reluctance linear machine in cylindrical form with three-phase has a distinctively simple and compact construction consisting of a magnetic shaft (usually the ‘*mover*’), and an outer cylindrical assembly (usually the ‘*stator*’) containing a number of identical phase sets. Each set consists of a magnetic core and an enclosed solenoidal winding. Figure 7.1 shows the machine structure of a three-phase CLRM. The CLRM has an active stator, a passive mover and a longitudinal flux configuration.

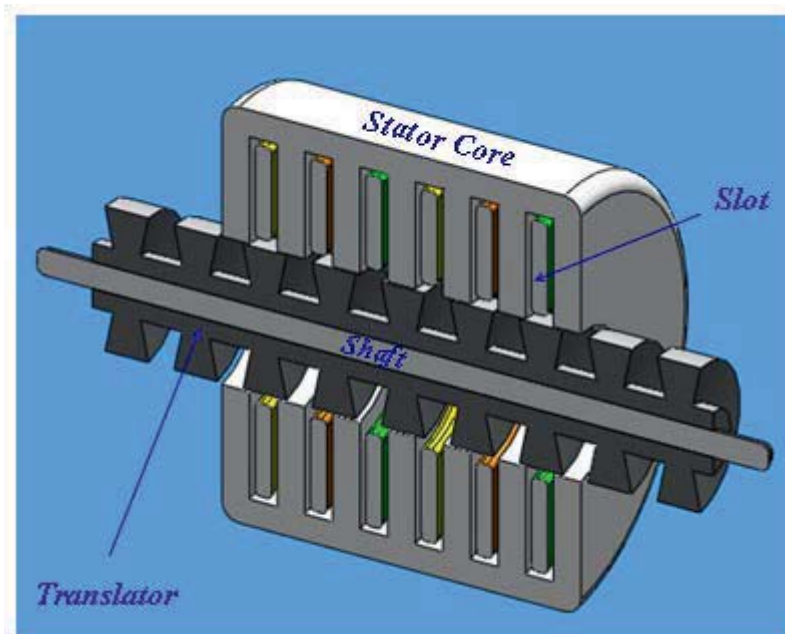


Figure 7.1 : Three-Phase Cylindrical Linear Reluctance Generator

The reluctance machine is a type of synchronous machine that induces non permanent magnetic poles on the ferromagnetic mover. Force is generated through the phenomenon of magnetic reluctance. It has wound field coils like those of a DC motor for its stator windings and has no coils

or magnets on its mover. It can be seen that both the stator and mover have salient poles ; hence, the machine is a doubly salient machine.

### 7.3 Cylindrical Linear Switched Reluctance Machine

Cylindrical Linear Switched Reluctance Machines (CLSRM) are generally similar to series-excited DC and synchronous reluctance machines. CLSRMs are alternatively known as Linear Variable Reluctance Machines (LVRM), reflecting the origins of the technology being derived from variable reluctance stepper machines. The LVRMs are often referred to as CLSRMs to indicate the combination of a LVRM and the switching inverter required to drive it [42].

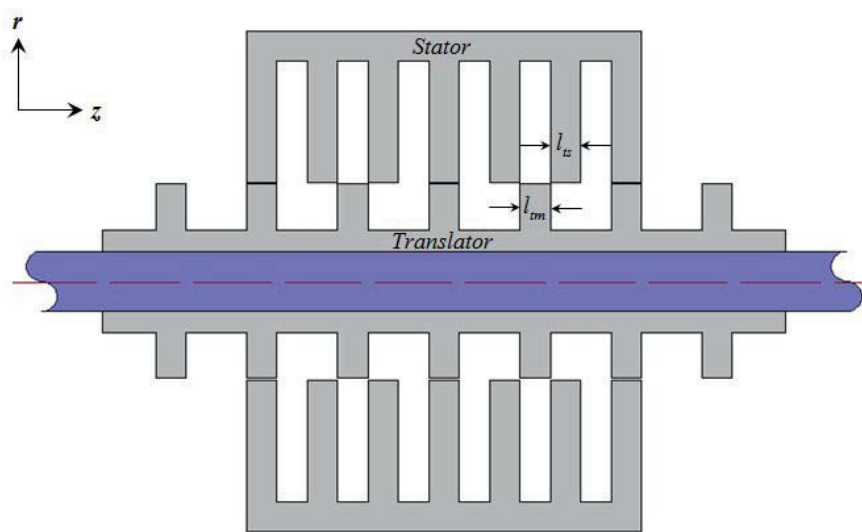


Figure 7.2 : Cylindrical Linear Switched Reluctance Machine

The advantages of CLSRM are simple, rugged machine construction, cooling characteristics, high performance and low cost. Consequently, CLSRM has been the focus of intensive research efforts during the past decades for industrial application. But, CLSRM has essentially high force ripple due to its double salient structure. In order to apply CLSRM to the industrial field, the force ripple has to be reduced. The force ripple depends essentially on geometry and electric design parameters. Especially, the geometric design parameters are relative to the salient pole shapes, such as stator tooth width and mover tooth width. The electric design parameters are relative to turn-on angle (also called advance angle),  $\theta_{on}$ , and turn-off angle,  $\theta_{off}$  [43]. The stator phase must be excited when its inductance starts rising and must be de-excited when the phase inductance ceases to increase. Thus, the switching function must ensure that current in phase winding reaches its reference value at the desired instant of inductance rise and is again brought to zero when inductance reaches its maximum and does not increase further. Due to delay in current rise and fall on account of winding inductance, the switch must be closed at a turn-on angle and must similarly

be opened at a turn-off angle. These switching angles are variable and depend mainly on speed and desired current in phase windings of CLSRM [44].

However, the CLSRM has a drawback of reduced efficiency due to the absence of magnets and of the force ripple by double salient pole structure. Above all, The switched reluctance generator requires the inverter system for switching drive ; it is vulnerable to heat which temperature of chamber in internal combustion engine is very high, even if reluctance machine has no magnets in itself.

The reluctance machine is an electric machine in which force is produced by the tendency of its moveable part to move to a position where the inductance of the excited winding is maximized. The force characteristics of reluctance generator are dependent on the relationship between the stator flux linkages and the mover position as a function of the stator current. A typical phase inductance versus mover position depends on a given phase current. The inductance corresponds to that of stator phase coil of the generator neglecting the fringing effect and saturation. The significant inductance profile changes are determined in terms of the stator and mover axial length and number of mover poles.

### 7.4 Proposal of Study Models

Various methods to minimizing force ripple and increase magnetic flux has appeared in the literature. The most popular approach for this purpose has been selected to optimal teeth length and shapes of stator and mover each other. Some of the previous studies have outlined methods of parameter analysis through arrangement of stator and mover teeth [43].

The force ripple minimization and increasing magnetic flux method proposed in this study is based on shape of mover teeth in geometric aspect. It is investigated in three cases of mover shape as shown figure 7.3 ; in all cases, axial length of stator teeth is fixed as 5 [mm] and that of mover teeth is various with 5 [mm], 7.85 [mm], and combination of 5 [mm] and 7.85 [mm]. The significant inductance profile changes are determined in terms of the stator and mover teeth width and number of mover teeth.

The reason why the mover teeth is selected in 7.85 [mm] that is to gain smooth force curve with increased linkage flux as the mover teeth is longer than stator teeth. Thereby, it can be taken a relationship of inductance characteristic following mover shape ; it is 5 [mm], 7.85 [mm] and mixed type of 5 [mm] and 7.85 [mm]. Based on the study, the new proposed trapezoidal shape of mover teeth is focused on concentrating magnetic flux, and axial length of mover connected into shaft is introduced to secure magnetic flux at least along with stator teeth.

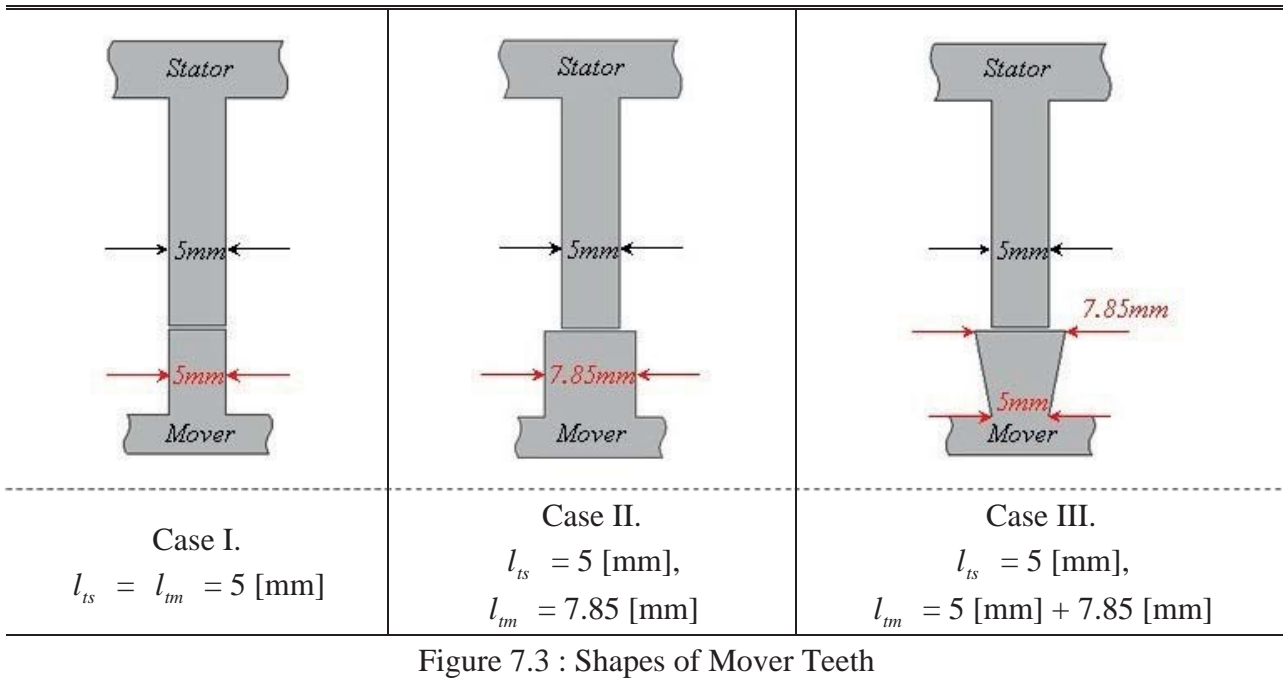


Figure 7.3 : Shapes of Mover Teeth

Above all, it is assumed that turn-on angle ( $\theta_{on}$ ) and turn-off angle ( $\theta_{off}$ ) is excited ideally for constant force generation according to the number and width of stator and mover poles.

There are three different case of mover shape :

#### 7.4.1 Case I

If the current continues beyond the positive slope region, then a negative force is produced with equal stator and mover teeth width, because there is no zero slope inductance region, as seen from figure 7.4. Due to the negative force generation, the average force per phase is reduced. To eliminate the negative force generation, phase current must be made zero beyond  $d_1$  [45]. Also, this case generates higher force ripple by structure reason of equivalence of the stator and mover pole width.

#### 7.4.2 Case II (Rectangle Shape)

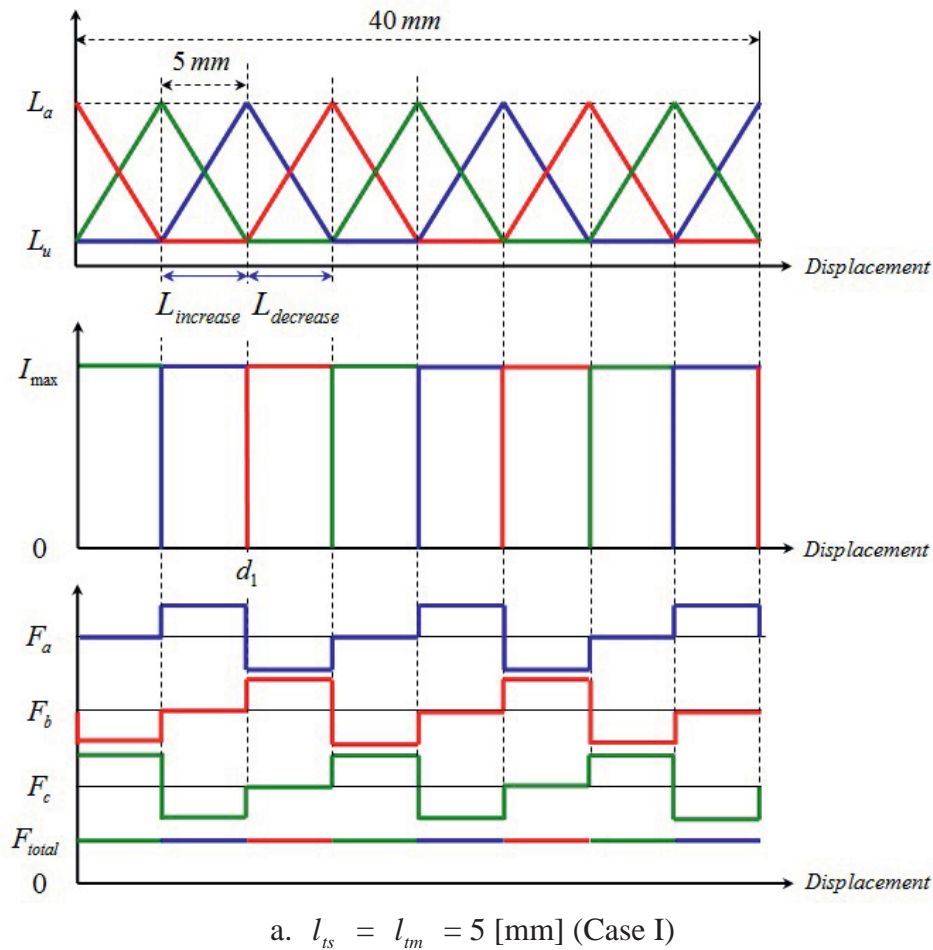
When the mover teeth width is greater than the stator teeth width, there is no tangible benefit in terms of force production if ideal current switching is assumed. Furthermore, this adds to the lamination iron volume and weight. However, with the mover teeth width is greater than the stator teeth width, this will increase the average force produced in the machine much more than that with equal stator and mover teeth width, case I. Even though the force produced in case II is greater than that in case I, the current is different with the current in case II being higher than that of case I. It

can be seen that it is very advantageous to have the mover teeth width greater than the stator teeth width. Therefore, many of the practical designs have mover pole arc slightly greater or almost equal to stator pole width in the machines.

### 7.4.3 Case III (Trapezoid Shape)

Case III is similar to the case II in all aspects except weight. It has an advantage over case II in the way that the flux leakage is relatively small and also the iron volume of mover is lighter. For this reason, this enables high-speed operation of the mover. In addition, this case is expected to decrease force ripple and increase average force neglecting the saturation due to the effective structure of the mover shape. The characteristics such as inductance and force will be investigated through comparing the case II.

The various inductance and force profiles are derived from figure 7.4 depending on the axial length of mover and stator.



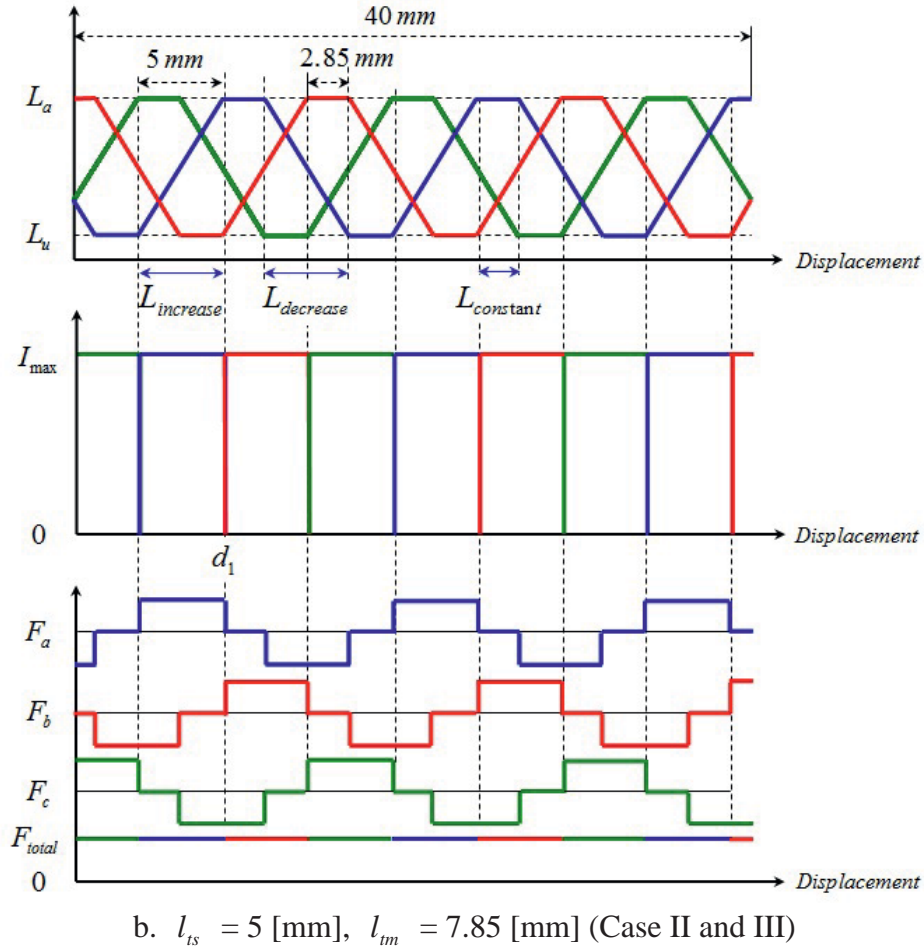


Figure 7.4 : Ideal Inductance and Force Profile

From figure 7.4, the ideal inductance and force curve is predicted ; where each length of the stator and mover teeth is same as 5 [mm] ( $l_{ts} = l_{tm}$ ), while the stator teeth is fixed of 5 [mm] and the mover teeth is 7.85 [mm] in given by figure 7.4.b. The force developed by a phase in which current flows tends to move the mover in such a direction as to increase the phase inductance, i.e. the aligned position. This position is called aligned position, and the phase inductance is at its maximum value as the magnetic reluctance of the flux path is at its minimum. When the mover pole pair is exactly aligned with the stator pole pair for any current flowing in the phase, no force is produced because the mover is at a position of maximum inductance ; the sign of the force depends on the sign of the inductance slope.

Three distinct inductance regions emerge :

- $L_{increase}$  ; Teeth overlap, so that the flux path is mainly through the stator and mover teeth. This increases the inductance with the mover position and gives it a positive slope. A current impressed in the winding during this time produces a positive force. This time section comes to an end when the overlap of teeth is complete.



- $L_{const}$  ; During this period, movement of mover teeth does not alter the complete overlap of the stator teeth. This has the effect of keeping the inductance maximum and constant, and this inductance is known as aligned inductance,  $L_a$ . Therefore, force generation is zero. As there is
- no change in the inductance in this region, force generation is zero even when a current is present in this interval. In spite of this fact, it serves a useful function by providing time for the stator current to come to zero or lower levels when it is commutated, thus preventing negative force generation for part of the time if the current has been decaying in the negative slope region of the inductance.
- $L_{decrease}$  ; The mover teeth is moving away from overlapping the stator teeth in this region and the inductance decreases, making a negative slope of the inductance region. The operation of the machine in this region results in negative force. (i.e., generation of electrical energy from mechanical input to the SRM)

The minimum constant of inductance region is called as unaligned inductance,  $L_u$ . In this region, the stator and mover teeth are not overlapping and the flux is predominantly determined by the air path, thus making the inductance minimum and almost a constant. Hence, these regions do not contribute to force generation.

### 7.5 Analytical Calculation

The analytical expression consists of the geometrical and physical parameter attribution. This operation requires representative modeling of the machine which is simple and fast to solve as the analytical modeling based on the reluctance network modeling.

The design verification process includes an analytical calculation and FEA. An analysis using equivalent magnetic circuit will help to information of quantitative force and magnetic energy. Meanwhile, an analysis by FEM brings about the results comparison of characteristics ; each rectangular and trapezoidal shape of mover teeth.

Flux linkage (inductances) is estimated analytically at two positions of the mover relative to the stator ; the position where mover teeth and stator teeth are misaligned (minimum phase inductance) and the position where mover teeth and stator teeth are aligned (maximum phase inductance). The magnetomotive force  $\Theta_a$  consumed by the air-gap is equal to the total of Ampere turns.

$$\Theta_a = N_c \cdot I \quad (7.1)$$

### 7.5.1 Rectangular Shape

Figure 7.5 and 7.6 shows a part of the generator's half cross-section containing adjacent phases and the mover in the aligned and unaligned position relative to the excited phase, respectively. In the method for estimating the inductance, it is assumed that the iron-core is infinitely permeable with the field lines being perpendicular to the iron-core surface. This method is based on an approximation of field lines by circular arc segment, and it accounts for the distribution of the phase winding.

#### Aligned Position

The reluctance network model at aligned position is shown on the figure 7.5 takes into account the leakage effects. The aligned or so called maximum inductance position, it is dependent on the excitation current and is calculated as follows.

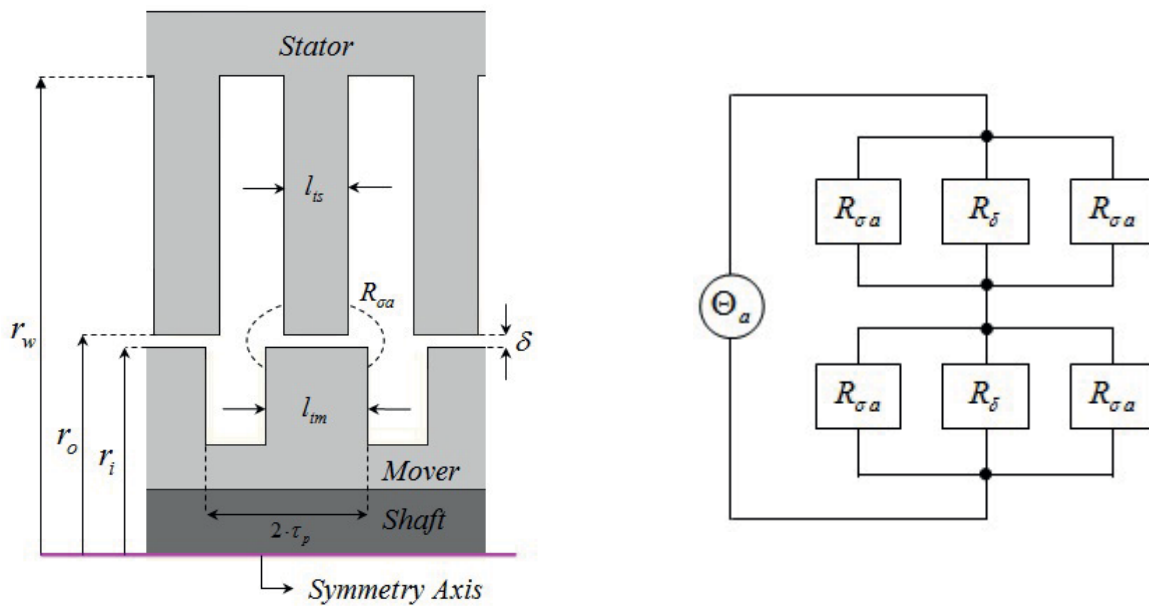


Figure 7.5 : Aligned Position of Rectangle Shape

The reluctance in air-gap and leakage in air-region is expressed as (7.2) and (7.3), respectively.

$$R_\delta = \frac{1}{\mu_0} \cdot \frac{\delta}{2\pi \cdot (r_o - r_i) \cdot l_{im}} \quad (7.2)$$

$$R_{\sigma a} = \frac{1}{\mu_0} \cdot \frac{\pi}{1} \cdot \frac{1}{2\pi \cdot (r_o - r_i)} \cdot \frac{1}{\ln\left(\frac{l_{im}}{\delta}\right)} \quad (7.3)$$

Unaligned Position

The configuration and equivalent magnetic circuit modeling in minimum inductance position is shown figure 7.6. The leakage reluctance interacting with the stator according to the movement of mover can be separated with two categories ; stator teeth and mover side ( $R_{\sigma u1}$ ), slot and mover-teeth ( $R_{\sigma u2}$ ).

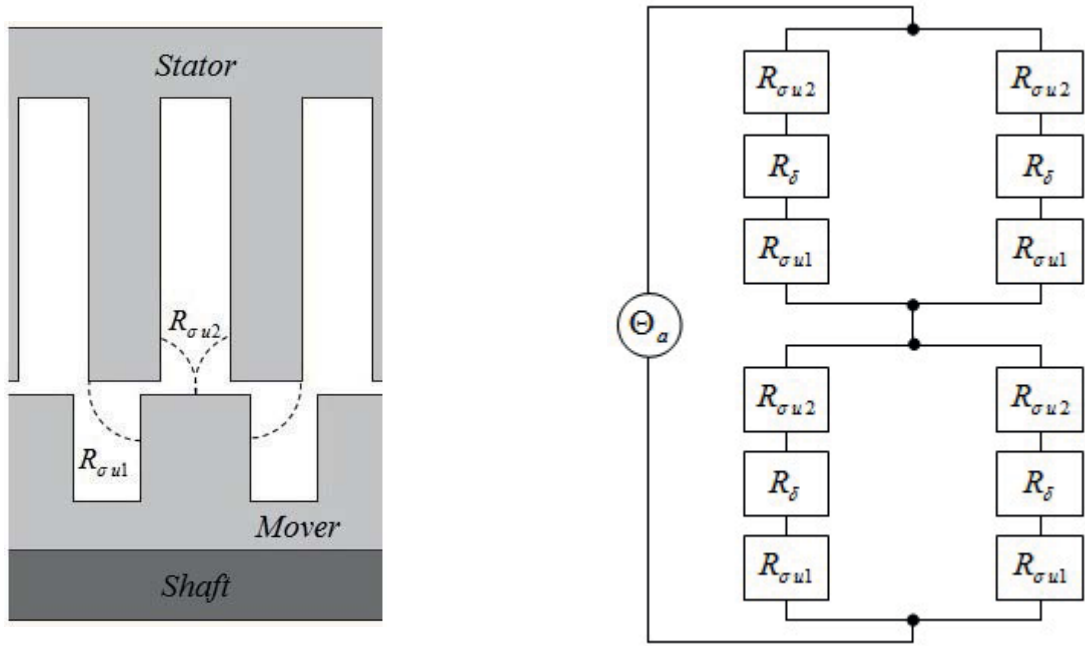


Figure 7.6 : Unaligned Position of Rectangle Shape

$$R_{\sigma u1} = \frac{1}{\mu_0} \cdot \frac{\tau_p - l_m}{2\pi \cdot (r_o - r_i) \cdot l_m} + \frac{1}{\mu_0} \cdot \frac{\pi}{2} \cdot \frac{1}{2\pi \cdot (r_o - r_i)} \cdot \frac{1}{\ln\left(\frac{l_m}{\tau_p - l_m}\right)} \quad (7.4)$$

$$R_{\sigma u2} = \frac{1}{\mu_0} \cdot \frac{\frac{l_{ts}}{2}}{2\pi \cdot (r_w - r_o) \cdot \frac{l_m}{2}} + \left[ \frac{1}{\mu_0} \cdot \frac{\tau_p - \frac{l_m}{2}}{2\pi \cdot (r_o - r_i) \cdot \frac{l_m}{2}} + \frac{1}{\mu_0} \cdot \frac{\pi}{2} \cdot \frac{1}{2\pi \cdot (r_o - r_i)} \cdot \frac{1}{\ln\left(\frac{l_m}{\tau_p - \frac{l_m}{2}}\right)} \right] \quad (7.5)$$

$R_{\sigma u1}$  indicates the leakage reluctance which occurs between stator teeth and mover side.

$R_{\sigma u2}$  represents the leakage reluctance which occurs between slot and mover-teeth.

### 7.5.2 Trapezoidal Shape

The equivalent magnetic circuit of trapezoidal mover shape is same to that of rectangular mover shape. Since the width of mover teeth is equal to that of rectangular shape of mover, the reluctance in air-gap is also identical with that of rectangular shape of mover. The configuration for maximum and minimum magnetic energy calculation is drawn in figure 7.7.

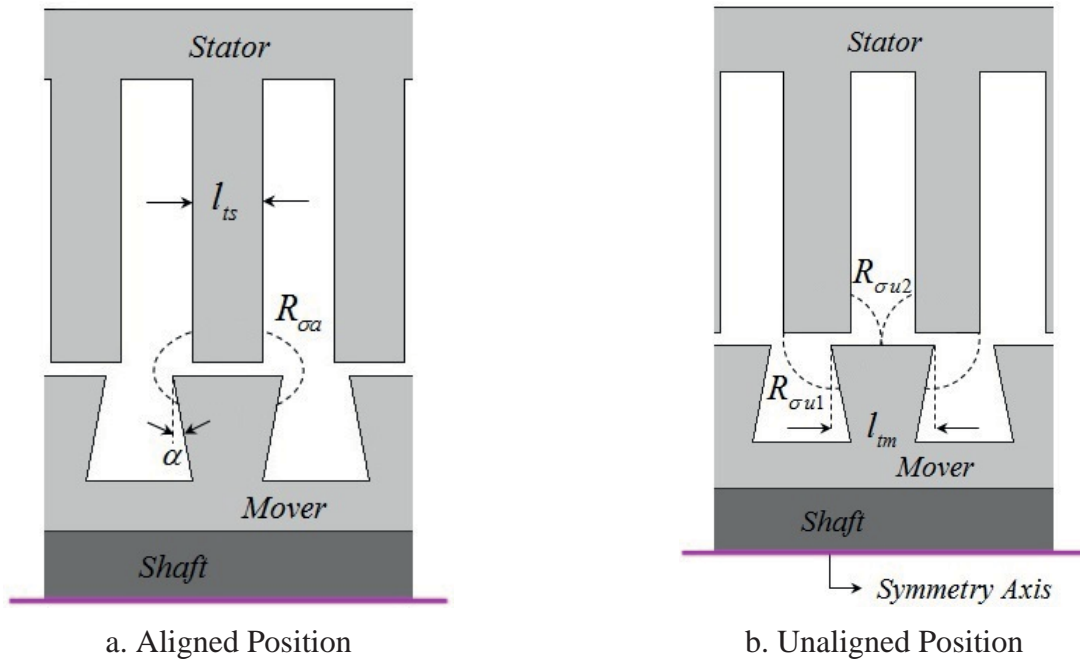


Figure 7.7 : Trapezoidal Shape

#### Aligned Position

The leakage reluctance in aligned position is expressed in equation (7.6). Meanwhile, the  $R_{\sigma u1}$  and

$R_{\sigma u2}$  represents the leakage reluctances in unaligned position as shown figure 7.7.b.

$$R_{\sigma\alpha} = \frac{1}{\mu_0} \cdot \left( \pi + \frac{\pi}{k} \right) \cdot \frac{1}{2\pi \cdot (r_o - r_i)} \cdot \frac{1}{\ln\left(\frac{l_{tm}}{\delta}\right)} \quad (7.6)$$

where, coefficient  $k$  is expressed as  $\frac{180 \text{ Deg.}}{\alpha}$ .

$$R_{out1} = \frac{1}{\mu_0} \cdot \frac{l_{tm} - l_{ts}}{2\pi \cdot (r_o - r_i) \cdot l_{tm}} + \frac{1}{\mu_0} \cdot \left( \frac{\pi}{2} + \frac{\pi}{k} \right) \cdot \frac{1}{2\pi \cdot (r_o - r_i)} \cdot \frac{1}{\ln\left(\frac{l_{ts}}{l_{tm} - l_{ts}}\right)} \quad (7.7)$$

$$R_{out2} = \frac{1}{\mu_0} \cdot \frac{\frac{l_{ts}}{2}}{2\pi \cdot (r_w - r_o) \cdot \frac{l_{tm}}{2}} + \left[ \frac{1}{\mu_0} \cdot \frac{\frac{l_{tm} - l_{ts}}{2}}{2\pi \cdot (r_o - r_i) \cdot \frac{l_{tm}}{2}} + \frac{1}{\mu_0} \cdot \frac{\pi}{2} \cdot \frac{1}{2\pi \cdot (r_o - r_i)} \cdot \frac{1}{\ln\left(\frac{l_{ts}}{l_{tm} - l_{ts}}\right)} \right] \quad (7.8)$$

Based on the above calculated reluctances, the average force is developed over an elementary axial displacement  $\tau_p$ , can be calculated starting from the energy variation  $\Delta W$ , by difference between maximum ( $W_{max}$ ) and minimum magnetic energy ( $W_{min}$ ).

$$W_{max} = 2 \cdot \Theta_a^2 \cdot R_{max} \quad (7.9)$$

$$W_{min} = 2 \cdot \Theta_a^2 \cdot R_{min} \quad (7.10)$$

where,  $R_{max}$  and  $R_{min}$  indicates the synthetic reluctance at aligned and unaligned position respectively.

$$R_{max} = \frac{2 \cdot R_\delta + R_{\sigma a}}{R_\delta \cdot R_{\sigma a}} \quad (7.11)$$

$$R_{min} = \frac{2}{R_\delta + R_{out1} + R_{out2}} \quad (7.12)$$

Eventually, the average force and force density can be obtained as below equations :

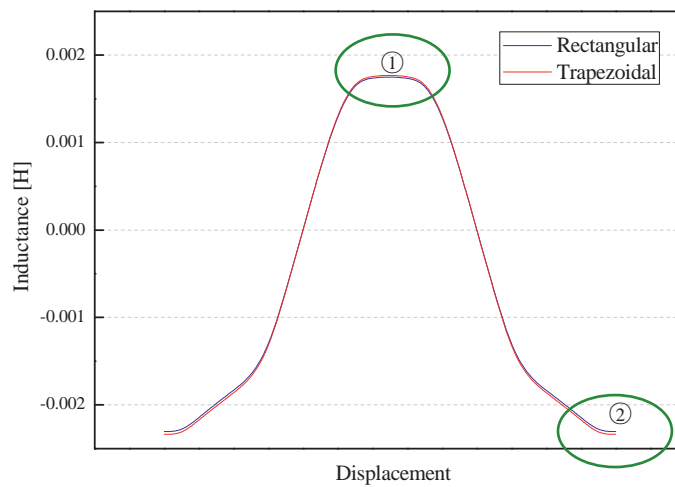
$$\Delta W = W_{max} - W_{min} \quad (7.13)$$

$$F_{ave} = \frac{\Delta W}{\tau_p} \quad (7.14)$$

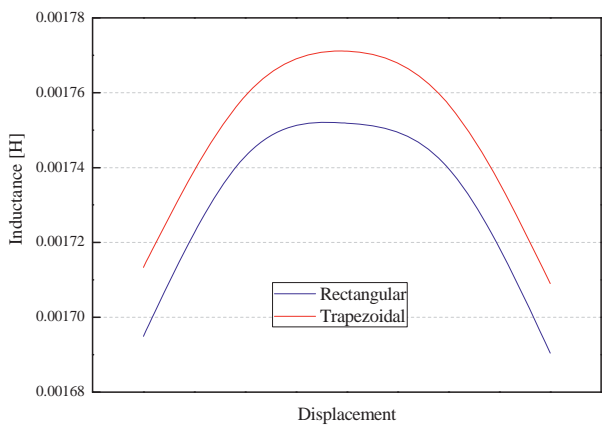
$$F_{den} = \frac{F_{ave}}{2 \cdot \pi \cdot r_i \cdot \tau_p} \tag{7.15}$$

### 7.6 Comparison Results

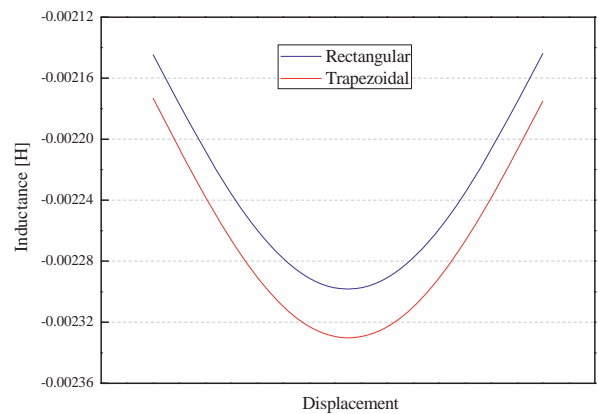
The design of generator using analytical magnetic circuit techniques enables it to access easily understanding of characteristics. Also, FEA is used to verify the result from analytical calculation by equivalent magnetic circuit. With this result, the inductance curves versus position for a given current show the characteristic of two different shapes with rectangular and trapezoidal mover.



a. Inductance Curve of One-Cycle



b. Maximum Inductance, ①



c. Minimum Inductance, ②

Figure 7.8 : Comparison of Inductance Profile



The force in the machine is produced when its' stator winding is energized ; in result the stator pole pulls the nearest mover pole to align in the region where reluctance is minimum and inductance maximum. The inductance starts increasing with relative approach of mover pole to energized stator poles.

Different inductance profile within the one-cycle by the mover shapes is indicated in figure 7.8 ; it shows inductance line distribution at a rated current in case rectangular and trapezoidal shape of mover teeth by FEM. As mover teeth travels towards stator teeth, inductance increases until completely aligned each other. The trapezoidal shape of mover teeth leads to improved results than rectangular shape in inductance respects. It is actually the fact that this mover shape further expands an effective magnetic flux. As a result, trapezoidal shape brings better results in both of energy and force characteristics than rectangular shape as shown figure 7.9.

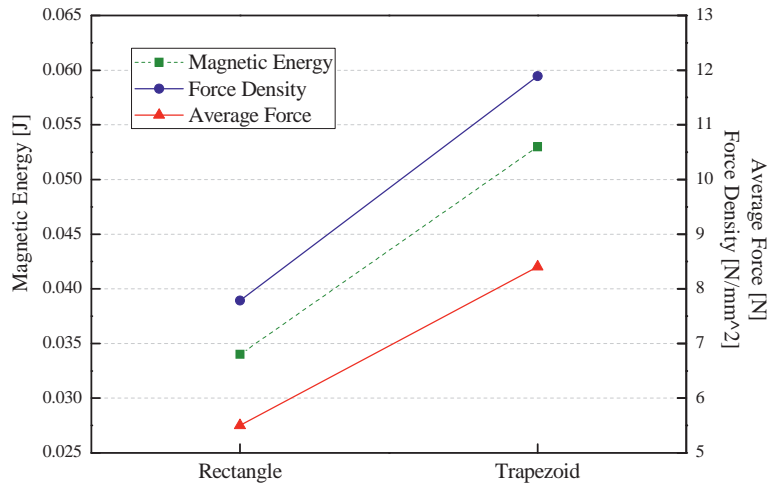


Figure 7.9 : Comparison by Mover Shape

Through above graph, their arithmetic values are listed in table 7.1. The characteristics of trapezoidal mover shape show better results than that of rectangular one as a whole ; average force, force density and magnetic energy. This means that the trapezoidal type is capable of producing high force and decreasing force ripple.

Table 7.1 : Compare Energy and Force

	Magnetic Energy [J]	Average Force [N]	Force Density [ $N/mm^2$ ]
Rectangular	0.034	5.502	7.784
Trapezoidal	0.053	8.404	11.89

## **7.7 Discussion**

This study presents the new shape of mover teeth of cylindrical reluctance generator using analytical design by equivalent magnetic circuit and verification by FEM. These methods enable to obtain an approximate insight into the value of force and magnetic energy. The calculation results show the possibilities of improving the force and magnetic energy of the generator by modification of the cylindrical mover teeth. From this study, it is made clear that the trapezoidal shape of mover teeth could be improved by approximately 65 [%] from the rectangular shape of that in magnetic energy, average force and force density.



---

## 8 Transverse Flux Machine

### 8.1 Introduction

Several linear machine candidates exist including the PM machine, switched reluctance machine, and induction machine. Moreover, these are in different varieties such as transverse flux and longitudinal flux machine. Most research to date has focused on the PM machine : however, this machine experiences significant cogging forces at low speeds due to attraction between the high energy PMs and stator teeth. These forces cause vibrations and noise. Some research has been devoted to both the reluctance and induction machines, but their poor performance at low speeds has deemed them unsuitable for internal combustion engine [46].

As an alternative to these machines, this chapter develops an innovative transverse flux linear generator. The Transverse Flux Machines (TFMs) are a relatively new topology of electrical machines. The machine obtained is capable of producing force density up to three times larger than conventional machines [47]. However, the TFMs have some important shortcomings ; the most notable problem is the very complex construction with true 3-D field pattern because of the high number of poles and of the magnetic circuit topology. In addition, the leakage fluxes in the stator poles of TFM have greater values than in the conventional machines. For this reason, the TFM design procedure cannot be a simple one. As yet reported, the TFM also has quite low power factor, which increases the power rating required for the drive inverter substantially [48]. The application as generator depends very much on the dynamic requirements of the load.

The TFM, with or without magnets in the mover, has a homopolar type stator winding. The homopolar magnetomotive force is modulated in the air-gap by the stator pole pattern and it interacts with the magnets placed on, or in the mover. In such case, the stator is salient, and the mover can be either salient or non-salient. If there are no magnets on the mover, then the mover must be built up with salient poles resulting from a double-salient structure of the machine as in the switched reluctance machine's case, but with the same number of poles in both parts. In almost all prototypes, the stator core is assembled in a carrier, which must be of non magnetic and preferable non conductive material, but with good thermal conductivity. If the non magnetic steel and aluminum meet these requirements, the first is preferred because of its lower specific weight. Best is filled plastic material with conductivity good thermal conductivity.

In design of TFM, the estimation procedure by 3-D FEM offers the possibility to optimize the magnetic circuit of the TFM and to set its dimensions. The main goal of a TFM design is to achieve the highest force density possible at a given machine volume and input power. The high value of the

armature winding inductance is another important aspect which has to be taken into account in the TFM design ; consequently it causes a low value of the power factor. Therefore, the effective magnetic coupling between the stator and mover must be improved, thus increasing the power factor, but without entailing sacrifice of the machine performance in other respects.

This study covers the analysis and design of electrically excited Linear Transverse Flux Machine (LTFM). It consists of two kinds of variable reluctance generator and magnets type ; the former is Transverse Flux Electric excited (TFE), and the latter is Transverse Flux Permanent Magnet excited (TFPM). First of all, the liberal approximation such as Equivalent Magnetic Circuit (EMC) is made to obtain the idealized model and in order to keep the initial analysis simple excluding the saturation effects. It also suggests comparison on the result between 2-D and 3-D using Equivalent Magnetic Circuit Network (EMCN) method. As for the TFM, it is indispensable to analyze 3-D modeling due to the asymmetric structure in all the axis of  $x$ ,  $y$ , and  $z$ -axis. At last, it is performed to verify the consistency of results between analytical calculation and numerical calculation by *3-D FLUX* software developed by *CEDRAT Group*.

### 8.2 Subjects of Investigation

The simplest feature of TFM is the similar to the configuration of switched reluctance machine. It has salient poles on both the stator and mover, but only one pair of member (stator or mover) carries excitation windings. The principle of operation is the same with a longitudinal flux counterpart of linear reluctance machine, which tends to align the mover in the minimum reluctance position with respect to the stator. Thus, it can be classified as one variety of variable reluctance machines. The polarity of generated force depends on only the relative position of mover, not the direction of current [49]. The usual TFM's topology implies a toroidal stator winding carrying current on the circumferential direction. The homopolar MMF produced is modulated by stator poles to produce a heteropolar flux density distribution in the air-gap. The stator core is salient and the mover can be built up with or without salient poles. The mover is usually provided with magnets which are magnetized perpendicularly or parallel to moving direction of the mover.

By structural and number of phase classification, it deals with TFE of reluctance type with single-phase system as single-sided topology and TFPM with single-phase system as double-sided topology. The analytical calculation of 2-D and 3-D by EMCN method is evaluated in each topology. Finally, the analytical result of double-sided TFPM topology is compared to numerical result simulated by FLUX 3-D software for a review of the validity of the 3-D result.

The analytical design procedure is summarized by the flow chart of figure 8.1.

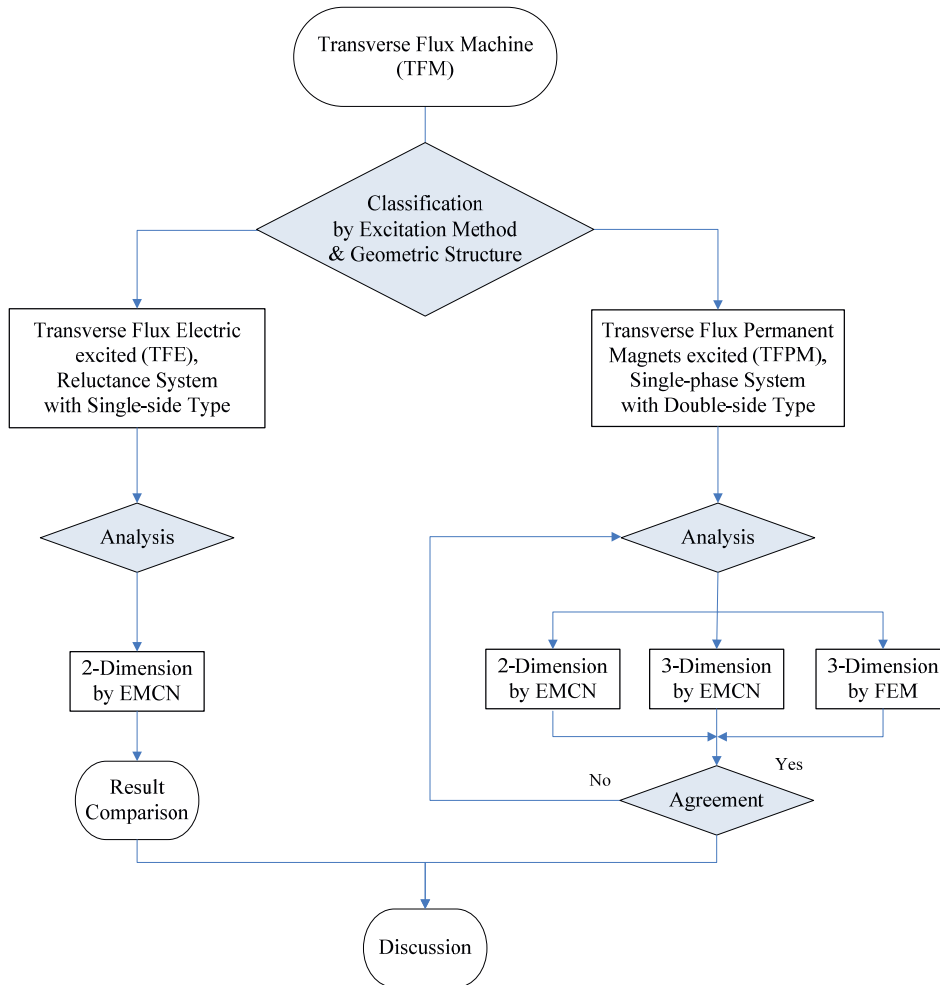


Figure 8.1 : Analysis Process

### 8.2.1 Single-sided TFE

The TFE machine is a variable reluctance type and it has a simple modular construction. This structure has been chosen because of the possibility to implement the control strategy of the machine from a customarily single-phase power converter. The working principle of the TFE machine is quite simple, similar to that of the linear switched reluctance machine. In particular, single-sided machines are easier to manufacture and have better prospects for practical applications. Besides, this machine has the advantage that is lower cogging force. When supplying the coil of a module with the stator teeth and the unaligned mover teeth, the mover teeth will tend to align with the stator teeth. Hence, the mover will be displaced one step length into the desired direction. The most important issue concerning this machine is, of course, the developed tangential force. This is influenced by the length of air-gap, the MMF of the coil, and the active cross-section of the poles [50].

In figure 8.2, the simplest variant with two modules is presented. The stator coil is surrounded by *U-shaped* soft iron parts arranged on the mover circumference. In order to establish the magnetic

circuit adequately, an additional return path may be provided optionally by *I-shaped* soft iron pieces between the active stator poles. This reduces the leakage flux of the mover which weakens the main flux of the stator. All soft iron parts must be made of laminated steel in order to avoid important core losses due to the eddy-currents.

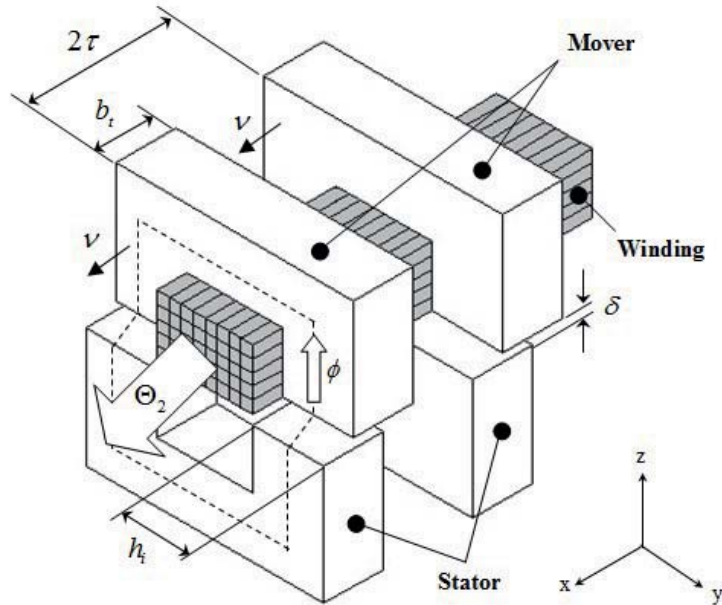


Figure 8.2 : Fundamental Building Block of Single-sided TFE Machine

8.2.2 Double-sided TFPM

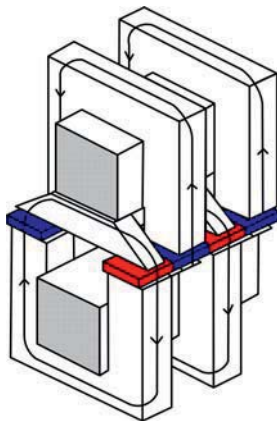


Figure 8.3.a :  
Topology with Flat Magnets

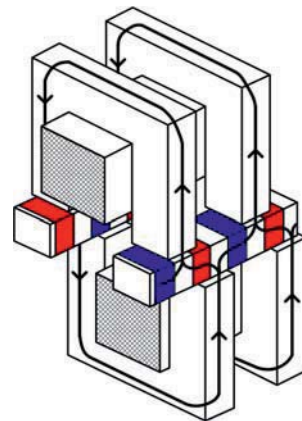


Figure 8.3.b : Topology with Inserted Magnets  
and Concentrating Flux Poles in the Mover

Figure 8.3 : Double-sided TFPM Machine

There are at least two double-sided topologies that can be used for building up the TFPM topologies with magnets on the mover. One consists of a mover with flat magnets inserted in between nonmagnetic material parts and two identical opposite stators. A variant of such a topology is

shown in figure 8.3.a : it has U-shaped stator pole core and I-shaped return flux mover core. The other possible double-sided topology has a mover with concentrating flux poles and magnets inserted in between them, and magnetized in the direction of the mover movement. The variant of this double-sided TFPM topology shown in figure 8.3.b ; it has two identical opposite stators with U-shaped pole core. In both cases presented for the double-sided TFPM, the stators are shifted with 180 electrical degrees.

The laminated U-shaped pole cores of the stator are fixed to the pole mounting rings made of aluminum to improve heat dissipation. The rings are fastened to the aluminum housing of the machine. It must be mentioned that the mover structure with inserted magnets and flux concentrating poles seems to be the best solution for the TFPM construction as well as the special return flux I-shaped cores are provided on the stator, although it implies some technological difficulties compared to the single-sided TFE machine.

### 8.3 Analytical Calculation of TFE

#### 8.3.1 Fundamental Operation Principle

This study is examined as fundamental operation principle of the single-sided TFE with an ideal model as shown figure 8.4. Although the ideal model may not be accurate due to absence of notable non-linear characteristics such as saturation, the machine characteristics can be modelled with simple mathematical equations, which can provide the intuitive insights into the operations of the machine. The fundamental building block is consisted of two sets of U-shaped cores and windings that wrap around one set of the cores. In this configuration, the upper set of cores with the windings is defined as a stator, and the lower set of cores is defined as a mover for the sake of definition and ease of identification; however, the definition is interchangeable as either the upper or lower core can be restricted to a location while the other can move freely.

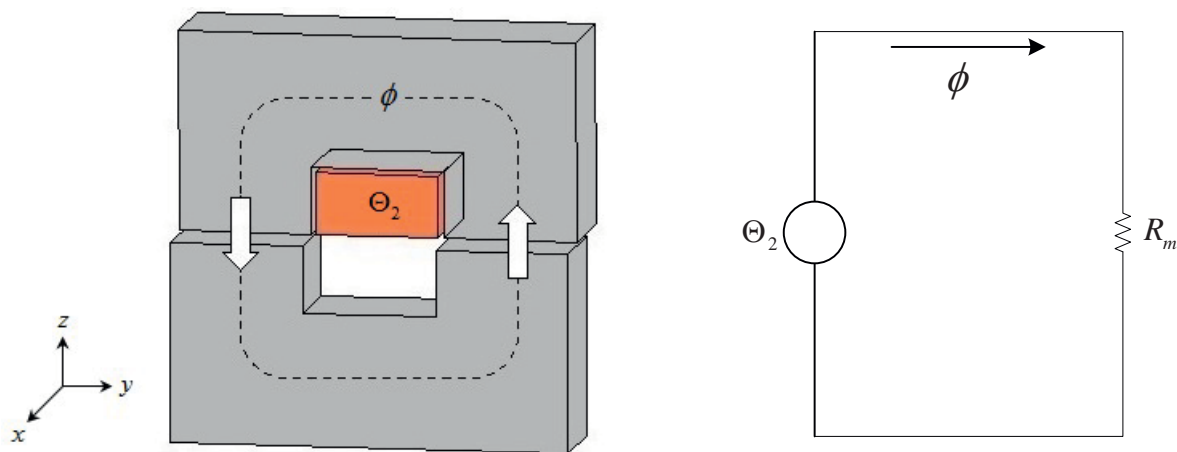


Figure 8.4 : EMC of TFE

The analysis of the TFM can also be performed using the EMCN method. The MMF,  $\Theta_2$ , is analogous to current source, while magnetic flux,  $\phi$ , and magnetic reluctance,  $R_m$ , can be related with current and resistors of electric circuits respectively.

Depending on the initial position of the teeth, the force can be applied 3-dimensionally. The forces in the direction of  $x$ -,  $y$ -, and  $z$ -axis are referred as *thrust force*, *lateral force*, and *normal / attractive force*, respectively. As prescribed in the paragraph, 8.4.3 and 8.4.4, the thrust force and the lateral force behaves similarly. However, the normal / attraction force behaves differently from the other two forces. Therefore the thrust force and lateral force are analyzed together, while normal / attraction force needs separate analysis. Although the MMF is generated in all directions, mechanical parts are usually installed to restrict the mover from moving in the direction of  $y$ -axis and  $z$ -axis in typical linear generator applications, and the mover is only allowed to move freely in the direction of  $x$ -axis. The variable reluctance type can only generate attractive force, and repelling force can not be generated. A main advantage of the TFE machines is that the space of electric circuits does not share the space of magnetic circuits. Due to that reason, the TFE machines can obtain the advantages such as higher efficiency and higher thrust density.

### 8.3.2 Analytical Calculation of MMF

The force calculation of electric machines can be effected by three methods in principle, according to the Ampere's Law and Lorentz Law, magnetic energy (co-energy) and magnetic tensor. The last method requires the local distribution of the magnetic field and is so rare in the analytical calculation only in cases usable [51]. In this paragraph, the method based on the principle of conservation of energy and energy storage methods is used to analyze acting on TFE generator of reluctance type.

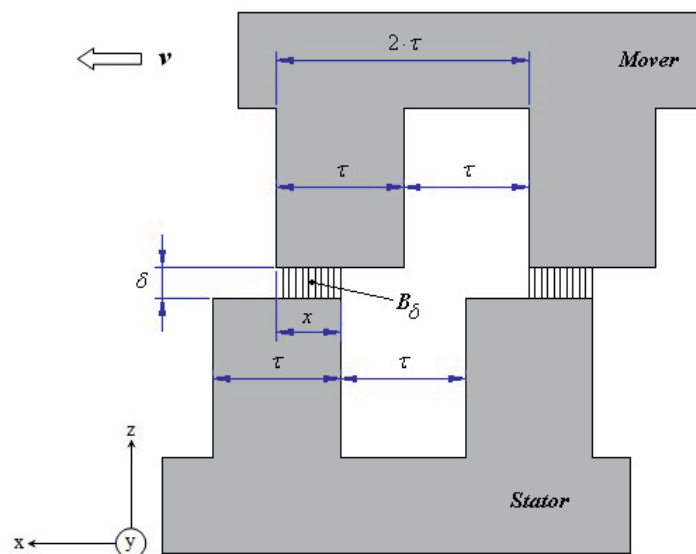


Figure 8.5 : Cross-section of TFE Machine

In figure 8.5, the cross-section of the TFE is shown to analyze the operating principle in detail. In this figure, each tooth is positioned  $2\tau$  apart, where the width of core-pole is set as  $\tau$ . Here,  $\delta$  and  $B_\delta$  represents the length and flux density in the air-gap, respectively.

In the analysis, it is assumed that the permeability of magnetic material is to be infinitely greater than that of free space ; consequently, the magnetic energy is assumed to be stored in the air-gap alone as shown in equation (8.1).

$$\Theta = \oint H \cdot dl = H_s \cdot l_s + H_\delta \cdot \delta \approx H_\delta \cdot \delta \quad (8.1)$$

where,  $l_s$ ,  $H_s$ , and  $H_\delta$  are defined as mean core length, flux intensity of core, and flux intensity of air-gap, respectively.

As it can be seen in figure 8.2, each core has two air-gaps. The  $\Theta$  is defined as the force generated in one of two air-gaps alone, while  $\Theta_2$  is defined as the force generated in both air-gaps. Therefore, if each air-gap generates the identical amount of force, the relationship between  $\Theta$  and  $\Theta_2$  can be defined as shown in equation (8.2).

$$\Theta = \frac{\Theta_2}{2} \quad (8.2)$$

It also should be noted that,

$$H_\delta = \frac{\Theta}{\delta}, \quad H_\delta = \frac{B}{\mu_o} \rightarrow B = \frac{\Theta \cdot \mu_o}{\delta} \quad (8.3)$$

where,  $H$ ,  $B$ , and  $\mu_o$  are the flux intensity, flux density, and permeability of air, respectively.

In order to calculate the force, the energy stored in the magnetic field can be used, and the energy can be evaluated in terms of magnetic energy,  $W_m$  and co-energy,  $W_{co}$ .

$$W_m = \int_V \int_0^B H(B) \cdot dB dV [J] \quad (8.4)$$

$$W_{co} = \int_V \int_0^H B(H) \cdot dH dV [J]$$

where,  $V = \delta \cdot h_i \cdot x$



The magnetic energy,  $W_m$ , plus the co-energy,  $W_{co}$ , is the amount of electric energy transferred from or to the electric source. In  $W_m$ , flux linkage,  $\psi$  (not shown in the equation), is chosen as independent variable, where as in  $W_{co}$ , current,  $I$  (not shown in the equation), is chosen as independent variable instead [52, 53].

### 8.3.3 Thrust Force in the Direction of X-axis

If the magnetic flux density,  $B$ , is linearly related to the magnetic field intensity,  $H$ , then the total energy stored in a steady magnetic field in equation (8.4) and the magnetic energy and co-energy become numerically the same. In other words, if a linear system is assumed, the superposition theory can be utilized to separately calculate the force acting on the system in the direction of  $x$ -,  $y$ -, and  $z$ -axis while other variables are held constant. Therefore, the partial derivative of equation (8.4) with respect to  $x$  yields the thrust force in the direction of  $x$ -axis. Equation (8.5) shows the derivation using the co-energy equation.

$$\begin{aligned} W_{co}(\Theta, x) &= \int_v \int_0^H B(H) \cdot dH \, dV \\ &= \int_0^x \int_0^B B \frac{dB}{\mu_0} \delta \cdot h_i \cdot dx = \int_0^x \frac{B^2}{2 \cdot \mu_0} \delta \cdot h_i \cdot dx = \frac{B^2}{2 \cdot \mu_0} \delta \cdot h_i \cdot x \\ &= \frac{B^2}{2 \cdot \mu_0} \delta \cdot h_i \cdot x = \frac{\mu_0^2 \cdot \Theta^2}{\delta^2} \cdot \frac{1}{2 \cdot \mu_0} \delta \cdot h_i \cdot x = \frac{\mu_0 \cdot \Theta^2}{2 \cdot \delta} h_i \cdot x \end{aligned} \quad (8.5)$$

where,  $dH = \frac{dB}{\mu_0}$ ,  $dV = \delta \cdot h_i \cdot dx$ ,  $B = \frac{\Theta \cdot \mu_0}{\delta}$

Using the derived co-energy equation (8.5), the force in the direction of  $x$ -axis can be obtained as in equation (8.6).

$$F_x(\Theta, x) = \frac{dW_{co}}{dx} = \frac{\mu_0 \cdot \Theta^2}{2 \cdot \delta} \cdot h_i \quad (8.6)$$

where,  $\Theta$  indicates MMF, while  $F_x$  indicates mechanical force.

Equation (8.6) indicates that the force in the direction of  $x$ -axis is independent of position variable  $x$ . However, it should be noted that the equation only shows the behavior while position  $x$  is from  $0$  to  $\tau$ . While the position is from  $\tau$  to  $2\tau$ , the force is equal in magnitude and opposite in sign, since the teeth of the mover interact with the nearest teeth of stator, and the attraction causes opposite force while the position is from  $\tau$  to  $2\tau$ . Therefore, in order to move the machine in positive direction, the current should be only applied during  $0 < x < \tau$ , and switched off during  $\tau < x < 2\tau$ .

Figure 8.6 illustrates the force in the direction of  $x$ -axis while a constant current is applied during  $0 < x < \tau$ , and zero current during  $\tau < x < 2\tau$ .

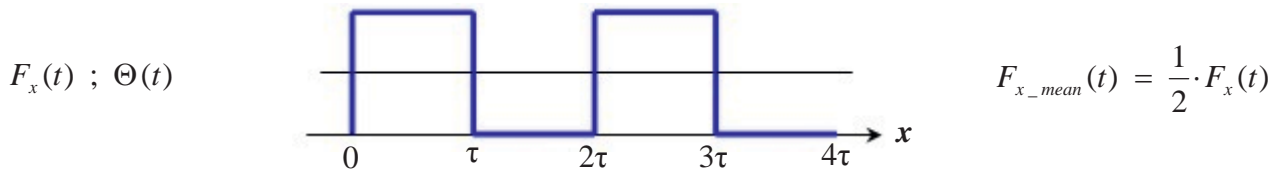


Figure 8.6 : Thrust Force in the Direction of X-axis

From the figure, the average force is a half of the force in equation (8.6). Therefore, the average force can be expressed as

$$F_{x\_mean} = \frac{F_x}{2} = \frac{\mu_0 \cdot \Theta^2}{4 \cdot \delta} \cdot h_i \quad [N] \quad (8.7)$$

Also thrust force per air-gap,  $F_{ax}$ , can be expressed as

$$F_{ax} = \frac{F_{x\_mean}}{A_\delta} = \frac{F_{x\_mean}}{2 \cdot \tau \cdot h_i} = \frac{\mu_0}{8 \cdot \delta \cdot \tau} \cdot \Theta^2 \quad \left[ \frac{N}{m^2} \right] \quad (8.8)$$

Here, the  $A_\delta$  is defined as the area covered by an air-gap during one period,  $2 \cdot \tau \cdot h_i$ .

### 8.3.4 Lateral Force in the Direction of Y-axis

The lateral force in the direction of  $y$ -axis can be derived using the identical method as shown in the previous paragraph. By applying partial derivative of equation (8.4) with respect to  $h_i$  yields the thrust force in the direction of  $y$ -axis. Equation (8.9) shows the derivation using co-energy equation.

$$\begin{aligned} W_{co}(\Theta, h_i) &= \int_V \int_0^H B(H) \cdot dH dV \\ &= \int_0^{h_i} \int_0^B B \frac{dB}{\mu_0} \delta \cdot x \cdot dh_i = \int_0^{h_i} \frac{B^2}{2 \cdot \mu_0} \delta \cdot x \cdot dh_i = \frac{B^2}{2 \cdot \mu_0} \delta \cdot h_i \cdot x \\ &= \frac{B^2}{2 \cdot \mu_0} \delta \cdot h_i \cdot x = \frac{\mu_0^2 \cdot \Theta^2}{\delta^2} \cdot \frac{1}{2 \cdot \mu_0} \delta \cdot h_i \cdot x = \frac{\mu_0 \cdot \Theta^2}{2 \cdot \delta} h_i \cdot x \end{aligned} \quad (8.9)$$

where,  $dH = \frac{dB}{\mu_0}$ ,  $dV = \delta \cdot x \cdot dh_i$ ,  $B = \frac{\Theta \cdot \mu_0}{\delta}$

This yields the identical result as equation (8.5). By taking derivative with respect to  $h_i$  yields the

lateral force.

$$F_y(\Theta, h_i) = \frac{dW_{co}}{dh_i} = \frac{\mu_0 \cdot \Theta^2}{2 \cdot \delta} \cdot x \quad (8.10)$$

### 8.3.5 Attractive / Normal Force in the Direction of Z-axis

The flux in the air-gap not only generates force in the direction of  $x$ -axis and  $y$ -axis, but also causes the force in the direction of  $z$ -axis, which can be referred as attractive / normal force. This force acts on to minimize the air-gap,  $\delta$ , and the identical method shown in previous two paragraphs can be used. Equations (8.11) and (8.12) derive the co-energy and the force with respect to the direction of  $z$ -axis.

$$W_{co}(\Theta, \delta) = \frac{\mu_0 \cdot \Theta^2}{2 \cdot \delta} \cdot h_i \cdot x \quad (8.11)$$

$$F_z(\Theta, \delta) = \frac{dW_{co}}{d\delta} = -\frac{\mu_0 \cdot \Theta^2}{2 \cdot \delta^2} \cdot x \cdot h_i \quad (8.12)$$

Here, equation (8.12) derives the force generated by single air-gap. Since there are two air-gaps and the number of cores ( $N_{core}$ ) per phase, rearranging equation (8.12) yields equation (8.13).

$$F_{z-phase} = \frac{\mu_0 \cdot \Theta^2}{2 \cdot \delta^2} \cdot x \cdot h_i \times 2 \times N_{core} = -N_{core} \cdot \frac{\mu_0 \cdot \Theta^2}{\delta^2} \cdot x \cdot h_i \quad (8.13)$$

As it can be seen from the equation (8.13), the attractive force is proportional to the inverse square of air-gap length ; therefore, the air-gap length and its relation to attractive force must be considered carefully during design. Another notable characteristic is that the attractive force is the function of  $x$ . Assuming that  $\delta$  and  $h_i$  holds at constant values, the attractive force changes as linear motion travels in the direction of  $x$ -axis.

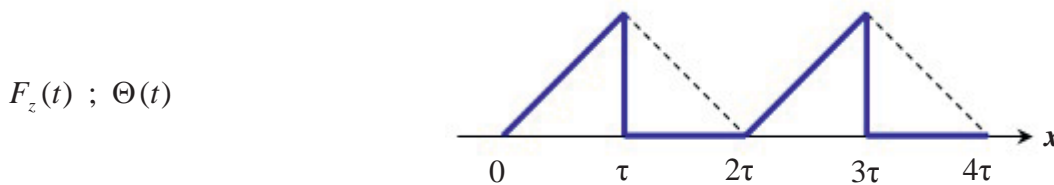


Figure 8.7 : Force in the Direction of Z-axis

Figure 8.7 illustrates the force characteristic in the direction of  $z$ -axis, as a function of position and MMF. During its operation, the current is only applied during  $0 < x < \tau$ , and removed while  $\tau < x < 2\tau$ , as it was explained in paragraph 8.3.3, and the generated force is shown with thick block line. In contrast, the dotted line shows the amount force if the current is constant for all time. The maximum attractive force occurs when the teeth of stator and the mover is aligned, which is equivalent to  $x = \tau$ . The minimum attractive force is zero, which occurs when the teeth are totally unaligned, which is equivalent to  $x = 0$ .

### 8.4 Analytical Calculation by 2-D EMC

In an electric-excited TFE of reluctance type, the average force can be similarly determined as having the above-mentioned energy method.

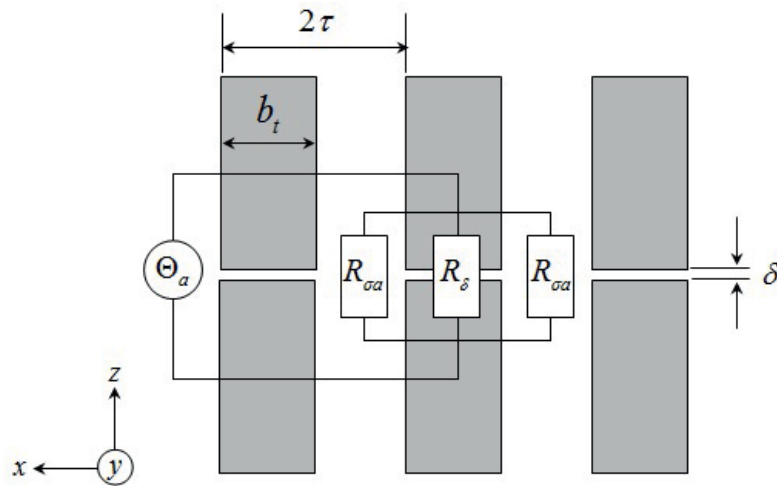


Figure 8.8 : Maximum Magnetic Energy in TFE (2-D)

Figure 8.8 shows the arrangement of the relations of the most important dimensions for the position of "tooth" against "tooth" for conformity and the EMC. The proposed EMC in TFE topology consists of two main parts, i.e., air-gap and leakage reluctance which also exist in the air region network.

$$\Theta_a = N_c \cdot I \tag{8.14}$$

$$R_{\delta} = \frac{\delta}{\mu_0 \cdot h_i \cdot b_t} \tag{8.15}$$

$$R_{\sigma a} = \frac{1}{\mu_0} \cdot \frac{\pi}{1} \cdot \frac{1}{h_i \cdot \ln\left(\frac{b_t}{\delta}\right)} \tag{8.16}$$

where,  $\Theta_a$ ,  $R_\delta$  and  $R_{\sigma u}$  are represent MMF, reluctance in air-gap and leakage reluctance in nonmagnetic material parts, respectively.

The configuration for the position of “tooth” against “slot” is shown in figure 8.9. Also, it is expressed as an EMC in that position.

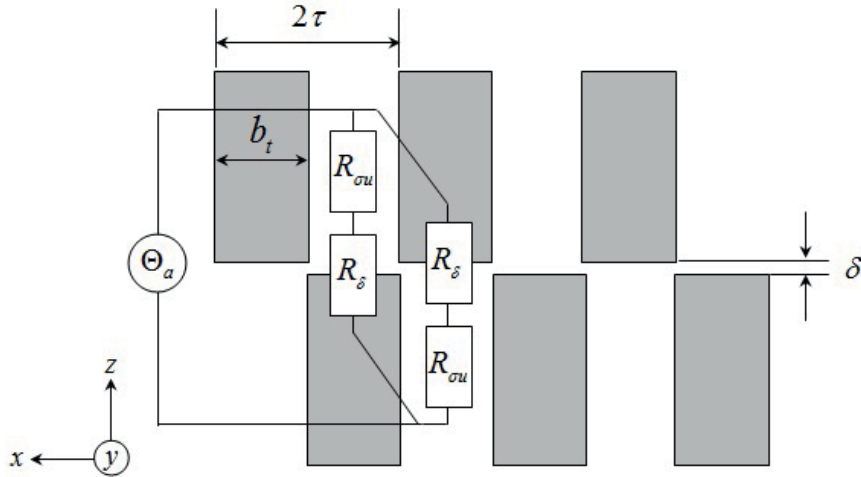


Figure 8.9 : Minimum Magnetic Energy in TFE (2-D)

From above figure, the values of these reluctances can be calculated by applying Ampere’s and Kirchoff’s Law. The leakage reluctance value under unaligned-position is given by

$$R_{\sigma u} = \frac{1}{\mu_0} \cdot \frac{2\tau - b_t}{h_i \cdot b_t} + \frac{1}{\mu_0} \cdot \frac{\pi}{2 \cdot h_i} \cdot \frac{1}{h_i \cdot \ln\left(\frac{b_t}{2 \cdot \tau - b_t}\right)} \quad (8.17)$$

By the EMC, it can be the difference of co-energy from the two positions and is calculated as follows

$$\Delta W_m = \Delta W_m \Big|_{x=0} - \Delta W_m \Big|_{x=r} = \Theta_a^2 \left[ \frac{2R_\delta + R_{\sigma u}}{R_\delta \cdot R_{\sigma u}} - \frac{2}{R_\delta + R_{\sigma u}} \right] \quad (8.18)$$

Hence, the average force and force-density using the magnetic energy is achieved by equation (8.18) and (8.19), respectively. By calculating the force density, it is caused by the fact that the force in TFE machine is formed by one pole pitch during the movement.

$$F_{ave} = \frac{\Delta W_m}{\tau} \quad (8.19)$$

$$F_{den} = \frac{F_{ave}}{2\tau \cdot h_i} \quad (8.20)$$

## 8.5 Analytical Calculation of TFPM

### 8.5.1 Two-Dimension EMC

The most common approach for force calculation by EMC method is based on analytical implementations of the virtual work method using spatial derivatives of air-gap reluctances [54 ~ 56], discrete evaluation of energies at two positions [57, 58], or electrical-equivalent circuit formulas based on flux linkages and currents [59].

Figure 8.10 shows the arrangement of a TFPM machine which is magnetized into  $x$ -axis direction as a version of rectangular coordinates including the corresponding EMC sketch. The EMC shown in the configuration can be calculated using the following formulas.

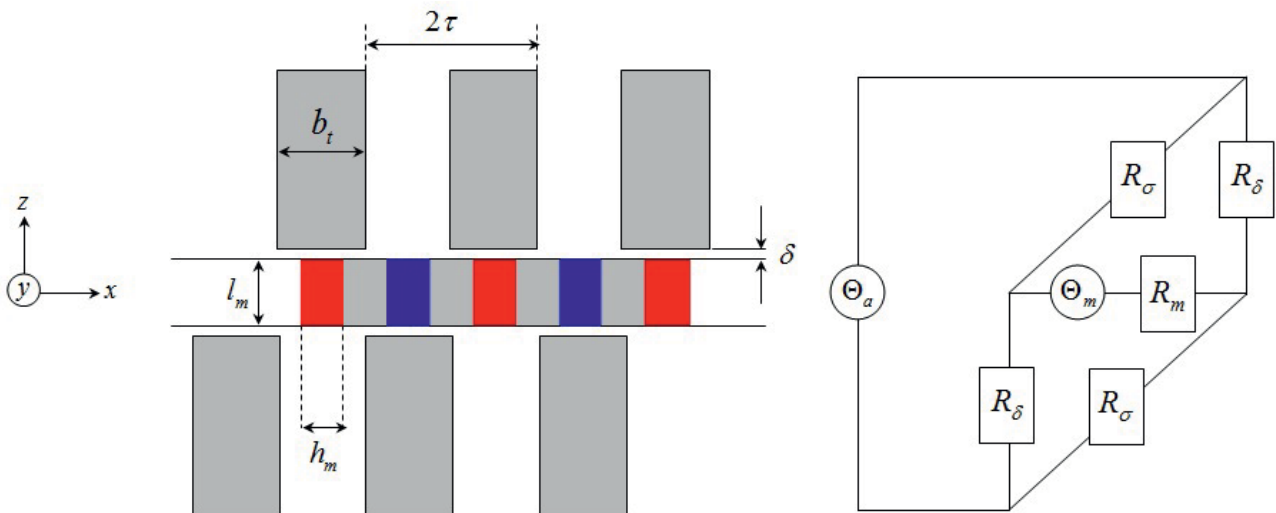


Figure 8.10 : EMC in TFPM (2-D)

The MMF and reluctance in air-gap in double-sided topology are

$$\Theta_m = \frac{B_{rem} \cdot h_m}{\mu_0 \cdot \mu_r} \quad (8.21)$$

$$R_\delta = \frac{2 \cdot \delta}{\mu_0 \cdot h_i \cdot b_t} \quad (8.22)$$

$$R_m = \frac{1}{\mu_0} \cdot \frac{1}{h_i \cdot l_m} \cdot \frac{h_m}{\mu_r} \quad (8.23)$$

$$R_{\sigma} = \frac{1}{\mu_0} \cdot \frac{\tau - b_i + h_m}{h_i \cdot (\tau - h_m)} + \frac{1}{\mu_0} \cdot \frac{\pi}{2 \cdot h_i} \cdot \frac{1}{\ln\left(\frac{\tau - h_m}{\delta}\right)} \quad (8.24)$$

As given the equation (8.23) and (8.24), each of them represents reluctances in magnet and leakage in nonmagnetic material parts.

Correspond to the EMC is calculated as the flux in each branch of the stator and mover to

$$\phi_{a\delta} = \frac{\Theta_a \cdot (R_{\sigma} + R_m)}{2 \cdot R_{\delta} \cdot R_{\sigma} + (R_{\sigma} + R_{\delta}) \cdot R_m} \quad (8.25)$$

$$\phi_{a\sigma} = \frac{\Theta_a \cdot (R_{\delta} + R_m)}{2 \cdot R_{\delta} \cdot R_{\sigma} + (R_{\sigma} + R_{\delta}) \cdot R_m} \quad (8.26)$$

$$\phi_{m\delta} = \frac{\Theta_m \cdot R_{\sigma}}{2 \cdot R_{\delta} \cdot R_{\sigma} + (R_{\sigma} + R_{\delta}) \cdot R_m} \quad (8.27)$$

$$\phi_{m\sigma} = \frac{\Theta_m \cdot R_{\delta}}{2 \cdot R_{\delta} \cdot R_{\sigma} + (R_{\sigma} + R_{\delta}) \cdot R_m} \quad (8.28)$$

The difference of the co-energy of the two positions for a pole element is

$$\begin{aligned} \Delta W_m &= \Delta W_m \Big|_{x=0} - \Delta W_m \Big|_{x=r} \\ &= [2(\phi_{a\delta} + \phi_{m\delta})^2 R_{\delta} + 2(\phi_{a\sigma} - \phi_{m\sigma})^2 R_{\sigma} + (\phi_{a\delta} - \phi_{a\sigma} + \phi_{m\delta} + \phi_{m\sigma})^2 R_m] - \\ &\quad [2(\phi_{a\delta} - \phi_{m\delta})^2 R_{\delta} + 2(\phi_{a\sigma} + \phi_{m\sigma})^2 R_{\sigma} + (\phi_{a\delta} - \phi_{a\sigma} - \phi_{m\delta} - \phi_{m\sigma})^2 R_m] \end{aligned} \quad (8.29)$$

The resulting average force and force density is calculated using the following equations.

$$F_{ave} = \frac{\Delta W_m}{\tau} \quad (8.30)$$

$$F_{den} = \frac{F_{ave}}{2\tau \cdot h_i} \quad (8.31)$$

### 8.5.2 Three-Dimension EMCN

The 3-D EMC is proposed to improve analytical modeling by taking into consideration the pole-to-pole flux leakage. Due to the complex geometry of TFPM, there is no symmetry considering 2-D axis. So, the calculation of force and force density using magnetic energy has also been carried out based on the 3-D EMCN. The analysis by 3-D EMCN method of TFPM is necessary, although the 3-D EMCN methods are very complicated to be analyzed in characteristics of TFPM. It enables very accurate field and force predictions [60]. By consequence, the analysis must be in the 3-D axis, some simplifications may be done [61]. Therefore, it needs an evaluation of comparison and consonance between 2-D and 3-D EMCN results. Finally, the result by 3-D EMCN method is compared with the result by the 2-D calculation described in the previous study.

Figure 8.11 presents the 3-D configuration of the TFPM which was selected as a more effective model by concentrating magnetic flux from the figure 8.3. The great advantage of this TFPM with inner mover is the system improvements that results from reducing the mass of the mover. The passive back irons in the mover are inserted and developed to demonstrate the principles of force generation effectively. The magnetic polarities between moving N- and S-pole, and stators generate the total thrust force in one direction. The flux originating from the magnets crosses the stator teeth and the stator yoke. Similar to the switched reluctance machine drives, the TFPM has the thrust force ripple which has limited its use in some applications. This force ripple could be minimized by controlling the current shape [62].

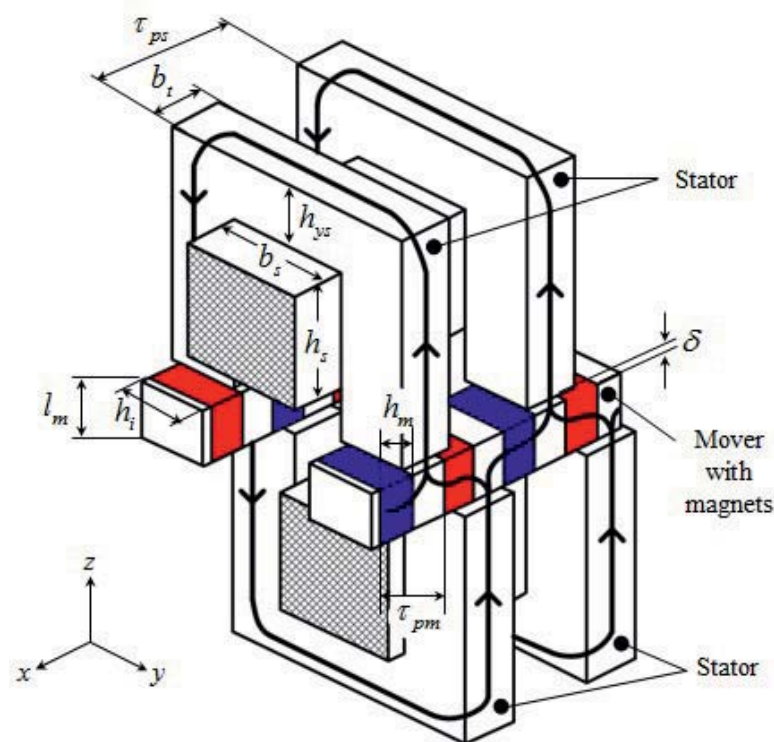


Figure 8.11 : Fundamental Building Block of TFPM Machine



Analytical modeling of the TFPM machines is a complex task because the flux paths in these machines are truly 3-D. At first, the flux paths and corresponding reluctances are identified for the TFPM topology with the basic configuration. The useful flux that is linked to the winding and contributes to the force production is in the radial direction. The 3-D analysis is considered by dividing two positions (maximum and minimum magnetic energy) in the same way like 2-D analysis. For the calculations, the reluctances of the U-shaped core constituting the stator of the TFPM machine with the basic topology are described.

Aligned Position

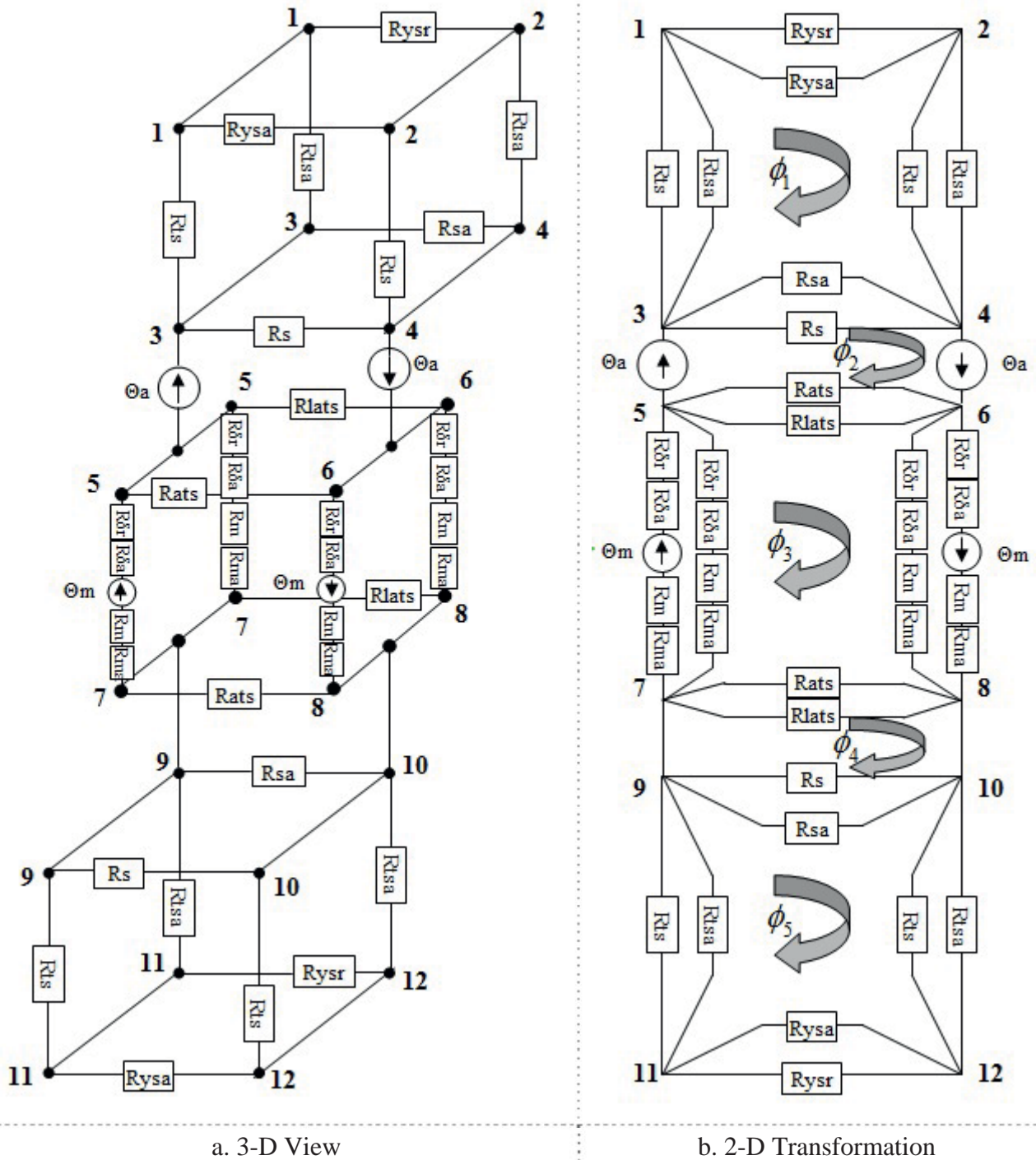


Figure 8.12 : Maximum Magnetic Energy in TFPM (3-D)

In aligned position, the EMC for one pole element is expressed in figure 8.12 ; at first, it represents 3-D configuration and then indicates 2-D sketch for the sake of convenient calculation.

The reluctances are calculated by mathematical expression as in the following.



The  $R_{ysr}$  and  $R_{ysa}$  indicate the reluctance in the stator back-iron and in the air region between stacks, respectively.

$$R_{ysr} = \frac{b_t}{\mu_0 \mu_{fe} h_{ys} (b_s + 2h_i)}, \text{ for reluctance of axial direction in the stator back-iron} \quad (8.32)$$

$$R_{ysa} = \frac{\tau_{ps} - b_t}{\mu_0 h_{ys} h_i}, \text{ for reluctance of axial direction between stacks in the air} \quad (8.33)$$

The  $R_{ts}$  and  $R_{tsa}$  represent the reluctance of  $z$ -axis and axial direction in the stator teeth, respectively.

$$R_{ts} = \frac{1}{\mu_0 \mu_{fe} h_i b_t} \cdot \left( h_s + \frac{h_{ys}}{2} \right) \quad (8.34)$$

$$R_{tsa} = \frac{b_t}{\mu_0 \mu_{fe} h_i \left( h_s + \frac{h_{ys}}{2} \right)} \quad (8.35)$$

The  $R_s$  and  $R_{sa}$  show the leakage reluctance of  $y$ -axis and axial direction in slot, respectively.

$$R_s = \frac{b_s}{\mu_0 h_s b_t}, \text{ for leakage reluctance of } y\text{-axis direction in slot} \quad (8.36)$$

$$R_{sa} = \frac{\tau_{ps}}{\mu_0 h_s b_s}, \text{ for leakage reluctance of axial direction in slot} \quad (8.37)$$

The  $R_{\delta r}$  and  $R_{\delta a}$  express the reluctance of  $z$ -axis and axial direction in air-gap, respectively.

$$R_{\delta r} = \frac{\delta}{\mu_0 h_i h_m}, \text{ for reluctance of } z\text{-axis direction in air-gap} \quad (8.38)$$

$$R_{\delta a} = \frac{\tau_{pm} - h_m}{\mu_0 h_i l_m}, \text{ for reluctance of axial direction in air-gap} \quad (8.39)$$

The  $R_{ats}$  and  $R_{lats}$  are the reluctance caused by y-axis and leakage of axial direction in air region between stator stacks, respectively. They can be obtained conveniently by the formulas and using the figure 8.13 expressed with y- and z-axis 2-D coordinate.

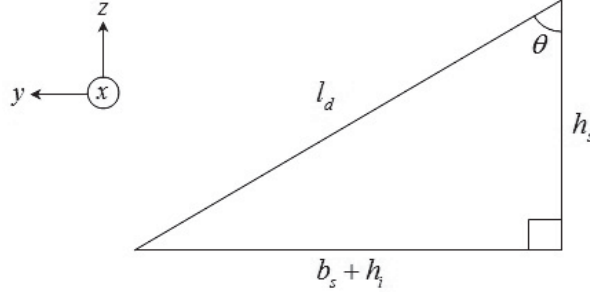


Figure 8.13 : Configuration for  $R_{ats}$  and  $R_{lats}$

$$\theta = \tan^{-1} \left( \frac{b_s + h_i}{h_s} \right) \quad (8.40)$$

$$l_d = \sqrt{(b_s + h_i)^2 + h_s^2} \quad (8.41)$$

$$R_{ats} = \frac{\theta \cdot l_d}{\mu_0 h_i b_t} \quad (8.42)$$

$$R_{lats} = \frac{\theta \cdot l_d}{\mu_0 h_i (\tau_{ps} - b_t)} \quad (8.43)$$

The  $R_m$  and  $R_{ma}$  signifies the reluctance of axial and y-axis direction in magnet, respectively.

$$R_m = \frac{h_m}{\mu_0 h_i l_m} \quad (8.44)$$

$$R_{ma} = \frac{h_m}{\mu_0 h_i (\tau_{pm} - l_m)}, \quad (8.45)$$

In aligned position, the matrix equation for the flux can be expressed as equation (8.46) by figure 8.12.b converted from 3-D organization.



$$\begin{aligned}
 \begin{pmatrix} \phi_1 \\ \phi_2 \\ \phi_3 \\ \phi_4 \\ \phi_5 \end{pmatrix} &= \begin{pmatrix} \frac{R_{ysr} \cdot R_{ysa}}{R_{ysr} + R_{ysa}} + 2 \cdot \left( \frac{R_{tsa} \cdot R_{ts}}{R_{tsa} + R_{ts}} \right) + \frac{R_{sa} \cdot R_s}{R_{sa} + R_s} & -\frac{R_{sa} \cdot R_s}{R_{sa} + R_s} & 0 \\ -\frac{R_{sa} \cdot R_s}{R_{sa} + R_s} & \frac{R_{sa} \cdot R_s}{R_{sa} + R_s} + \frac{R_{ats} \cdot R_{lats}}{R_{ats} + R_{lats}} & -\frac{R_{ats} \cdot R_{lats}}{R_{ats} + R_{lats}} \\ 0 & -\frac{R_{ats} \cdot R_{lats}}{R_{ats} + R_{lats}} & 2 \cdot \left( \frac{R_{ats} \cdot R_{lats}}{R_{ats} + R_{lats}} \right) + 2 \cdot \left( \frac{R_{\delta a} + R_{\delta r} + R_m + R_{ma}}{2} \right) \\ 0 & 0 & -\frac{R_{ats} \cdot R_{lats}}{R_{ats} + R_{lats}} \\ 0 & 0 & 0 \end{pmatrix} \begin{pmatrix} 0 \\ 0 \\ 0 \\ 0 \\ 0 \end{pmatrix} \\
 & \begin{pmatrix} 0 & 0 \\ 0 & 0 \\ -\frac{R_{ats} \cdot R_{lats}}{R_{ats} + R_{lats}} & 0 \\ \frac{R_{ats} \cdot R_{lats}}{R_{ats} + R_{lats}} + \frac{R_{sa} \cdot R_s}{R_{sa} + R_s} & -\frac{R_{sa} \cdot R_s}{R_{sa} + R_s} \\ -\frac{R_{sa} \cdot R_s}{R_{sa} + R_s} & -\frac{R_{sa} \cdot R_s}{R_{sa} + R_s} + 2 \cdot \left( \frac{R_{ts} \cdot R_{tsa}}{R_{ts} + R_{tsa}} \right) + \frac{R_{ysa} \cdot R_{ysr}}{R_{ysa} + R_{ysr}} \end{pmatrix}^{-1} \begin{pmatrix} 0 \\ 2\Theta_a \\ 2\Theta_m \\ 0 \\ 0 \end{pmatrix} \\
 & \tag{8.46}
 \end{aligned}$$

Unaligned Position

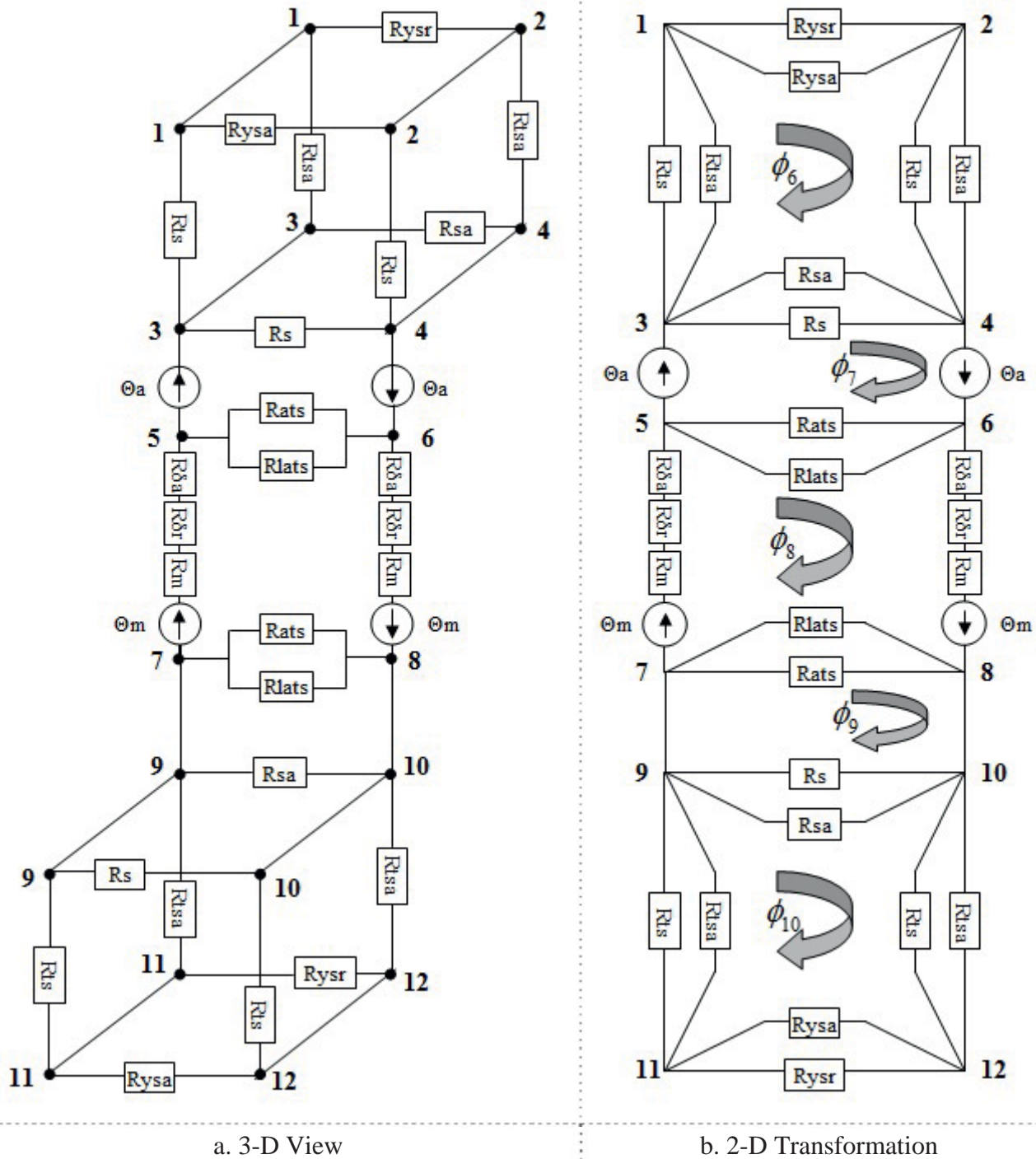


Figure 8.14 : Minimum Magnetic Energy in TFPM (3-D)

The calculation for the flux matrix equation in unaligned position is achieved identically as the formula in aligned position.



$$\begin{array}{c} \phi_6 \\ \phi_7 \\ \phi_8 \\ \phi_9 \\ \phi_{10} \end{array} = \begin{array}{ccc} \frac{R_{ysr} \cdot R_{ysa}}{R_{ysr} + R_{ysa}} + 2 \cdot \left( \frac{R_{tsa} \cdot R_{ts}}{R_{tsa} + R_{ts}} \right) + \frac{R_{sa} \cdot R_s}{R_{sa} + R_s} & - \frac{R_{sa} \cdot R_s}{R_{sa} + R_s} & 0 \\ - \frac{R_{sa} \cdot R_s}{R_{sa} + R_s} & \frac{R_{sa} \cdot R_s}{R_{sa} + R_s} + \frac{R_{ats} \cdot R_{lats}}{R_{ats} + R_{lats}} & - \frac{R_{ats} \cdot R_{lats}}{R_{ats} + R_{lats}} \\ 0 & - \frac{R_{ats} \cdot R_{lats}}{R_{ats} + R_{lats}} & 2 \cdot \left( \frac{R_{ats} \cdot R_{lats}}{R_{ats} + R_{lats}} \right) + 2 \cdot (R_{\delta a} + R_{\delta r} + R_m) \\ 0 & 0 & - \frac{R_{ats} \cdot R_{lats}}{R_{ats} + R_{lats}} \\ 0 & 0 & 0 \end{array} \cdot \begin{array}{c} 0 \\ 0 \\ - \frac{R_{ats} \cdot R_{lats}}{R_{ats} + R_{lats}} \\ \frac{R_{ats} \cdot R_{lats}}{R_{ats} + R_{lats}} + \frac{R_{sa} \cdot R_s}{R_{sa} + R_s} \\ - \frac{R_{sa} \cdot R_s}{R_{sa} + R_s} \\ - \frac{R_{sa} \cdot R_s}{R_{sa} + R_s} + 2 \cdot \left( \frac{R_{ts} \cdot R_{tsa}}{R_{ts} + R_{tsa}} \right) + \frac{R_{ysa} \cdot R_{ysr}}{R_{ysa} + R_{ysr}} \end{array}^{-1} \cdot \begin{array}{c} 0 \\ 2\Theta_a \\ 2\Theta_m \\ 0 \\ 0 \end{array} \quad (8.47)$$

In addition, the calculation of the average force and force density is same as 2-D EMC calculation method.

$$F_{ave} = \frac{W_m}{\tau_{pm}} \quad (8.48)$$

$$F_{den} = \frac{F_{ave}}{2\tau_{pm} \cdot h_i} \quad (8.49)$$

## 8.6 Comparison Results

In a prior study, the analytical model for the analysis of the TFPM was established. Based on the given mathematical model, analytical calculation using the magnetic energy and force characteristics was computed by a 2-D and 3-D EMCN method respectively. This performance roughly analyzed with the help of the developed analytical models. However, previous experience of the TFM showed that the analytical models cannot be relied to a great extent. Thus, it is required for 3-D FEM analysis, which is a kind of numerical calculation for verification of analytical

calculation. At last, the results are compared to those obtained by 2-D and 3-D analytical models.

### 8.6.1 Limitations of 2-D Analysis

The movement of the magnets and the winding layout is in the same direction. Thus, it is difficult to directly compute the force from the 2-D FEM analysis. Also, it is very difficult to investigate of the pole to pole axial leakage flux which is the most interesting aspect of the TFM design in a 2-D FEM analysis. However, the 2-D FEM analysis does allow the prediction of the magnet flux and the stator fluxes in the machine to some extent by applying appropriate modifications. As a result, a 2-D FEM analysis is not preferred for the reason as above.

### 8.6.2 FE Simulation by 3-D Analysis

In this paragraph, the result of the FE analysis is provided. Considering the period of the movement, one pole element was modeled in a manner that allows automatic remeshing at different mover position. FLUX 3-D software provided by CEDRAT was used for this purpose [63]. Today, the program allows the aspects related to the linear machine modelling and time stepping has also become available after required extra efforts, although this program was originally made for rotating machines.

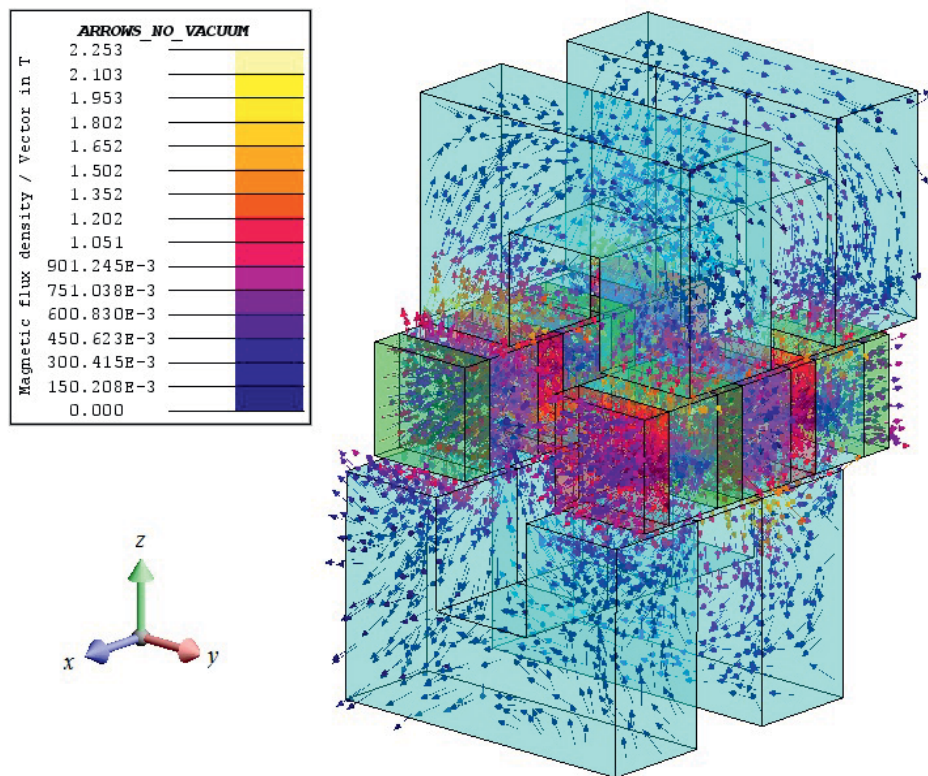


Figure 8.15 : The Investigated 3-D FEM of TFPM Machine

Figure 8.15 indicates the direction and degree of the magnetic flux by excited winding and magnets. Based on this simulation, the evaluation of the results will be performed with the analytical calculated results.

### 8.6.3 Verification by 3-D FEM

Generally, the serious loss in force is caused by high stator leakage flux. It can be become evident from 3-D FE analysis. A comparison between analytical calculation and 3-D FE analysis result by the magnetic energy, average force and force density is given for in table 8.1. The result by 3-D FEM is coincide with over 90 [%] in comparison previous analytical results by 2-D and 3-D EMCN.

Table 8.1 Estimation by EMC and FEM

TFPM			
	Analytical Calculation (EMCN)		Numerical calculation
	2-D	3-D	3-D FEM
Magnetic Energy [J]	0.08	0.081	0.074
Average Force [N]	8.89	8.959	8.216
Force Density [N/mm <sup>2</sup> ]	49.4	49.77	45.64

## 8.7 Discussion

In this study, two different kinds of TFM are discussed ; TFE and TFPM with single -phase system. In a correlation between two models, the former is considered as single-sided reluctance type, the latter is regarded as model that consists of double-sided stators with magnets in mover. The design process of these models takes advantage of the methods by 2-D and 3-D EMCN analysis. Finally, the analytical calculations by EMCN method are evaluated through 3-D FEM simulated result. As a result, the results of analytical estimation by EMCN are much satisfied with that of FE analysis by FLUX 3-D.

However, this study was overlooked the leakage flux generated from z-axis direction between the upper and lower stator cores. To reduce the errors shown in the table 8.1, it needs more investigation of the leakage flux generated in the area above.

It will give elaborate information about the design rules and performance data of LTFM and in parallel tools for the calculation, simulation and design will be available.

---

## 9 Selection of Optimal Topology

### 9.1 Introduction

In a previous study, we have investigated the characteristics of each topology by EMCN method ; Cartesian topology, cylindrical topology, hybrid stepping machine, cylindrical reluctance type and transverse flux machine. The magnetic energy and force performance could be obtained by this method taking leakage into account. Its advantages are a relatively low computational complexity and respectable accuracy, achieved through a division of the geometry that is coarser than in FE analysis. It is also easily extended into a 3-D model, accordingly it was analyzed by applying TFM. These advantages make EMC attractive as a design tool.

In general the whole paths of the actual leakage flux are not important in the ideal conditions, but it is necessary for the exact application of simple general formula for permeance calculation. In such case the leakage flux lines are divided into suitable partial fluxes and permeance estimated by appropriate geometrical assumptions. This assumed flux paths technique has been found to be useful in the past, but depends to some extent on the skill and care by which it is applied.

Meanwhile, the approach is also possible by use of numerical method, however the numerical result obtained does not give an analytical formula which would be very useful for an iterative design process. Even at present, it is believed that such detailed numerical computations should be left to the final stages of the machine's design process or precomputed for a nominal configuration to form a data base for reference purposes.

This chapter contains the electrical characteristic results based on the performances by both EMCN method and FE analysis in the whole models. It examines closely the conformity between the analytical calculation and FE analysis results of all studied topologies representing the device as a magnetic circuit (reluctance network). And then, the difference by number of phase is accomplished through the universal and mathematical analysis. At last, cylindrical topology with single-phase is selected for optimal model by comparing the structural features and the characteristics of each topology. In the next step, the topology will be taken with magnetic flux saturation by nonlinear iron property into account. This study will be discussed in more detail in the next *Chapter 10 Detailed Design*.

### 9.2 Operating Characteristic

The decisive components for selecting the optimal model is related to the generator topology,

number of phases, power to weight and volume ratio, and reactive power consumption. First of all, the evaluations of each topology are carried out by parameters such as magnetic energy, force density, efficiency, and volume weight ratio studied in previous chapter. Especially, this machine always absorbs reactive power. The reactive component of the current causes additional losses and additional heating [64].

### 9.2.1 Voltage Equations

A circuit equivalent of the generator can be used to understand how the current in the generator is related to the induced electromotive force. The equivalent circuit is only an approximation but it gives the energy balance of the machine completely and nonlinear properties of the elements. The voltage equations can be easily obtained from the space vector equation. In principle, it can derive all the necessary equations for power and torque balance from the representation. Figure 9.1 shows the equivalence of a generator where the induced voltage is described by an electromotive force.

These voltage equations can be assigned to an equivalent circuit as shown in figure 9.1.

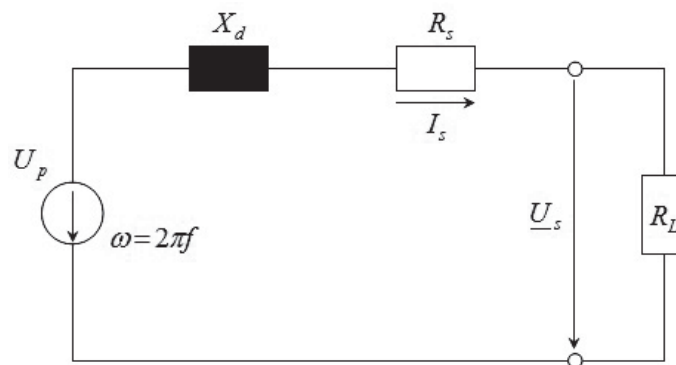


Figure 9.1 : No-load ( $I_s = 0 \rightarrow U_s = U_p$ )

This voltage is referred to as the no-load voltage, which is the measurable voltage at the coil ends when no current flows through the generator.

$$U_s = U_p + \cancel{jX_d I_s} \quad (I_s = 0) \quad (9.1)$$

Meanwhile, it exists the second term of equation (9.1) under the load condition. Where,  $X_d$  is the reactance of the generator and will be further described below, and  $R_s$  is the resistance in the coil windings. The outer circuit, or the load, can be either purely resistive or reactive. In this work the load is assumed to be strictly resistive and is described by a resistance  $R_L$ . The voltage over the load  $U_s$  will thus be in phase with the armature current  $I_s$ .

The voltage equation is simplified to

$$\begin{aligned}
 U_s &= R_s I_s + j \cdot X_\sigma I_s + j \cdot X_h \cdot I_s + U_p \\
 &= R_s I_s + j \cdot X_d I_s + U_p \\
 &= (R_s + j \cdot X_d) I_s + U_p
 \end{aligned}
 \tag{9.2}$$

where,  $X_d$  represents the reactance.

### 9.2.2 Generator in Stand-alone Operation

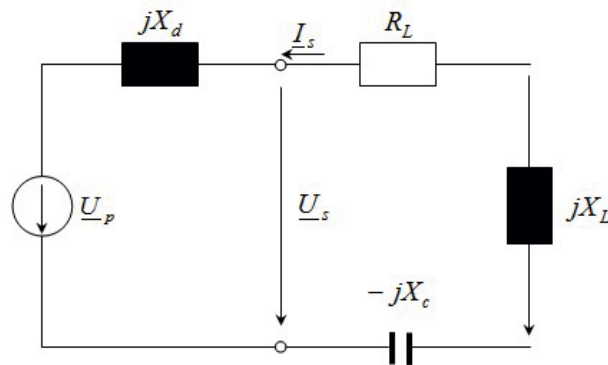


Figure 9.2 : Generator under General-Load

There are linked in the resistance, inductance, and capacitance.

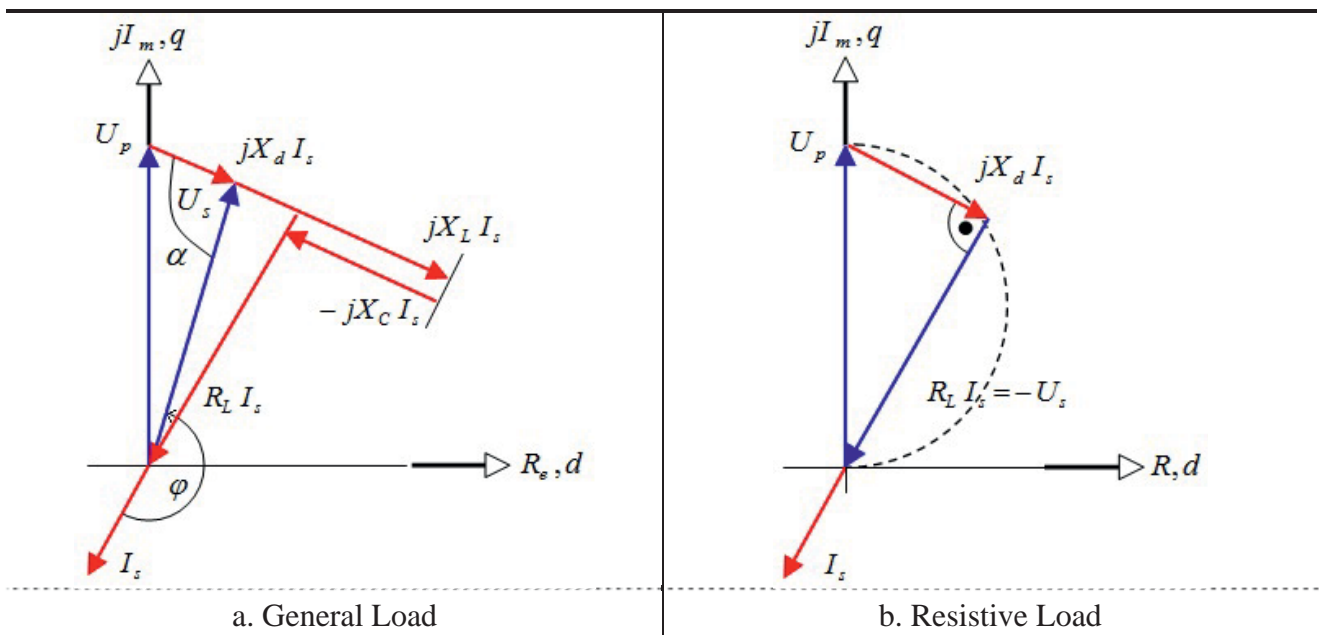


Figure 9.3 : Generator under Load [64]

In the general case, the voltage equation is expressed using the *Cosine Theory* [65] :

In conclusion,

$$\left(\frac{U_s}{U_p}\right)^2 + \left(\frac{I_s}{I_k}\right)^2 + 2\frac{U_s}{U_p}\frac{I_s}{I_k}\sin\varphi = 1 \quad (9.3)$$

$$y^2 + x^2 + 2xy\sin\varphi = 1$$

It can be obtained of the ellipse equation whose position and form is dependent of the load.

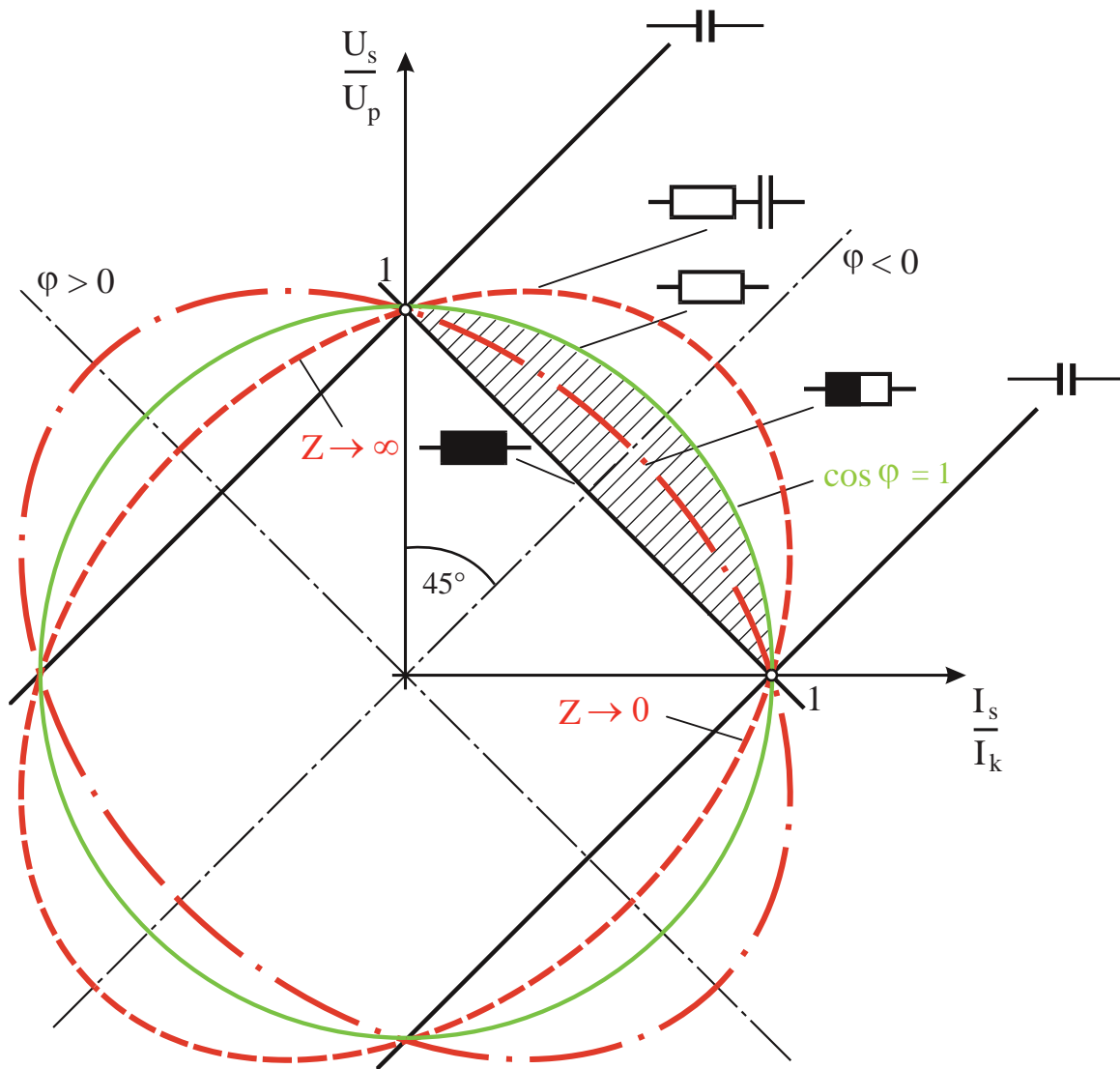
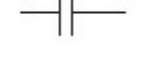


Figure 9.4 : Load-dependent Ellipses of the Terminal Voltage [64]

The largest voltage drop occurs when a purely inductive load is supplied. The reason is that the inductive load needs additional reactive power.

Table 9.1 : Loading Condition, Shape and Position of the Ellipse

$Z_L$	$\cos \varphi$	$\sin \varphi$	
	1	0	Circle, $x^2 + y^2 = 1$
	$0 < \cos \varphi < 1$	$1 > \sin \varphi > 0$	Ellipse, $-45^\circ$ inclined
	0	1	Ellipse, $-45^\circ$ inclined with an axis $\infty$ line
	0	-1	Ellipse, $+45^\circ$ slanted with an axis $\infty$ line
	$0 < \cos \varphi < 1$	$-1 < \sin \varphi < 0$	Ellipse, $+45^\circ$ slanted

The most common practice is the resistive-inductive load in the loading condition. The component of magnetizing current lags voltage by 90 [Deg.], whereas load current is in phase with voltage. A power factor represents the offset in time or delay, between voltage and the current being delivered and is defined as the cosine of that offset. If the delay is 0 [Deg.] (voltage and current in phase), the power factor would be 1.0 (because  $\cos 0 = 1$ ) and if the delay is a full 90 [Deg.] (this would be all magnetizing current), the power factor would be 0.0 ( $\cos 90 = 0$ ). In order to achieve a constant voltage with a high utilization of machine, a control device using  $I_\mu$  is absolutely necessary.

### 9.3 Evaluation Standard

The characteristics of each topology are evaluated by electrical parameters such as input current density and resultant reactive power, and geometrical parameters such as weight. These results of each topology were achieved by equivalent magnetic circuit analysis defined in the previous chapters.

In order to select the optimal topology on the basis of these characteristics, it is also considered by three categories ;

- Advantages / Disadvantages of each topology
- Academic difference of single- and three-phase
- Comparative evaluation by weight factors



### 9.3.1 Characteristics Evaluation of Each Topology

#### Cartesian Topology

In Cartesian type with a simple structure, the coil windings are inserted into a steel structure to create the coil assembly. But this structure has an end winding which cause a leakage flux and losses, as a result has a bad effect on the system. Also, the iron core significantly increases the force output of the generator due to focusing the magnetic field created by the winding. It brings about another weakness of intensely heavy volume compared to the force ; consequently it has approximately greater decuple weight than the other topologies. Besides, it also leads to higher reactance and lower power factor relatively.

#### Cylindrical Topology

Among the various linear generators, cylindrical types with magnet excitation are particularly popular, since they conform to a compact structure and a low weight compared to the force. It has higher efficiency and reliability than the flat type. Moreover, the amount of coil is less and the benefit with the cylindrical arrangement has a positive effect on the system that it has no end windings ; thus, the copper loss becomes less than that of flat type. Meanwhile the flux in the mover tends to concentrates toward the shaft, and consequently the saturation generates in the back iron of the mover because of the radial force is perpendicular to the direction of movement. Thus, it needs the detailed analysis to not occur the saturation of the magnetic flux.

In addition, it leads to the high speed operation of mover because of light weight. As a result, the cylindrical type is recommended as the most suitable model in linear oscillating generator for these features.

#### Hybrid Stepping Generator

Hybrid stepping generator has an existence of end of windings. In common with Cartesian topology, it brings about a high reactive power relatively which is resulting in low power factor and required to main the voltage to deliver active power. It is an inevitable phenomenon in the flat type such as Cartesian topology. End winding is undesired since they increase the cost of the device and the resistance of each phase without providing a useful advantage. Also, the sequential structure consisting of the magnets and iron cores leads to the low speed of mover.

#### Tubular Reluctance Machine

The linear generators using tubular reluctance machines have significant advantages that a neutralization of normal forces, low reactance and high power factor. Moreover, it is superior over

permanent magnet generators in terms of capability to operate in harsh environments and at elevated temperatures. However, due to the reluctance principle, the force density is low and the construction requires a small air-gap and tight production tolerances.

### Transverse Flux Machine

Transverse flux machine inherently takes on unconventional structures due to its 3-D flux paths. In this machine, the plane on which the flux path lies in transverse, or perpendicular to the direction of movement. There has been discussion favoring the transverse flux because of its capabilities to obtain a high force density. However, there are drawbacks to a transverse flux design ; the design and the construction can become difficult, resulting in a high price that must be paid by relatively low power factor. Due to the intricate structure of a transverse flux machine, vibration and force ripple occurs which is larger than other type machines. Moreover due to the high forces during the combustion process, this is relevant for all types but a transverse flux translator consists of many parts, which have to be fixed against the high acceleration of an oscillating machine.

## 9.3.2 Academic Difference of Single-Phase and Three-Phase

### Introduction

For the development of oscillating free piston internal combustion engines, single-phase generators or three-phase generators are applicable. Goal of these considerations is to generally evaluate the utilization of both systems in terms of force density and losses. As constants a permanent magnet excitation with trapezoidal spatial flux density distribution is assumed.

### Continuous Motion

If continuous motion is assumed, the same considerations are applicable as with rotating machines. In principle a three-phase winding generates a travelling wave of current sheet  $A$  which interacts with the first harmonic of the flux density distribution  $\hat{B}$ , thus producing thrust  $\tau w$  according to (9.4).

$$\tau w = \frac{1}{2} \hat{A} \cdot \hat{B} \cdot \cos \alpha \quad (9.4)$$

with optimised control  $\alpha$  becomes zero and the maximum thrust is available.

Improvement of thrust is possible if higher harmonics of the flux density distribution find similar

waves of the current sheet to form additional thrust components. Assuming a rectangular spatial distribution of the current sheet in the air-gap and an inverter driven machine with nearly rectangular current feeding over time a practical increase of the average thrust of approximately 17 [%] will be possible [66]. But, this will be connected with thrust oscillations of up to 30 [%] because the current sheet move now not continuous but within discrete time steps while rotor or translator move continuously.

If a single-phase machine is applied the current sheet is alternating in place but can be dissolved in a forward and backward moving travelling wave ;

$$A^{(1)}(\gamma, t) = \hat{A} \cdot \sin(\omega \cdot t) \cdot \sin \gamma \tag{9.5}$$

$$A^{(1)}(\gamma, t) = \frac{1}{2} [\cos(\omega \cdot t - \gamma) - \cos(\omega \cdot t + \gamma)]$$

One wave can be used for the continuous motion thus producing half of the thrust of a three-phase system if same pole pitch and same current sheet is assumed. As the losses have to be calculated for both waves an increase of current sheet violates the condition of constant losses. With respect to rectangular distribution of current sheet the same considerations as above are applicable but will not change the relation.

Limited Motion

If we assume a limited motion by one pole pitch only what is typically possible in oscillating machines, the calculation approach for the thrust has to be modified.

While in the three-phase system operated on an inverter bridge, the current sheet is more or less sinusoidal, also a magnet width - pole pitch ratio which emphasizes the first harmonic of the flux density distribution ( $\alpha \cdot p \approx 0.72$ ) is preferable. With the single-phase system instead a more rectangular flux density distribution is the best approach as the one-phase is operated on a 4 Quadrant chopper which can produce a nearly rectangular current sheet (figure 9.5).

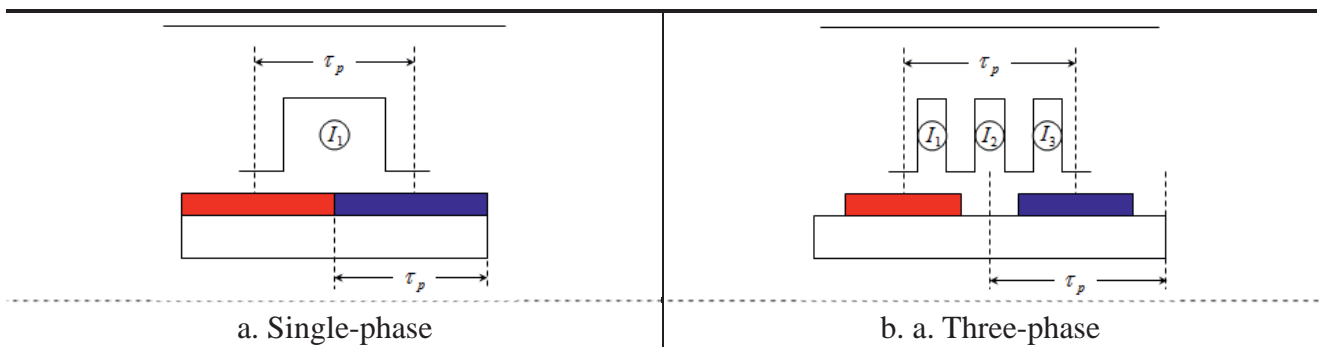


Figure 9.5 : Comparison of the Geometric Conditions of a Single-phase and a Three-phase System

Calculating the inductances from the flux linkage, we find different expressions ;

$$\hat{\Psi}^{(1)} = (w_s \cdot \zeta_s)^2 \cdot \frac{1}{2} \cdot \frac{\mu_0 \cdot \tau_p \cdot l_E}{\delta''} \cdot I_s, \text{ for rectangular flux distribution} \quad (9.6)$$

$$\hat{\Psi}^{(3)} = (w_s \cdot \zeta_s)^2 \cdot \frac{2}{\pi^2} \cdot m_s \cdot \frac{\mu_0 \cdot \tau_p \cdot l_E}{\delta''} \cdot I_s, \text{ as conventional cyclic inductance} \quad (9.7)$$

$$\frac{L_h^{(1)}}{L_h^{(3)}} = \frac{1 \cdot \pi^2}{2 \cdot 2 \cdot m_s} = 0.82 \quad (9.8)$$

The copper losses can be calculated for one slot and one phase with the copper volume,  $V_{cu}$  ;

$$P_{vcu} = J^2 \cdot \frac{V_{cu}}{\kappa} = R_s \cdot I_s^2 \quad (9.9)$$

with current density  $J$ , and conductivity  $\kappa$ .

Assuming same losses in both single-phase and three-phase system, we find equal current densities and

$$V_{cu}^{(1)} = 3 \cdot V_{cu}^{(3)} \text{ as } I_s^{(1)} = 3 \cdot I_s^{(3)} \quad (9.10)$$

For the voltage we have two options ; We can assume same terminal voltage or same voltage of the intermediate circuit. This depends on application and load of the generator. If we have an automotive application in mind, we have an on board battery with limited voltage and so in practice we have to compare systems with same intermediate circuit voltage. With the 4 Quadrant chopper and the single-phase system, we have  $\sqrt{3}$  higher phase voltage than with the 6 pulse bridge inverter. With the absolute value of the voltage and setting the winding factors to unity, we find approximately.

$$|U_s| \approx \omega_s \cdot L_h \cdot I_s$$

$$\left| \frac{U_s^{(1)}}{U_s^{(3)}} \right| = \sqrt{3} = 0.82 \cdot \frac{(w_s^{(1)})^2}{(w_s^{(3)})^2} \cdot \frac{I_s^{(1)}}{I_s^{(3)}} = 0.82 \cdot \frac{(w_s^{(1)})^2}{(w_s^{(3)})^2} \cdot 3 \quad (9.11)$$

$$\frac{(w_s^{(1)})^2}{(w_s^{(3)})^2} = \frac{\sqrt{3}}{3 \cdot 0.82} = \frac{1}{0.82 \cdot \sqrt{3}} = 0.704$$



$$\frac{w_s^{(1)}}{w_s^{(3)}} = 0.84 \quad (9.11)$$

From the winding ratio, we can calculate now the current sheet ;

$$\frac{A_s^{(1)}}{A_s^{(3)}} = \frac{w_s^{(1)} \cdot I_s^{(1)}}{m_s \cdot w_s^{(3)} \cdot I_s^{(3)}} = \frac{0.84 \cdot 3}{3 \cdot 1} = 0.84 \quad (9.12)$$

With the same flux density amplitude, we find the thrust ratio ;

$$\frac{\tau_w^{(1)}}{\tau_w^{(3)}} = \frac{B_\delta^{(1)} \cdot A_s^{(1)}}{B_\delta^{(3)} \cdot A_s^{(3)}} = \frac{B_\delta^{(1)}}{\left( \frac{\wedge^{(3)}}{B_\delta} \right)} \cdot \frac{A_s^{(1)}}{A_s^{(3)}} = \frac{0.84}{\frac{1}{\sqrt{2}}} = 1.19 \quad (9.13)$$

The thrust of a single-phase system can under the assumed circumstances be 19 [%] higher than the thrust of a three-phase system.

### Summary

In a comparative study for an oscillating machine moving just one pole pitch forward and backward the thrust of a single-phase system was found to be nearly 20 [%] higher than that of three-phase system. This result is on the first glance unorthodox but valid under the close to practice assumptions summarised here ;

- Same pole pitch and number of pole pairs
- Both winding factors approximately 1
- Same losses
- Same amplitudes of flux density but different spatial flux density distributions
- Three-phase system fed from conventional 6 pulse bridge inverter and single-phase system fed from 4 Quadrant chopper and both with same voltage of intermediate circuit.

### 9.3.3 Comparative Evaluation by Factor Variations

The choice of the optimal model should be examined carefully among the proposed topologies which were analyzed respectively in previous chapters. It can be decided by as well the factors such as force density, reactive power, coil loss and efficiency of electrical variances, as machine weight, mover speed, control simplicity and manufacture convenience of mechanical variances.

Above all, each criterion is assigned to a score of weight factor and it is differentiated by importance factor through comparison with other factors.

In most cases, an efficiency and force density is one of the most important factors in the design of electrical machine ; thus, it has been assigned the largest weight factors because they are very important factors for the selection of the optimal model. Among others, hybrid stepping and transverse flux machine takes considerably precedence over other models in terms of force density by decoupling of the space requirement of the path carrying permanent magnet excitation flux and the space occupied by the armature windings. Although cylindrical type with permanent magnet tends to depreciate in terms of the force density compared to the aforementioned two types, it gives the highest performance when it comes to efficiency. In addition, this model has better property by virtue of the increment of useful magnetic flux with inserting of permanent magnet than reluctance machine.

In general, cylindrical topology regardless of permanent magnet type or reluctance type is superior to flat type in copper loss due to the absence of end windings. It leads to effect of the lower reactive power consumption to current density ratio in a specific frequency. Furthermore, it indicates that flat type machine needs more coils to produce a force than cylindrical type with regard to the losses consisted of copper and iron loss. Meanwhile, transverse flux machine has advantage relatively lower copper losses and simpler windings than other flat type machines.

As contrasted with flat type, cylindrical type is smaller and lighter relatively. Especially, it enables to high speed operation to lightweight of mover. On the contrary, cylindrical type is more difficult than flat type due to the structural reason in manufacture. However, this was solved with the advent of SMC ; SMC components have the potential advantages that are the possibility for compact designs through the use of 3-D geometries, efficient manufacturing process for high volume production, and low total price and weight as a result of derived savings on other components and processes in the construction. In short, SMC components provide better properties, fewer parts, more integrated design, more complex geometries, lower price and more environmentally-friendly techniques [67]. It operates at low speed due to large number of poles and increasing volumetric mass density of the mover with permanent magnets inserted in between nonmagnetic material parts in the case of hybrid stepping and transverse flux machine. In other words, there exist large attractive forces between stator and mover in these machines ; consequently it gives rise to a low speed operation. In addition, they are difficult to manufacture due to the complicated construction. Particularly, low speed of mover in transverse flux machine results in large number of coil turns for rated voltage, high inductance, and low power factor.

As analyzed in the previous paragraph 9.3.2, the thrust of a single-phase system can be better than that of a three-phase system. Furthermore, it is easier to control a single-phase system than a three-



9 Selection of Optimal Topology

phase system in a control method.

In conclusion, it can be expressed as shown in the following table 9.2.

Table 9.2 : Measurement of Each Topology by Criterion

Criterion	Weight Factor	Cartesian		Cylindrical		Hybrid Stepping		Tubular Reluctance		TFM	
		Rank	Point	Rank	Point	Rank	Point	Rank	Point	Rank	Point
[Symbol]	[F]	[R]	[F][R]	[R]	[F][R]	[R]	[F][R]	[R]	[F][R]	[R]	[F][R]
Force Density	7	3	21	2	14	5	35	1	7	4	28
Efficiency	6	2	12	5	30	4	24	1	6	3	18
Reactive Power	5	2	10	5	25	3	15	4	20	1	5
Weight	4	1	4	4	16	2	8	5	20	3	12
Control	3	5	15	4	12	3	9	1	3	2	6
Speed	2	4	8	3	6	1	2	5	10	2	4
Manufacture	1	5	5	3	3	2	2	4	4	1	1
$\sum [F][R]$	28	-	75	-	106	-	95	-	70	-	74
$\sum \{[F][R] / [F]\}$	-	-	2.68	-	3.79	-	3.40	-	2.50	-	2.65

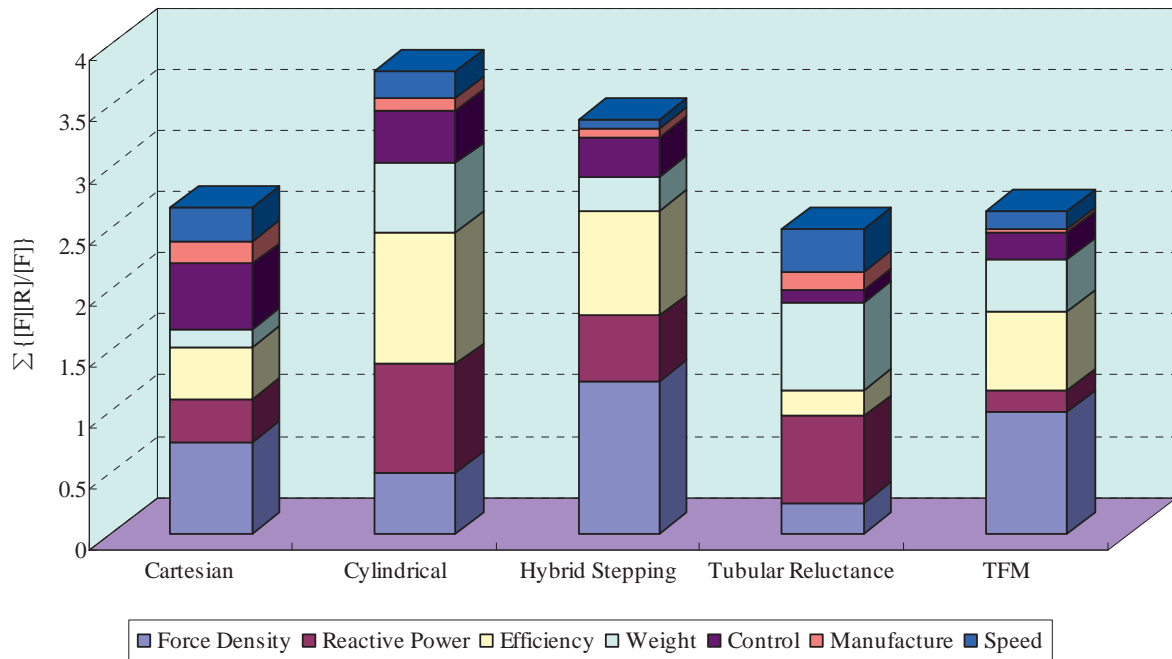


Figure 9.6 : Comparative Study on the Characteristics of Each Topology

where, [F] means the weight factor, which indicates that it has a greater effect on choice of optimal model, the higher the number. The [R] indicates a ranking of weight value through relative comparison between different topologies, and also represents a priority as the number is higher. The expression of examined variant can be expressed by the weight factor and ranking using in total 8 criteria.

At last, cylindrical topology with permanent magnet of single-phase system is selected as optimal model for linear oscillating generator.

### Summary

The evaluation by factor variation of each topology is achieved based on the followings ;

- Cartesian Topology : One-Phase System with Two Magnets and Two Pole-Pairs  
(Chapter 4.4.1)
- Cylindrical Topology : One-Phase System (Chapter 5.5.1)
- Hybrid Stepping Generator : Proposal Model (Chapter 6.6)
- Cylindrical Reluctance Machine : Trapezoidal Shape Mover (Chapter 7.4.3 & 7.5.2)
- Transverse Flux Machine : Transverse Flux Permanent magnet Machine (TFPM)  
(Chapter 8.5)

## 9.4 Discussion

This chapter has performed the choice of optimal model through the characteristics and comparative analysis of 5 kinds of topologies for linear oscillating generator ; Cartesian, cylindrical, hybrid stepping, tubular reluctance, and transverse flux machine. It consists of the characteristic analysis by equivalent circuit and its phasor diagram, and comparative analysis by the scientific acquaintance between single-phase and three-phase in terms of the force density. Besides, it has been established by the evaluation of 8 kinds of criteria and its weighting value that has significant effects on selection of optimal model, as well as by measurement of the ranking and score through relative comparison of each topology.

Based on the above analysis and evaluation, ultimately cylindrical topology with permanent magnet of single-phases system is selected as optimum model for linear oscillating generator. It will be continuously achieved taking magnetic flux saturation of iron core into account for practical application.



---

## 10 Detailed Design of Optimal Model

### 10.1 Introduction

There were investigations of the various topologies for linear oscillating generator of Cartesian, cylindrical, hybrid stepping, tubular reluctance, and transverse flux types respectively in the previous chapters. The characteristic data for each topology are accomplished by equivalent magnetic circuit method which makes use of the minimum and maximum magnetic energy using the leakage reluctances. Besides, this study is added to the optimal process by design variables, analysis by number of phase, buried type of permanent magnet, shape of the mover, and 3-D analysis using equivalent magnetic circuit network method separately in each topology.

Ultimately, it is selected to the single-phase cylindrical topology as the optimum topology for linear oscillating generator in this design process.

Accurate modeling of a machine in different methods is employed to carry out the calculation including numerical methods and equivalent magnetic circuit which is a kind of analytical methods. These methods try to find out closed form expressions for magnetic fields in a machine. However, they cannot consider iron saturation which has significant effect on magnetic fields of machines. It is not easy to model the magnetic flux leakage by some sort of approximation. The numerical methods such as the FEM are widely used for field in electrical machines. Although they are very accurate, they are time consuming and can hardly be used in iterative machine design optimizations and initial design procedures where several parameters change in wide ranges [68].

Meanwhile, the equivalent magnetic circuit has been known as an effective means for modeling to make quicker and more accurate calculations for many years. This is developed and extended in corporation with FEM resulting in very accurate field and force prediction. However, this model is too complicated to be used in an iterative machine design procedure especially in case of 3-D analysis. Besides, this method can hardly model most phenomena related to permanent magnet machines such as nonlinearity, eddy current, etc [69].

In addition, this chapter shows that it is possible to accurately predict power loss in ferromagnetic laminations under magnetic flux by specially considering the dependence of hysteresis, classical, and excess loss components on the magnetic induction derivative. As well as considering the iron loss, the calculation of copper loss and eddy-current loss in PM is considered for a more accurate performance characteristics of the machine. Usually, the eddy-current loss in a linear PM machine is neglected, since high-order time harmonics in the stator current waveform and space harmonics in the winding distribution are generally considered to be negligible. Significant eddy-current loss in the armature will not only compromise the machine efficiency, but may also result in excessive

heating, which could lead to irreversible deterioration in the machine performance [70]. Magnetic flux in electrical machine cores is often nonsinusoidal, and leads to an overall iron loss figure different from the one expected under a sinusoidal regime. Especially significant is the presence of third harmonic component in the tooth region of stator cores in electrical machines [71]. Thus, correct prediction of power losses under a distorted flux waveform is therefore an important prerequisite to machine design, particularly when dealing with large apparatus where stringent efficiency standards are required [72].

Finally, it will be discussed about comparison result of the analytical calculations using equivalent magnetic circuit method and influence of the magnetic flux saturation in cylindrical topology by the concrete dimension.

## 10.2 Magnetic Saturation Effects

An important part of electrical machines is made of ferromagnetic materials. These materials consist of nonlinear magnetic characteristics. When the total magnetomotive force (which depends on the stator current) in the machine increases, saturation of the ferromagnetic parts appears. The result of the saturation effects is a variation of the stator inductances. These parameters are used in the mathematical model of the machine and particularly in the electromechanical force expressions. Consequently, the control of the machine is drastically affected in terms of precision and dynamics [73].

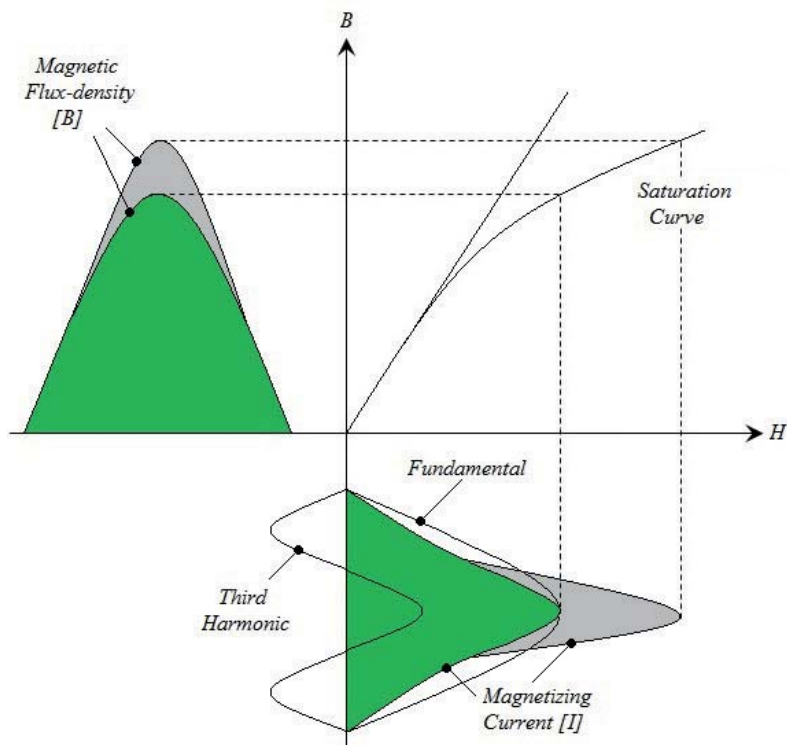


Figure 10.1 : Relationship between Magnetic Flux and Current [74]

Figure 10.1 illustrates B-H curve characteristic by magnetic core. When the amplitude of the voltage (or flux) is large enough to enter the nonlinear region of the B-H curve, the magnetizing current needed will be greatly distorted from sinusoidal. As the magnitude of the flux density increases, the core becomes more saturated, and the magnetizing current is greater.

Overexcitation is basically caused by overvoltage. As in figure 10.2, overvoltage drives the peak operation point of the generator excitation characteristics up to saturation region. The degree of the saturation depends on the generator design.

Saturation is most clearly seen in the magnetization curve (also called B-H curve or Hysteresis curve) of a substance. As the  $H$  field increase, the  $B$  field approaches a maximum value asymptotically, the saturation level for the substance.

The relation between the magnetizing field  $H$  and the magnetic field  $B$  can also be expressed as the magnetic permeability :  $\mu = B/H$  or the relative permeability  $\mu_r = \mu/\mu_0$ , where  $\mu_0$  is the vacuum permeability. The permeability of ferromagnetic materials is not constant, but depends on  $H$ . In saturable materials the relative permeability increases with  $H$  to a maximum, then as it approaches saturation inverts and decreases toward one.

Different materials have different saturation levels. For example, high permeability iron alloys used in electrical machines reach magnetic saturation at 1.6 ~ 2.2 [T], whereas ferrites saturate at 0.2 ~ 0.5 [T]. Some amorphous alloys saturate at 1.2 ~ 1.3 [T]. This study set a goal of approximately 1.6 ~ 1.7 [T] of the magnetic flux density in the iron core under a given input value.

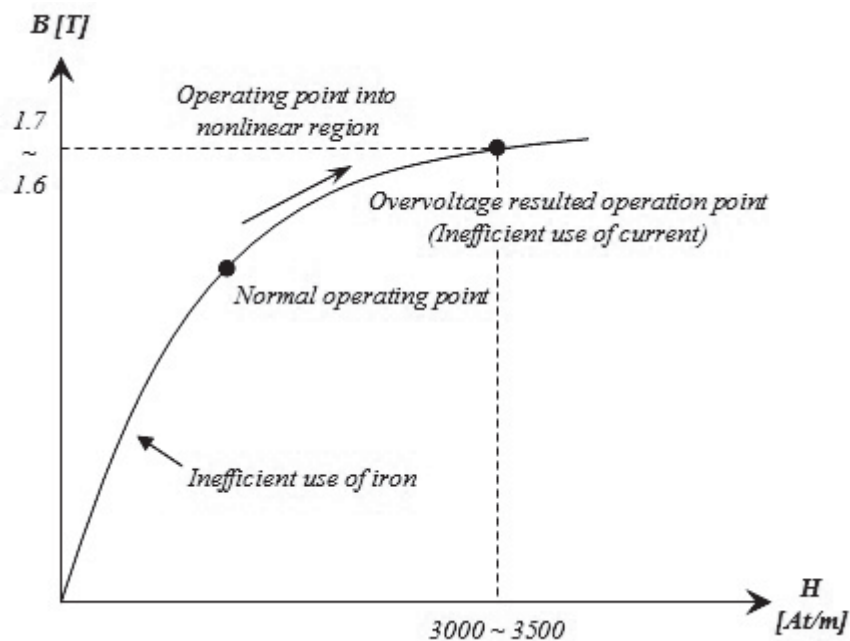


Figure 10.2 : B-H Curve [74]



### 10.3 Design considering Nonlinearity of Core

Among the various topologies proposed in the previous study, the single-phase cylindrical with back-iron in the mover was chosen as the optimum model. Now, it will be analyzed taking the nonlinearity of magnetic saturation in the iron core into account. The configuration shows the description for the analysis in the figure 10.3.

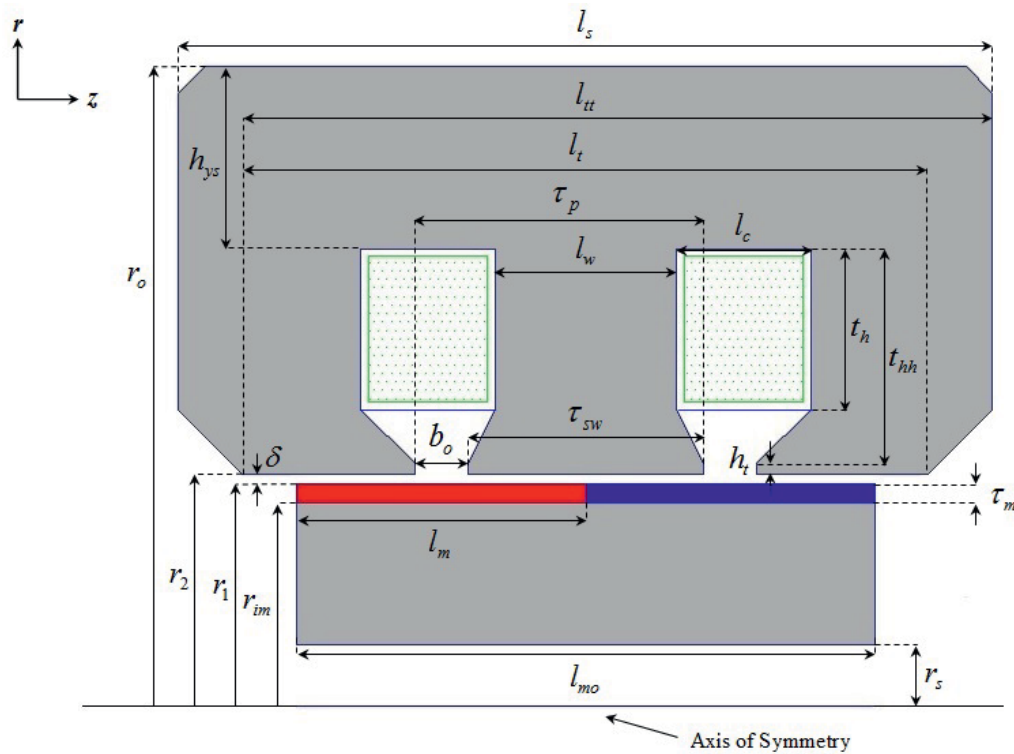


Figure 10.3 : Single-Phase Cylindrical Topology

#### 10.3.1 Calculation of Magnetic Field Distribution

In order to establish an analytical expression for the magnetic field distribution in the cylindrical machine, the following assumption is made : the relative permeability of stator iron is infinite, and the stator windings are replaced by an equivalent current sheet travelling in space and varying in time. This current sheet is located at the stator surface between the stator and the effective air-gap. The magnetic field analysis is confined to two region, the air / winding region in which the permeability is  $\mu_0$ , and the permanent magnet region in which the permeability is  $\mu_0 \mu_r$ . In the case of permanent magnet region, the analysis of magnetic field is achieved in *Paragraph 10.5.10*. To begin with, it requires consideration about the magnetic field distribution in air-gap region.

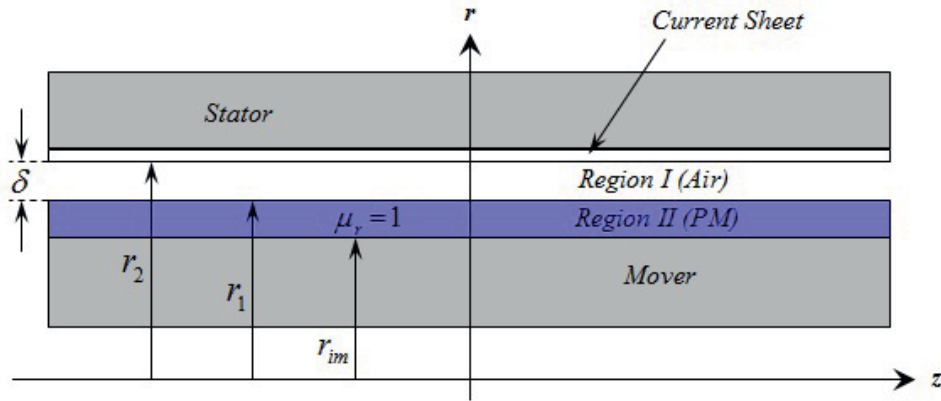


Figure 10.4 : Analytical Field Model

The partial differential equation for quasi-stationary magnetic fields in continuous and isotropic region can be expressed in terms of the magnetic vector potential  $A$ , subject to the *Coulomb gauge*,

$$\left. \begin{array}{l} B = \mu_0 H \\ \nabla^2 A_r = 0 \end{array} \right\} \quad \text{in the air / winding / iron-core} \quad (10.1)$$

The flux density components are deduced from  $A_\theta$  by

$$B_z = \frac{1}{r} \frac{\partial}{\partial r} (r A_\theta) \quad B_r = -\frac{\partial}{\partial z} (A_\theta) \quad (10.2)$$

Since the field is axially symmetric,  $A$  only has the component  $A_\theta$ , which is independent of  $\theta$ .

$$\frac{\partial}{\partial z} \left( \frac{1}{r} \frac{\partial}{\partial z} (r A_\theta) \right) + \frac{\partial}{\partial r} \left( \frac{1}{r} \frac{\partial}{\partial r} (r A_\theta) \right) = 0 \quad \text{in the air / winding / iron-core} \quad (10.3)$$

The boundary conditions to be satisfied by the solution to (10.3) are

$$B_{Iz} \Big|_{r=r_2} = 0 \quad B_{IIz} \Big|_{r=r_1} = 0 \quad (10.4)$$

The current distribution of a phase winding, as shown figure 10.5, may be expanded into a Fourier series,

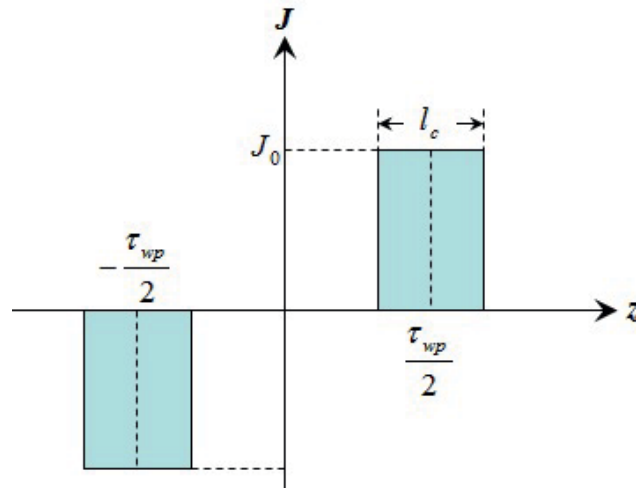


Figure 10.5 : Equivalent Current Sheet Distribution

The time-varying magnetic field distribution due to the current sheet distribution  $J(z)$  can be derived, which is expressed using *Fourier series* of the form.

$$\begin{aligned}
 J(z) &= \sum_{n=1,2,\dots}^{\infty} J_n \sin k_n z \\
 &= \sum_{n=1,2,\dots}^{\infty} \left[ \frac{4J_0}{\pi \cdot (2n-1)} \sin \frac{(2n-1) \cdot \tau_{wp}}{2 \cdot \tau_p} \sin \frac{(2n-1) \cdot l_c}{2 \cdot \tau_p} \right] k_n z
 \end{aligned} \tag{10.5}$$

where,  $k_n = (2n-1)\pi / \tau_p$  and  $\tau_{wp}$  indicates the winding pitch.

Solving equation (10.3) subject to the boundary conditions of (10.4) yields (10.6), for the component flux density distributions, where,  $BI_0(k_n r), BI_1(k_n r)$  are modified *Bessel* functions of the first kind, and  $BK_0(k_n r), BK_1(k_n r)$  are modified *Bessel* functions of the second kind, of order zero and one, respectively.

The resulting flux density for the region can be obtained by equation (10.3) for the definition of the magnetic vector potential.

$$\begin{aligned}
 B_{I_r}(r, z) &= - \sum_{n=1,2,\dots}^{\infty} [a_{I_n} BI_1(k_n r) + b_{I_n} BK_1(k_n r)] \cos(k_n z) \\
 B_{I_z}(r, z) &= \sum_{n=1,2,\dots}^{\infty} [a_{I_n} BI_0(k_n r) - b_{I_n} BK_0(k_n r)] \sin(k_n z)
 \end{aligned} \tag{10.6}$$

where, the analytical expression for  $a_n$  and  $b_n$  is appeared in [70].

Derivation of Partial Differential Equations in Each Region

It can be achieved by the derivation with *Maxwell's Equations* for quasi-static magnetic fields. The *Poisson's* equation in 2-D of the machine can be simplified depending on which excitation is present in each particular region.

Table 10.1 : Governing Partial Differential Equations [75]

Region	$\mu_r$	Equation
Stator-iron	$\infty$	$\nabla^2 \cdot A = 0$
Windings	1	$\nabla^2 \cdot A = -\mu_0 \times J$
Air-gap	1	$\nabla^2 \cdot A = 0$
Permanent Magnets	$\mu_r$	$\nabla^2 \cdot A = -\nabla \times B_r$
Back-iron in Mover	$\infty$	$\nabla^2 \cdot A = 0$

Through the figure 10.4, table 10.1 shows the governing equation for each region only with the excitation due to the stator current sheet. Eddy currents still exist in these permanent magnets due to their considerable conductivity. The equations for stator and air-gap are *Laplace* equations while for permanent magnets and mover back-iron are *Poisson's* equations [75].

**10.3.2 Flux Calculation**

Stator Region

First, the flux characteristics inside the stator are calculated in the stator region. They consist of the fluxes in the tooth-tip, tooth, and yoke, respectively ; it represents in order of mentioned as follows.

$$\phi_{tooth-tip} = \int_{\frac{b_o}{2}}^{\frac{b_o}{2} + \frac{\tau_{sw}}{2}} 2 \cdot \pi \cdot r_2 \cdot B_\delta dz \tag{10.7}$$

where,  $B_\delta$  is determined analytically using formula of  $B_{lr}(r, z)$ , and it is described in equation (10.6).

The resulting flux density in the tooth-tip region can be obtained from

$$B_{tooth-tip} = \frac{\phi_{tooth-tip}}{\pi \cdot \left\{ [r_2 + h_t + (t_{hh} - t_h)]^2 - r_2^2 \right\}} \quad (10.8)$$

Next, the flux passing through the tooth can be obtained from the following integration :

$$\phi_{tooth} = \int_{\frac{b_2}{2} - z_d}^{\frac{b_o}{2} + \tau_{sw} - z_d} 2 \cdot \pi \cdot r_2 \cdot B_\delta dz \quad (10.9)$$

where,  $z_d$  is the axial displacement of the moving PM armature. The flux is dominantly in radial direction. The average flux density in the tooth can be estimated by

$$B_{tooth} = \frac{\phi_{tooth}}{2 \cdot \pi \cdot \left[ r_2 + h_t + (t_{hh} - t_h) + \frac{t_h}{2} \right] l_w} \quad (10.10)$$

The flux passing through the yoke is same as in the tooth given in (10.9). However, the resulting flux density component in yoke region is essentially in the axial direction and can be evaluated analytically by

$$B_{yoke} = \frac{\phi_{tooth}}{\pi \cdot [r_o^2 - (r_o - h_{ys})^2]} \quad (10.11)$$

### Mover Region

As mentioned earlier, *Chapter 5 Cylindrical Topology*, the flux in the back-iron of mover tends to concentrate in the direction of shaft. As a result, it is important to not saturate the iron in that place. The flux density in the back-iron of mover is expressed as equation (10.12).

$$B_{bi-mover} = \frac{\int_{\frac{b_0}{2} - z_d}^{\frac{b_0}{2} + \tau_{sw} - z_d} 2 \cdot \pi \cdot r_s \cdot B_\delta dz}{2 \pi \cdot (r_{im}^2 - r_s^2)} \quad (10.12)$$

### 10.3.3 Resistance Calculation

A cylindrically wound coil resistance is obtainable using the number of turns and total length of a conductor. Naturally, the coil diameter is a prerequisite of the resistance calculation.

$$l_{coil} = 2 \cdot N_c \cdot \left[ 2 \cdot \left( r_o - h_{ys} - \frac{t_h}{2} \right) \cdot \pi \right] \quad (10.13)$$

$$R_{es} = l_{coil} \cdot k_{res} \quad (10.14)$$

where,  $N_c$  represents the number of turn, and  $k_{res}$  signifies the coil resistance per kilometer in chosen coil diameter.

### 10.3.4 Flux Linkage and Force Calculation

The flux linkage with the stator coil may be obtained by the following integration. The force generated by Lorentz Law is determined by quantity of the flux in the air-gap and number of turns and circuit in the coil.

$$\phi_\delta = \int_{-\tau_m}^{\tau_m} 2 \cdot \pi \cdot r_1 \cdot B_\delta dz \quad (10.15)$$

The force, resulting from the interaction between the winding current and the permanent magnet field, is given by

$$F_{orce} = \int_V (J_n \times B) dV = 2 \cdot \pi \cdot \Theta \cdot l_m \cdot \frac{\phi_\delta}{(r_1^2 - r_{im}^2) \cdot \pi} \quad (10.16)$$

where,  $J_n$  denotes the current density vector in the winding region, and is expressed in equation (10.48). Also,  $\Theta$  means the magnetomotive force.

### 10.3.5 Comparison of Force Characteristics between Analytical and Numerical Calculation

According to the above analyses, the force characteristics are classified as three kind of analytical and numerical calculation. There are two categories of the force tendency of an initial design process through equivalent magnetic circuit (EMC) and of a detailed design considering magnetic saturation in the analytical method. The numerical analysis is verified by FLUX software of CEDRAT based on the analytical calculations.

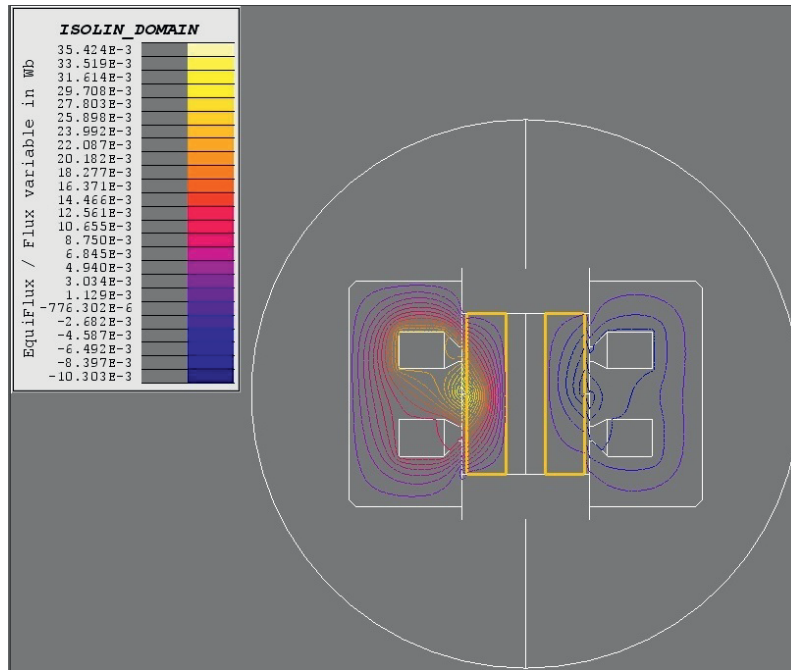


Figure 10.6 : Flux Characteristic of Optimal Model

Thus, the distribution of magnetic flux by the numerical calculation using FLUX is displayed in figure 10.6. The maximum flux density is approximately 1.8 [T] under a given input in the whole regions.

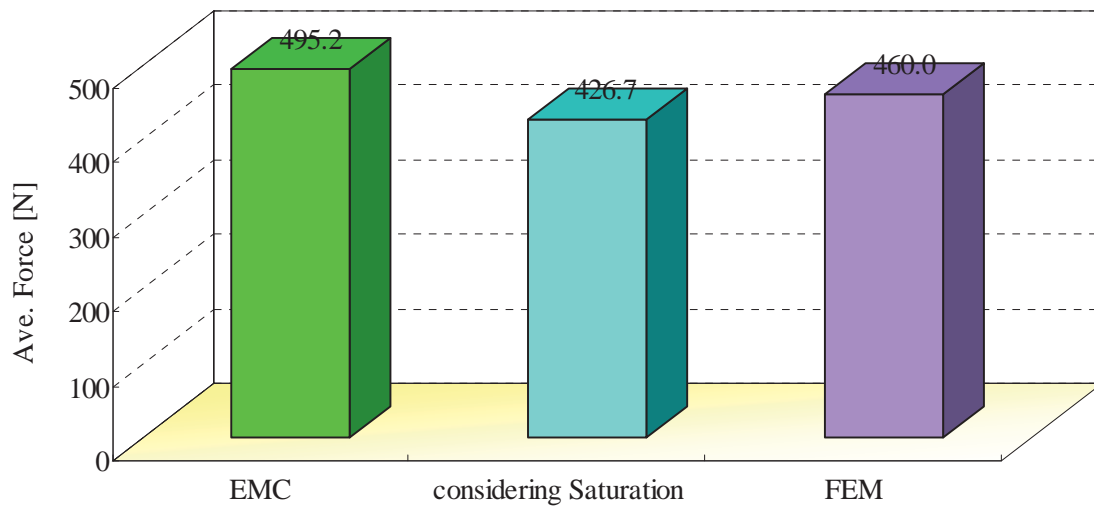


Figure 10.7 : Comparison of Average Force by Calculation Methods

Figure 10.7 indicates the variety of force characteristics by three kinds of analysis. There are small differences in the average force value between analytical calculation with considering saturation and FEM. It should be noted that the effect of the slot-openings may not be accounted for by slotting factor. Nevertheless, in terms of the average force, all of the preliminary design by EMC and the detailed design considering saturation is within less than 8 [%] compared to the FEM result.

## 10.4 Calculation of Machine Weight

A calculation of weight has a decisive effect on production and the material cost of the machine. This cylindrical type has the advantage of being lighter than the flat type. In particular, the light weight of mover can be obtainable for a higher force relatively and it enables to high speed operation. Furthermore, the calculated results of this generator weight are needed to determine not only the losses such as iron loss, copper loss, and eddy-current loss by permanent magnet, but also thermal coefficient in next *Chapter 12 Thermal Analysis*.

### 10.4.1 Stator Region

There are comprised of tooth-tip, tooth, and yoke in stator part. Above all, it will be calculated by dividing the kinds of above components respectively.

#### Tooth-Tip

$$A_{tooth-tip} = \left\{ [r_2 + h_t + (t_{hh} - t_h)]^2 - r_2^2 \right\} \cdot \pi \quad (10.17)$$

$$V_{tooth-tip} = A_{tooth-tip} \cdot l_{tt} \quad (10.18)$$

A volume is expressed as the product of the cross-sectional area ( $A_{tooth-tip}$ ) and axial length ( $l_{tt}$ ).

#### Tooth

$$A_{tooth} = [(r_0 - h_{ys})^2 - \{(r_0 - h_{ys} - t_h)\}^2] \cdot \pi \quad (10.19)$$

$$V_{tooth} = A_{tooth} \cdot l_t \quad (10.20)$$

Like the preceding equation (10.18),  $V_{tooth}$  indicates the volume in tooth.

#### Yoke

$$A_{yoke} = [r_0^2 - \{r_0 - (t_{hh} + h_t + r_2)\}^2] \cdot \pi \quad (10.21)$$



$$V_{yoke} = A_{yoke} \cdot l_s \quad (10.22)$$

### 10.4.2 Mover Region

The mover consists of the permanent magnet and back-iron core surrounding it. The volume of back-iron in the mover is only calculated here, and the calculation of permanent magnet is accomplished in the *Paragraph 10.4.4*.

$$A_{bi-mover} = (r_{im}^2 - r_s^2) \cdot \pi \quad (10.23)$$

$$V_{bi-mover} = A_{bi-mover} \cdot l_{mo} \quad (10.24)$$

### 10.4.3 Coil Region

The weight of total coil is multiply of the winding number and length of the one coil. A cross-section of coil can be expressed as the equation (10.25).

$$A_{coil} = \left( \frac{d_{coil}}{2} \right)^2 \cdot \pi \quad (10.25)$$

$$V_{coil} = A_{coil} \cdot l_{coil} \quad (10.26)$$

$$\gamma_{coil} = V_{coil} \cdot \rho_{coil} \quad (10.27)$$

where,  $d_{coil}$  represents the diameter of coil, and  $l_{coil}$  comes from the equation (10.13).

The density of copper ( $\rho_{coil}$ ) is approximately 8960 [ $kg/m^3$ ]. Using the value, it can measure the weight ( $\gamma_{coil}$ ) of copper region by its dimension.

### 10.4.4 PM Region

The equation (10.28) indicates the volume of permanent magnet.

$$V_{pm} = (r_1^2 - r_{im}^2) \cdot l_{mo} \cdot \pi \quad (10.28)$$

$$\gamma_{pm} = V_{pm} \cdot \rho_{pm} \quad (10.29)$$

The total weight ( $\gamma_{pm}$ ) of the permanent magnet is calculated by multiplying the density ( $\rho_{pm}$ ) of NdFeB magnet of 7400 [ $kg/m^3$ ] and the volume measured as above equation (10.28).

#### 10.4.5 Summary

Through the above equations, the volumes of each region such as iron core, coil, and permanent magnet are provided. All materials have their unique physical, mechanical, and electrical properties. For example, SMC materials are isotropic 3-D core materials with a maximum relative permeability in the range 100 ~ 700, which means that the material is 100 ~ 700 times better at conducting magnetic flux than air. The isotropic 3-D resistivity lies in the range 20 ~ 10000 [ $\mu\Omega m$ ], which is considerably higher than laminated sheet metal, which is around 0.2 [ $\mu\Omega m$ ]. SMC components therefore do not need to be laminated to minimize eddy current loss [76].

The weight of generator can be classified separately according to the stator and mover. Particularly, the weight information of the mover helps to evaluate its speed. In addition, the weight of each material can be measured for the cost of materials. This is given in the equation (10.30).

$$V_{stator} = [(V_{tooth-tip} + V_{tooth} + V_{yoke}) + V_{coil}]$$

$$V_{mover} = V_{bi-mover} + V_{pm} \quad (10.30)$$

$$V_{iron-core} = (V_{tooth-tip} + V_{tooth} + V_{yoke}) + V_{bi-mover}$$

$$\gamma_{iron-core} = V_{iron-core} \cdot \rho_{iron-core} \quad (10.31)$$

In the above volume equations (10.31), the specific weight is calculated by multiplying the density of each material. The  $\rho_{iron-core}$  indicates the density of iron core material.

### 10.5 Calculation of Losses

As investigated in the previous chapters, a permanent magnet generator of cylindrical linear type with back-iron in the mover can be used especially in hybrid vehicles to power traction drives due to its high force density, wide speed range, and high efficiency. In particular, the back-iron core in this mover structure has a double face ; one is the advantage that its establishment causes an efficient flux path, the other is that it leads to the increasing of the material cost due to adding of the

iron core volume.

Therefore, this paragraph will investigate the various losses for the sake of the accurate performance evaluation of the machine ; copper loss, eddy-current loss of the permanent magnet and iron loss consisting of hysteresis, eddy current, and excess loss.

First of all, the calculation of the iron loss with the help of the *Steinmetz* equation is still used at high frequencies up to 1000 [Hz] in the field of automotive applications, but it is no longer accurate enough. Thus, the theory of *Bertotti* is recommended as a newer approach, in which the iron losses are composed of the three components : hysteresis, eddy-current and excess loss. Here, the excess loss describes that the loss incurred in the magnetizable domains of the material with the migration of block wall and it is still based on empirical factors from curve fitting [77].

The total iron loss  $P_{iron}$ , i.e., the loss which is absorbed by a unit mass, is commonly separated into three contributions.

$$P_{iron} = P_{hyst} + P_{ed} + P_{excess} \quad (10.32)$$

The individual parameter of the loss equations must be adjusted to measured data by *Epstein* or *Single Sheet Tester*. There are proposals to describe these losses with empirical equations with up to 8 parameters in relation to the iron loss. In order to build more favorable and accurate assessment, the total iron loss will be achieved based on a physical approach using the material data and the sheet thickness [78]. The material information can be obtained by the manual of relevant manufacturer.

### 10.5.1 Hysteresis Loss

The specific hysteresis loss can be described by the following equation according to [78].

$$P_{hyst} = k \frac{4H_c}{\rho} B_{max} \cdot f \quad (10.33)$$

The hysteresis loss  $P_{hyst}$  corresponds to the area of the static hysteresis loop multiplied by frequency  $f$ . For a rectangular shaped hysteresis loop with the coercivity  $H_c$  and maximum induction level  $B_{max}$  an approximation can be given by equation (10.33). The  $\rho$  is the material density and  $k$  is a dimensionless constant, which is close to 1 for a rectangular shape hysteresis loop.

Compared with the measurement in Epstein, the hysteresis loss deteriorates considerably through the manufacturing process. The main factors here are caused by not only the structural changes at

the plate contour from the stamping process or laser cutting, but also mechanical stresses in the packaging or the mounting of the stator core.

By a magnetic annealing after punching, the punching-related micro structural changes can be eliminated. Also, an insulating oxide layer or a phosphating is applied to the metal sheet by annealing process (*Ludwig* process). In this case, the advantage is also the extensive removal of burrs that affect the eddy-current loss unfavorable. The hysteresis loss is increased by the additional processing allowance  $k_{bh}$  considering the influences of the manufacturing technology. For stamped and not finally annealed metal sheets usually  $k_{bh} = 1.5$  is used.

### 10.5.2 Eddy Current Loss

The eddy-current loss which arises by the swirling in the sheet edges is predictable by the conductivity  $\sigma$  and thickness  $d$  with a simple approach from the classical Maxwell Equations.

$$P_{ed} = \frac{\pi^2 \sigma \cdot d^2}{6 \rho} B_{\max}^2 \cdot f^2 \quad (10.34)$$

In most cases, the approach does not take displacement current into account because the sheet thickness is so small that the effect is negligible. By the quadratic influence of sheet thickness and the frequency, thin sheets should be used preferably at high supply frequency. For higher frequency eddy-current losses grow to the main contribution to total loss. For a strip material of 0.1 [mm] thickness this is the case at a few kHz and for 0.35 [mm] thickness at a few hundred Hz. A retroactive effect of the eddy currents also arise at high frequency on the magnetic field, as a result it gives rise to a change of the magnetization curve.

This is especially related to currents containing harmonic components as a result of converter supply, where higher frequency harmonics by ampere turns result in significantly smaller induction amplitudes, therefore it leads to smaller loss (decreasing by  $B^2$ ). It can be shown that no difference in the eddy-current loss as a function of, e.g., the clock frequency of the inverter occurs for a frequency-independent magnetization curve.

The influence of manufacturing technology must be taken into account by an additional processing allowance  $k_{bh}$  again. It results from cutting-air of punch and also by tool wear, mostly the stamping burrs. Particularly, thin sheets ( $d \leq 0.1$ [mm]) are critical, in which laser- or water jet cutting is preferred.

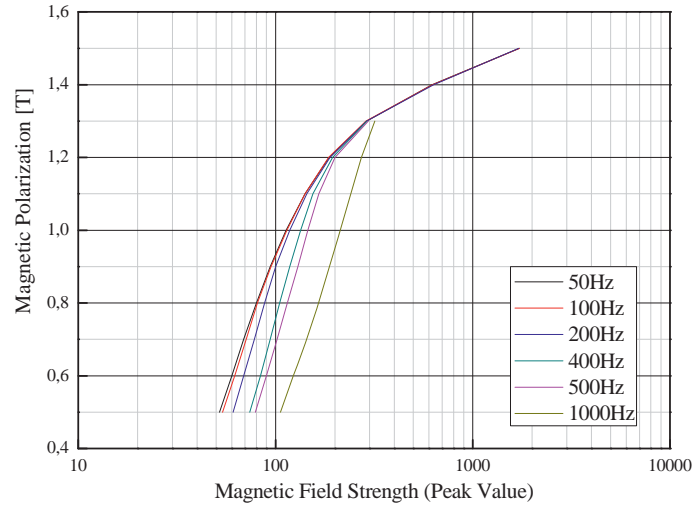


Figure 10.8 : Influence of the Frequency of the Magnetization Curve [79],  
(Quote : Material Specification M250-35, ThyssenKrupp)

Also the burr-free sheets with laser method can be produced in proper process control when the laser cutting is still more expensive than the punching. The ridges at the punched sheet metal may be removed after the packaging by etching of the air-gap surfaces with 30 [%] phosphoric acid. However, this process step is to be integrated poorly in a series production

In a few cases, the wire cutting process is used. For this purpose, the circular blanks are only adhesively bonded to a package (baked varnish technology) and then eroded out the slot and air-gap contour. The conclusions between the individual sheets can be largely prevented through a careful process control. The pollution of the dielectric (pure water) by the burn-up of the baking lacquer layers must be removed by continuous changes of water. Typical values for the eddy-current additional processing allowance is in punched sheets with  $k_{bh} = 1.5 \sim 2.5$ .

### 10.5.3 Excess Loss

This loss was described by Bertotti for the first time and can be attributed to the magnetic domain structure of the material with sliding *Bloch* walls. During magnetization the Bloch walls can not be moved unresistingly, so that an additional energy demand arises. This loss strongly depends on the microscopic structure and the distribution of magnetizable domains in material, is also more statistical nature and only occurs at frequencies above 300 ~ 400 [Hz] significantly.

$$P_{exc} = \frac{C}{\rho} B_{max}^{1.5} \cdot f^{1.5} \quad (10.35)$$

The factor  $C$  is the second adjustable factor in measurements and in principle inversely proportional to the number of available magnetizable domains in the considered cross-section.

Since the inner structure of material is fixed after the rolling process, it can be assumed that a manufacturing process influence is generally negligible. Unless that the inner crystalline structure of the material is changed dramatically, e.g., by bending or other deformations of the sheets.

#### 10.5.4 Total Losses

The three loss components can be summarized as follows equation (10.36) :

$$P_{fe} = \frac{1}{\rho} \left( 4k H_c B_{\max} f \cdot k_{bh} + \frac{\pi^2 \sigma \cdot d^2}{6} B_{\max}^2 f^2 \cdot k_{bw} + C B_{\max}^{1.5} f^{1.5} \right) \quad (10.36)$$

A fit can be easily achieved again by adjusting  $k$  and  $C$  with the measured values of material data sheets.

#### 10.5.5 Comparison of the Loss Calculation using Example M250-35

According to the material data sheet of *ThyssenKrupp*, this material has the following parameters :

Table 10.2 : Material Data Sheet of M250-35 [79]

Sheet Thickness, $d$	0.35 [mm]
Relative Permeability at 1 [T], 50 [Hz]	7018
Density, $\rho$	7600 [ $kg/m^3$ ]
Conductivity, $\sigma$	$1.67 \times 10^6$ [ $1/\Omega m$ ]
Coercive Force, $H_c$	30 [ $A/m$ ]

The factors  $k$  and  $C$  were adjusted for the frequency range 50~1000 [Hz] with  $k=1$  and  $C=3.1$  on the loss table for  $B_{\max} = 1$  [T]. The comparison of the curve fitting with the measured losses is shown in figure 10.9.

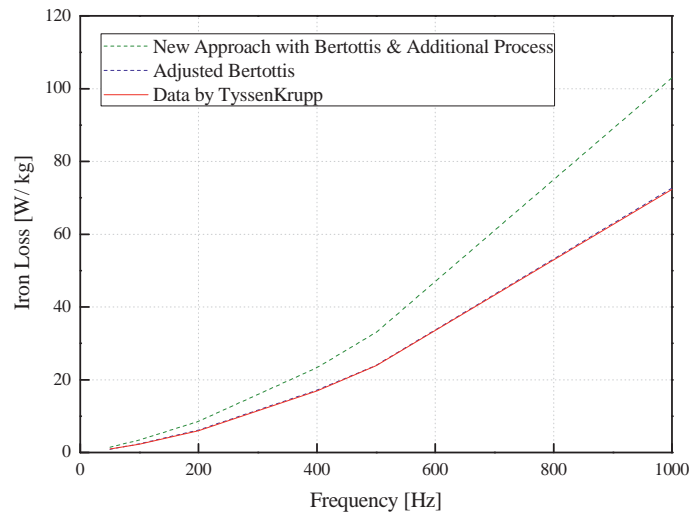
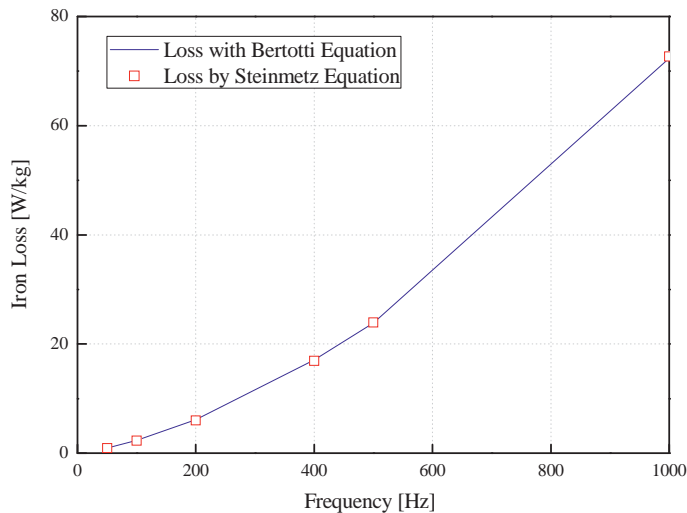


Figure 10.9 : Parameter Adjustment of the Loss Equations to the Measured Data,  $k = 1$ ,  $C = 3.1$   
 (Additionally, the influence of technology factors is entered with  $k_{bh} = k_{bw} = 1.5$ )

The fit according to equation (10.35) is almost perfect, the error is negligible. Figure 10.10 shows the comparison of the new equation and the Steinmetz equation for the frequency range up to 1000 [Hz].



Frequency	Bertotti	Steinmetz
[Hz]	[W/kg]	
50	0.95	0.915
100	2.36	2.29
200	6.159	5.99
400	17.12	16.91
500	23.87	23.949
1000	72.36	72.672

Figure 10.10 : Comparison of Losses by Steinmetz and Bertotti

It is clear that the loss by Steinmetz are calculated somewhat lower up to 400 [Hz], also provides the Steinmetz equation too pessimistic values. A description of the eddy-current loss with a purely quadratic function approach is not satisfied any more in this frequency range. Where the curves intersect, the choice of interpolation points for the Steinmetz equation is achieved (here 50 [Hz] and

500 [Hz]). As shown in figure 10.8, the new equation is much more accurate in the entire frequency range.

### 10.5.6 Loss Analysis for using Example M400-50

The method presented here will be applied to other types of electrical steel.

#### Iron Losses for the Sheet Grade M400-50

Here, a good fit is also achieved to the loss data of the material data sheet.

The other sheet data is reported according to Table 10.2.

Table 10.3 : Material Data Sheet of M400-50 [80]

Sheet Thickness, $d$	0.5 [mm]
Relative Permeability at 1 [T], 50 [Hz]	5927
Density, $\rho$	7700 [ $kg/m^3$ ]
Conductivity, $\sigma$	$2 \times 10^6$ [ $1/\Omega m$ ]
Coercive Force, $H_c$	50 [ $A/m$ ]

Figure 10.11 shows the loss at  $B_{max} = 1$  [T] with the parameters  $k=1$ ,  $C=1$ .

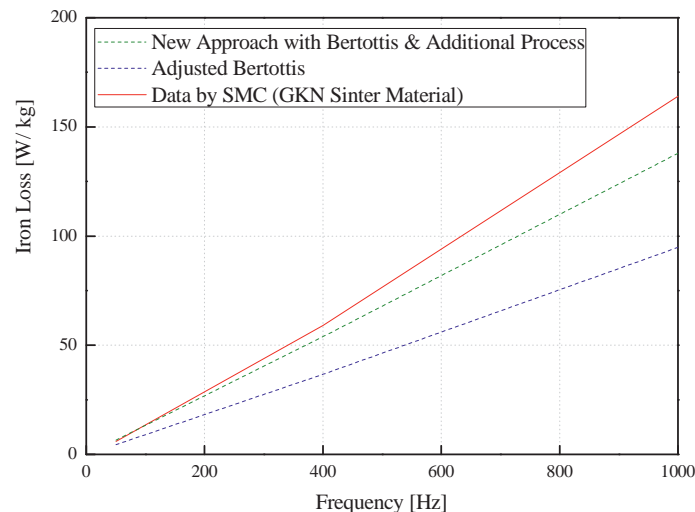


Figure 10.11 : Loss Adjustment for M400-50 Measured at the Sampling Points,

$$k=1, C=1, B_{max} = 1 \text{ [T]}$$

Green Dash Line : Technology Factors with  $k_{bh} = k_{bw} = 1.5$

The maximum error occurs approximately 2.3 [%] at 1000 [Hz]. The error results in somewhat higher loss than measured value. It is negligible in most of the applications if the technology factors  $k_{bh}$  and  $k_{bw}$  is mathematically taken into account. The reason should be sought in the eddy-current term, since *skin effect* is already expected at these thicknesses below 1000 [Hz].

### 10.5.7 Calculation of Iron Loss Improvement of the Approach for Eddy Current Loss

As described in the paragraph 10.5.2 previously, the equation (10.36) based on Bertotti Theory can be trusted with respect to the eddy-current loss of a linear current density distribution over the cross section of sheet metal. This approach is largely justified with relatively thin iron-silicon sheets up to 0.5 [mm] and frequencies up to 500 [Hz]. At higher conductivity of the material and higher frequencies, this eddy-current term is too inaccurate. Then the skin effect, i.e., non-linear current density distribution can be taken into account over the cross-section of the sheet.

#### Theoretical Principle

The eddy-current loss that occurred in the plate edges by the eddy current is no longer simple relationship as shown in the equation (10.34) [78].

$$F(x) = \frac{3}{x} \cdot \frac{\sin h(x) - \sin(x)}{\cosh(x) - \cos(x)} \tag{10.37}$$

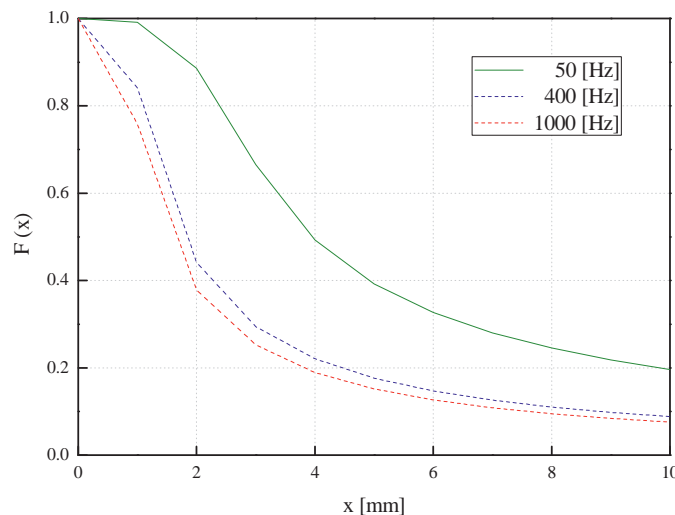


Figure 10.12 : The Calculation of the Eddy Current Loss, M400-50A

$$x = \beta \cdot d \tag{10.38}$$

$$\beta = \sqrt{\pi \cdot f \cdot \sigma \cdot \mu} \tag{10.39}$$

With retroactive effect of the current on the exciting field, the calculation is performed ; for example, it is analogous to the calculation of the unilateral skin effect under solution of the Maxwell Equations for the magnetomotive force, the induction and *Ohm's Law*. This is described in detail in [81]. The function occurring here is shown in figure 10.12.

The effective value of the current density results in

$$|J| = J = \beta \cdot \sqrt{2} H_0 \frac{\sqrt{\cosh 2\beta \cdot y - \cos 2\beta \cdot y}}{\sqrt{\cosh \beta \cdot d + \cos \beta \cdot d}} \tag{10.40}$$

where,  $y$  represents the coordinate iron sheet thickness.

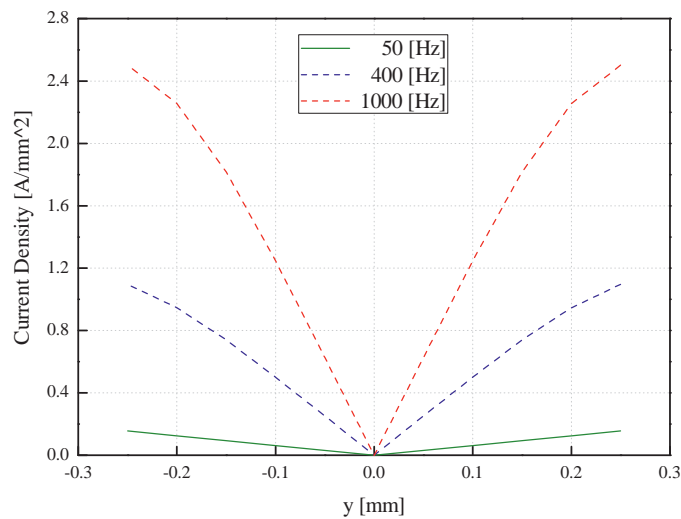


Figure 10.13 : Current Density  $J(y)$  by the Plate Thickness, M400-50A

It should be noted that the permeability depends on the flux density and is also frequency-dependent. In most case, this is listed on the material data sheets. The frequency dependence of the induction distribution and the current density distribution over the plate thickness is shown on the example of the material *M400-50* in figure 10.12 and figure 10.13 on a flux density amplitude of 1 [T]. It can be seen that as the frequency increases, the distribution of  $B$  is always uneven while the amplitude of the eddy-current density  $J$  increases toward the edge, but it still remains largely linear over the sheet thickness in the frequency range.

Generally, it is used from 0.1 to 0.2 [mm] of the iron sheet thickness over 1000 [Hz] of frequency.

Further obtained from [81] for the eddy-current loss in the volume  $V$  of the sheet.

$$P_{ed} = V \frac{1}{\sigma \cdot d} \int_{-\frac{d}{2}}^{+\frac{d}{2}} J^2 dy = V \frac{1}{6} \sigma \pi^2 f^2 d^2 B_{\max}^2 \frac{3}{x} \cdot \frac{\sin h(x) - \sin(x)}{\cos h(x) - \cos(x)} \quad (10.41)$$

That is, the loss of equation (10.34) is supplemented by the additional term with the hyperbolic and the  $x$ , which corresponds to the unilateral skin effect of the reduced conductor height.

Since the fraction term in equation (10.41) goes to  $3/x$  at high frequencies, the loss increases proportionally at constant flux density to  $d \cdot f^{1.5}$  and no longer square. Division of equation (10.41) by the mass  $M = V \cdot \rho$  provides the specific eddy-current loss.

$$P_{ed} = \frac{\pi^2 \sigma \cdot d^2}{6 \rho} B_{\max}^2 f^2 \frac{3}{x} \frac{\sin h(x) - \sin(x)}{\cos h(x) - \cos(x)} \quad (10.42)$$

The necessary permeability for the evaluation of this equation must be taken from the material sheet in accordance with the flux density  $B_{\max}$  and the frequency. Namely if this extended equation is to be used, the design calculation of the magnetization curve must be known for determination of  $\mu_r$  for the respective frequency. This can be done by interpolation of the given  $\mu_r$  values. For a given induction, a plot  $\mu_r(f)$  through logarithmic function of the type

$$\mu_r(f) = a \cdot \ln(f) - b \cdot f^{\frac{1}{2}} + c \quad (10.43)$$

with the constants  $a, b, c$  good approach (figure 10.14), which facilitates the analytical calculation a little.

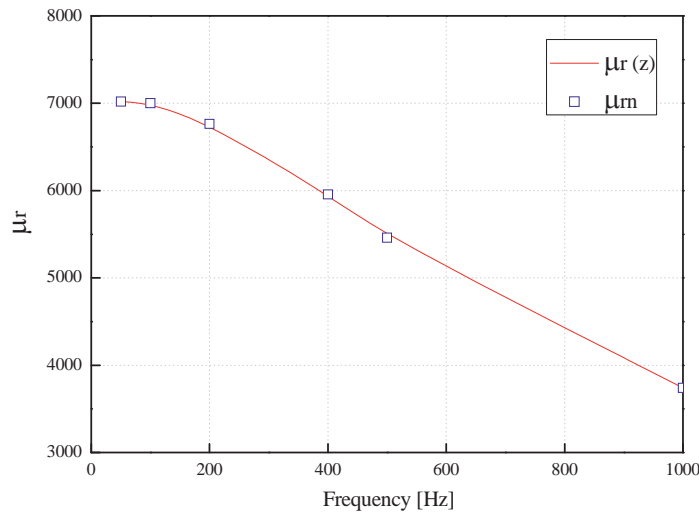


Figure 10.14 : Adaptation of the Logarithmic Approximation  $\mu_r(z)$ , Equation (10.31) to the Measured Values for  $\mu_m(f \cdot 2n)$  (M250-35A,  $B_{\max} = 1$  [T],  $50$  [Hz]  $\leq f \leq 1000$  [Hz])

Then, the total loss of equation (10.36) result in

$$P_{fe} = \frac{1}{\rho} \left( 4k H_c B_{\max} f \cdot k_{bh} + \frac{\pi^2 \sigma \cdot d^2}{6} B_{\max}^2 f^2 \cdot \frac{3 \sin h(x) - \sin(x)}{x \cos h(x) - \cos(x)} k_{bw} + C B_{\max}^{1.5} f^{1.5} \right) \quad (10.44)$$

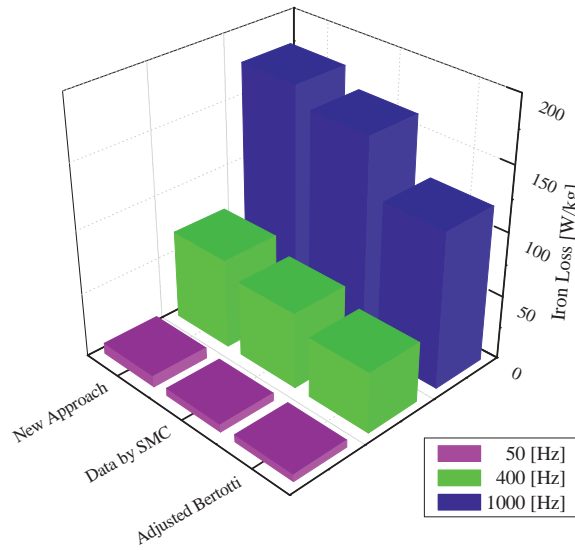
A fit can easily achieve again by adjusting  $k$  and  $C$  with the measured values of material data sheets. Carrying the frequency-dependent permeability, however, makes sense only if corresponding data is available or can be measured.

### 10.5.8 Comparison of the Iron Loss using Example Soft Magnetic Composites

The adjustment to the support points of the measured loss values on the material sheet [82] made for 0.5 [mm] sheet thickness. For SMC frequency-dependent permeability values are not available for the time. Therefore it could be used here only the static permeability, whereby the curve fitting has a provisional nature.

Table 10.4 : Material Data Sheet of PM4EM11 in GKN Sinter Metals [82]

Sheet Thickness, $d$	0.5 [mm]
Density, $\rho$	7500 [ $kg / m^3$ ]
Static rel. Permeability at 1 [T]	472
Conductivity, $\sigma$	$3.571 \times 10^{-9}$ [ $1 / \Omega m$ ]
Coercive Force, $H_c$	249 [ $A / m$ ]



Frequency [Hz]	$B_{max} = 1$ [T]		
	50	400	1000
Data by SMC (PM4EM11 GKN Sinter Metals)	6.0	59.0	164.0
Adjusted Bertottis	5.74	47.29	121.31
New Approach with Bertottis & Additional Process	8.56	69.86	177.75

Figure 10.15 : Parameter Fit for GKN Sinter Metals,  $k=0.85$ ,  $C=2$ ,  $k_{bh}=k_{bw}=1.5$ ,  
 Max. Error in 50 [Hz] = 0.67 [%], 400 [Hz] = 1.48 [%], and 1000 [Hz] = 1.46 [%]

The absence of frequency-dependent permeability are obtained for  $k$  and  $C$  in both cases physically unrealistic values, although the fitting must be regarded as good and easier to perform than without taking into account the current displacement.

### 10.5.9 Copper Loss

A single-phase cylindrical permanent magnet generator employs a 3-pole magnetized armature, having radially magnetized ring permanent magnets, and a SMC stator which carries a single-phase coil. Such a coil is easy to manufacture and results in a very high packing factor, which is

conductive to high efficiency. The magnetized armature generates a magnetic field which is linked with the single-phase coil. The force is produced as the result of the interaction between the permanent magnetic field and the stator current when it is synchronized with the armature movement. This windings bring several benefits : volume of copper used in the end-windings is reduced which effectively reduces the axial length (no overlapping windings). Lower amount of copper also helps in reducing *Joule Losses* and improving efficiency. In other words, copper loss results from *Joule Heating* and is also referred to as equation (10.45) in reference to *Joule's First Law*.

$$P_{coil} = k_f \cdot i^2 \cdot R_{es} \text{ [W]} \quad (10.45)$$

Copper loss is the term often given to heat produced by electrical currents in the conductors of machine windings. This is an undesirable transfer of energy, which results from induced currents in adjacent components.

where,  $k_f$  is the fill-factor, and can be expressed as  $\frac{A_{coil} \cdot N_c}{\pi \cdot [(r_0 - h_{ys}) - (r_0 - h_{ys} - t_h)] \cdot l_c}$ .

### 10.5.10 Eddy Current Loss in Permanent Magnets

#### Introduction

One of the major problems of PM machines that employ sintered permanent magnets is thermal demagnetization, which is mainly caused by the eddy-current loss of the permanent magnets. This loss results from the time and space harmonics in the air-gap magnetic field produced by slotting effects, as well as the non-sinusoidal stator MMF and phase current waveforms. Especially for NdFeB permanent magnets that have relatively high temperature coefficients of remanent and coercivity and moderately high electrical conductivity. However, the permanent magnet loss is usually neglected for the PM machines due to their very high resistivity. Moreover the eddy-current loss is generally small in comparison with the copper losses and the iron ones. Accordingly, the permanent magnets are often segmented into several pieces to prevent the eddy currents. This paragraph presents a calculation of the eddy-current losses in the permanent magnets using the mathematical equations.

#### Representation of Stator Winding in Air-Gap Field

The influence of armature reaction is relative to the mover. As a result, the analytical equations should be transformed to the translational mover coordinate system. Then the eddy-current density in permanent magnets can be described as follows.

The armature reaction field equations, in terms of  $A_\theta$ , are therefore given by equation (10.46).

$$\begin{aligned} \frac{\partial}{\partial z} \left( \frac{1}{r} \frac{\partial}{\partial z} (r A_{I\theta}) \right) + \frac{\partial}{\partial r} \left( \frac{1}{r} \frac{\partial}{\partial r} (r A_{I\theta}) \right) &= -\mu_0 \sum_{n=1}^{\infty} J_n \sin(n)z && \text{in the winding} \\ \frac{\partial}{\partial z} \left( \frac{1}{r} \frac{\partial}{\partial z} (r A_{II\theta}) \right) + \frac{\partial}{\partial r} \left( \frac{1}{r} \frac{\partial}{\partial r} (r A_{II\theta}) \right) &= 0 && \text{in the air / permanent magnets} \end{aligned} \quad (10.46)$$

Solving equation (10.46) by satisfying the boundary conditions of equation (10.4) and assuming  $\mu_r = 1$ .

According to the model of linear cylindrical machine, the equivalent structure can be shown in figure 10.4. For calculating eddy current loss in permanent magnet, the stator is represented by an equivalent current sheet and the magnetization of the permanent magnet is replaced by an equivalent current density.

The stator current sheet is given by a symmetrical sinusoidal single-phase system :

$$i = \sqrt{2} I_{rms} \cos(\omega t - \theta) \quad (10.47)$$

For the following step it is appropriate to represent the current sheet by Fourier series. The current density  $J_s(z)$  is characterized only by the function representing the azimuthal component  $J_\theta(z)$  of the axial coordinate, which can be expressed using Fourier series expansion as [83].

$$J_s(z) = \sum_{n=1}^{\infty} \sum_{k=1}^{\infty} J_n I_k = \sum_n \sum_k \hat{J}_{s(n,k)} e^{j(n\omega t - kz)} \quad (10.48)$$

where,  $I_k$  and  $k$  are the  $n^{th}$ -order stator harmonic current and the order number of the time harmonic, respectively. Moreover,  $J_n$  is the  $n^{th}$ -order Fourier coefficient.  $J_n$  is given by

$$J_n = -\frac{4 N_c}{n \pi \tau_p} \sin\left(\frac{n \pi}{2}\right) \quad (10.49)$$

where,  $n$  is the  $n^{th}$ -order number of the space harmonic.

### Representation of Permanent Magnets in No-load Magnetic Field

To take the no-load field into account, the permanent magnets are replaced by an equivalent current

density. As with the *Paragraph 10.3.1*, the magnetic field distribution in permanent magnet region is as follows.

$$B = \mu_0 \mu_r H + \mu_0 M \quad \text{in the permanent magnets} \quad (10.50)$$

where,  $M$  is the remanent magnetization, and is related to remanence  $B_{rem}$  by  $M = B_{rem} / \mu_0$ . The governing field equations is

$$\nabla^2 A_{II} = -\mu_0 \nabla \times M \quad \text{in the permanent magnets} \quad (10.51)$$

In cylindrical coordinate system, the magnetization  $M$  is given by

$$M = M_r e_r + M_z e_z \quad (10.52)$$

where  $M_r$  and  $M_z$  denote the components of  $M$  in the  $r$  and  $z$  directions, respectively.

This model shows radially magnetized machine topology, in which  $M_z = 0$  and  $M_r$  have the distribution which may be expanded into a Fourier series of the form

$$M_r = \sum_{n=1,2,\dots}^{\infty} 4 \left( \frac{B_{rem}}{\mu_0} \right) \frac{\sin k_n \cdot (\pi/2) \alpha_p}{k_n \pi} \cos k_n z \quad (10.53)$$

where,  $\alpha_p$  is the ratio of magnet pole-length  $l_m$  to pole-pitch  $\tau_p$ .

In common with the case of air-gap region,  $A$  only has the component  $A_\theta$  in the permanent magnet region because the field is axially symmetric and is independent of  $\theta$ .

$$\frac{\partial}{\partial z} \left( \frac{1}{r} \frac{\partial}{\partial z} (r A_{II\theta}) \right) + \frac{\partial}{\partial r} \left( \frac{1}{r} \frac{\partial}{\partial r} (r A_{II\theta}) \right) = -\mu_0 \nabla \times M = \sum_{n=1,2,\dots}^{\infty} \frac{4}{\tau_p} B_{rem} \sin(n) \frac{\pi l_m}{2 \tau_p} \quad (10.54)$$

The boundary conditions are applied equally as equation (10.4).

The resulting flux density for the permanent magnet region can be obtained by equation (10.54) for the definition of the magnetic vector potential.

The electric field strength can be replaced by the product of the current density and the resistivity of the permanent magnet  $E = \rho_m \cdot J$ . Thereby, the current density can be written as

$$J_m(z) = \frac{z}{\rho_m} \frac{dB}{dt} \quad (10.55)$$

where,  $\rho_m$  is the electric resistivity of permanent magnet.

### The Calculation of Eddy Current Loss in Permanent Magnets

The induced eddy currents in the permanent magnets are not resistance limited due to the skin effect of the permanent magnets when the generator operating at high speed [84]. The skin depth of the permanent magnets can be calculated from (10.56).

$$\delta_{sd} = \sqrt{\frac{\rho_{pm}}{\pi f \mu_0}} \quad (10.56)$$

Consequently, it is evident that the skin depth, at the inducing frequencies of interest, is greater than both the axial length and the radial thickness of the permanent magnets [85]. Thus, the induced eddy-current density in the permanent magnets can be obtained from the following :

$$J_e(r, z, t) = -\sigma_{pm} \frac{\partial A_\theta(r, z, t)}{\partial t} + C(t) \quad (10.57)$$

$C(t)$  is a function of time which is introduced to ensure that the zero net total current flows in each permanent magnet at any instant, i.e.,

$$\int_{r_{im}}^{r_1} \int_{z_0 - \frac{l_m}{2}}^{z_0 + \frac{l_m}{2}} J_e \cdot dz \cdot dr = \int_{r_{im}}^{r_1} \int_{z_0 - \frac{l_m}{2}}^{z_0 + \frac{l_m}{2}} \left[ -\sigma_m \frac{\partial A(r, z, t)}{\partial t} + C(t) \right] \cdot dz \cdot dr = 0 \quad (10.58)$$

The calculation of eddy-current loss is simplified considerably by using *Poynting's Vector*, which is a powerful means of obtaining the total power [86]. The Poynting's Vector is defined in terms of the vector product of the electrical intensity and the magnetic field intensity over the surface of a region. When the problem of magnetic field is expanded in two dimensions, the eddy current loss is calculated with

$$P_{pm} = \iint_S \frac{J_e^2(r, z)}{\sigma_m} dA = \frac{1}{\sigma_m} \frac{\omega}{2\pi} \int_{r_{im}}^{r_1} \int_{z_0 - \frac{l_m}{2}}^{z_0 + \frac{l_m}{2}} \int_0^{2\pi} 2\pi r \cdot J_e^2(r, z, t) dt \cdot dz \cdot dr \quad (10.59)$$

The following is assumption for this calculating eddy-current loss of permanent magnet in specified above [84].

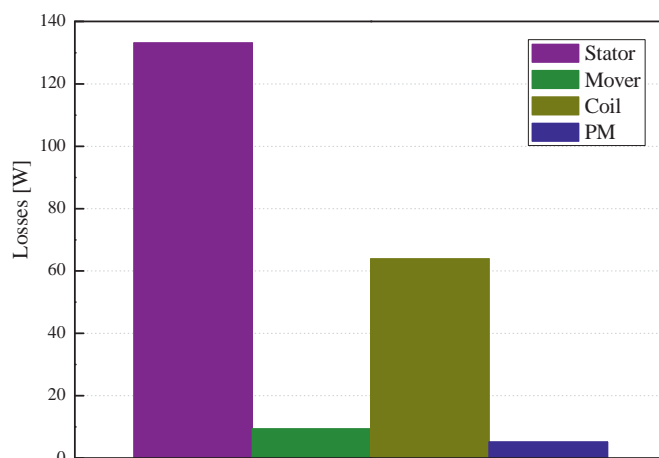
- The axial length of the machine is infinite so that the field distribution is axially-symmetric and periodic in the  $z$  direction
- The stator winding is represented by an equivalent ampere conductor distribution
- The relative permeability of the radial array permanent magnet and mover core are unity and a constant, respectively

### Summary

Different analytical approaches are developed and proposed for calculating both the stator field and slotting based losses. An axial and a circumferential segmentation (electrical insulation) of the permanent magnets are taken into account. The segmentation of the permanent magnets is a typical counteraction to reduce the losses [87]. At last, the eddy current loss in permanent magnets can be estimated through the thermal analysis. These predictions are valid for a wide range of machine geometries and operation frequencies.

### 10.5.11 Comparison Results

In conclusion, the research of the losses such as iron loss, copper loss, and eddy current loss in PM is carried out by analytical and numerical calculation. The actual values of each loss make it possible to predict the machine performance and allow us to make a design of process occurring in the machine.



Loss	[W]
Stator	133.15
Mover	9.39
Copper	63.9
Eddy Current in PM	5.2

Figure 10.16 : Comparison of Losses,  $k=1$ ,  $C=1$ ,  $k_{bh}=k_{bw}=1.5$ , in 50 [Hz]



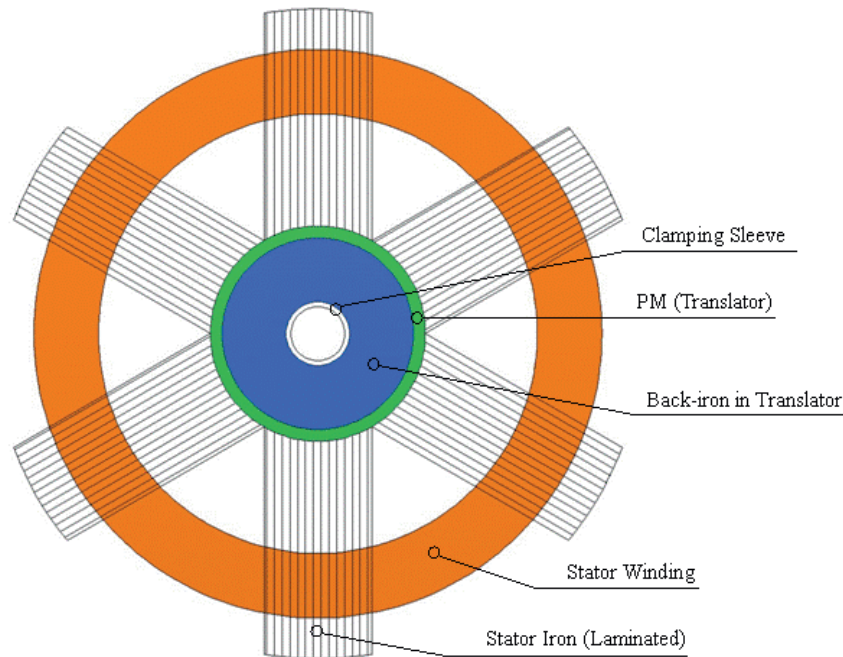


Figure 10.18 : Construction of the Cylindrical Generator in Star shape with 6 Sectors

## 10.7 Discussion

Many application areas demand analytical results for realistic model incorporating the appropriate nonlinear effects. For instance, practical design considerations require that some degree of saturation occurs in the magnetic circuit of the electrical generator. First, it deals with the nonlinearity of saturation overlooked in the previous study using equivalent magnetic circuit. Based on this analytical calculation, the numerical calculation is carried out using FLUX 2-D of FEA software. And then, it is compared and evaluated with the results between analytical and numerical calculation. As a result, it shows that the results are in agreement with each other. Moreover, the weight of generator is investigated by kinds of the material and region in terms of the material cost and thermal analysis beforehand. This approach is extended to accurate prediction of power loss for detailed design. It is classified by three kinds of losses ; iron loss, copper loss, and eddy-current loss in PM. Here, the iron loss is analyzed through different types of material, and is also considered by three components of losses ; hysteresis, classical, and excess loss.

Finally, it will make the detailed design perfect through the design process by equivalent magnetic circuit method and the analyses considering the nonlinearity and losses of the materials selected for cylindrical topology as optimal model.



---

# 11 Shaft Design through Kinetic Characteristic

## 11.1 Introduction

Electrical machinery with rotating or linear mass requires a support system that can resist dynamic forces and the resulting vibrations. The excess of such vibrations may be detrimental to the machinery and its support system. Especially, it becomes more and more important for dynamic equipment foundations due to various design criteria and methods and procedures of analysis, design and construction. For stable operation of the equipment foundations, kinetics is an important tool in understanding the motion of objects whether translational, oscillatory, or circular. In case of translating or linear oscillating masses, the behavior of variables such as speed and acceleration (deceleration) must be described by the equations of motion.

First, this study accomplishes the establishment of kinetic equation taking mechanical load into account. It will not only help to model and evaluate the performance of linear oscillation motion, but also be beneficial for the design of shaft for fatigue strength. Generally, the designer of electric machine has overlooked the modeling of shaft considering dynamic behavior by mechanical load. As a result, it can not give useful information to design of linear oscillation movement. In the past, the fatigue strength has been determined for axial, bending and torsional load independently [88]. But, a general approach to design with combined loads requires a fatigue strength that does not depend on the type of loading. Measured differences in the fatigue strength are attributed to the size of a shaft. In particular, shaft bending appears prominently in this linear system because there is no support apparatus at the center of the shaft.

The reliable design of power transmitting shafts is predicated on three major elements. First, the fatigue (stress-life) characteristics in expected service environment must be established. This can be accomplished from full-scale component fatigue test data or approximated, using test specimen data. Second, the expected load-time history of the shaft must be obtained or assumed from field service data and then properly simulated analytically. At last, a reliable mathematical model is needed which rationally considers both the fatigue characteristics of the shaft and its loading history to arrive at the proper shaft diameter for the required service life and reliability.

Furthermore, bolted joints are treated which have to transit mechanical loads connected with the shaft and which are designed with high duty bolts. The bolts must be designed such that the shaft fulfills its allotted function and withstands the mechanical loads occurring.

The first studies of fatigue by this process was done by *Wöhler* [89], observing that metals failed under repeated loading despite stress levels far below the elastic limit. The *Wöhler* curve represents maximum allowable stress amplitude versus number of cycles at fracture for a given mean stress.



The principal objective of this investigation is to develop an approach to shaft design and to bolt selection from a strength standpoint. It will be accomplished for single-phase cylindrical linear oscillating generator taking the moving displacement (stroke) and mechanical load condition into account.

## 11.2 Kinetic Equation considering Mechanical Load

In order to determine the correct machine for particular application, it is necessary to be familiar with the following dynamic relations by mechanical load.

### 11.2.1 Numerical Calculation

It describes the basic principle of kinetic characteristics based on the physical theory by linear motion.

#### Displacement

Displacement is defined as the distance between initial point and final point in a straight line and is vector quantity. It can be expressed by equation (11.1) using the function of time,  $t$ .

$$S = \hat{S} \cdot \sin(\omega t) \quad (11.1)$$

where,  $\omega = 2 \cdot \pi \cdot f$ , and frequency,  $f$ , indicates the number of travel per minute.

#### Velocity

Velocity is defined as the rate of change of displacement and is vector quantity.

$$v = \frac{\Delta s}{\Delta t} = \frac{dS}{dt} = \hat{S} \cdot \omega \cdot \cos(\omega t) \quad (11.2)$$

where,  $\Delta s$  and  $\Delta t$  indicate a change of displacement and time, respectively.

#### Acceleration

Acceleration is defined as the rate of change of velocity and is a vector quantity. It is produced when a force acts on a mass. The greater the mass (of the object being accelerated), the greater the amount of force needed (to accelerate the object).



$$a = \frac{\Delta v}{\Delta t} = \frac{d^2 S}{dt^2} = -\hat{S} \cdot \omega^2 \cdot \sin(\omega t) \quad (11.3)$$

where,  $\Delta v$  indicates a change of velocity.

### Force by Newton's Second law

*Newton's Second Law* provides an exact relationship between force, mass and acceleration. As the force acting upon an object is increased, the acceleration of the object is increased. Also, as the mass of an object is increased, the acceleration of the object is decreased. It can be expressed as a mathematical equation (11.4).

$$F = m \cdot a = m \cdot \left[ -\hat{S} \cdot \omega^2 \cdot \sin(\omega t) \right] \quad (11.4)$$

$$\hat{F} = m \cdot \left( -\hat{S} \cdot \omega^2 \right)$$

where,  $m$  represents the mass of the object.

### **11.2.2 Analytical Calculation**

Based on the above analysis, the equivalent expression considering moving displacement and mechanical load is as in the following :

#### Displacement, Velocity, and Acceleration

Since  $a$  is uniform, its magnitude is

$$a = \frac{\text{change in speed}}{\text{change in time}} = \frac{dv}{dt} = \frac{v - v_0}{t} \quad (11.5)$$

In this case, the average speed will be the speed at  $t/2$  and  $v_0$  is an initial speed. Hence :

$$v_{ave} = \frac{v_0 + v}{2} \quad (11.6)$$

$$S = v_{ave} \cdot t = \frac{(v_0 + v_0 + a \cdot t)}{2} \cdot t = v_0 \cdot t + \frac{1}{2} a \cdot t^2 = \frac{(v_0 + v)}{2} \cdot \frac{(v - v_0)}{a}$$

$$a_{ave} = \omega \cdot v_{ave}$$



The  $v_{ave}$  and  $a_{ave}$  describe the average velocity and average acceleration, respectively.

### Time functions

Assuming the velocity-time curve of a moving object is uniform, the acceleration time in specific frequency is given by

$$t = \int dt = \int_{s_0}^s \frac{1}{v} ds = \frac{v-v_0}{a} \quad (11.7)$$

The function of displacement according to time is expressed by (11.8).

$$S = S_0 + v_0 \cdot t + \frac{1}{2} a \cdot t^2 \quad (11.8)$$

The symbol  $S_0$  is the initial displacement.

### Force Calculation considering Mechanical Load

The calculation of effective force considering mechanical load can be accomplished by double of mass and acceleration through Newton's Second Law. The total mass consists of the magnet and back-iron core with the mover ( $m_m$ ), and mechanical load ( $m_l$ ). The average force is expressed as two divided by  $\pi$  of the maximum force.

$$F_{\max} = m \cdot a = (m_m + m_l) \cdot \left[ \frac{S_t \cdot \omega^2}{2} \right] \quad (11.9)$$

$$F_{ave} = \frac{2 \cdot F_{\max}}{\pi} \quad (11.10)$$

## **11.3 Determination of Shaft Diameter**

A shaft is the component of a mechanical device that transmits linear or rotational motion and power. It is integral to any mechanical system in which power is transmitted from a prime mover, such as an electric machine or an engine, to other parts of the system. The shaft of transmission equipment has suffered from the fatigue such as axial, bending and torsion stress depends on its application field. The fatigue in linear or rotating shafts is a phenomenon that has been known and

studied for nearly a century [88]. Thus, it is necessary to analyse fatigue performance for long life cycles of utilization.

### 11.3.1 Design Procedure

Only solid circular steel and steel alloy shafts are considered. In steel shafts with relatively long lifetimes, the fatigue strength approaches a value known as the endurance limit. Generally, the procedure for shaft design means the decision of shaft diameter by three stresses such as axial, bending, and torsional fatigue strength considering the relationship of the load moment in specific material. In sequence, the appropriate stresses must be calculated, and they must be determined by an adequate factor of safety and the endurance limit of the material. Additionally it can be made for stress concentrations, temperature and surface condition by forming a coefficient for each applied stress. At last, the shaft is adequately designed to prevent fatigue failure for the specified operating conditions.

### 11.3.2 Fatigue Failure

Failure from fatigue is statistical in nature as much as the fatigue life of a particular specimen cannot be precisely predicted but rather the likelihood of failure based on a large population of specimens [89]. This fatigue is caused by repeated cycling of the loads. The fatigue strength is dependent on the type of loading (axial, bending, or torsion) and it has resulted in three separate fatigue strengths being defined. In particular, this linear motion is implemented by designing shafts using axial and bending stress among the three fatigue strengths.

The state of stress to be considered is caused by force (torque) transmitted to the shaft, axial forces imparted to the shaft, bending of the shaft due to its weight or loads, and torsion by rotating of shaft. The characteristics of these three basic types or cases are given here : axial strength ( $\sigma_a$ ), bending strength ( $\sigma_b$ ), and torsion strength ( $\sigma_t$ ).

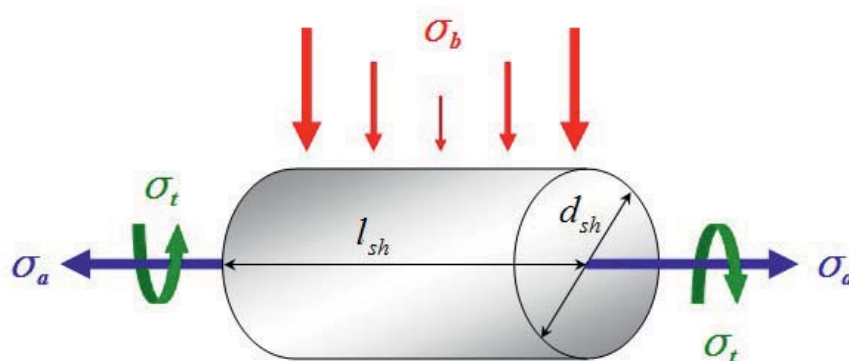


Figure 11.1 : Three Strengths ; Axial, Bending, and Torsion



### Axial Strength

Axial stress is referred to as normal stress since it acts in line with the material. Most simple form is tension stress since its effect is independent of the length of the material. The formula for definition of axial stress can be expressed as follows.

$$A_{rea} = \frac{\pi \cdot d_{sh}^4}{4} \quad (11.11)$$

$$\sigma_a = \frac{F_{max}}{A_{rea}} \quad (11.12)$$

where,  $A_{rea}$  is cross-section area of the shaft, and  $F_{max}$  represents the maximum force considering mechanical load given by equation (11.9).

### Bending Strength

The first step in shaft design is to draw the bending moment diagram for the loaded shaft or the combined bending moment diagram. The bending stress is larger than the direct stress by axis when a shaft is easily subjected to bending moment in such a linear motion case. From the bending moment diagram, the points of critical bending stress can be determined.

The force and moment acting on shaft indicates equation (11.13) and (11.14), respectively.

$$P_s = m \cdot g \quad (11.13)$$

where,  $g$  is gravity acceleration.

$$M_b = \frac{P_s \cdot l_{sh}}{8} \quad (11.14)$$

The effective nominal stress is [90]

$$\sigma_b = \frac{32 \cdot M_b}{\pi \cdot d_{sh}^3} \quad (11.15)$$

### Torsion Strength

Torsion occurs when any shaft is subjected to a torque in case of a rotating motion in general. This is true whether the shaft is rotating (such as drive shafts on engines, motor and generators) or



stationery (such as with a bolt or screw). This torque makes the shaft twist and one end rotates relative to the other inducing shear stress on any cross-section.

It represents as the equation (11.16) for circular solid [91].

$$\sigma_t = \frac{16 \cdot T_m}{\pi \cdot d_{sh}^3} \quad (11.16)$$

where,  $T_m$  is close to zero, which represents the twisting moment. In this study, the torsional strength is excluded because it has little impact on the shaft due to the linear motion.

### Total Strength

The total strength acting on the shaft is expressed by sum of the axial and bending strength.

$$\sigma_{sh} = \sigma_a + \sigma_b \quad (11.17)$$

### Wöhler Curve

First systematic study to characterize the fatigue behavior of materials cyclic stress range was conducted by Wöhler [92]. In high-cycle fatigue situations, materials performance is commonly characterized by an *S-N Curve*, also known as a Wöhler curve. This is a graph of the magnitude of a cyclic stress against the logarithmic scale of cycles to failure.

### Alternating Strength by Wöhler Curve

By Wöhler curve, we can find the endurance limit value of selected material ; it is marked as  $\sigma_{en}$  in failure cycle  $10^6 < N < 10^7$ .

$$\zeta = \frac{\sigma_{en}}{\sigma_{al}} \rightarrow \sigma_{al} = \frac{\sigma_{en}}{\zeta} \quad (11.18)$$

The safety factor,  $\zeta$ , is a ratio of maximum strength to intended loads for the actual item that was designed. The value to use for safety factor is based on judgment. It depends on the consequences of failure, that is, cost, time, safety, etc. Some factors to consider when selecting a value for safety factor are how well the actual loads, operating environment, and material strength properties are known, as well as possible inaccuracies of the calculation method. Values typically range from 1.3 to 6 depending on the confidence in the prediction technique and the criticality of the application. Unless experience or special circumstances dictate it, the use of safety factor values of less than 1.5



is not normally recommended [90].

### Summary

Its features for this study may be summarized as follows ;

- The Wöhler curve shows fatigue life corresponding to a certain stress amplitude
- The Wöhler diagram can be used to design for finite (and infinite) life
- For steel, the fatigue limit corresponds to  $10^6 < N < 10^7$

### **11.3.3 Determination of Shaft Diameter**

Through the earlier analytical calculation, we can attain the total strength acting on the shaft,  $\sigma_{sh}$ . It must not be greater than alternating strength ( $\sigma_{al}$ ) by the endurance limit value of selected material and safety factor as expression (11.19). Finally, the diameter of shaft is decided by satisfying maximum value below the calculated alternating strength.

$$|\sigma_{sh}| \leq \sigma_{al} \quad (11.19)$$

## **11.4 Machine Elements Assemblies with Shaft**

Virtually all machines involve the transmission of power and/or motion from an input source to an output work site. The input source, usually an electric machine or internal combustion engine, typically supplies power as a linear driving force to input shaft of the machine under consideration. The power transmission to or from linear moving shaft is accomplished either by coupling the liner moving shaft end-to-end with a power source, or by attaching power input or output components such as pistons or connecting rods to the shaft in linear systems. For the transfer of power bolted or screw connections are intended to fasten together machine components. The joints and connections between parts must be given special attention by the designer because they always represent geometrical discontinuities that tend to disrupt uniform force flow. In this study, it deals with the analysis about threaded joint by means of a threaded fastening such as a bolt or a screw.

### **11.4.1 Bolt of Uniform Strength**

Bolts are subjected to shock and impact loads in certain applications. The bolts of cylinder head of an internal combustion engine or the bolts of connecting rod are the examples of such applications. In such cases, resilience of the bolt is important design consideration to prevent breakage at the threads. Resilience is defined as the ability of the material to absorb energy when deformed

elastically and to release this energy when unloaded. A resilience bolt absorbs shocks and vibrations like leaf springs of the vehicle. In other words, the bolt acts like a spring.

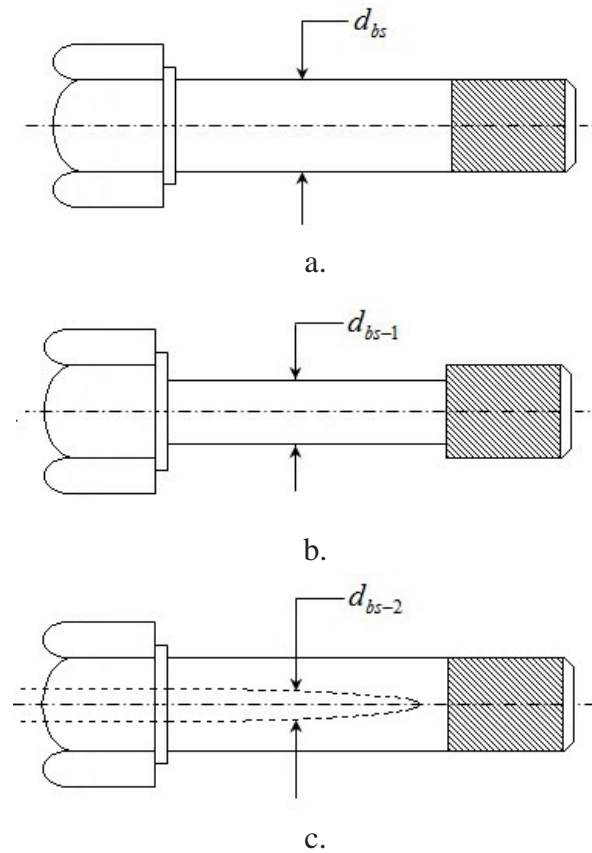


Figure 11.2 : Bolts of Uniform Strength [93]

Figure 11.2.a shows an ordinary bolt with usual shape. The major diameter of thread as well as the diameter of the shank is  $d_{bs}$ . The core diameter of the threads is  $d_{bs-1}$ . When this bolt is subjected to tensile force, there are two distinct regions of stress.

- The diameter of threaded portion  $d_{bs-1}$  is less than the shank diameter  $d_{bs}$ . The threaded portion is also subjected to stress concentration. Therefore, stress induced in the threaded portion is more than the stress in the shank portion. The energy absorbed by each unit volume of bolt material is proportional to the square of the stress. Hence, a large part of the energy is absorbed in the threaded portion of the bolt.
- The diameter of the shank is more than the core diameter of the threaded portion. There is no stress concentration in the shank. Therefore, when the bolt is subjected to tensile force, the stress in the shank portion is less than the stress in the threaded portion. The energy absorbed in the shank, which is proportional to the square of the stress, is less than the energy absorbed in the threaded part.

The resilience of the bolt can also be increased by increasing its length [93]. The strain energy absorbed by the shank is linearly proportional to its length. The ideal bolt will be one which is subjected to same stress level at different cross-sections in the bolt. It is called the bolt of uniform strength.

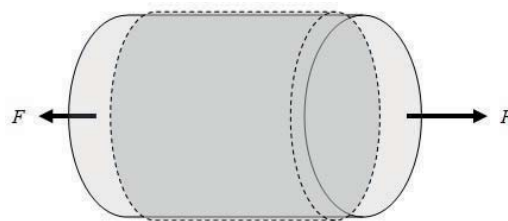
There are two ways to reduce the cross-sectional area of the shank and convert an ordinary bolt into a bolt of uniform strength. They are illustrated in figure 11.2.b and c. One method is to reduce the diameter of the shank as shown figure 11.2.b. In this method, the diameter of the shank is usually reduced to the core diameter of the threads. Therefore, the cross-sectional area of the shank is equal to the cross-sectional area of the threaded portion. When this bolt is subjected to tensile force, the stress in the shank and the stress in the threaded portion are equal. In the second method, the diameter of the hole ( $d_{bs-2}$ ) is obtained by equating the cross-sectional area of the shank to that of the threaded part. In another method, the cross-sectional area of the shank is reduced by drilling a hole, as illustrated in figure 11.2.c. Both methods reduce cross-sectional area of the shank and increase stress and energy absorption.

$$\frac{\pi}{4} \cdot d_{bs}^2 - \frac{\pi}{4} \cdot d_{bs-2}^2 = \frac{\pi}{4} \cdot d_{bs-1}^2 \quad \text{or} \quad d_{bs-2} = \sqrt{d_{bs}^2 - d_{bs-1}^2} \quad (11.20)$$

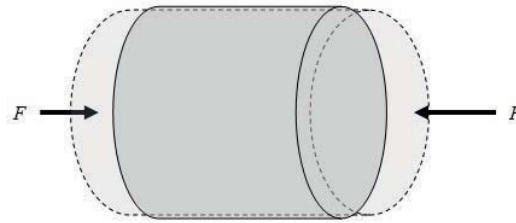
Machining a long hole is difficult operation compared with turning down the shank diameter. Drilled hole results in stress concentration. Therefore, a bolt with reduced shank diameter is preferred over a bolt with an axial hole [93].

#### 11.4.2 Tensile and Compressive Strength in Forms of Normal Stress

The needed strength and rigidity of this connection is achieved, in the first place, by tensile strength and compressive strength of the connected parts against each other. The magnitude of the forces should be enough to prevent joint separation in the connection. Both the tensile strength and the compressive strength are in parallel with the surface normal vector, and thus perpendicular to the cutting plane of a workpiece. Thus, both types of strength are normal stress. As mentioned above in *11.3.2 Fatigue Failure*, an axial strength can be reinterpreted to a tensile strength and compressive strength by direction of the applied force.



a. Tensile Strength



b. Compressive Strength

Figure 11.3 : Normal Stress

The selected material for joint components is the steel grade ST series (*DIN 17100*). It is low carbon, high strength structural steel which can be readily welded to other weldable steel. With its low carbon equivalent, it possesses good cold-forming properties. Among the many types of rigid connections, the most commonly used is considered here : the connection of bolt or screw with a shaft.

### 11.4.3 Choice of Bolt

#### Tensile Strength

For the calculation of permissible tensile strength shown figure 11.3.a, the following procedure is given.

$$\sigma_{ten} = \frac{2 \cdot \sigma_{yi}}{\zeta} \quad (11.21)$$

where,  $\sigma_{yi}$  is the yield strength in the bolt, and varies slightly over 285 ~ 355 [ $N/mm^2$ ] by its thickness in DIN 17100 steel sheet [94]. The yield strength in shear is equal to half of the yield strength in tension [93].

#### Compressive Strength

Given the geometry of the joint component, and force applied as a compressive strength to the component. The procedure is completely the same as in calculating the tensile strength ; it has only difference that the mechanism of the pressure has a negative sign as shown figure 11.3.b.

$$\sigma_{comp} = \sigma_{ten} \quad (11.22)$$



### Force on the Bolt

The strength of the bolt or screw in tension is given by

$$F_{bs} = \frac{\pi}{4} \cdot d_{bs}^2 \cdot \frac{2 \cdot \sigma_{yi}}{\zeta} \quad (11.23)$$

### Decision of the Size

The size of bolt can be obtained from the equation (11.24).

$$d_{bs} = \sqrt{\frac{4}{\pi} \cdot F_{bs} \cdot \frac{\zeta}{2 \cdot \sigma_{yi}}} \quad (11.24)$$

Generally, the approximate relationship between  $d_{bs}$  and  $d_{bs-1}$  can be used [93].

$$d_{bs-1} = 0.8 \cdot d_{bs} \quad (11.25)$$

From a specification, the standard size of the bolt is selected.

### Summary

Assuming infinite thickness of the shaft, the shear stress can be left out of consideration in the connection of coupling components with shaft. The bending stress can also be ignored because the length of bolt is considerably shorter than that of shaft. Besides the effects in the types of bolt such as machine screws, thread cutting screws, and hex bolts with different heads do not take into account.

## 11.5 Concrete Dimension of Machine Elements and Shaft

The figure 11.4 indicates the specific dimension of the shaft and coupled bolts using the analytical calculation by kinetic equations based on the mechanical theories.

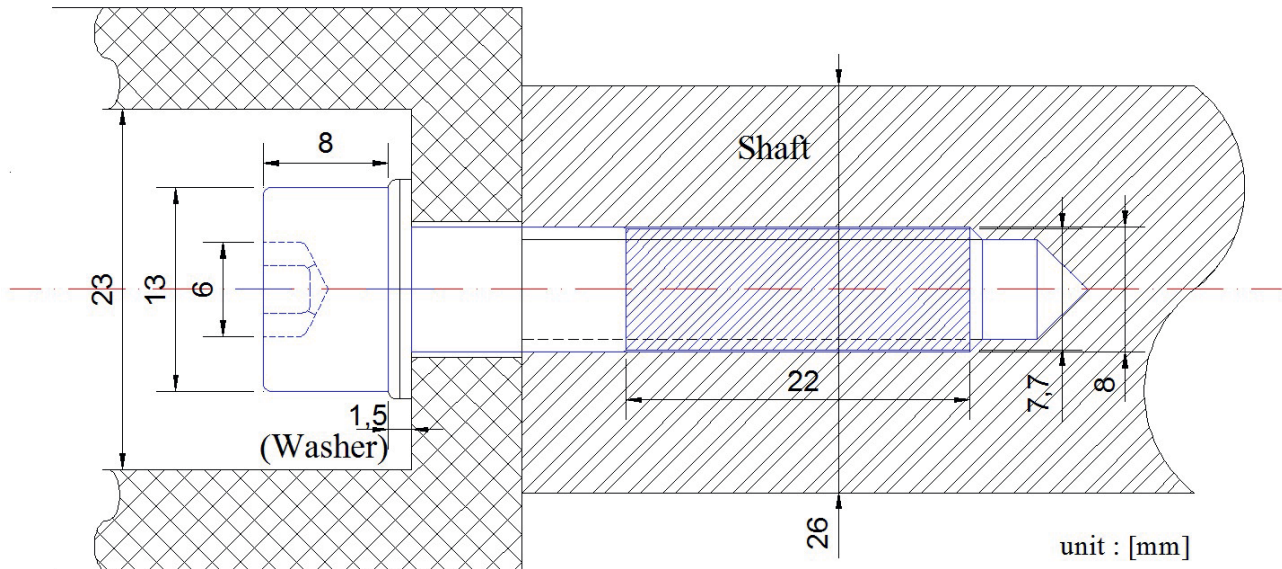


Figure 11.4 : Dimension of Mechanical Part in Cylindrical Linear Generator

## 11.6 Discussion

The dynamic analysis of single-phase cylindrical topology is performed by using the combination of electric and kinetic equation considering stroke and mechanical load. It provides useful information to analysis the dynamics characteristics of the generator as well as to design of the shaft. Based on this characteristic, an empirical design procedure for shafts with fatigue loadings is presented. The shaft design consists of the determination of the correct shaft diameter to ensure satisfactory strength and rigidity when the shaft is transmitting power under various operating and loading conditions. The shaft diameter is determined by using the axial and bending strength of the selected material by Wöhler curve. In addition, the consideration of the bolt coupling is achieved by influences such as uniform and normal strengths, load, and others for ideal alignment of the shaft, which is made of steel and therefore very rigid, to some intermediate resilient element that can be deformed by relatively small force and decrease the additional load of the shaft. In conclusion, the shaft design and machine element is closely related with the dynamic performances by mechanical load conditions.



---

## 12 Thermal Analysis

### 12.1 Introduction

Previous research for the linear oscillating generator has suggested that the cylindrical topology with permanent magnet and back-iron in the mover is verified as optimum model in terms of the electrical and structural aspects. The thermal performance of the generator will determine the power rating of the generator. In order to preserve the optimal conditions ensuring the good operation of the generator, it is imperative to well understand and control the thermal behavior of the generator. This good understanding needs the ideal design of cooler to ensure the operating temperatures do not exceed the acceptable limits of used materials. As a result, it is obvious that the consideration of thermal characteristic can show the temperature distribution in the generator.

Fundamental knowledge of linear oscillating generator in various aspects such as electrical and mechanical properties has been explored through the previous chapters. In this chapter, it is written with the objective to investigate and analyze thermal characteristics and simulation using heat transfer theory in the linear oscillating generator design. This study provides information about the thermal behavior of the generator letting obtain the whole generator temperatures. It enables the design to very effective and efficient consideration for the linear oscillating generators.

### 12.2 Determination of Heat Transfer Coefficients

In the simplest terms of the heat transfer, the discipline of heat transfer is concerned with only two things : temperature and the flow of heat. Temperature represents the amount of thermal energy available, whereas heat flow represents the movement of thermal energy from place to place according to the *First Law of Thermodynamics* [95].

The process for the thermal analysis of the cylindrical topology is achieved through the internal heat generation and convection. The internal heat generation can be applied to bodies only and it has unit energy / time / volume. The convection, as one of the kind of heat transfer mechanisms such as conduction and radiation, can be explained as heat energy transferred between a boundary surface and a heat transport by a fluid (e.g. water) in motion at different temperatures. As regards this convection, at least one type of thermal boundary condition must be presented to prevent the thermal equivalent of rigid body motion. Given temperature or convection load should not be applied on surfaces that already have another heat load or thermal boundary condition applied to it. For this simulation, it is noticed that the radiation effect is not considered. Radiation effect is almost negligible because the existence of the air-gap between the stator and mover is very narrow.



In this practical study, the heat transfer from the surface is governed by convection. This effect can be described by the corresponding *Convection Heat Transfer Coefficients*. It depends on the surface and environment temperatures. In this work the convective heat transfer coefficient has to be examined for the horizontal cylinder surfaces model geometries. The heat transfer in electrical conductors is computed by an analytical calculation (of the heat conduction equations) in the steady state regime and by a numerical algorithm in a transient state regime. Therefore, the convection coefficient for the analytical solution has to be linearized and to be presented in an approximated form in order to obtain simple but sufficiently accurate equations of the convection coefficients.

The mainly applied round geometry has been studied. Many correlations exist between the different calculation methods. The literature [96] presents simple algorithms for the calculation of convective coefficients of the cylinders. This work follows the procedure proposed by [97], where many approaches of the various procedures are summarized. The equations of this procedure were validated by the numerical calculation. All notations of physical constants and material properties will be used from the works [97, 98].

### 12.2.1 Nusselt Number using Dittus-Boelter equation

The *Nusselt Number* is the ratio of convective to conductive heat transfer across the boundary. This for a cylinder is transformed from classical equation (12.1). Convection heat transfer coefficient

$\kappa_{conv}$  [ $W/m^2 \cdot ^\circ C$ ] can be expressed with the dimensionless Nusselt Number as

$$Nu = \frac{\kappa_{conv} \cdot l_{sur}}{\xi} \quad (12.1)$$

where,  $l_{sur}$  indicates the characteristic length of the surface, and  $\xi$  is the thermal conductivity of the coolant.

According to *Dittus-Boelter* equation [97] is expressed by

$$Nu = 0.023 \cdot Re^{\frac{4}{5}} \cdot Pr^{\frac{1}{3}} \quad (12.2)$$

### 12.2.2 Prandtl Number

The *Prandtl Number* is a dimensionless number approximating the ratio of momentum diffusivity (kinematic viscosity) and thermal diffusivity [99]. It describes the thickness ratio of velocity and the thermal boundary layers. The Prandtl Number is often used in heat transfer and free and forced convection calculations. It depends on the fluid properties and can be expressed as

$$\text{Pr} = \frac{c_p \cdot \nu_{kv}}{\xi} \quad (12.3)$$

where,  $c_p$  is the specific heat capacity in the given a specific material, and  $\nu_{kv}$  is the kinematic viscosity.

### 12.2.3 Reynolds Number

The *Reynolds Number*, is a dimensionless number that gives a measure of the ratio of inertial forces to viscous forces, can be defined for a number of different situations where a fluid is in relative motion to a surface. In other words, the ratio between inertia and viscous forces is described by the Reynolds Number and can be described by the equation (12.4) [99]. These definitions generally include the fluid properties of density and viscosity, plus a velocity and a characteristic length or characteristic dimension.

$$\text{Re} = \frac{v_{cool} \cdot l_{sur}}{\nu_{kv}} \quad (12.4)$$

where,  $v_{cool}$  is the speed of the coolant on the surface.

As with Nusselt Number equation, Reynolds Number in case of a cylinder can be expressed as

$$\text{Re} = \frac{v_{cool} \cdot [2 \cdot (r_h - r_0)] \cdot D_e}{\nu_{kv}} \quad (12.5)$$

where,  $D_e$  is density of the coolant material, and  $r_h$  indicates the radius of the coolant material covering the surface as shown in figure 12.1.

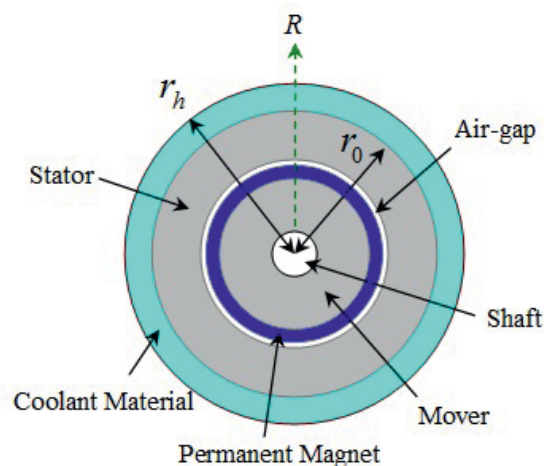


Figure 12.1 : Coolant Material : Insulation Class H (180 [°C])

Now it can calculate the thermal analysis using numerical method based on the above analytical modeling. The internal heat coefficients of each region are entered into their losses, namely the input values of each region such as stator, mover, winding, and permanent magnet are decided by the calculated values from losses studied in the previous *Chapter 10. Detailed Design*. It can be summarized again as follows :

$$\begin{aligned}
 h_{stator} = & \frac{4k H_c \cdot f \cdot k_{bh}}{\rho} (B_{tooth-tip} + B_{tooth} + B_{yoke}) \\
 & + \frac{\pi^2 \sigma \cdot d^2 \cdot f^2 \cdot k_{bw}}{6\rho} (B_{tooth-tip} + B_{tooth} + B_{yoke})^2 \\
 & + \frac{C f^{1.5}}{\rho} (B_{tooth-tip} + B_{tooth} + B_{yoke})^{1.5} \left[ \frac{W}{m^3} \right]
 \end{aligned} \tag{12.6}$$

$$h_{mover} = \frac{4k H_c \cdot f \cdot k_{bh}}{\rho} B_{bi-mover} + \frac{\pi^2 \sigma \cdot d^2 \cdot f^2 \cdot k_{bw}}{6\rho} (B_{bi-mover})^2 + \frac{C f^{1.5}}{\rho} (B_{bi-mover})^{1.5} \left[ \frac{W}{m^3} \right] \tag{12.7}$$

As mentioned above, Joule Heating comes from copper loss.

$$h_{coil} = \frac{i^2 \cdot R_{es}}{\left( \frac{d_{coil}}{2} \right)^2 \cdot \pi \cdot l_{coil}} \cdot \frac{A_{coil} \cdot N_c}{\pi \cdot [(r_0 - h_{ys}) - (r_0 - h_{ys} - t_h)] \cdot l_c} \left[ \frac{W}{m^3} \right] \tag{12.8}$$

$$h_{pm} = \frac{1}{\sigma_m} \frac{\omega}{2\pi} \int_{r_m}^{r_1} \int_{z_0 - \frac{l_m}{2}}^{z_0 + \frac{l_m}{2}} \int_0^{2\pi} 2\pi r \cdot J_e^2 \times (r, z, t) dt \cdot dz \cdot dr \left[ \frac{W}{m^3} \right] \tag{12.9}$$

In order listed from the equation (12.6) to (12.9), they describe the internal heat coefficient of the stator, mover, coils, and permanent magnet respectively.

#### 12.2.4 Convection Heat Transfer by Water

To analyze of thermal performance, convection heat transfer happens in the outer surface. The heat transfer coefficients in the outer surface depends on many factors such as the speed of the flow, temperature, outer surface dimensions and even the surface characteristics of the translating parts. In this cooling method, cooling *Water Jackets* are provided around the generator. The water when circulated through the jackets, it absorbs heat of combustion. This hot water will then be cooling in the radiator partially by a fan and partially by the flow developed by the forward motion of the vehicle. The cooled water is again recirculated through the water jackets.

The heat transfer coefficients in the outside region between the outer surface and external air can be described with the use of Nusselt Number, and then it is expressed as  $h_{conv\_water}$ .

$$h_{conv\_water} = \frac{\xi_{water}}{2 \cdot r_h} \cdot Nu_{water} \left[ \frac{W}{m^2 \cdot K} \right] \quad (12.10)$$

where,  $\xi_{water}$  is the conductivity of water, and  $Nu_{water}$  is Nusselt Number of the water material.

### 12.3 Assignment of Heat Transfer Coefficients

Figure 12.2 represents the overview about heat transfer flow of cylindrical topology using the formulas of heat transfer theory. The validation is carried out on a 3-D model made of basic elements taking into account the geometry of each part such as stator, mover, coil, and permanent magnet region.

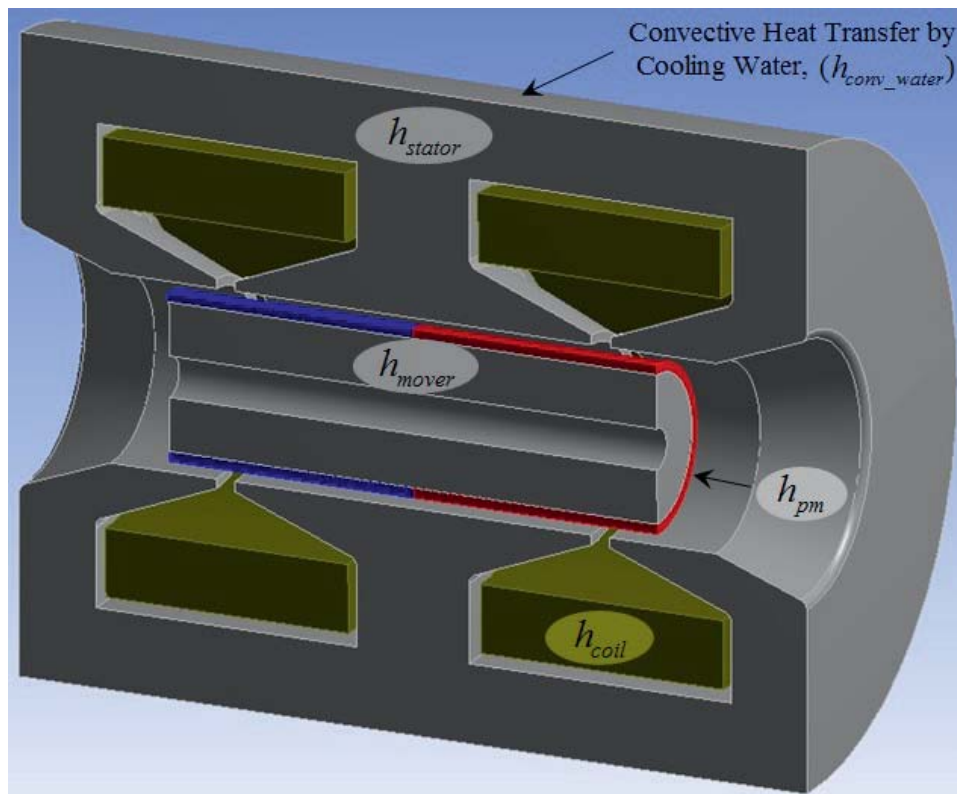


Figure 12.2 : Cylindrical Topology with Heat Generation

Resistive losses, permanent magnet losses and iron losses are represented by individual heat flow sources. The results presented thereafter correspond to a 3-D model of the complete cylindrical linear oscillating generator.



## 12.4 Simulation Results

Thermal analysis needs a good knowledge of the phenomena playing a role. The predominant phenomena occurring in the studied cylindrical topology of the linear oscillating generator are : the conductive heat exchange between the various solids parts of the machine and the convective heat exchange between the walls and the fluids.

In conventional engines force exerted on cylinder, due to thermal expansion of the gas pressure, is brought to the crank gear along the connecting rod axis, and available to drive the crank gear as a fraction of the available force. As a result, it is found a large amount of heat is liberated in exhaust gasses without converting into useful work and the IC engine still require improvements to eliminate drawbacks of its mechanism. It is evident when investigating the cycle of internal combustion engine, only 40 [%] or lesser amount of heat energy is converted in to useful work and the major part of energy is dissipated as losses. Therefore there is a necessity of the free piston IC engine. A benefit is that the mechanical friction can be reduced relative to crankshaft-driven geometries since there is only one moving engine part and no piston side loads. In this arrangement mechanical losses in the system are dramatically reduced since there is essentially one moving part, and this allows engine operation at a more or less constant piston speed. Also, combustion seems to be faster than in conventional slider-crank configurations. For this reasons, it is necessary that the analysis should be achieved by the material features of each region and various frequencies.

This thermal analysis can be achieved by numerical calculation through the simulation with *ANSYS* program.

### 12.4.1 Comparison by Each Region

Generally a four-stroke engine (also known as four-cycle) runs at between 500 [rpm] to 4000 [rpm], whereas the analysis of temperature characteristics in the generator is achieved by actually expected operating frequency range between 100 [Hz] and 150 [Hz].

#### Stator Core

Iron loss occurs as a result of the material's resistance to being magnetized (hysteresis loss) and as a result of electrical currents which counteract changes in the magnetic field in the material (eddy-current loss). In an internal combustion engine the water jacket is a series of holes either cast or bored through the main engine block and connected by inlet and outlet valves to a radiator. As a result, the temperatures generated in the stator core has a value of 66 [°C] at 150 [Hz] of operating frequency. The temperature difference between 100 [Hz] and 150 [Hz] is not exceeding 1.2 [°C]. The temperature in stator core region is rising faster than that of mover core. The temperature distributions are constant above 3000 [Sec.] in both frequency range.

### Mover Core

The temperature distribution curves of the mover core appear identically to the curve of the stator core. The temperature of the mover core in each frequency rises rather more than that of the stator core. That is because the magnetic flux tends to converge to the mover in the direction of shaft as mentioned *Chapter 5. Cylindrical Topology (5.2 Configuration)*. Additionally, the temperature characteristics of the mover appear the highest at 66.96 [°C] under 150[Hz] in the entire region, because it is located farthest from the cooling system by a water jacket.

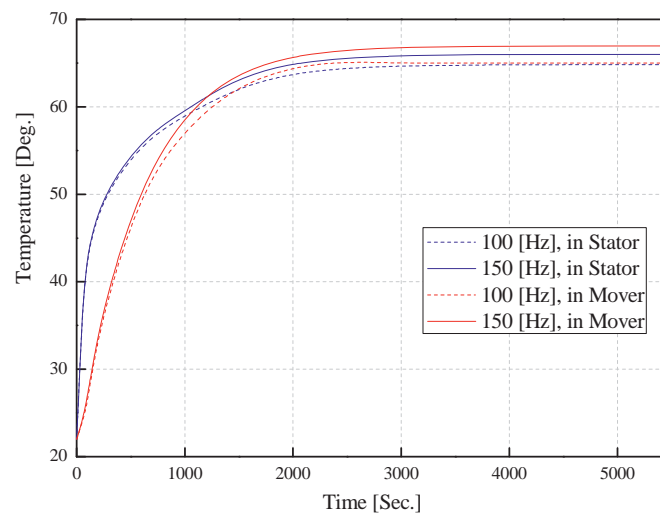


Figure 12.3 : Temperature Distributions in Stator & Mover Core by Frequency

### Coils

Heat generation in linear oscillating generator refers to resistance heating and eddy currents in copper wire where electrical energy is converted to heat. The maximum temperature in the coil region is 64.9 [°C] in between 100 [Hz] and 150 [Hz] of the frequency range.

### Permanent Magnet

Compared to other materials used, permanent magnet temperature is one of the key items to be emphasized in generator design. The intensity of magnetization and the coercive force are elements which determine the performance of permanent magnet. Particularly, the magnetic properties of NdFeB deteriorate rapidly in more than about 120 ~ 180 [°C] depending on the grade of material and the permeance coefficient of permanent magnet in operation. Consequently, the maximum temperature is at 65.1 [°C] below 100 [Hz], it is approximately 66.5 [°C] in 150 [Hz].

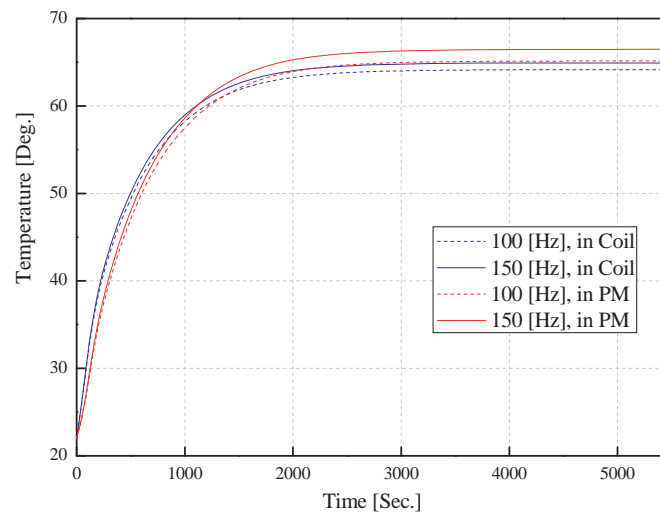


Figure 12.4 : Temperature Distributions in Coil & Permanent Magnet by Frequency

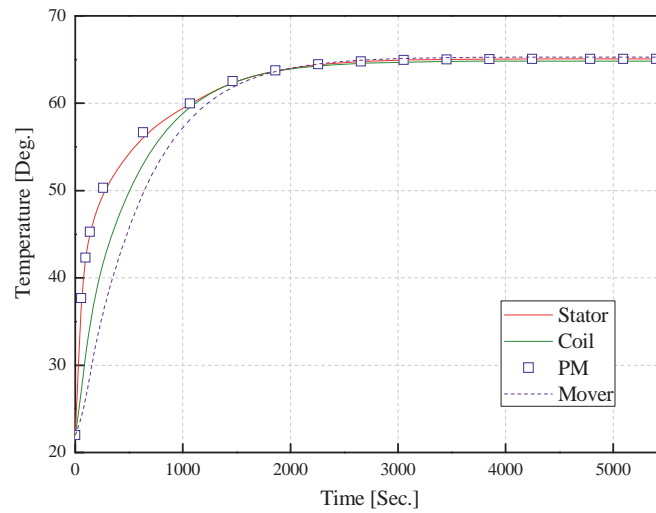
### 12.4.2 Comparison by Frequency

The heat transfer from the hot combustion gases includes forced convection through the hot gas boundary layer, conduction through the cylinder wall, and forced convection into the fluid coolant in the head, engine block, and piston. The heat transfer process is periodic due to the piston motion. However, the engine speed is usually high enough so that the temperature fluctuations only penetrate about a millimeter into the cylinder wall. The speed by frequency is inversely proportional to the penetration depth ; since the penetration depth is a very small fraction of the cylinder wall thickness, the cylinder wall can be assumed to have a temperature profile that is not changing in time.

To examine the characteristic by operating frequencies, they were investigated some trends of the temperature distribution in 50 [Hz], 500 [Hz], and 1000 [Hz].

#### 50 [Hz]

The temperature in all regions keep within 66 [°C] and maintain a constant over 3000 [Sec.]. Among others, the maximum temperature in the mover is 64.79 [°C] and the highest in the entire regions.



	Stator	Coil	PM	Mover
Maximum Temperature [°C]	64.59	64.33	64.60	64.79

Figure 12.5 : Temperature Distributions in 50 [Hz]

500 [Hz]

The higher frequency, the temperature differential is getting wider among the regions in the constant state. Also, the maximum temperature of mover is at 160.87 [°C] and is the highest in entire region likewise the case of 50 [Hz].

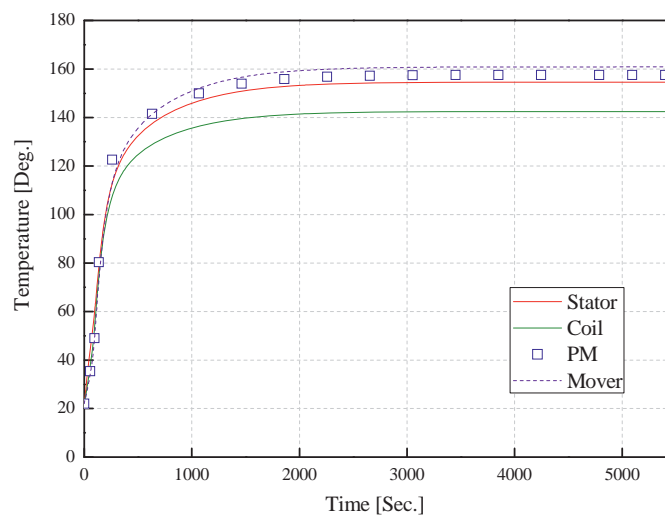


Figure 12.6 : Temperature Distributions in 500 [Hz]



### 1000 [Hz]

The temperature variation between 50 [Hz] and 500 [Hz] is within about 96 [°C] in terms of maximum and minimum value. But its deviation in 1000 [Hz] is approximately 237 [°C] and it is about two and a half times greater compared to the case of 50 [Hz] and 500 [Hz]. As shown figure 12.9, the temperature in coil region is the lowest at 320.98 [°C] and it in mover is the highest at 379.95 [°C] in given 1000 [Hz].

Therefore, it needs the improved (direct) cooling methods to reduce the temperature distributions at 1000 [Hz], which is achieved by using thicker coils or shorter winding, etc.

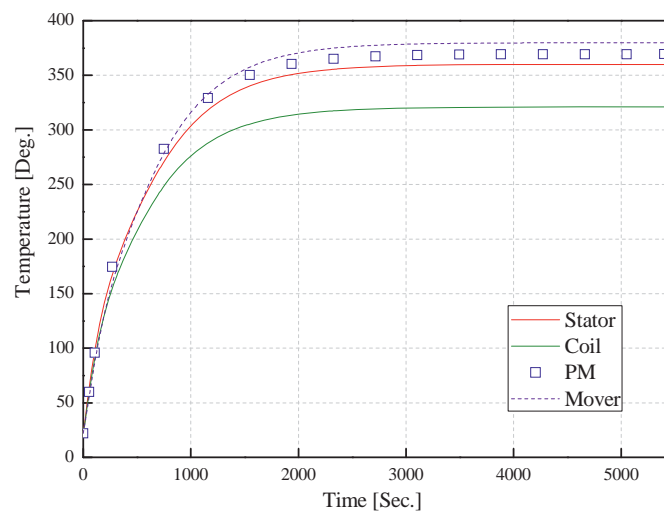


Figure 12.7 : Temperature Distributions in 1000 [Hz]

### 12.4.3 Summary

The comparative analysis for temperature distributions is achieved by category of each region and frequency respectively. In the case of up to 500 [Hz], the maximum temperature can be bearable a temperature of 180 [°C] according to the *Insulation Class H* type. The temperature of mover core is the highest in the entire region with regard to analysis of frequency.

This result is provided under the following assumptions ;

- Each coefficient for determination of internal heat magnitude is specified as follows ;  
 $k=1$ ,  $C=1$ ,  $k_{bh} = 1.5$ , and  $k_{bw} = 1.5$
- Convection is treated as a boundary condition
- The temperature of the coolant water is assumed as 60 [°C], and it is independent of time
- The initial temperature is set to 22 [°C]
- Coolant water is configured to a thickness of 10 [mm]

- The temperatures in each region and by frequency are measured at the maximum values

## 12.5 Discussion

Thermal analysis is very important in generator application to evaluate the effect of temperature in the system. To improve efficiency of the generator, it is necessary to carefully investigate the thermal characteristic in order to determine the best cooling solutions.

The heat sources boundary condition is applied by convection which is a kind of heat transfer mechanisms. The mathematical modeling for the thermal analysis of cylindrical linear model is accomplished based on the losses studied in the previous *Chapter 10 Detailed Design*. The next, a detailed study is furthered by designing a thermal model using FEM. After numerical analysis, there are two categories by operating frequency and certain regions such as stator, mover, coils, and permanent magnet including air-gap.

As a result, it shows that this generator is satisfied with the insulation class H in the frequency range from 50 [Hz] to 500 [Hz]. In addition, the temperature distribution of the mover is the highest by comparative estimation in entire regions. The reason for the magnetic flux tends to concentrate to the mover in cylindrical type, particularly. Therefore, it can be observed that this model is closely sensitive to the temperature distribution of the mover. In case of 1000 [Hz], it will need a more additional cooling method or equipment to satisfy the insulation class.

The focus of the analysis is to develop a thermal model and to study the heat distribution in linear oscillating generator.



## 13 Assessments

### 13.1 Introduction

In previous study, the cylindrical generator of single-phase system has been implemented as prototype. The test bench for measurement of the machine has accomplished as shown in figure 13.1. It concentrates on two tasks ; first, calculate the power data from the design drawings of the test machine, second measure induced synchronous voltage and short-circuit current at different speed on the test setup.

The model assumed a constant angular velocity for the motor driving the test bench. Meanwhile, it helps the importance in this generator has warranted an investigation of them in case of short-circuit test.

This chapter presents the experiment results to verify the design, and to investigate the performance of the machine as a generator.

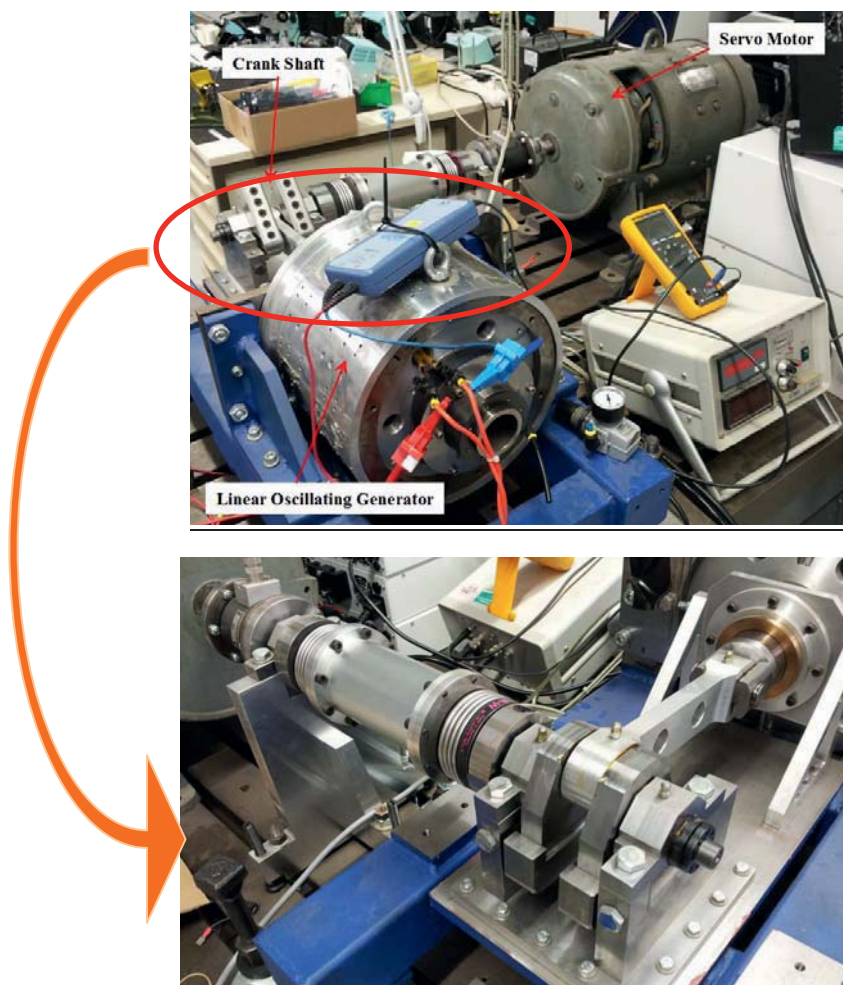


Figure 13.1 : Test Environment for Measurement of Cylindrical Generator



## 13.2 Determination of the Parameters of the Equivalent Circuit from Test Data

The equivalent circuit of a synchronous generator that has been derived contains three quantities that must be determined in order to completely describe the behaviour of a real synchronous generator

- The saturation characteristic : relationship between  $I_f$  and flux linkage (and therefore between  $I_f$  and  $U_p$ )
- The synchronous reactance,  $X$
- The resistance,  $R$

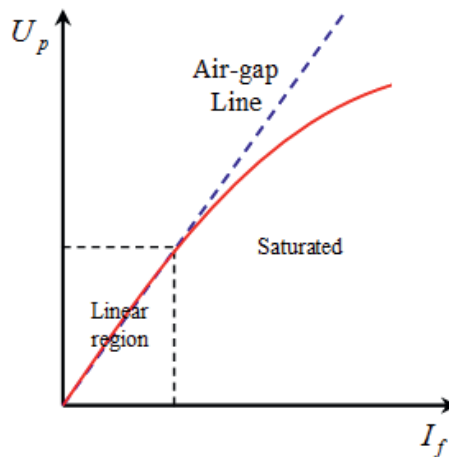


Figure 13.2 : Voltage vs. Current Plot [100]

In the plot above, the air-gap line (dotted blue) gives the relationship between mmf and flux density in the air-gap. (Induced voltage is proportional to flux density). At higher field current levels, the iron in the machine saturates and the percentage of field mmf applied to the air-gap is reduced. As a result, the induced voltage falls below the air-gap line.

As synchronous machines operate at effectively constant speed, the open-circuit test provides the relationship between field current and induced voltage for all load conditions.

They must be determined in order to completely describe the behaviour of a real synchronous generator. Consequently, the above quantities could be determined by performing the following tests.

- Open-circuit test
- Short-circuit test

### 13.2.1 Open Circuit Test

The mover voltage is equal to the terminal voltage. In other words, the terminals are disconnected from all loads, and the field current is set to zero. The generator is turned at the rated speed. Then the field current is gradually increased in steps, and the terminal voltage is measured at each step along the way (frequency). It is thus possible to obtain an open-circuit characteristic of a generator from this information.

$$U_s = (R_s + j \cdot X_d) I_s + U_p \quad (13.1)$$

The equation (13.1) can be assigned to an equivalent circuit shown in figure 13.3. The terminal voltage is a function of the exciting current and the magnetization characteristic. The effective reactance is the reactance at the operating  $X_d$ .

$$U_p = j \cdot X_d I_f \quad (13.2)$$

The stator resistance is often neglected against the much larger reactors.

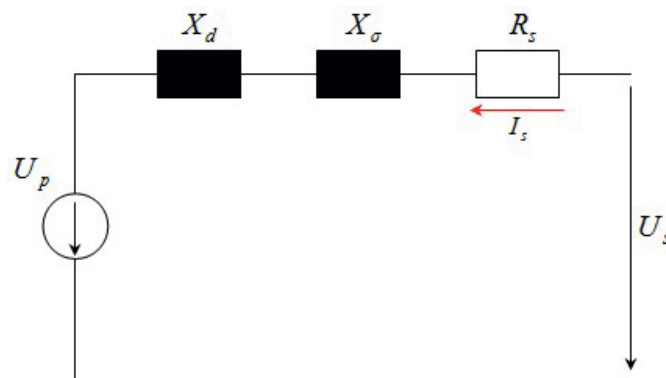


Figure 13.3 : No-load



### 13.2.2 Short Circuit Test

The mover voltage is suspended by the voltage drop across the reactance  $-j \cdot X_d I_k$  except for the small stray voltage drop. The machine is demagnetized. Its voltage equation is as follows ;

$$0 = j X_d I_s + U_p \tag{13.3}$$

$$I_s = -I_k = -\frac{U_p}{j X_d} = j \frac{U_p}{X_d}$$

The real power is zero and the power is also zero. The short-circuit is a reactive power state. The short-circuit per-phase equivalent circuit and phasor diagram is shown in figure 13.4.

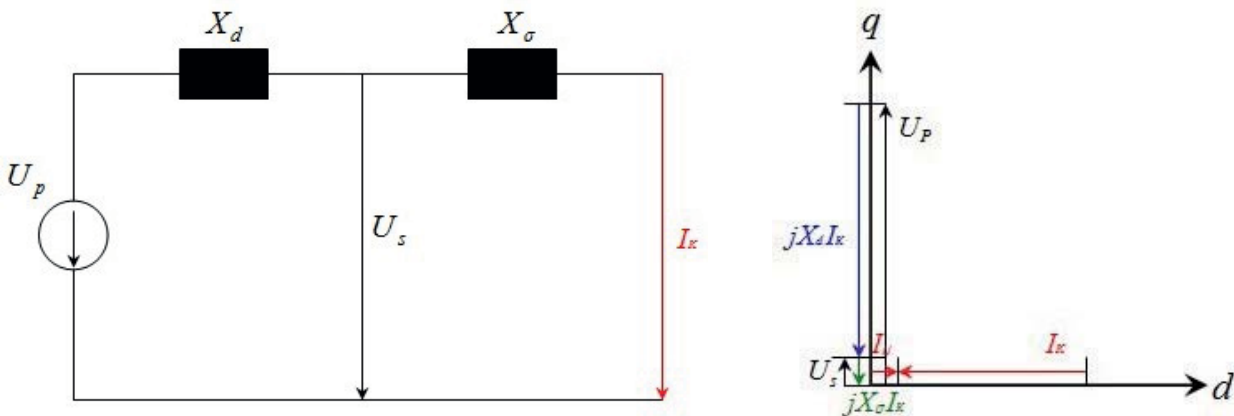


Figure 13.4 : Short-circuit and Phasor Diagram

In contrast to the asynchronous machine, the synchronous machine give a continuous short-circuit current. This is in the asynchronous machine with terminal short-circuit = 0, when all transient phenomena have subsided. The duration of short-circuit current of the synchronous machine is usually measured at least 3 times of the rated current.

## 13.3 Measurements

### 13.3.1 Open Circuit Test

In this test, the machine is run at a discrete speed with the terminals of the machine disconnected from any external circuit.

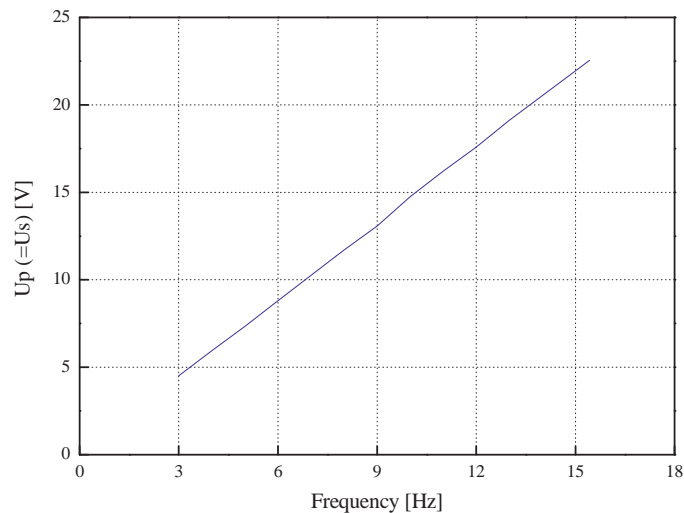


Figure 13.5 : Voltage Characteristic by Different Frequencies under No-load Test

As there is no armature current, the measured terminal voltage is the induced voltage. As shown figure 13.5, the open-circuit voltage is linearly related to the speed.

### 13.3.2 Short Circuit Test

The short-circuit test is carried out with the terminals of the machine short circuited. When short circuited, armature reaction prevents the machine from saturating. Synchronous reactance is usually significantly larger than armature resistance. As a result, the armature current significantly lags the induced voltage.

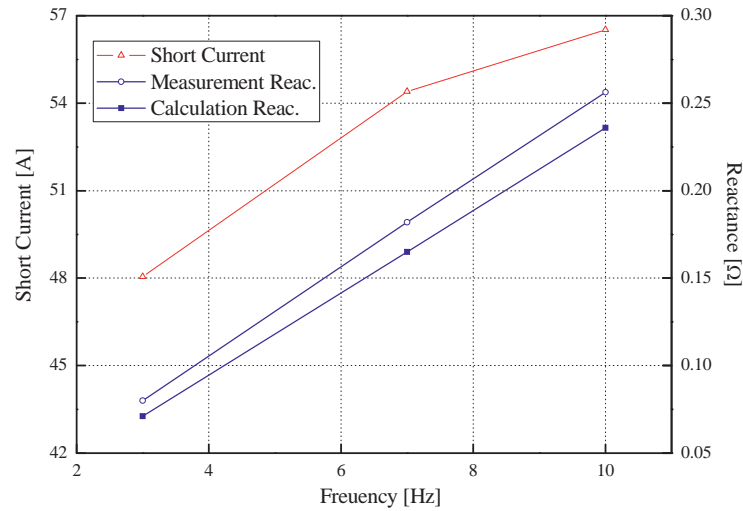


Figure 13.6 : Voltage Characteristic by Different Frequencies under Short-Circuit Test

Synchronous reactance is a combination of armature winding leakage reactance and a reactance used to represent armature reaction. The synchronous machine test gives the induced voltage and the current when armature reaction is greatest, for a range of field current values. This data can be used to approximate the synchronous reactance of the machine.

The following expression indicates the analytical formula for the reactance calculation.

The main field voltage

$$U_p = j \cdot \frac{\omega}{\sqrt{2}} \cdot \Psi = j \cdot X_d \cdot I_f + j \cdot X_s \cdot I_s \quad (13.4)$$

Is composed of the mover voltage and the armature reaction along  $j \cdot X_s \cdot I_s$

$$U_p = j \cdot X_d \cdot I_f \quad (13.5)$$

The voltage equation is of the form

$$U_s = R_s I_s + j X_\sigma I_s + j X_d I_s + U_p \quad (13.6)$$

With the synchronous reactance

$$X_d = X_d + X_\sigma \quad (13.7)$$

Compared to the analytical calculation, the reactance by the measurement data can be achieved as follows.

$$Z \approx \frac{U_{oc}}{I_{sc}}, \quad X \gg R \tag{13.8}$$

$$X = \sqrt{Z^2 - R^2}$$

Similar to the open-circuit test, the short-circuit current varies linearly with the speed. In the figure 13.6, the blue lines represent the reactance, and both of the measurement and analytical calculation has a margin of error within 11 [%].

### 13.3.2 On Load Test

Stand alone operation of a synchronous generator is in some ways the simplest form of operation. If stand alone operation is used, a generator is connected to a load and is responsible for supplying all power and reactive power required by the load. The phasor diagram in the figure 13.7 is equal to the resistive phasor diagram in the figure 9.3.

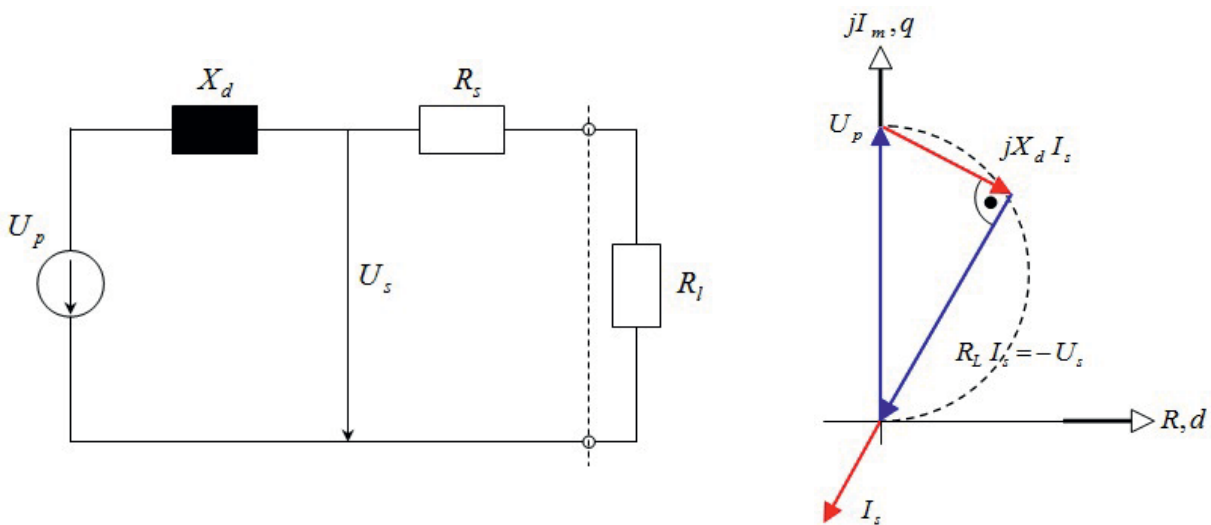


Figure 13.7 : Equivalent Circuit and Phasor Diagram of Generator with Resistive Load



In an experiment, it is achieved by the load of variable resistance ; their value is set in 0.6 [Ω], 0.68 [Ω], 0.82 [Ω], and 0.9 [Ω] from the figure 13.8 to the figure 13.11, respectively.

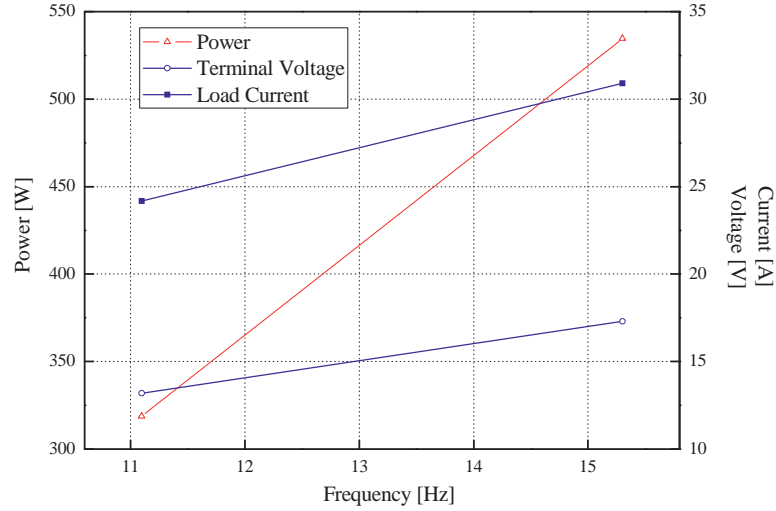


Figure 13.8 : Load Current, Terminal Voltage and Power at 0.6 [Ω]

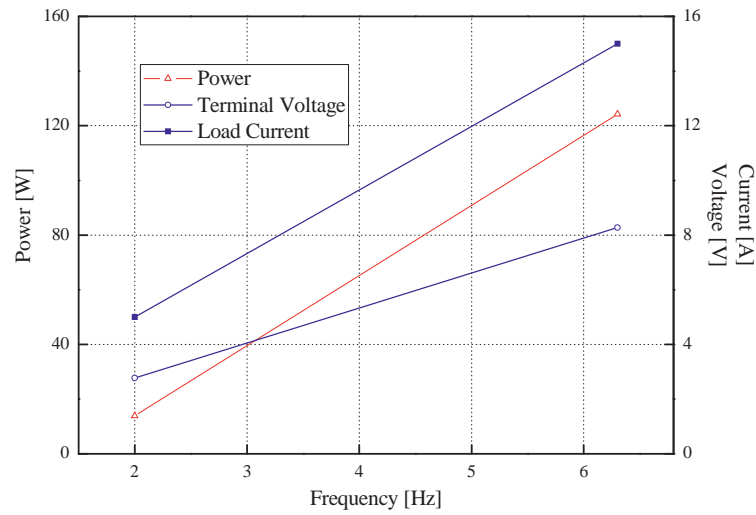


Figure 13.9 : Load Current, Terminal Voltage and Power at 0.68 [Ω]

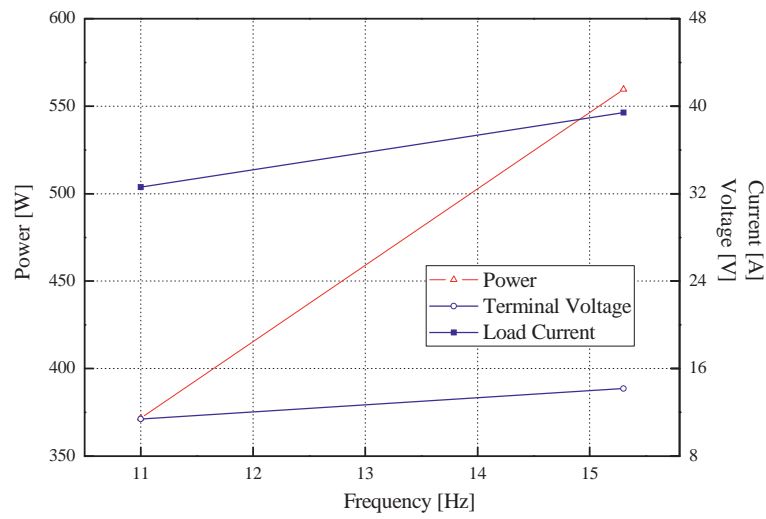


Figure 13.10 : Load Current, Terminal Voltage and Power at 0.82 [Ω]

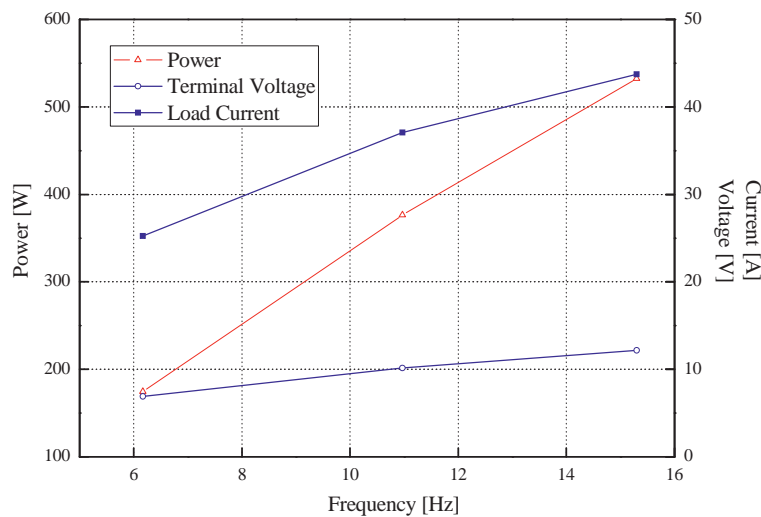


Figure 13.11 : Load Current, Terminal Voltage and Power at 0.9 [Ω]

Under different adjustable resistance condition, as the frequency is higher, all of the power, terminal voltage, and load current increase. Moreover, as the adjustable resistance increases, the load current is also higher. Meanwhile the terminal voltage decrease, consequently the power of the machine will be decreased.



## **13.4 Discussion**

The evaluation of the designed and manufactured generator should be achieved by assessment. The study is concluded by an open-circuit test, short-circuit test, and load test to evaluate the performance of the cylindrical linear oscillating generator. In this measurement, it is assumed that the electrical resistance of the circuit is zero and flux linkage is constant. Each test gives the effective results for more accurate and sustainable operation of the machine.

---

## 14 Conclusion & Outlook

### 14.1 Conclusion

The objective of this thesis is to evaluate a linear oscillating generator. In this study, analysis techniques are used to evaluate different topologies for the linear oscillating generator. Five different linear oscillating generator designs are evaluated. These designs include Cartesian topology, cylindrical topology, hybrid stepping generator, cylindrical reluctance machine, and transverse flux machine. The weight factors of electrical analysis and structural aspect is dependent on the design concept.

This thesis is mainly on comparative study of linear oscillating generators for hybrid electric vehicle applications. Nowadays, oscillating principles are mostly using linear motion because of the absence of mechanical devices such as a crankshaft and a connecting rod. It contributes to higher efficiency and lightweight of the machine. On the other hand, a comprehensive study of linear oscillating generators is still missing concerning the generator topology, number of phases, excitation method, bearing construction, voltage stability under load, sensor and inverter equipment. Based on the questions, the five different topologies are presented ; Cartesian topology, cylindrical topology, hybrid stepping generator, cylindrical reluctance machine, and transverse flux machine in this work.

First of all, it is achieved by correcting data about existing machines a literature study. The properties of each proposed topology are investigated by machine dimensioning with help of the equivalent circuit method considering leakage elements as initial modeling. In addition, certain topology is accomplished by optimal process and 3-D EMC analysis adding to the 2-D EMC. In the next step, the optimal model is selected by comparing each topology using the weight factors of electrical analysis and structural aspect. Finally, the single-phase cylindrical topology with back-iron in the PM mover has a preference for the optimal model. The iron saturation which has significant effect on magnetic fields of machines is achieved for accurate modeling of the machine. Besides, the power losses are examined for a more accurate performance characteristics of the machine not only iron loss such as hysteresis and eddy-current by different materials and various frequencies, but also cooper loss and eddy-current loss of PM.

Linear oscillating generator with linear mass requires a support system that can resist dynamic forces and the resulting vibrations. It becomes more and more important for dynamic equipment foundations due to various design criteria and methods and procedures of analysis, design and construction. Therefore, the reliable design of power transmitting shaft and bolted joints combined with it is performed using fatigue (stress-life) characteristics for stable operation of the equipment foundations. Also, in order to preserve the optimal conditions ensuring the good operation of the



generator, it is established to well understand and control the thermal behavior of the generator.

This good understanding needs the ideal design of cooler to ensure the operating temperatures do not exceed the acceptable limits of used materials. As a result, it is obvious that the consideration of thermal characteristic can show the temperature distribution under the operating frequency in the generator. At last, this study is achieved by elaborate manufacture and close assessment for the performance evaluation.

The results of this study will give elaborate information about the design rules and the performance data of linear oscillating gensets and in parallel tools for the calculation, simulation and the design of linear oscillating machines will be available. It can be useful to more accurate machine design and more accurately prediction of machine performance. The proposed methods allow us to draw a very important design rule, as a result it can be provided to less time of the machine design and analysis.

## **14.2 Outlook**

Henceforth, it is to be studied in respect of the feasibility of the free piston engine using a linear oscillating generator as a primary power unit. Linear combustion engine is suitable for serial hybrid vehicles. A free piston engine linear generator can offer a compact, mechanically simple design for a PPU that can be man-portable or vehicle distributed. Because the piston is not constrained by connecting rod, the engine can achieve variable compression ratios, making it adaptable to a wide range of fuels, including natural gas, diesel fuels, and other potential alternative fuels. The main challenge in developing a successful free piston engine linear generator is to develop an efficient linear generator to convert the piston motion directly into electrical power. This solution presents for future very clearly system power.

It will be achieved easily and precisely by the proposed method in this study.



---

## Symbols and Acronyms

$A$	Current sheet
$A$	Potential
$A_s, A_{rea}$	Cross-section area
$a$	Acceleration
$\alpha$	Mechanical degree, Optimal control
$\alpha_p$	Ratio of magnet pole length
$B$	Magnetic flux density
$B$	Flux density distribution
$B$	Bessek funtion
$B_{rem}$	Residual magnetic flux density
$b_0$	Length of slot-opening
$b_s$	Breadth of slot
$b_t$	Thickness of pole
$C$	Second adjustable factor
$C(t)$	Time function
$C_p$	Specific heat capacity
$d$	Diameter
$d$	Thickness
$d, q$	Coordinate axis
$D_e$	Density of coolant material
$\Delta$	Difference
$\nabla$	Coulomb gauge
$\delta_{sd}$	Skin depth of PM
$E$	Electric field strength
$F_{bs}$	Strength of bolt
$F_{ave}$	Average force
$F_{den}$	Force density
$f$	Frequency
$\gamma$	Travelling wave
$\gamma$	Weight
$H, H_s$	Magnetic field
$H_c$	Coercive force
$h_i$	Width of pole



$h_m, \tau_m$	Height of PM
$h_t$	Height of teeth
$h_y, h_{ys}$	Height of yoke
$h_s, t_h$	Height of slot
$I_f$	Exciting current
$I, i, I_s$	Current
$I_k$	$n^{\text{th}}$ -order stator harmonic current and short-circuit current
$I_\mu$	Magnetizing current
$J$	Current density
$k$	Coefficient related to the $\alpha$
$k$	Coefficient for expression of Bessel function
$k$	Adjusting coefficient with measured value of material data
$k$	Order number of the time harmonic
$k_{bh}$	Technical factor for hysteresis loss
$k_{bw}$	Technical factor for eddy-current loss
$k_f$	Fill factor
$k_{res}$	Coil resistance per kilometer
$\kappa$	Conductivity
$L, L_h$	Inductance
$l, l_z, l_s, l_E, l_{core}$	Length of conductor
$l_m$	Length of PM
$l_{mo}$	Length of mover
$l_t$	Length of pole in stator
$l_{tt}$	Pole-pitch in stator
$l_\delta, \delta$	Length of air-gap
$l_{ts}, l_{tm}$	Teeth length of stator and translator in cylindrical reluctance machine
$l_d$	Length of hypotenuse
$\lambda, \Psi$	Flux linkage
$M$	Magnetization
$M, m$	Mass
$m_m$	Mass of mover
$m_l$	Mass of load
$m_s$	Number of phase
$\mu$	Permeability
$\mu_0$	Permeability of free space (or air)



$\mu_r$	Relative permeability
$\mu_{fe}$	Permeability of ferromagnetism
$N$	Number of cycle of fatigue limit
$P$	Loss
$P_s$	Force and moment
$\phi$	Magnetic flux
$\varphi$	Load angle
$R_m$	Reluctance
$R_s$	Resistance
$R_L$	Load resistance
$R_{m\delta}$	Reluctance in air-gap
$\rho$	Density
$\rho_m$	Electric resistivity of PM
$r$	Radius
$r_{cs}$	Radius to the tooth-tip from center
$r_2, r_0$	Radius to the stator from center
$r_1, r_i$	Radius to the mover from center
$r_{im}$	Radius to the PM from center
$r_s$	Radius to the shaft from center
$r_w$	Radius to the shaft from center
$S$	Displacement
$\sigma$	Conductivity
$\sigma$	Strength
$\sigma_{en}$	Endurance limit value
$\sigma_{al}$	Alternating strength
$T_m$	Torsion strength
$t$	Time
$t_{hh}$	Total length of slot and tooth-tip
$\tau, \tau_p, \tau_{ps}$	Pole pitch
$\tau_{pm}$	Pole pitch of PM
$\tau_{sw}$	Length of tooth
$\tau_w$	Thrust ratio
$\tau_{wp}$	Winding pitch
$\theta$	Tangent angle
$\theta_{on}$	Turn-on angle of switch



$\theta_{off}$	Turn-off angle of switch
$\Theta, \Theta_a, \Theta_m$	Magnetomotive force and by PM
$U_p$	Load Voltage
$U_s$	Speed
$\nu$	Kinematic viscosity
$\nu_{kv}$	Speed of coolant
$W_m$	Magnetic energy
$W_{co}$	Magnetic co-energy
$w_m$	Width of PM
$w_t$	Width of teeth
$w_s$	Winding ratio
$X$	Arbitrary position
$X_d$	Reactance
$X_L$	Inductive reactance
$X_C$	Capacitive reactance
$\xi$	Thermal conductivity
$Z$	Impedance
$z_d$	Axial displacement
$\zeta$	Safety factor

## Subscripts

$a$	Axial
$a$	Aligned
$ave$	Average
$a, b, c$	Each phase
$a\delta$	by armature in air-gap
$a\sigma$	Leakage by armature
$ats, lats$	in y-axis and axial direction in air region between stator stacks
$b$	Bending
$b$	in the slot of aligned-position in cylindrical topology
$bs, bs-1, bs-2$	Shank portion of bolt
$core$	Core
$comp$	Compression
$cu, coil$	Copper

<i>con</i>	Convective
$\wedge$	Amplitude
<i>dx</i>	Exiguity distance between adjacent flux lines
$\delta r, \delta a$	in z-axis and axial direction in air-gap
<i>ed</i>	Eddy-current
<i>hyst</i>	Hysteresis
<i>i, j</i>	Indices of progression
<i>I, II</i>	Region
max, min, <i>mean</i>	Maximum, Minimum, and Average
<i>m</i>	PM
<i>me</i>	in PM edge
<i>mm</i>	between PMs
<i>ma</i>	Y-axis direction in PM
<i>m<math>\delta</math></i>	by PM in air-gap
<i>m<math>\sigma</math></i>	Leakage by PM
<i>n</i>	Ordinal number
<i>ns</i>	between PM of unaligned-position in cylindrical topology
<i>oc</i>	Open-circuit
<i>PM</i>	Permanent magnet
<i>r, z</i>	Coordinate plane
<i>rms</i>	Root mean square
<i>s, sa</i>	in y-axis and axial direction in slot
<i>sc</i>	Short-circuit
<i>sh</i>	Shaft
<i>sur</i>	Surface
$\sigma$	Leakage
$\sigma_1$	by left-side of aligned-position in cylindrical topology
$\sigma_2$	by right-side of aligned-position in cylindrical topology
$\sigma_3$	by unaligned-position in cylindrical topology
$\sigma_a$	Leakage in aligned position
$\sigma_{u1}$	Leakage of lower part in unaligned position
$\sigma_{u2}$	Leakage of upper part in unaligned position
<i>t</i>	Torsion
<i>ten</i>	Tensile
<i>ts, tsa</i>	in z-axis and axial direction in stator teeth
<i>u</i>	Unaligned
<i>V, V1, V2</i>	Volume of constant permeability and field with field dependent permeability
<i>x</i>	Arbitrary distance to a flux line from specific position
<i>x, y, z</i>	Coordinate



$y$	Arbitrary distance between PMs
$y_i$	yield
$y_{sr}, y_{sa}$	in back-iron of stator and air region
0	Initial value
(1), (3)	Single- and Three-phase

## Indices

APU	Auxiliary Power Unit
CLRM	Cylindrical Linear Reluctance Machine
CLSRM	Cylindrical Linear Switched Reluctance Machine
Deg.	Degree
EMC	Equivalent Magnetic Circuit
EMCN	Equivalent Magnetic Circuit Network
FEM, FEA	Finite Element Method, Finite Element Analysis
HEV	Hybrid Electric Vehicle
HSPM	Hybrid Stepping Permanent Magnet
IC	Internal Combustion
LTFM	Linear Transverse Flux Machine
LVRM	Linear Variable Reluctance Machine
MMF	Magneto Motive Force
Nu	Nusselt number
Pr	Prandtl number
Re	Reynolds number
Sec.	Second
SMC	Soft Magnetic Composite
SRM	Switched Reluctance Machine
TFE	Transverse Flux Element
TFM	Transverse Flux Machine
TFPM	Transverse Flux Permanent Magnet
2-D	Two Dimension
3-D	Three Dimension



---

## List of Figures

Figure 2.1	Linear Machine .....	5
Figure 2.2	Typical Series Hybrid Electric System .....	8
Figure 2.3	Free Piston Linear Combustion Engine .....	9
Figure 3.1	Analysis Flow .....	11
Figure 3.2	Cartesian Topology .....	12
Figure 3.3	Cylindrical Topology .....	13
Figure 3.4	Hybrid Stepping .....	14
Figure 3.5	Tubular Reluctance .....	15
Figure 3.6	Transverse Flux Machine (TFM) .....	15
Figure 4.1	Cartesian Topology .....	22
Figure 4.2	Force by Interaction of a PM and Stator-Teeth .....	23
Figure 4.3	Type I .....	23
Figure 4.4	Type II .....	24
Figure 4.5	Type III .....	24
Figure 4.6	Cross-Section of Cartesian System .....	25
Figure 4.7	Type I with Assembly .....	26
Figure 4.8	Leakage Flux between Magnets .....	27
Figure 4.9	Leakage Flux in Magnet Edge .....	27
Figure 4.10	Type II with Assembly .....	28
Figure 4.11	Type III with Assembly .....	30
Figure 4.12	Magnetic Flux Characteristics .....	32
Figure 4.13	Force by Height of PM .....	33
Figure 4.14	Force by Width of PM .....	34
Figure 4.15	Force and Flux-Density by Width of Yoke .....	34
Figure 4.16	Force and Flux-Density by Length of Yoke .....	35
Figure 4.17	Force and Flux-Density by Width of Teeth .....	36
Figure 4.18	Configurations of Width of Teeth at Constant Width of Magnet .....	36
Figure 4.19	Force and Flux Density by Length of Slot-Opening .....	37
Figure 4.20	Force Density & Efficiency .....	39
Figure 5.1	Cylindrical Topology .....	42
Figure 5.2	Force by Interaction of a PM and Armature .....	43
Figure 5.3	Flux Characteristics by Translator Position .....	44
Figure 5.4	Single-Phase System .....	45
Figure 5.5	Unaligned Position .....	46
Figure 5.6	Permeance at Unaligned Position .....	46



Figure 5.7	Aligned Position .....	47
Figure 5.8	Permeance at Unaligned Position .....	48
Figure 5.9	One-Phase System with Long-stroke .....	49
Figure 5.10	Unaligned Position .....	50
Figure 5.11	Aligned Position .....	51
Figure 6.1	Hybrid Stepping Generator .....	54
Figure 6.2	HSPM Machine with Surface Mounted PMs Mover .....	55
Figure 6.3	HSPM Machine with Flux Concentrating PMs Mover .....	56
Figure 6.4	Flux Characteristic of Surface Mounted PMs Mover Machine .....	57
Figure 6.5	Surface Mounted PMs Mover Machine .....	58
Figure 6.6	Flux Characteristic of Flux Concentrating PMs Mover Machine .....	58
Figure 6.7	Flux Concentrating PMs Mover Machine .....	59
Figure 6.8	Comparison of Categories .....	60
Figure 6.9	Novel Model .....	61
Figure 6.10	Configuration of New Hybrid Stepping Generator .....	61
Figure 6.11	Comparison of Flux Concentrating PMs Mover (Slanted) and Proposed Flux Concentrating PMs Mover .....	64
Figure 7.1	Three-Phase Cylindrical Linear Reluctance Generator .....	68
Figure 7.2	Cylindrical Linear Switched Reluctance Machine .....	69
Figure 7.3	Shapes of Mover Teeth .....	71
Figure 7.4	Ideal Inductance and Force Profile .....	73
Figure 7.5	Aligned Position of Rectangle Shape .....	75
Figure 7.6	Unaligned Position of Rectangle Shape .....	76
Figure 7.7	Trapezoidal Shape .....	77
Figure 7.8	Comparison of Inductance Profile .....	79
Figure 7.9	Comparison by Mover Shape .....	80
Figure 8.1	Analysis Process .....	85
Figure 8.2	Fundamental Building Block of Single-sided TFE Machine .....	86
Figure 8.3	Double-sided TFPM Machine .....	86
Figure 8.4	EMC of TFE .....	87
Figure 8.5	Cross-section of TFE Machine .....	88
Figure 8.6	Thrust Force in the Direction of X-axis .....	91
Figure 8.7	Force in the Direction of Z-axis .....	92
Figure 8.8	Maximum Magnetic Energy in TFE (2-D) .....	93
Figure 8.9	Minimum Magnetic Energy in TFE (2-D) .....	94
Figure 8.10	EMC in TFPM (2-D) .....	95
Figure 8.11	Fundamental Building Block of TFPM Machine .....	97
Figure 8.12	Maximum Magnetic Energy in TFPM (3-D) .....	99
Figure 8.13	Configuration for $R_{ats}$ and $R_{lats}$ .....	101



Figure 8.14	Minimum Magnetic Energy in TFPM (3-D) .....	103
Figure 8.15	The Investigated 3-D FEM of TFPM Machine .....	105
Figure 9.1	No-load ( $I_s = 0 \rightarrow U_s = U_p$ ) .....	108
Figure 9.2	Generator under General-Load .....	109
Figure 9.3	Generator under Load .....	109
Figure 9.4	Load-dependent Ellipses of the Terminal Voltage .....	110
Figure 9.5	Comparison of the Geometric Conditions of a Single-phase and a Three-phase System .....	114
Figure 9.6	Comparative Study on the Characteristics of Each Topology .....	118
Figure 10.1	Relationship between Magnetic Flux and Current .....	122
Figure 10.2	B-H Curve .....	123
Figure 10.3	Single-Phase Cylindrical Topology .....	124
Figure 10.4	Analytical Field Model .....	125
Figure 10.5	Equivalent Current Sheet Distribution .....	126
Figure 10.6	Flux Characteristic of Optimal Model .....	130
Figure 10.7	Comparison of Average Force by Calculation Methods .....	130
Figure 10.8	Influence of the Frequency of the Magnetization Curve, (Quote : Material Specification M250-35, ThyssenKrupp) .....	136
Figure 10.9	Parameter Adjustment of the Loss Equations to the Measured Data, $k=1, C=3.1$ .....	138
Figure 10.10	Comparison of Losses by Steinmetz and Bertotti .....	138
Figure 10.11	Loss Adjustment for M400-50 Measured at the Sampling Points, $k=1, C=1, B_{\max} = 1$ [T] Green Dash Line : Technology Factors with $k_{bh} = k_{bw} = 1.5$ .....	139
Figure 10.12	The Calculation of the Eddy Current Loss, M400-50A .....	140
Figure 10.13	Current Density $J$ (y) by the Plate Thickness, M400-50A .....	141
Figure 10.14	Adaptation of the Logarithmic Approximation $\mu_r(z)$ , Equation (10.31) to the Measured Values for $\mu_m(f, 2n)$ (M250-35A, $B_{\max} = 1$ [T], $50$ [Hz] $\leq f \leq 1000$ [Hz]) .....	143
Figure 10.15	Parameter Fit for GKN Sinter Metals, $k=0.85, C=2, k_{bh} = k_{bw} = 1.5$ , Max. Error in $50$ [Hz] = $0.67$ [%], $400$ [Hz] = $1.48$ [%], and $1000$ [Hz] = $1.46$ [%] .....	144
Figure 10.16	Comparison of Losses, $k=1, C=1, k_{bh} = k_{bw} = 1.5$ , and $50$ [Hz] .....	149
Figure 10.17	Dimension of Cylindrical Linear Generator .....	150
Figure 10.18	Construction of the Cylindrical Generator in Star-shape with 6 Sectors .....	151
Figure 11.1	Three Strengths ; Axial, Bending, and Torsion .....	157
Figure 11.2	Bolts of Uniform Strength .....	161
Figure 11.3	Normal Stress .....	163



## List of Figures

---

Figure 11.4	Dimension of Mechanical Part in Cylindrical Linear Generator .....	165
Figure 12.1	Coolant Material : Insulation Class H (180 [°C]) .....	169
Figure 12.2	Cylindrical Topology with Heat Generation .....	171
Figure 12.3	Temperature Distributions in Stator & Mover Core by Frequency .....	173
Figure 12.4	Temperature Distributions in Coil & Permanent Magnet by Frequency .....	174
Figure 12.5	Temperature Distributions in 50 [Hz] .....	175
Figure 12.6	Temperature Distributions in 500 [Hz] .....	175
Figure 12.7	Temperature Distributions in 1000 [Hz] .....	176
Figure 13.1	Test Environment for Measurement of Cylindrical Generator .....	179
Figure 13.2	Voltage vs. Current Plot .....	180
Figure 13.3	No-load .....	181
Figure 13.4	Short-circuit and Phasor Diagram .....	182
Figure 13.5	Voltage Characteristic by Different Frequencies under No-load Test .....	183
Figure 13.6	Voltage Characteristic by Different Frequencies under Short-Circuit Test .....	184
Figure 13.7	Equivalent Circuit and Phasor Diagram of Generator with Resistive Load .....	185
Figure 13.8	Load Current, Terminal Voltage and Power at 0.6 [ $\Omega$ ] .....	186
Figure 13.9	Load Current, Terminal Voltage and Power at 0.68 [ $\Omega$ ] .....	186
Figure 13.10	Load Current, Terminal Voltage and Power at 0.82 [ $\Omega$ ] .....	187
Figure 13.11	Load Current, Terminal Voltage and Power at 0.9 [ $\Omega$ ] .....	187



---

## List of Tables

Table 4.1	Object Function, Design Variables, and Constraints .....	32
Table 4.2	Comparison Result between Initial and Optimal Design .....	37
Table 7.1	Compare Energy and Force .....	80
Table 8.1	Estimation by EMC and FEM .....	106
Table 9.1	Loading Condition, Shape and Position of the Ellipse .....	111
Table 9.2	Measurement of Each Topology by Criterion .....	118
Table 10.1	Governing Partial Differential Equations .....	127
Table 10.2	Material Data Sheet of M250-35 .....	137
Table 10.3	Material Data Sheet of M400-50 .....	139
Table 10.4	Material Data Sheet of PM4EM11 in GKN Sinter Metals .....	144





---

## Bibliography

- [1] C. C. Chan, *The state of the art of electric and hybrid vehicles*, Proc. IEEE, vol. 90, pp. 247-275, 2002
- [2] S. Barsali, C. Miulli, and A. Possenti, *A control strategy to minimize fuel consumption of series hybrid electric vehicles*, IEEE Trans. On Energy Conversion, Vol. 19, No. 1, pp., 187-195, 2004
- [3] ERIC R. LAITHWAITE, *Linear Electric Machines- A Personal View*, PROCEEDINGS OF THE IEEE, VOL. 63, NO. 2, FEBRUARY 1975
- [4] S.ANasar, I.Boldea, *Linear Motion Electric Machines*
- [5] Tae-Won Lee, *The Finite Element Analysis and the Optimum Geometric Design of Linear Motor*
- [6] Sigitas Kudarauskas, *Introduction to oscillating electrical machines*
- [7] Park, K.; Hong, E.; and Lee, H. K., *Linear Motor For Linear Compressor* (2002). International Compressor Engineering Conference. Paper 1544
- [8] Boucherot, P., 1908, *Appareils et machines à courant et mouvement alternatifs*, *Bulletin de la Société internationale des Électriciens*, Paris, décembre: p. 731-755
- [9] Koenig W., *antriebe fuer Kleinkompressor, insbesondere fuer Kältemaschinen*, Deutsche Patentschrift, N. 584764, 1935
- [10] Cadman R. V., *A TECHNIQUE FOR THE DESIGN OF ELECTRODYNAMIC OSCILLATING COMPRESSORS*, Ph.D. Thesis, Purdue University, USA, 1967
- [11] Pollak, E, *Performance Study of Oscillating Electrodynamic Compressor*, Ph.D. Thesis, Purdue University, USA, 1978
- [12] NISHIOKA K., *NONLINEAR ANALYSIS OF ELECTROMAGNETIC LINEAR MOTOR COMPRESSORS*, Ph.D. Thesis, Purdue University, USA, 1980
- [13] Lee, H. K.; Song, G. Y.; Park, J. S.; Hong, E. P.; Jung, W. H.; and Park, K. B., *Development of the Linear Compressor for a Household Refrigerator* (2000). International Compressor Engineering Conference. Paper 1364.
- [14] Jarret J., *Etude du transfert de l'énergie dans les machines a mouvement rectiligne alternatif a reluctance variable*, RGE, No. 2, 1960, pp. 109-114
- [15] Jörgen Hansson and Mats Leksell, *Performance of a Series Hybrid Electric Vehicle with a Free-Piston Energy Converter*
- [16] G. Maggetto and J. Van Mierlo, *Electric and electric hybrid vehicle technology : A survey*, in *Proc. Electric, Hybrid, and Fuel Cell Vehicles*, Apr. 2000, pp. 1/1–111.
- [17] P. A. J. Achten, J. P. J. van den Oever, J. Potma, and G. E. M. Vael, *Horsepower with Brains: the Design of the CHIRON Free Piston Engine*, SAE paper, 2000
- [18] <http://www.lceproject.org/en/principle/>
- [19] Waqas M. Arshad, Thomas Bäckström, Peter Thelin and Chandur Sadarangani, *Integrated Free-Piston Generators : An Overview*



- [20] J.D. Law, T.J. Busch, and T.A. Lipo, *Magnetic circuit Modeling of the field regulated reluctance machine Part I : model development*, IEEE Trans. Energy Conversion, vol. 11, no. 1, 1996
- [21] You-Chiuan Hsu, Min-Fu Hsieh, Richard A. McMahon, *A General Design Method for Electric Machines Using Magnetic Circuit Model Considering the Flux Saturation Problem*, PEDS2009
- [22] Y.G. Guo and J.G. Zhu, *STUDY OF PERMANENT MAGNET TRANSVERSE FLUX MOTORS WITH SOFT MAGNETIC COMPOSITE CORE*, Australasian Universities Power Engineering Conference (AUPEC 2004)
- [23] P. G. Dickinson, A. G. Jack, and B. C. Mecrow, *Improved permanent magnet machines with claw pole armatures*, International Conference on Electrical Machines, CD-ROM pages 5, Brugge, Belgium, August 2002
- [24] Min-Fu Hsieh, You-Chiuan Hsu, *A Generalized Magnetic Circuit Modeling Approach for Design of Surface Permanent-Magnet Machines*, IEEE TRANSACTIONS ON INDUSTRIAL ELECTRONICS, VOL. 59, NO. 2, FEBRUARY 2012
- [25] V. Ostovic, J. M. Miller, V. K. Garg, R. D. Schultz, and S. H. Swales, *A magnetic-equivalent-circuit-based performance computation of a Lundell alternator*, IEEE Trans. Ind. Appl., vol. 35, no. 4, pp. 825-830, July 1999
- [26] J.Mizia, K.A.damiak, A.R.Eastham, G.E .Dawson, *FINITE ELEMENT FORCE CALCULATION : COMPARISON OF METHODS FOR ELECTRIC MACHINES*, IEEE TRANSACTIONS ON MAGNETICS, VOL. 24, NO. I, JANUARY 1988
- [27] Ronghai Qu, and Thomas A. Lipo, *Analysis and Modeling of Airgap & Zigzag Leakage Fluxes in a Surface-Mounted-PM Machine*, 0-7803-7420-7/02/\$17.00 © 2002 IEEE
- [28] Jasbir S.Arora, *'Introduction to Optimum Design'* (Second Edition)
- [29] Sun-Ki Hong, Ho-Yong Choi, Jae-Won Lim, Hyo-Jae Lim, Hyun-Kyo Jung, *Analysis of Tubular-type Linear Generator for Free-Piston Engine*
- [30] W.-J. Kim, M. T. Berhan, D. L. Trumper and J. H. Lang, *Analysis and Implementation of a Tubular Motor with Halbach Magnet Array*, 0-7803-3544-9/96 55.00 © 1996 IEEE
- [31] A. Cosic, J. Lindback, W. M. Arshald, M. Ieksell, P. Thelin, and E. Nordlund, *Application of a free-piston generator in a series hybrid vehicle*, presented at the Proc. 4th Int. Symp. Linear Drive Ind. Appl., LDIA 2003, Birmingham, U.K., 8–10, 2003
- [32] C. Wang, S. A. Nasar, Boldea, *Three phase flux reversal machine (FRM)*, IEE Trans. Electrical power application, vol. 146, No.2, pp. 139-146, March 1999
- [33] D . S . More, B .G . Femandes, *Novel Three Phase Flux Reversal Machine with Full Pitch Winding*, the 7<sup>th</sup> International Conference on Power Electronics
- [34] Pia Salminen, Markku Niemelä, Juha Pyrhönen and Juhani Mantere, *Performance analysis of fractional slot wound PM-motors for low speed applications*, 0-7803-8486-5/04/\$20.00 © 2004 IEEE

- [35] Sungin Jeong, *Modeling of linear oscillating generator for internal combustion engine*, Jahresbericht 2009, IMAB
- [36] J. Vining, T.A. Lipo, G. Venkataramanan, *Design and Optimization of a Novel Hybrid Transverse / Longitudinal Flux, Wound-Field Linear Machine for Ocean Wave Energy Conversion*, 2009 IEEE Energy Conversion Congress and Exposition
- [37] J. A. Güemes, A. M. Iraolagoitia, M. P. Donsión and J. I. Del Hoyo, *Analysis of Torque in Permanent Magnet Synchronous Motors with Fractional Slot Windings*, Proceedings of the 2008 International Conference on Electrical Machines
- [38] Jawad Faiz, Mahdi Ebrahimi-salary and Gh. Shahgholian, *Cogging Force Alleviation in Linear Permanent Magnet Generators*, IEEE AFRICON 2009, 978-1-4244-3919-5/09/\$25.00 ©2009 IEEE
- [39] Flux Software, *Parametric Design of Linear Reluctance Actuators*, R.E.Clark, University of Sheffield
- [40] J. Corda, *Cylindrical Linear Stepper Motor*
- [41] J. Corda, M. Wilkinson, *MODELLING OF STATIC THRUST CHARACTERISTICS OF CYLINDRICAL LINEAR SWITCHED RELUCTANCE ACTUATOR*, 'Electrical Machines and Drives', 11-13 September 1995, Conference Publication No. 472
- [42] Myo Min Thet, *Design and Calculation of 75W Three-phase Linear Switched Reluctance Motor*, World Academy of Science, Engineering and Technology 24 2008
- [43] Y. H. Kim, J. H. Choi, S. I. Jeong, Y. D. Chun, S. Kim, J. Lee, M. S. Chu, K. J. Hong, and D. H. Choi, *Optimal design of switched reluctance motor using two-dimensional finite element method*, JOURNAL OF APPLIED PHYSICS, 2002 American Institute of Physics, VOLUME 91, NUMBER 10
- [44] Hamid Ehsan Akhter, Virendra K.Sharma, A.Chandra, *Starting Performance of Switched Reluctance Motor With Fixed Turn-off Angle Control Scheme*, 0-7803-7414-6102/\$17.00 02002 IEEE
- [45] R. Krishnan, *Switched Reluctance Motor Drives ; Modeling, Simulation, Analysis, Design, and Applications*
- [46] J. Vining, T.A. Lipo, G. Venkataramanan, *Design and Optimization of a Novel Hybrid Transverse / Longitudinal Flux, Wound-Field Linear Machine for Ocean Wave Energy Conversion*, 978-1-4244-2893-9/09/\$25.00 ©2009 IEEE
- [47] Nicolas Dehlinger, Maxime R. Dubois, *Clawpole Transverse Flux Machines with Amorphous Stator Cores*, Proceedings of the 2008 International Conference on Electrical Machines
- [48] Harris. M. R, Pajooman. G. H., Abu Shark. S. M., *The problem of power factor in VRPM (Transverse-flux) electrical machines*, Proc. of IEE-EMD '97, pp.386-390
- [49] Junghwan Chang, Dohyun Kang, Jiyoung Lee, and Jungpyo Hong, *Development of Transverse Flux Linear Motor With Permanent-Magnet Excitation for Direct Drive Applications*, IEEE TRANSACTIONS ON MAGNETICS, VOL. 41, NO. 5, MAY 2005



- [50] Dan-Cristian POPA, Vasile IANCU and Loránd SZABÓ, *Linear Transverse Flux Motor for Conveyors*
- [51] D.C. Popa, V. Iancu, L. Szabó, *Linear Transverse Flux Motor for Conveyors*, 6th International Symposium on Linear Drives for Industrial Application (LDIA), Lille (France), paper 188
- [52] Dipl.Ing. Hailong Gao, *Numerisches Berechnungsverfahren fuer Synchronmaschinen in Transversalfluss-Bauweise*, Reihe 21 Elektrotechnik Nr.151
- [53] DMITRY SVECHKARENKO, *On Design and Analysis of a Novel Transverse Flux Generator for Direct-driven Wind Application*, Doctoral Thesis Stockholm, Sweden 2010
- [54] S. A. Nasar, *Electromagnetic Energy Conversion Devices and Systems*
- [55] R. Qu and T. A. Lipo, *Analysis and modeling of air-gap and zigzag leakage fluxes in a surface-mounted permanent magnet machine*, *IEEE Trans. Ind. Appl.*, vol. 40, no. 1, pp. 121–127, Jan./Feb. 2004
- [56] V. Ostović, *Dynamics of Saturated Electric Machines*. New York, Springer-Verlag, 1989
- [57] P. Sewell, K. J. Bradley, J. C. Clare, P. W. Wheeler, A. Ferrah, and R. Magill, *Efficient dynamic models for induction machines*, *Intl. J. Numer. Model.*, vol. 12, pp. 449-464, 1999
- [58] H. Meshgin-Kelk, J. Milimonfared, and H. A. Toliyat, *A comprehensive method for the calculation of inductance coefficients of cage induction machines*, *IEEE Trans. Energy Conversion*, vol. 18, pp. 187-193, Jun. 2003
- [59] J. Perho, *Reluctance network for analysing induction machines*, *Acta Polytechnica Scandinavica, Electrical Engineering Series*, vol. 110, pp. 1-147, Dec. 2002
- [60] J. D. Law, T. J. Busch, and T. A. Lipo, *Magnetic circuit modelling of the field regulated reluctance machine. Part I: model development*, *IEEE Trans. Energy Conversion*, vol. 11, pp. 49-55, Mar. 1996
- [61] Iron Boldea and S. A. Nasar, *Electric Drives : Second Edition*
- [62] ALIJA COSIC, *Analysis of a Novel Transverse Flux Machine with a Tubular Cross-section for Free Piston Energy Converter Application*, Doctoral Thesis, Stockholm, Sweden
- [63] *FLUX 10 3D Application*, GROUPE CEDRAT
- [64] W.-R. Canders, (TU Braunschweig) : Vorlesungsskript, *Grundlagen der Elektrischen Energietechnik - Elektromechanische Energieumformung 2013*, TU-Braunschweig, Institut für Elektrische Maschinen, Antriebe und Bahnen
- [65] A.V.Bakshi U.A.Bakshi, *Electrical Circuit Analysis*
- [66] W.-R. Canders, (TU Braunschweig) : Vorlesungsskript, *Drehstromantriebe und deren Simulation, 2010*, Master Kurs, TU-Braunschweig, Institut für Elektrische Maschinen, Antriebe und Bahnen
- [67] <http://www.sintex.com/SMC.2174.aspx>
- [68] B. Sheikh-Ghalavand, S. Vaez-Zadeh, and A. Hassanpour Isfahani, *An Improved Magnetic Equivalent Circuit Model for Iron-Core Linear Permanent-Magnet Synchronous Motors*, *IEEE TRANSACTIONS ON MAGNETICS*, VOL. 46, NO. 1, JANUARY 2010



- [69] S. Han, T. M. Jahns, and W. L. Soong, *A magnetic circuit model for an IPM synchronous machine incorporating moving airgap and crosscoupled saturation effects*, in Proc. Int. Conf. Electrical Machines and Drives, IEMDC 2007, Antalya, Turkey, May 3–5, 2007, pp. 21–26.
- [70] Yacine Amara, Jiabin Wang, and David Howe, *Analytical Prediction of Eddy-Current Loss in Modular Tubular Permanent-Magnet Machines*, IEEE TRANSACTIONS ON ENERGY CONVERSION, VOL. 20, NO. 4, DECEMBER 2005
- [71] H. Shimanaka, Y. Ito, K. Matsumura, and B. Fukuda, *Recent development of non-oriented electrical steel sheets*, J. Magn. Magn. Mater., vol. 26, pp. 57-64, 1982
- [72] G. Neidhofer and A. Schwengeler, *The application and significance of magnetic materials in large generator construction*, J. Magn. Magn. Mater.. vol. 9, pp. 112-122, 1978
- [73] Thierry Lubin, Hubert Razik, and Abderrezak Rezzoug, *Magnetic Saturation Effects on the Control of a Synchronous Reluctance Machine*, IEEE TRANSACTIONS ON ENERGY CONVERSION, VOL. 17, NO. 3, SEPTEMBER 2002
- [74] Yilu Liu and Zhenyuan Wang, *Modeling of Harmonic Sources - Magnetic Core Saturation*
- [75] Dong Liu, *Validation of Eddy Current Loss Models for Permanent Magnet Machines with Concentrated Windings*
- [76] <http://www.sintex.com/SMC-Properties---Compared.2266.aspx>
- [77] Prof. Dr.-Ing. W.-R. Canders, *Berechnung von Eisenverlusten Physikalisch basierter Ansatz nach Bertottis Theorie*, TB 13-03-03
- [78] W. Pieper and J. Gerster, *Total power loss density in a soft magnetic 49% Co–49% Fe–2% V-alloy*, JOURNAL OF APPLIED PHYSICS 109, 07A312 (2011)
- [79] Material Specification, ThyssenKrupp, M250-35
- [80] Material Specification, ThyssenKrupp, M400-50
- [81] Küpfmüller, *Einführung in die Theoretische Elektrotechnik*, Springer Verlag, Berlin, Heidelberg, New York, 1968
- [82] <http://www.gkn.com/sintermetals/capabilities/soft-magnetic-pm/Pages/materials.aspx>
- [83] C. Bode, W.-R. Canders, *Advanced Calculation of Eddy Current Losses in PMSM with tooth windings*, XIX International Conference on Electrical Machines - ICEM 2010, Rome
- [84] Yunkai Huang, Jianning Dong, Long Jin, Jianguo Zhu, and Youguang Guo, *Eddy-Current Loss Prediction in the Rotor Magnets of a Permanent Magnet Synchronous Generator With Modular Winding Feeding a Rectifier Load*, IEEE TRANSACTIONS ON MAGNETICS, VOL. 47, NO. 10, OCTOBER 2011
- [85] Kais Atallah, David Howe, Philip H. Mellor, and David A. Stone, *Rotor Loss in Permanent-Magnet Brushless AC Machines*, IEEE TRANSACTIONS ON INDUSTRY APPLICATIONS, VOL. 36, NO. 6, NOVEMBER/DECEMBER 2000
- [86] Kyoung-Jin Ko, Ji-Hwan Choi, Seok-Myeong Jang, and Jang-Young Choi, *Analysis of eddy current losses in cylindrical linear oscillatory actuator with Halbach permanent magnet array mover*, Journal of Applied Physics 111, 07B547 (2012); doi: 10.1063/1.3678316



- [87] Cornelius Bode, *Analytische und numerische Verfahren zur Beschreibung von Wirbelstromeffekten in elektrischen Maschinen*, Dissertation 2013 TU Braunschweig
- [88] James D. Grounds, *AN EPIRICAL DESIGN PROCEDURE FOR SHAFTS WITH FATIGUE LOADINGS*, DARCO- ITC-02-08-76-017
- [89] Stuart H. Loewenthal, *Factors That Affect the Fatigue Strength of Power Transmission Shafting and Their Impact on Design*, NASA Technical Memorandum 83608
- [90] Stuart H. Loewenthal, *Design of Power-Transmitting Shafts*, NASA, Reference Publication 1123 July 1984
- [91] *TORSION of SHAFTS*, Department of Chemical Engineering Strength of Materials for Chemical Engineers
- [92] <http://www.dynamics.group.shef.ac.uk/people/graeme/mec415.htm>
- [93] V. B. Bhandari, *Design of Machine Elements*
- [94] <http://www.ice-steels.com/steel-plate-sheet/DIN-17100-ST-50.html>
- [95] [http://www.efunda.com/formulae/heat\\_transfer/home/overview.cfm](http://www.efunda.com/formulae/heat_transfer/home/overview.cfm)
- [96] Incropera, Frank, P., DeWitt, David P. *Introduction to heat transfer*. John Willey & Sons, USA, 1985. ISBN 0-471-80126-7
- [97] R. Shankar Subramanian, *Heat transfer in Flow Through Conduits*, Department of Chemical and Biomolecular Engineering Clarkson University
- [98] Wongyala, Nawin. *Erwärmung elektrischer Leiter*. Diplomarbeit, Universität der Bundeswehr München, 1999
- [99] Eduardo Burguete, *Development of Thermal Model of PMSM for Direct Drive Application*, Master Thesis in Course of Studies Industrial Engineering in subject area Electrotechnic by Erasmus student Eduardo Burguete Archel
- [100] [http://people.ucalgary.ca/~aknigh/electrical\\_machines/synchronous/design/tests.html](http://people.ucalgary.ca/~aknigh/electrical_machines/synchronous/design/tests.html)



